VOLUME 81 NOVEMBER 3, 1977 NUMBER 22

JPCHAx

THE JOURNAL OF PHYSICAL CHEMISTRY

PUBLISHED BIWEEKLY BY THE AMERICAN CHEMICAL SOCIETY

THE JOURNAL OF

PHYSICAL CHEMISTRY

Published by the
AMERICAN CHEMICAL SOCIETY
BOOKS AND JOURNALS DIVISION

D. H. Michael Bowen, Director

Marjorie Laflin, Assistant to the Director

Editorial Department: Charles R. Bertsch, Head; Marianne C. Brogan, Associate Head; Joseph E. Yurvati, Assistant Editor

Magazine and Production Department: Bacil Guiley, Head

Research and Development Department: Seldon W. Terrant, Head

Advertising Office: Centcom, Ltd., 25 Sylvan Road South, Westport, Conn. 06880.

Published biweekly by the American Chemical Society at 20th and Northampton Sts., Easton, Pennsylvania 18042. Second class postage paid at Washington, D.C. and at additional mailing offices.

Editorial Information

Instructions for authors are printed in the first issue of each volume. Please conform to these instructions when submitting manuscripts.

Manuscripts for publication should be submitted to *The Journal of Physical Chemistry*, Department of Chemistry, University of Minnesota, Minneapolis, Minn. 55455. Correspondence regarding **accepted papers and proofs** should be directed to the Editorial Department at the address below.

Page charges of $60.00 per page may be paid for papers published in this journal. Payment does not affect acceptance or scheduling of papers.

Bulk reprints or photocopies of individual articles are available. For information write to Business Operations, Books and Journals Division at the ACS Washington address.

Requests for **permission to reprint** should be directed to Permissions, Books and Journals Division at the ACS Washington address. The American Chemical Society and its Editors assume no responsibility for the statements and opinions advanced by contributors.

Subscription and Business Information

1977 Subscription rates—including surface postage

	U.S.	PUAS	Canada, Foreign
Member	$24.00	$33.00	$34.00
Nonmember	96.00	105.00	106.00
Supplementary material	15.00	19.00	20.00

Air mail and air freight rates are available from Membership & Subscription Services, at the address below.

New and renewal subscriptions should be sent with payment to the Office of the Controller at the ACS Washington address. **Changes of address** must include both old and new addresses with ZIP code and a recent mailing label. Send all address changes to Membership & Subscription Services. Please allow six weeks for change to become effective. **Claims for missing numbers** will not be allowed if loss was due to failure of notice of change of address to be received in the time specified: if claim is dated (a) North America—more than 90 days beyond issue date, (b) all other foreign—more than 1 year beyond issue date; or if the reason given is "missing from files". Hard copy claims are handled by Membership & Subscription Services.

Microfiche subscriptions are available at the same rates but are mailed first class to U.S. subscribers, air mail to the rest of the world. Direct all inquiries to Special Issues Sales, at the ACS Washington address or call (202) 872-4554. **Single issues** in hard copy and/or microfiche are available from Special Issues Sales at the ACS Washington address. Current year $4.75. Back issue rates available from Special Issues Sales. **Back volumes** are available in hard copy and/or microform. Write to Special Issues Sales at the ACS Washington address for further information. **Microfilm** editions of ACS periodical publications are available from volume 1 to the present. For further information, contact Special Issues Sales at the ACS Washington address. **Supplementary material** mentioned in the journal appears in the microfilm edition. Single copies may be ordered directly from Business Operations, Books and Journals Division, at the ACS Washington address.

	U.S.	PUAS, Canada	Other Foreign
Microfiche	$2.50	$3.00	$3.50
Photocopy			
1–7 pages	4.00	5.50	7.00
8–20 pages	5.00	6.50	8.00

Orders over 20 pages are available only on microfiche, 4 × 6 in., 24X, negative, silver halide. Orders must state photocopy or microfiche if both are available. Full bibliographic citation including names of all authors and prepayment are required. Prices are subject to change.

American Chemical Society
1155 16th Street, N.W.
Washington, D.C. 20036
(202) 872-4600

Editorial Department
American Chemical Society
P.O. Box 3330
Columbus, Ohio 43210
(614) 421-6940 ext. 3171

Membership & Subscription Services
American Chemical Society
P.O. Box 3337
Columbus, Ohio 43210
(614) 421-7230

Notice to Authors last printed in the issue of January 13, 1977

THE JOURNAL OF

PHYSICAL CHEMISTRY

Volume 81, Number 22 November 3, 1977

JPCHAx 81(22) 2045–2136 (1977)

ISSN 0022-3654

COMMUNICATIONS TO THE EDITOR

■ Supplementary and/or miniprint material for this paper is available separately (consult the masthead page for ordering information); it will also appear following the paper in the microfilm edition of this journal.

* In papers with more than one author, the asterisk indicates the name of the author to whom inquiries about the paper should be addressed.

AUTHOR INDEX

ANNOUNCEMENT

On the last two pages of this issue you will find reproduced the table of contents of the October 1977 issue of the *Journal of Chemical and Engineering Data.*

THE JOURNAL OF
PHYSICAL CHEMISTRY

VOLUME 81, NUMBER 22 NOVEMBER 3, 1977

Multistep Collisional Deactivation of Chemically Activated Ethylcyclobutane†

Richard J. McCluskey and Robert W. Carr, Jr.*

Department of Chemical Engineering and Materials Science, University of Minnesota, Minneapolis, Minnesota 55455 (Received April 13, 1977)

Publication costs assisted by the University of Minnesota

The photolysis of ketene in the presence of methylcyclobutane, cyclohexane, and oxygen was investigated at pressures between 2 and 0.16 Torr at 298 K. Chemically activated ethylcyclobutane was formed at energies approximately 50 kcal/mol in excess of the threshold energy for unimolecular decomposition to ethylene and butene-1 by the addition of $CH_2(^1A_1)$ to the methyl group of methylcyclobutane. Cyclohexane, which was present as an internal standard, added $CH_2(^1A_1)$ to yield methylcyclohexane which decomposed by at most 7% at the lowest pressures. Experimental evidence was obtained that the collisional deactivation of hot ethylcyclobutane occurs by a multistep process with methylcyclobutane as the principal collision partner. Theoretical calculations, using RRKM theory and a stepladder deactivation model, showed that the data could be fit by deactivation step sizes in the range from 1.5 to 4 kcal/mol. Possibilities for small values of ΔE are briefly mentioned.

Introduction

Chemical activation has been used in numerous studies to investigate intermolecular energy transfer. Typically the bimolecular addition of two species produces an adduct molecule with nonthermal equilibrium amounts of vibrational energy which may either react unimolecularly, if it has sufficient energy to do so, or may loose energy in bimolecular collisions. If only a portion of the energy in excess of the reaction threshold energy is lost on collision, the molecule will cascade through reactive energy states until ultimately either experiencing reaction or being stabilized by being collisionally carried below the reaction threshold. The ratio of decomposed to stabilized molecules may be experimentally measured as a function of total pressure. Using RRKM theory to estimate microcanonical decomposition frequencies, and kinetic theory to estimate the collision rate, information on transition probabilities may be obtained.

In a previous paper[1] on the multistep collisional deactivation of chemically activated methylcyclobutane, formed by addition of $CH_2(^1A_1)$ to cyclobutane, we pointed out that only one reliable study[2] of energy transfer to a polyatomic deactivator molecule had been done in a methylene chemical activation system at that time. Evidence for multistep deactivation of chemically activated spiropentane from $CH_2(^1A_1)$ reaction with methylenecyclopropane has recently been published.[3] The work reported here is a study of energy transfer from chemically activated ethylcyclobutane, formed by the addition of $CH_2(^1A_1)$ to methylcyclobutane, in experiments where methylcyclobutane is the predominant collision partner. The data provide further evidence of the inadequacy of the strong collision assumption for highly vibrationally excited molecules.

In all studies using polyatomic bath gases a stepladder deactivation model has proven adequate to describe experimental data. This is a simple one parameter model, whose lone adjustable parameter, ΔE, the stepladder step size, has the significance of being the average amount of vibrational energy transferred per collision. The variation of ΔE with the type of collider molecule has received most attention, but the dependence of ΔE on the nature of the excited molecule has not. Because of the experimental difficulties associated with low pressure few analyses of

† USERDA document no. E-2026-31.

excited molecule–polyatomic collider systems have been accomplished. With the exception of work[4] on the stabilization of activated secondary alkyl radicals no homologous series has been examined.

Experimental Section

Methylcyclobutane (MCB) was purchased from Chemical Samples Co. (99% stated purity). The impurities determined by gas chromatography did not interfere with the reaction or the product analysis. Phillips research grade cyclohexane was used as an internal standard. Ketene was prepared by pyrolysis of acetic anhydride and purified by several in vacuo trap-to-trap distillations from −78 to −196 °C.

A Osram HBO 500 W/2 superpressure Hg arc lamp was the radiation source. Its radiant intensity distribution was measured photoelectrically between 310 and 370 nm with a Jarrell-Ash 82-000 spectrometer and 1-P28 photomultiplier. Two Pyrex reaction vessels were used: a 55 cm^3 cylindrical cell and a 2000 cm^3 spherical flask. Photolysis times, using unfiltered light, varied from 0.25 to 4 h. Reaction mixture compositions were MCB:ketene:O_2: cyclohexane = 10:1:1:1.

Product analyses were performed on a Barber-Colman 5000 gas chromatograph with a flame ionization detector. A 7 m by 0.65 cm o.d. 3% squalane on firebrick column was used routinely at 35 °C with 140 cm^3/min He carrier at 40 psig. Gas handling was done with a conventional Pyrex vacuum system having glass–teflon valves, and routinely evacuated to 10^{-5} Torr before each experiment. Reactor pressures were determined by Hg manometer. For the 55-cm^3 reactor, the reaction pressure was measured directly. For the 2000-cm^3 reactor, the pressure of the reactants in a small section of vacuum line was measured and the reaction pressure obtained from the volume ratio of reactor to line section.

Mechanism

The important reaction paths for the reaction of $CH_2(^1A_1)$ with MCB are shown in eq 1–10.[5]

$$CH_2CO + h\nu = CH_2(^1A_1) + CO \quad (1)$$

$$CH_2(^1A_1) + \square \rightarrow \square^* \xrightarrow{\omega} \square \quad (2)$$

$$\square^* \xrightarrow{k_a} C_2H_4 + 1\text{-}C_4H_8 \quad (3)$$

$$CH_2(^1A_1) + \square \rightarrow \square^* \xrightarrow{\omega} \square \quad (4)$$

$$\square^* \rightarrow C_2H_4 + 2\text{-}C_4H_8 \quad (5)$$

$$\square^* \rightarrow 2C_3H_6 \quad (6)$$

$$CH_2(^1A_1) + \square \rightarrow \square^* \xrightarrow{\omega} \square \quad (7)$$

$$\square^* \rightarrow 2C_3H_6 \quad (8)$$

$$CH_2(^1A_1) + \square \rightarrow \square^* \xrightarrow{\omega} \square \quad (9)$$

$$\square^* \rightarrow C_2H_4 + i\text{-}C_4H_8 \quad (10)$$

The asterisk represents a chemically activated species, and ω is the collision frequency. Collisional stabilization steps 2, 4, 7, and 9 are represented as occurring by a strong collision mechanism for simplicity only. It will be shown later that deactivation occurs by a multistep process.

Triplet methylene, $CH_2(^3B_1)$, which also results from ketene photolysis, is scavenged by molecular oxygen (reaction 11)[6]

$$CH_2(^3B_1) + O_2 = CO, CO_2, H_2, H_2O \quad (11)$$

If 1-butene were chemically activated by energy partitioning during ethylcyclobutane decomposition, any 1-butene decomposition would cause low experimental values of the amount of decomposed ethylcyclobutane to be obtained. To avoid this possible problem, cyclohexane was used as an internal standard. This also eliminated the analytical difficulty of chromatographic separation of the various butene products. Methylcyclohexane was formed as expected by insertion of $CH_2(^1A_1)$ into the C–H bonds of cyclohexane (reaction 12)

$$CH_2(^1A_1) + c\text{-}C_6H_{12} \rightarrow \quad (12)$$

The stability of methylcyclohexane toward secondary decomposition was tested by photolysis of cyclohexane: ketene:O_2 (10:1:1) mixtures at the lowest experimental pressure (0.16 Torr). A reaction carried out to a 2% yield of methylcyclohexane relative to cyclohexane also produced 0.1% cyclohexene as well as 0.1 and 0.05% of two other products which were not positively identified, but were judged from gas chromatographic analysis to be the C_4 and C_5 species, respectively. Further experiments at higher pressures showed the yield of cyclohexene was not pressure dependent whereas the yields of the C_4 and C_5 products decreased from their low pressure values. Currie, Sidebottom, and Tedder[7] have suggested that gas phase reaction of oxygen with cyclohexyl radicals produces cyclohexene, reaction 13. A similar process has been studied

$$\cdot + O_2 = \quad + HO_2\cdot \quad (13)$$

by Hendry and Schuetzle[8] in the liquid phase oxidation of 1,4-cyclohexadiene to benzene. Cyclohexene formation by reaction 13 is plausible, since the cyclohexyl radical may be generated by H-atom abstraction from cyclohexane by $CH_2(^3B_1)$, or by H and OH which are presumably intermediates in reaction 11. Since the C_4 and C_5 products were not observed at high pressure, there is a possibility they are formed by decomposition of vibrationally excited methylcyclohexane. If this is true the low pressure data could contain slight errors; the relative amounts of decomposed product to stabilized product would be calculated low by at most 7%, with smaller errors at higher pressures. The direction of this error would cause a slight overestimate of the amounts of energy transferred per collision, but when compared with the low pressure random experimental error of about 10%, virtually no effect on the analysis of energy transfer is expected. For this reason we did not investigate the origin of the pressure dependent minor products, or attempt to make corrections to D/S.

Experimental Results

A kinetic analysis of reactions 1–3 predicts that a plot of the ratio of the amount of ECB* which decomposes, to the amount stabilized by collisions (D/S) vs. ω^{-1} will be linear, eq 14, if deactivation occurs by a strong collision

$$D/S = k_a/\omega \quad (14)$$

mechanism, and concave upward if multistep deactivation occurs. Equation 15, which is derived for stepwise

$$D/S = \prod_{j=1}^{n} [(k_j/\omega) + 1] - 1 \quad (15)$$

deactivation by n equally spaced steps, illustrates the latter behavior. The measurement of D/S can be accomplished from the internal standard by noting that the relative yields of ECB* and methylcyclohexane, MCH, are independent of pressure, and that ECB* = $D + S$, thus, $(D + S)/[MCH] = \alpha$ where α is a constant. Dividing by S =

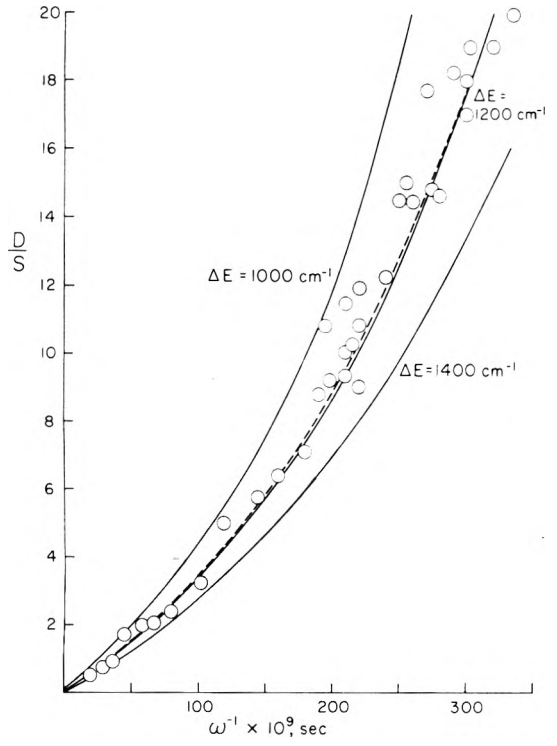

Figure 1. D/S vs. $\omega^{-1} \times 10^9$ in seconds: (O) experimental data; (---) least-squares data fit; (—) RRKM theory model I with $\langle E \rangle$ = 108.5 kcal/mol.

[ECB] yields $(D + S)/S = \alpha$[MCH]/[ECB], and as $p \rightarrow \infty$, $(D + S)/S \rightarrow 1$. Therefore

$$\alpha = |[\text{ECB}]/[\text{MCH}]|_{p=\infty}$$

and the value of D/S can be calculated from

$$D/S = (D + S)/S - 1 = |[\text{ECB}]/[\text{MCH}]|_{p=\infty} |\{\text{MCH}\}/\{\text{ECB}\}|_p - 1 \quad (16)$$

The determination of α was done by averaging [ECB]/[MCH] from seven experiments at pressures between 41 and 52 Torr, where RRKM calculations showed $D/S \leq 0.03$. No variation of [ECB]/[MCH] with pressure could be detected in these experiments. The average value of [ECB]/[MCH] was 1.76 ± 0.10 (±2σ).

The collision diameters used to compute the kinetic theory collision frequency are: cyclohexane, 7.3 Å; ECB, 7.0 Å;[5] MCB, 6.8 Å;[1] ketene, 5.45 Å;[1] O_2, 3.6 Å.[1] All species were assumed to have unit collisional efficiency except O_2, which was assigned an efficiency of 0.25.[9] The collision number for the 10:1:1:1 MCB:ketene:O_2:cyclohexane mixture was calculated to be 1.84×10^7 Torr^{-1} s^{-1}. The experimental results are presented as a plot of D/S vs. ω^{-1} in Figure 1. The data points show the increase of D/S with decreasing ω (decreasing pressure) as predicted by the mechanism. Furthermore, the curvature of the plot was accepted as proof that collisional deactivation of ECB* occurs by a multistep process. The dashed line in Figure 1 is a least-squares data fit, and the solid lines are the result of theoretical calculations described below. The limiting high pressure slope of Figure 1 yields the high pressure rate constant, $k_{a\infty}$. Thus $k_{a\infty}$ was determined to be 2.3×10^7 s^{-1}.

Theoretical Calculations

Rate coefficients for the unimolecular decomposition of ECB* were calculated with RRKM theory. Two harmonic

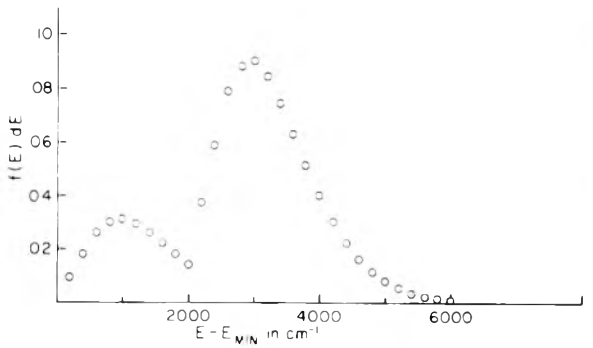

Figure 2. The energy distribution function $f(E)\,dE$ vs. $E - E_{min}$ in cm^{-1}. $\bar{E} = \Sigma\, f(E)\,dE$ = 8 kcal/mol.

oscillator models of ECB* and its activated complex were tested. The first model was adapted from model I for MCB used by Simons et al.,[9] by incorporating the same torsional frequencies for the ethyl side chain as used by Dorer and Rabinovitch[10] for ethylcyclopropane (225 cm^{-1}, 150 cm^{-1}). The second model, taken from Wang and Rabinovitch,[5] uses lower torsional frequencies (190 cm^{-1}, 90 cm^{-1}). The high pressure Arrhenius preexponential factor computed from each model was in agreement with the experimental A factor reported by Wellman and Walters[11] for the thermal decomposition of ECB. The vibrational frequencies for each model are listed in Table I.

The energy distribution of the activated ECB was obtained by the application of microscopic reversibility to the reverse of the $CH_2(^1A_1)$ addition reaction.[12] This distribution was convoluted with the radiation intensity distribution, which was primarily at 313 and 334 nm. The resulting bimodal distribution shown in Figure 2 was used in all calculations.

The steady state matrix equation was solved as before,[1] employing a stepladder model to determine transition probabilities. The matrix grain size was 200 cm^{-1}. The average energy of the excited ethylcyclobutane, $\langle E_{ecb} \rangle$, was treated as a parameter which could be varied within the thermochemical limits calculated below, and the average energy lost per collision, ΔE, was treated as an adjustable parameter.

Thermochemistry. The average internal energy of ethylcyclobutane, $\langle E_{ecb} \rangle$, is given by[13]

$$\langle E_{ecb} \rangle = -\Delta E_0(\text{eq } 2) + \int_0^T [C_v(CH_2) + C_v(\text{MCB})]\, dT' + E_{xs} + E_a - \langle E_{tr} + E_{rot} \rangle \quad (17)$$

where $-\Delta E_0$ (eq 2) = $\Delta H_f^\circ{}_0$ (MCB) + $\Delta H_f^\circ{}_0(CH_2{}^1A_1)$ − $\Delta H_f^\circ{}_0$(ECB) = 101 ± 4 kcal/mol; $\int_0^T [C_v(CH_2) + C_v(\text{MCB})]\, dT'$ is the thermal energy of the reactants, here equal to 5.17 kcal/mol; E_{xs} is the average excess photolysis energy carried by $CH_2(^1A_1)$ at the time of reaction; E_a is the activation energy of eq 2; and $\langle E_{tr} + E_{rot} \rangle$ is the average rotational and translational energy of ECB on formation, here equal to 2 ± 1 kcal/mol. Thermochemical data used are listed in Table II. The maximum value of E_{xs} can be calculated by considering the overall photochemical reaction 18. This assumes that all of the excess photon

$$CH_2CO + \text{MCB} + h\nu\ (313\text{ nm}) = \text{ECB} + CO \quad (18)$$

$$E_{xs,max} = -\Delta E_0(\text{eq } 18) + \Delta E_0(\text{eq } 2) = 9.8 \pm 4 \text{ kcal/mol} \quad (19)$$

energy is carried by $CH_2(^1A_1)$, and is retained at the time reaction occurs. The minimum value of E_{xs} is zero. Assuming E_a = 1 ± 1 kcal/mol, and using $\langle E_{tr} + E_{rot} \rangle$ = 2 kcal/mol leads to $\langle E_{ecb} \rangle_{min}$ = 105 ± 6 kcal/mol and

TABLE I: Frequency Assignments for ECB* and Activated Complex[c]

Assignment	ECB* frequency, cm^{-1} Model I[a]	Model II[b]
C-H stretch	3050, 2975(4), 2952(2), 2901(5)	2946(11), 2854
CH_3 and CH_2 def	1456(6), 1380	1438(7)
CH bend	1300	1310
CH_2 wag	1310, 1250(3)	1243(8)
CH_2 twist	1273, 1224(3)	
C-C stretch	1088	965(8)
CH_3 rock	1070, 1020	
Ring def	1004, 999, 926, 901, 898	
C-CH_3 stretch	920	
C-C stretch	768	735(5)
CH_2 rock	749, 737, 626	
C-H bend	700	
C-C bend	441, 350, 300	324(3), 150
Ring pucker	199	200
C-C torsion	225, 150	190, 90

Assignment	ECB → C_2H_4 + C_4H_6 frequency, cm^{-1} Model I	Model II
CH_2 wag	1310, 1257, 1234	1247(7)
CH_2 twist		
CH_3 rock, C-CH, str		974(7)
C-H bend		
C-CH_2 str	700(2)	724(3)
CH_2 rock	366	
Skel def, C-C bend	366, 350, 200	366(4), 150
Skel bend, C-C bend	225, 200, 150	163(3)

Assignment	ECB → $^1CH_2$ + MCB frequency, cm^{-1}
CH_3 and CH_2 def	1455(4), 1380, 1000(2)
C-CH_3 stretch	Reaction coord
CH_3 rock	400
C-C stretch	300
C-C bend	441, 300, 150
C-C torsion	125, 60

[a] References 6 and 7. [b] Reference 3. [c] Only altered frequencies are shown.

TABLE II: Thermochemical Data[a]

Species	$\Delta H_f^\circ{}_0$, kcal/mol	Ref
MCB	6.7	14
ECB	3.7	15
CH_2CO	−10.7	16
CO	−27.2	17
$CH_2(^1A_1)$	98 ± 4	

[a] All heat capacities were calculated using the statistical mechanical formula for harmonic vibrations.

$\langle E_{ecb}\rangle_{max}$ = 115 ± 2 kcal/mol.

Calculational Results

The results of RRKM calculations for model I are compared with the experimental data in Figure 1. It can be seen that excellent agreement is obtained for $\langle E_{ecb}\rangle$ = 108.5 kcal/mol and ΔE = 1200 cm^{-1}. The sensitivity to deactivation step size is illustrated by the inclusion of calculations for ΔE = 1000 cm^{-1} and ΔE = 1400 cm^{-1}, everything else remaining the same. Calculations based upon model II also give excellent agreement (not shown) at $\langle E_{ecb}\rangle$ = 108.5 kcal/mol, but for ΔE = 1000 cm^{-1} rather than ΔE = 1200 cm^{-1}. The microcanonical rate constants, $k(E)$, calculated for model II are 15–20% smaller than for model I. It was possible to obtain theoretically calculated values of D/S that agreed with the least-squares line of Figure 1 to within ±15% over the 0.16–2 Torr pressure range for $\langle E_{ecb}\rangle$ from 103 to 109 kcal/mol, for both model I and model II. However in the case of model I the range of ΔE giving a fit was 1.7 to 4 kcal/mol, and for model II it was 1.3 to 3.7 kcal/mol. The range of values obtained above is totally consistent with the reaction thermochemistry, and implies a range of 96 to 102 kcal/mol for $\Delta H_f^\circ{}_0[CH_2(^1A_1)] + E_{xs}$.

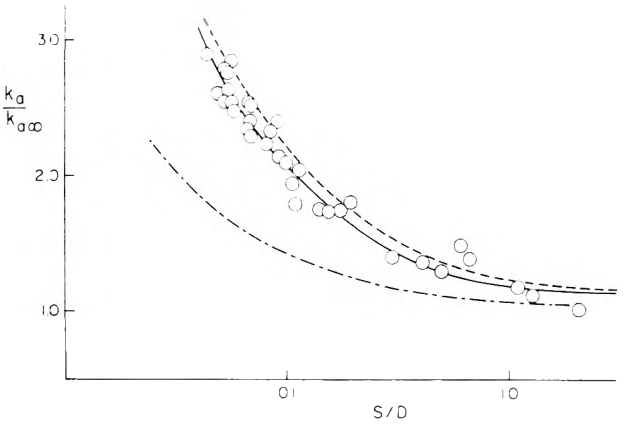

Figure 3. $k_a/k_{a\infty}$ vs. S/D: (O) experimental data; (—) model I, $\langle E\rangle$ = 108.5 kcal/mol, ΔE = 1200 cm^{-1}; (---) model I, $\langle E\rangle$ = 103.8 kcal/mol, ΔE = 600 cm^{-1}; (-·-·-) model I, $\langle E\rangle$ = 115.3 kcal/mol, ΔE = 4000 cm^{-1}.

It should be remembered that the values of $\langle E_{ecb}\rangle$ obtained from plots of D/S vs. ω^{-1} are dependent upon the collision diameters used. An alternative method, in which $k_a/k_{a\infty}$ is plotted vs. S/D, eliminates collision diameter as a parameter to be considered. A mathematical proof of this point is given in the Appendix. The data are shown plotted this way in Figure 3. Also shown in Figure 3 are the results of various theoretical calculations, all using

model I. It can be seen that, as in Figure 1, $\langle E_{ecb} \rangle = 108.5$ kcal/mol and $\Delta E = 1200$ cm^{-1} is in excellent agreement with the data. In all cases a criterion for accepting an RRKM calculation was that the theoretical value of $k_{a\infty}$ must be within ±15% of experiment. Without this criterion the range of data fits becomes larger than obtained by the method of Figure 1. It should be emphasized that accurate experimental values of $k_{a\infty}$ are essential to the use of $k_a/k_{a\infty}$ vs. S/D plots. In a sense, the dependence upon ω has been replaced by dependence upon $k_{a\infty}$, but this is not a disadvantage since $k_{a\infty}$ can be experimentally determined. The other curves have been added to illustrate the fit at lower energy and a small step size ($\langle E_{ecb} \rangle = 103.8$ kcal/mol and $\Delta E = 600$ cm^{-1} for example), and the lack of a fit near the upper thermochemical limit ($\langle E_{ecb} \rangle = 115$ kcal/mol). It should be stressed that the analysis by either the method of Figure 1 or of Figure 3 leads to the same conclusions regarding $\langle E_{ecb} \rangle$ and ΔE. In each case the values of ΔE that produce the closest agreement with experiment are about 3–3.5 kcal/mol, although other values within the stated range cannot be ruled out.

Discussion

The values for ΔE are the lowest yet obtained for relatively large polyatomic deactivator molecules by fitting the low pressure "upturn" region. Stepsizes could be underestimated if f(E) dE were much narrower than shown in Figure 2, there were a gross error in the RRKM model, or if $(ECB/MCH)|_{p=\infty}$ were greatly overestimated. None of these is considered likely. It has been shown[13] that use of a delta function approximation in place of the distribution function derived from microscopic reversibility raises ΔE only by about 1 kcal/mol. Two RRKM models were employed, and there is no reason to doubt the accuracy of the thermal rate data for ethylcyclobutane decomposition.[11]

Early chemical activation experiments[18] producing excited cyclopropane demonstrated the transfer of large amounts (>10 kcal/mol) of vibrational energy per collision. These results were confirmed by the work of Setser's laboratory on chemically activated 1,1,1-trifluoroethane and 1,2-dichloroethane.[19] Recent energy transfer results, all utilizing the stepladder deactivation model, have given estimates for ΔE of 7 kcal/mol for chemically activated spiropentane[3] and 4–6 kcal/mol for chemically activated methylcyclobutane.[1] Small stepsizes have been reported for deactivation of photoactivated cycloheptatriene.[20] The present study contributes additional evidence to what appears to be a trend of decreasing deactivation step size with increase in size of the activated molecule. Such a trend, if true, lends support to quasistatistical theories of energy transfer.[21] Further research is in progress to obtain additional information on this point.

Exceptions to a step size–molecular complexity correlation are Rynbrandt and Rabinovitch's[2] study of chemically activated 1,2-dimethylcyclopropane in which they found ΔE to be 11 kcal/mol, and the homologous series of secondary alkyl radicals investigated by Tardy and Rabinovitch.[4] The possibility that the lower ΔE's for MCB[1] and ECB is due to an energy storage capability of the cyclobutane ring cannot be ruled out, although it seems unlikely. No structural dependence of this sort was observed in the comprehensive energy transfer studies reported by Chan et al.[22] and by Troe and Luu.[23] In the case of secondary alkyl radical deactivation, Atkinson and Thrush[20] have posed the question whether radicals interact more strongly with nonradical collision partners, since no decrease in energy transfer was observed when the chain length was varied from butyl to octyl.

Acknowledgment. This work was supported by the U.S. Energy Research and Development Administration under Contract No. EY-76-S-02-2026.

Appendix

Proof that $k_a/k_{a\infty}$ vs. S/D plots are independent of collision number, Z.

If the stepladder model with no up transitions is a valid representation for energy transfer, then

$$D/S = \prod_{i=1}^{n}\left[1 + \frac{k(E_i)}{ZP}\right] - 1 = \sum_{i=1}^{n}\frac{k(E_i)}{ZP} + {}^1/_2\sum_{i,j}\frac{nk(E_i)k(E_i)}{(ZP)^2} + \cdots + \frac{\prod_{i=1}^{n} k(E_i)}{(ZP)^n} \quad \text{(A.1)}$$

where $k(E_i)$ is the microcanonical decomposition rate constant; Z is the collision number; P is the pressure; and $\Sigma_{i,j}$ implies summation over all pairs $i, j, i \neq j$.

This is strictly true only if the excited molecules are initially monoenergetic. In systems with initial energy distribution f_j

$$D/S = \sum_j f_j \prod_{i=1}^{n(j)}\left[1 + \frac{k(E_i)}{ZP}\right] - 1 \quad \text{(A.2)}$$

Since f_j is independent of the collision number the functional dependence of D/S on Z is still expressed, as in eq A.1, as an nth order polynomial in $(ZP)^{-1}$. Any proof based on eq A.1 also holds for the more general case of eq A.2

$$k_a \equiv ZP(D/S) \quad \text{(A.3)}$$

$$k_{a\infty} = \lim_{p\to\infty} ZP(D/S) = \lim_{p\to\infty}\sum_{i}^{n} k(E_i) + {}^1/_2\sum_{i,j}\frac{k(E_j)k(E_i)}{ZP} + \cdots + \frac{\prod_{i=1}^{n} k(E_i)}{(ZP)^n} = \sum_{i=1}^{n} k(E_i) \quad \text{(A.4)}$$

The variation of $k_a/k_{a\infty}$ with change in Z at any particular value of S/D is equal to $\partial(k_a/k_{a\infty})/\partial Z\,|_{D/S}\,\Delta Z$.

$$k_a/k_{a\infty} = \frac{1}{\sum_{i=1} k(E_i)} ZP\left[\sum_{i=1}^{n}\frac{k(E_i)}{ZP} + \frac{1}{2}\sum_{i,j}\frac{k(E_i)k(E_j)}{(ZP)^2} + \cdots + \prod_{i=1}^{n}\frac{k(E_i)}{ZP}\right] = \mathrm{f}[k(E_i), (ZP)] \quad \text{(A.5)}$$

The important point is that the ratio $k_a/k_{a\infty}$ depends on Z only through the product ZP. Therefore

$$\left.\frac{\partial(k_a/k_{a\infty})}{\partial Z}\right|_{D/S} = \left.\frac{\partial \mathrm{f}[k(E_i), ZP]}{\partial Z}\right|_{D/S} = \left.\frac{\partial \mathrm{f}(k(E_i), ZP)}{\partial (ZP)}\right|_{D/S} \quad \text{(A.6)}$$

$\partial f/\partial(ZP) = (n + 1)$th order polynomial in $(ZP)^{-1}$. Consider $F(D/S, Z, P) = D/S - \Pi_{i=1}^{n}[1 + (k(E_i)/ZP)] + 1 = 0$ by the implicit function theorem of calculus

$$\left.\frac{\partial(D/S)}{\partial P}\right|_Z \left.\frac{\partial Z}{\partial(D/S)}\right|_P \left.\frac{\partial P}{\partial Z}\right|_{D/S} = -1 \qquad (A.7)$$

$$\left.\frac{\partial(ZP)}{\partial Z}\right|_{D/S} = P + Z\left.\frac{\partial P}{\partial Z}\right|_{D/S}$$

$$= P - Z\frac{\partial(D/S)/\partial Z|_P}{\partial(D/S)/\partial P|_Z} \qquad (A.8)$$

From eq A.1 it can be shown that

$$\frac{\partial(D/S)/\partial Z|_P}{\partial(D/S)/\partial P|_Z} = \frac{P}{Z} \qquad (A.9)$$

It follows from eq A.6 and A.8 that

$$\left.\frac{\partial k_a/k_{a\infty}}{\partial Z}\right|_{D/S} = 0$$

Therefore plots of $k_a/k_{a\infty}$ vs. S/D are predicted by the stepladder model to be independent of the collision number, Z. Experimental values of $k_{a\infty}$ were obtained from the slope of D/S vs. ω^{-1} in the high pressure, nearly linear regime. Experimental values of k_a were calculated from the expression $k_a = \omega(D/S)$.

References and Notes

(1) R. J. McCluskey and R. W. Carr, Jr., *J. Phys. Chem.*, **80**, 1393 (1976).
(2) J. D. Rynbrandt and B. S. Rabinovitch, *J. Phys. Chem.*, **74**, 1679 (1970).
(3) H. M. Frey, G. E. Jackson, R. A. Smith, and R. Walsh, *J. Chem. Soc., Faraday Trans. 1*, **71**, 1991 (1975).
(4) D. C. Tardy and B. S. Rabinovitch, *J. Chem. Phys.*, **48**, 5194 (1968).
(5) F. Wang and B. S. Rabinovitch, *Can. J. Chem.*, **54**, 943 (1976).
(6) R. L. Russell and F. S. Rowland, *J. Am. Chem. Soc.*, **90**, 1671 (1968).
(7) J. L. Currie, H. W. Sidebottom, and J. M. Tedder, *J. Chem. Soc., Faraday Trans. 1*, **70**, 1851 (1974).
(8) D. G. Hendry and D. Schuetzle, *J. Am. Chem. Soc.*, **97**, 7123 (1975).
(9) J. W. Simons, W. L. Hase, R. J. Phillips, E. J. Porter, and F. B. Growcock, *Int. J. Chem. Kinet.*, **7**, 879 (1975).
(10) F. H. Dorer and B. S. Rabinovitch, *J. Phys. Chem.*, **69**, 1973 (1965).
(11) R. E. Wellman and W. D. Walters, *J. Am. Chem. Soc.*, **79**, 1542 (1957).
(12) B. S. Rabinovitch and R. W. Diesen, *J. Chem. Phys.*, 30, 735 (1959).
(13) R. J. McCluskey and R. W. Carr, Jr., to be published.
(14) S. W. Benson and H. E. O'Neal, *Natl. Stand. Ref. Data Ser., Natl. Bur. Stand.*, **No. 21** (1970).
(15) W. D. Good, R. T. Moore, A. G. Osborn, and D. R. Douslin, *J. Chem. Thermodyn.*, 6, 303 (1974).
(16) R. L. Nuttall, A. H. Laufer, and M. V. Kilday, *J. Chem. Thermodyn.*, **3**, 167 (1971).
(17) D. D. Wagman, W. H. Evans, I. Halow, V. B. Parker, S. M. Bailey, and R. H. Schumm, *Natl. Bur. Stand. (U.S.) Techn. Note*, **No. 270-1** (1965).
(18) J. W. Simons, B. S. Rabinovitch, and D. W. Setser, *J. Chem. Phys.*, **41**, 800 (1964).
(19) H. W. Chang, N. L. Craig, and D. W. Setser, *J. Phys. Chem.*, **41**, 800 (1964); D. W. Setser and E. E. Seifert, *J. Chem. Phys.*, **57**, 3623 (1972), and references therein.
(20) R. Atkinson and B. A. Thrush, *Proc. R. Soc. (London), Ser. A*, **316**, 131 (1970).
(21) Y. N. Lin and B. S. Rabinovitch, *J. Phys. Chem.*, **74**, 3151 (1970); R. B. Serauskas and E. W. Schlag, *J. Chem. Phys.*, **45**, 3706 (1966).
(22) S. C. Chan, B. S. Rabinovitch, J. T. Bryant, L. D. Spicer, T. Fujimoto, Y. N. Lin, and S. P. Pavlou, *J. Phys. Chem.*, **74**, 3160 (1970).
(23) J. Troe and S. H. Luu, *Ber. Bunsenges. Phys. Chem.*, **77**, 325 (1973).

An Analysis of Three Mechanisms for the Production of $Hg(^3P_1)$ from $Hg(^1P_1)$ by CO

Alan L. Rockwood and E. A. McCullough, Jr.*

Department of Chemistry and Biochemistry UMC 03, Utah State University, Logan, Utah 84322

(Received June 3, 1977)

Publication costs assisted by the Division of Research, Utah State University

Three mechanisms for the formation of $Hg(^3P_1)$ from $Hg(^1P_1)$ in the presence of CO are considered. In the first, electronically excited $CO(a^3\Pi)$ serves as an intermediate in the formation of $Hg(^3P_1)$. In the second, $CO^\dagger$ in a highly excited vibrational state but electronic ground state serves as an intermediate. The third mechanism is a one-step quenching of $Hg(^1P_1)$ to $Hg(^3P_1)$ by CO. Relative 254-nm emission from $Hg(^3P_1)$ is calculated as a function of [CO] for each mechanism using known and estimated rate constants. The first mechanism is shown to be inconsistent with experiment, and the second is shown to be unlikely. The third mechanism gives excellent agreement with experiment.

Introduction

It has been found that the ^3P_J states of Hg and Cd are formed from the respective $^1P_1$ states in the presence of a wide variety of monatomic and simple polyatomic quencher gases.[1-5] The mechanism for this process has been subject to some uncertainty. The Cd experiments have been interpreted in terms of a simple one-step quenching of $^1P_1$ to ^3P_J,[4,5] while in the Hg experiments two-step mechanisms involving internally excited quencher molecules as intermediates have also been suggested.[1-3] Except in favorable cases (e.g., the noble gas quenchers) it is not usually possible to decide immediately which mechanism is correct.

The effect was first observed when Hg was irradiated at 185 nm to produce $Hg(^1P_1)$.[1] In the presence of N_2 or CO 254-nm emission was observed, indicating the presence of $Hg(^3P_1)$. In the absence of quencher gas no emission was observed. When the 254-nm emission was corrected for quenching of $Hg(^3P_1)$ by N_2 or CO and the reciprocal relative intensity, $1/I_{254}^{corr}$, was plotted against the reciprocal quencher pressure the result was linear over the pressure range 0 to >100 Torr.[2] A two-step mechanism in which $N_2(A^3\Sigma)$ or $CO(a^3\Pi)$ served as an intermediate in the production of $Hg(^3P_1)$ was proposed,[1-3] although two other mechanisms were noted as possibilities. One alternative featured a vibrationally excited quencher molecule in its electronic ground state as intermediate, while the other was a simple one-step quenching of $Hg(^1P_1)$ to $Hg(^3P_1)$.

In an attempt to discriminate between these three mechanisms, we carried out a series of calculations to see if the experimental data with CO as quencher could be reproduced.

Calculations

All three mechanisms begin with the following steps:

$$Hg + h\nu(185\ nm) \rightarrow Hg(^1P_1) \quad (1)$$

$$Hg(^1P_1) \rightarrow Hg + h\nu(185\ nm) \quad (2)$$

$$Hg(^1P_1) + CO \rightarrow \text{quenching} \quad (3)$$

In these and subsequent reactions, if the electronic state of a species is not specified, the ground state is implied. Reaction 3 includes *all* processes which remove $Hg(^1P_1)$ *regardless* of the final products. The steady state $Hg(^1P_1)$ concentration is given by

$$[Hg(^1P_1)] = I_{185}^{abs}/(k_2 + k_3[CO]) \quad (4)$$

where I_{185}^{abs} is the light intensity absorbed per unit volume. We now consider the three possible mechanisms for producing $Hg(^3P_1)$.

A. *Electronic Intermediate Mechanism (EIM).* This mechanism is based on the reactions

$$Hg(^1P_1) + CO \rightarrow Hg + CO(a^3\Pi) \quad (5)$$

$$CO(a^3\Pi) + Hg \rightarrow Hg(^3P_1) + CO \quad (6)$$

$$CO(a^3\Pi) + CO \rightarrow \text{quenching} \quad (7)$$

$$CO(a^3\Pi) \rightarrow CO + h\nu(206\ nm) \quad (8)$$

The experimental data were corrected for the quenching of $Hg(^3P_1)$ so there is no need to include this step in the mechanism; the corrected emission at 254 nm is simply proportional to the rate of reaction 6. Previous treatments of the EIM have failed to give proper consideration to reaction 7. In fact, it will be shown that the inclusion of this step completely invalidates the EIM.

Applying the steady state approximation to $CO(a^3\Pi)$ and employing eq 4 we obtain

$$1/I_{254}^{corr} = (k_2 + k_3[CO])(k_6[Hg] + k_7[CO] + k_8)/k_5k_6I_{185}^{abs}[Hg][CO] \quad (9)$$

or

$$1/I_{254}^{corr} = A_{EIM}(1 + k_2/k_3[CO])(1 + k_8/k_6[Hg] + k_7[CO]/k_6[Hg]) \quad (10)$$

where A_{EIM} is a proportionality factor which depends on rate constants, the light absorbed, etc., but not on [CO]. Equation 10 contains a term linear in 1/[CO] multiplied by a correction factor linear in [CO]. In order for eq 10 to adequately represent the experimental data, which are linear in 1/[CO], the correction factor must be essentially constant over the pressure range of the experiments.

The values of k_7 and k_8 are respectively 1.2×10^{-10} cm^3 molecule^{-1} s^{-1} [6] and 1×10^2 s^{-1}.[7] Note that k_7 is a very large rate constant. We estimate that $k_6 < 5 \times 10^{-10}$ cm^3 molecule^{-1} s^{-1} because the rate constants for the total quenching of $CO(a^3\Pi)$ by most molecules are smaller than this.[6] Using the upper limit on k_6, the correction factor in eq 10 varies from near unity at $P_{CO} = 0$ to 2×10^4 at $P_{CO} = 100$ Torr with $P_{Hg} = 1.4 \times 10^{-3}$ Torr. Thus, the correction term is very far from remaining constant, and the EIM is immediately suspect.

The possibility that eq 10 appears linear in 1/[CO] because $k_2/k_3[CO] \gg 1$ over the whole pressure range can also be ruled out. The upper limit for k_2 is 7.7×10^8 s^{-1}, the value in the absence of radiation imprisonment.[8] For $Cd(^1P_1)$ reaction 3 has a cross section of 140 Å^2;[9] therefore, we conservatively estimate that for $Hg(^1P_1)$ the cross section must be >14 Å^2, leading to $k_3 > 7 \times 10^{-11}$ cm^3 molecule^{-1} s^{-1}. Using these limits, at $P_{CO} = 100$ Torr $k_2/k_3[CO] < 3$, probably very much less. Thus, the hypothesis that $k_2/k_3[CO] \gg 1$ is untenable for pressures greater than about 50 Torr.

Figure 1 shows a plot of eq 10 using the ratios $k_2/k_3 = 1.1 \times 10^{19}$ molecule cm^{-3} and $k_7/k_6 = 0.24$ obtained from the limiting rate constants discussed above. Some experimental points extracted from Figure 6 of ref 2 are also shown. Clearly, the EIM is not in accord with experiment.

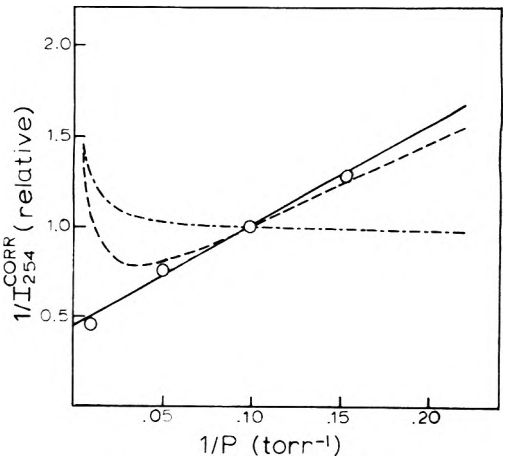

Figure 1. Double reciprocal plots for the EIM (– · –), VIM (– – –), and the DM (——) using the parameters discussed in the text. The experimental data (open circles) are from ref 2. The intensities have been normalized to unity at 0.1 Torr^{-1}.

B. *Vibrational Intermediate Mechanism (VIM).* In the VIM the intermediate is assumed to be vibrationally, but not electronically excited. The reactions are

$$Hg(^1P_1) + CO \rightarrow Hg + CO^\dagger \quad (11)$$

$$CO^\dagger + Hg \rightarrow Hg(^3P_1) + CO \quad (12)$$

$$CO^\dagger + CO \rightarrow 2CO \quad (13)$$

$$CO^\dagger \rightarrow CO + h\nu\ (\text{infrared}) \quad (14)$$

In this mechanism $CO^\dagger$ refers to the complete manifold of vibrational levels for which reactions 11 and 12 are energetically possible, $v = 21$–30. At steady state

$$1/I_{254}^{corr} = A_{VIM}(1 + k_2/k_3[CO])(1 + k_{14}/k_{12}[Hg] + k_{13}[CO]/k_{12}[Hg]) \quad (15)$$

which again consists of a term linear in 1/[CO] multiplied by a correction factor.

A proper analysis of the VIM requires some care. In particular, eq 15 must be applied cautiously since it lumps all the $CO^\dagger$ vibrational levels together, whereas complex, multistep sequences are actually involved, especially in those processes symbolized by reactions 13 and 14. We have based our analysis on a simple model which can be interpreted correctly in terms of eq 15.

Suppose that reaction 11 populates the first n accessible levels with the same rate constant, k_{11}, for each level while reaction 12 quenches the n levels with the same rate constant, k_{12}, for each. At low CO pressure there is no vibrational relaxation, and each level will have the same population. If the CO pressure is now raised to a point where relaxation is no longer negligible but still slow compared to quenching, the effective rate constant, k_{13}, for relaxation of the manifold is k_{13}^{21}/n where k_{13}^{21} is the relaxation rate constant for level 21. This result can be derived rigorously, but it is easily seen from qualitative arguments. Only relaxation from level 21 depletes the population of the manifold since for any higher level the molecules removed are added to the level directly below and remain in the manifold. If relaxation is only a small perturbation, we can compute the relaxation rate by using the population of level 21 in the absence of relaxation. Mathematically speaking, such a calculation is correct to first order in (relaxation rate/quenching rate). In the absence of relaxation the population of level 21 is $1/n$ times the population of the manifold, so k_{13} is $1/n$ times the rate

constant for relaxation of level 21. Assuming single quantum transitions only, precisely the same result obtains for the effective infrared emission rate constant k_{14}. At high [CO] this treatment generally *underestimates* k_{13} and k_{14}.

From an examination of eq 15 it is evident that $1/I_{254}^{corr}$ vs. 1/[CO] has a positive slope at low [CO], while at high [CO] the slope is negative. That is, there is a minimum in the curve at some [CO], and for the VIM to agree with experiment, this minimum must occur at $P_{CO} > 100$ Torr. Our calculations show that the break in the curve at the minimum is rather sharp.

Extrapolation of emission rate constants for $v = 1$–14 suggests a value of $\sim 3 \times 10^2$ s^{-1} for k_{14}^{21}.[10] A similar extrapolation of relaxation rate constants for $v = 1$–15[11] leads to an estimate of $5 \pm 2 \times 10^{-15}$ cm^3 molecule^{-1} s^{-1} for k_{13}^{21}. Based on the model discussed previously, we choose k_{13} to be in the range 5×10^{-16} to 5×10^{-15} cm^3 molecule^{-1} s^{-1} and k_{14} to be in the range 3×10^1 to 3×10^2 s^{-1}. The larger values apply if only the lowest level (level 21) participates in the mechanism while the smaller values are appropriate if all ten levels contribute roughly equally. We shall see that with the value of k_{12} required to fit the experimental data, k_{14}/k_{12}[Hg] is negligible, hence the precise value of k_{14} is unimportant.

Figure 1 gives a plot of eq 15 using $k_2/k_3 = 4.3 \times 10^{17}$ molecule cm^{-3} and $k_{13}/k_{12} = 2 \times 10^{-5}$. The sharp upward break at low 1/[CO] is characteristic of the VIM and in clear disagreement with experiment. The crucial questions are: what is the smallest value of k_{12} that will shift the minimum above 100 Torr, and is this value acceptable?

The minimum can be located from the equation

$$d(1/I_{254}^{corr})/d(1/[CO]) = 0 \quad (16)$$

which gives (neglecting the small effect of reaction 14)

$$[CO]_{min} = (k_2 k_{12}[Hg]/k_3 k_{13})^{1/2} \quad (17)$$

If the VIM is to agree with experiment at low pressure, k_2/k_3 must be 4.3×10^{17} molecule cm^{-3}. Applying the conditions $P_{Hg} = 1.4 \times 10^{-3}$ Torr, $(P_{CO})_{min} > 100$ Torr, and $k_{13} > 5 \times 10^{-16}$ cm^3 molecule^{-1} s^{-1}, we obtain $k_{12} > 2.8 \times 10^{-10}$ cm^3 molecule^{-1} s^{-1} (cross section >55 Å^2). The uncertainty due to model-independent factors (e.g., extrapolations) is about ±50%. We will consider possible errors in k_{12} introduced by the model itself in a later section. For now, we merely point out that the required k_{12} is very large.

C. *Direct Mechanism (DM).* The direct mechanism consists of a single step

$$Hg(^1P_1) + CO \rightarrow Hg(^3P_1) + CO \quad (18)$$

The rate law is

$$1/I_{254}^{corr} = A_{DM}(1 + k_2/k_3[CO]) \quad (19)$$

Of the three mechanisms, the DM is the only one giving a linear rate law without a correction factor.

The DM will fit the experimental data exactly if we choose $k_2/k_3 = 4.3 \times 10^{17}$ molecule cm^{-3}, as Figure 1 shows.

Discussion

The EIM with CO as quencher cannot be made to fit the experimental data using the known value of k_7 and any reasonable value of k_6. Even if k_6 had the impossibly large value of 5×10^{-8} cm^3 molecule^{-1} s^{-1} (cross section of 10 000 Å^2), the EIM still would not come close to agreeing with experiment. It may be concluded that this mechanism gives no contribution to the 254-nm emission. Some CO($a^3\Pi$) may indeed be produced by $Hg(^1P_1)$, but it is removed in reaction 7 far too rapidly to lead to $Hg(^3P_1)$. The fact that 254-nm emission is observed with noble gas quenchers shows that the EIM is not mandatory.[3]

For the VIM, analysis based on a simple model indicates that k_{12} must be greater than about 2.8×10^{-10} cm^3 molecule^{-1} s^{-1} if this mechanism is to be acceptable. This value is improbably, but not impossibly, large. However, when coupled with the fact that the VIM cannot be universal, as the noble gas experiments show, the very large k_{12} required seems sufficient reason to discard the VIM if more plausible alternatives exist.

One may, of course, take exception to this conclusion by arguing that it is based upon an oversimplified model. In order to assess the sensitivity of the model to the assumptions made, we carried out exact computer calculations on the VIM, explicitly including all ten vibrational levels with different rate constants k_{12}^v, k_{13}^v, and k_{14}^v for each. The k_{13}^v and k_{14}^v were extrapolated as described previously; the relative k_{12}^v were varied to check the error introduced by assuming them to be independent of v. We found that the model was quite insensitive to the extrapolations used for k_{13}^v and k_{14}^v and the relative values of the k_{12}^v, provided the largest and smallest values were within an order of magnitude of each other. In particular, the approximate formula for the minimum in terms of average rate constants, eq 17, agreed with the exact calculations to ±30% over a wide range of conditions. Thus, we are justified in basing our conclusions about the VIM on the simplified model, especially since the model usually errs on the conservative side.

Furthermore, there is ample experimental evidence which suggests that quite probably only level 21 would be important in the VIM, in which case the model becomes exact. The vibrational distributions produced in the quenching of $Hg(^3P_{1,0})$ by CO, NO, and HF and $Na(^2P)$ by CO have been measured,[12] and in all cases the rate constants fall off very rapidly for vibrational levels with energies above about 50% of the available energy. The threshold level for reaction 12, level 21, has an energy of 4.9 eV, appreciably more than half the available energy, 6.7 eV. Therefore, reaction 11 may be effectively limited to level 21, unless the rate constants for reaction 12 increase with vibrational level rapidly enough to offset the expected decrease in rate constants for reaction 11. If only level 21 does participate, then the lower limit on k_{12} increases tenfold to $\sim 2.8 \times 10^{-9}$ cm^3 molecule^{-1} s^{-1}, and the VIM almost certainly can be ruled out.

In both the EIM and VIM we have made the simplifying assumption that quenching collisions between internally excited CO and Hg (reactions 6 and 12) primarily give $Hg(^3P_1)$. If some quenching collisions yield products other than $Hg(^3P_1)$, then k_6 and k_{12} would be replaced with the rate constants for total quenching (A_{EIM} and A_{VIM} would also assume different values, of course); however, our conclusions regarding the validity of these two mechanisms would remain unaltered.

Our treatment of the DM ignores $Hg(^3P_2)$ and $Hg(^3P_0)$, which almost certainly are formed.[4] A detailed treatment, including individual production, quenching, and interconversion steps for $^3P_{2,1,0}$, yields exactly the same rate law as eq 19. The $^3P_{2,0}$ species merely provide alternative paths for the formation and destruction of $^3P_1$, and the relative contributions of these various paths cannot be determined from the steady-state Hg experiments.

The DM is quite capable of reproducing the experimental data over the entire pressure range. The value of k_2/k_3 required to fit the data is acceptable, for if the upper limit on k_2 is 7.7×10^8 s^{-1} (the unimprisoned value), the corresponding upper limit on k_3 is 1.8×10^{-9} cm^3 molecule^{-1}

s^{-1}, giving an upper limit cross section of 360 Å for reaction 3.[2] This value is not incompatible with that observed for Cd.[9] Note that it is the *total* quenching rate constant, k_3, which appears in eq 19; relative intensity data give no information about k_{18}, except it obviously cannot be zero and it must be $\leq k_3$.

For quenchers other than CO and the noble gases, little can be said with certainty. It seems likely that the reactions analagous to 7 and 13 would be rapid for many molecules, making the EIM and VIM unfavorable prospects. Furthermore, the formation of $Hg(^3P_1)$ occurs with so many different quenchers that a common mechanism seems probable. The DM is the best candidate among the three mechanisms considered here.

In summary, our conclusions for the production of $Hg(^3P_1)$ from $Hg(^1P_1)$ by CO are as follows: (a) the EIM cannot be the dominant mechanism; (b) the VIM is probably not the dominant mechanism; (c) the DM is the most likely mechanism.

References and Notes

(1) T. A. Gover and H. G. Bryant, Jr., *J. Phys. Chem.*, **70**, 2070 (1966).
(2) A. Granzow, M. Z. Hoffman, N. N. Lichtin, and S. K. Wason, *J. Phys. Chem.*, **72**, 3741 (1968).
(3) V. Madhaven, N. N. Lichtin, and M. Z. Hoffman, *J. Phys. Chem.*, **77**, 875 (1973).
(4) P. J. Young, G. Greig, and O. P. Strausz, *J. Am. Chem. Soc.*, **92**, 413 (1973).
(5) W. H. Breckenridge and J. Fitzpatrick, *J. Phys. Chem.*, **80**, 1955 (1976).
(6) G. W. Taylor and D. W. Setser, *J. Am. Chem. Soc.*, **93**, 4930 (1971).
(7) C. H. Johnson and R. S. Van Dyck, Jr., *J. Chem. Phys.*, **56**, 1506 (1972).
(8) J. G. Calvert and J. N. Pitts, Jr., "Photochemistry", Wiley, New York, N.Y., 1966, p 86.
(9) P. D. Morten, C. G. Freeman, R. F. C. Claridge, and L. F. Phillips, *J. Photochem.*, **3**, 285 (1974).
(10) G. Hancock and I. W. M. Smith, *Appl. Opt.*, **10**, 1827 (1971).
(11) H. T. Powell, *J. Chem. Phys.*, **59**, 4937 (1973).
(12) G. Karl, P. Kruus, and J. C. Polanyi, *J. Chem. Phys.*, **46**, 224 (1967); G. Karl, P. Kruus, J. C. Polanyi, and I. W. M. Smith, *ibid.*, **46**, 244 (1967); H. Heydtmann, J. C. Polanyi, and R. T. Tazuchi, *Appl. Opt.*, **10**, 1755 (1971); Y. Fushiki and S. Tsuchiya, *Chem. Phys. Lett.*, **22**, 47 (1973); D. S. Y. Hsu and M. C. Lin, *ibid.*, **42**, 78 (1976).

Theoretical and Experimental Studies of Polyion Effect on Ionic Reactions. 1. Reactions of Two Doubly Charged Counterions

Masaaki Ishikawa

Department of Polymer Chemistry, Kyoto University, Kyoto, Japan

(Received September 9, 1976; Revised Manuscript Received July 26, 1977)

The acceleration factor of the reaction of two doubly charged counterions in the presence of a polyion was calculated using the Lifson–Katchalsky method of treating polyion solutions. The theoretical values were of the right order of magnitude when compared with various experimental values. The dependence of the acceleration factor on the radius, the charge spacing, and the concentration of a rodlike polyion were calculated. Good agreement between the theoretical and experimental values was found with regard to the dependence of the acceleration factor on the polyion concentration. The relationship between the acceleration factor and the distribution of divalent counterions in the vicinity of the polyion was also discussed. According to the calculation, the decrement of the dielectric constant of the solvent in the vicinity of polyion only has a small effect on the acceleration factor. The acceleration factor for reactions of two doubly charged counterions is theoretically due to the increment of the activation entropy. The author's experimental results agreed with this prediction. The effect of the molecular charge (MC) on the acceleration factor and activation parameters for the Hg^{2+}-induced aquation of a cobalt complex with a 2+ charge was examined in solutions of oligo- and polyphosphates. The acceleration factor became significant at MC = 5, however, the acceleration parameters behaved in a complicated manner at MC = 4 and 5. It was concluded that the Lifson–Katchalsky theory is applicable to polyion effects on reactions of two doubly charged counterions.

I. Introduction

A great number of experimental and theoretical studies of the polyion effect on interionic reactions have been carried out.[1-13] Morawetz[2,3] interpreted the effect in terms of a concentration of reactants in a polyion domain. He explained some experimental data on the basis of a simple model for the polyion solution in which a region containing a uniform density of fixed charges is in Donnan equilibrium with a region from which the fixed charges are excluded.[2,3] He also calculated an effective local concentration of reactants from kinetic and dialysis data.[6] However, he did not calculate the acceleration factor theoretically except in a few cases.[3] Ise et al.[7-11] explained the polyion effect in terms of an ionic activity coefficient and proposed that the acceleration effect may be interpreted in terms of an activated complex in analogy to Brønsted's theory using the Manning treatment of polyion solutions. Good agreement between theoretical and experimental values for the acceleration factor was obtained in some interionic reactions between oppositely charged species.[10] However, they could not calculate theoretical values of the acceleration factor for interionic reactions between similarly charged species, nor interpret its dependence on the radius and charge spacing of a rodlike polyion.

Although the effect of simple salts on the activation parameters of interionic reactions has been clearly established, there has been no consensus of opinion with regard to polyions. Ise et al.[8] discussed the desolvation of reactants by polyions as reflected in the activation parameters. On the other hand, Morawetz[5] pointed out that these attempts were unwarranted because a number of factors may contribute to activation parameters, e.g., electrostatic and specific interactions between reactants

and polyions, and the decrement of the dielectric constant of the solvent in the polyion domain. Considering only the electrostatic interactions between reactants and polyions, Mita et al.[10] calculated the activation parameters of a reaction between oppositely charged monovalent ions on the basis of Manning's theory.

Matsui et al.[9] studied the effect of the addition of the oligomer of polyethylenimine on the reaction of bromoacetate and thiosulfate ions. However, the lower limit of the molecular charge on the appearance of the polyion effect on interionic reactions was not made clear, nor was the way in which the activation parameters vary with the addition of oligo ions.

Conway[14] showed theoretically that the dielectric constant varies considerably in the vicinity of polyions having high charge densities, however, there have been no reports on the influence of this factor on the acceleration factor.

In the present report, the following points are treated theoretically and experimentally using some reactions between divalent cations; (1) a comparison of the theoretical and experimental values of the acceleration factor; (2) the effect of the decrement of the dielectric constant of the solvent around polyions on the acceleration factor; (3) a comparison of theoretical and experimental values of the activation parameters; and (4) the effect of the molecular charge of oligo ions on the acceleration factor and the activation parameters.

II. Experimental Section

Materials. Sodium polyethylenesulfonate (NaPES) and sodium polystyrenesulfonate (NaPSS) were obtained from Polysciences Inc. The degrees of polymerization ($\bar{P}$) were reported as 750 and 500, respectively. These polymer solutions were purified by dialysis and treatment with ion-exchange resins. The concentration of these polyions was determined by conductometric titration with a strong polycation. Sodium polyphosphate having a high degree of polymerization, reported as 5000, was obtained by Dow Chemical Co. However, it took about 1 week to dissolve the polyion in water. As polyphosphate is easily hydrolyzed in water, $\bar{P}$ decreased considerably during this period. The end group of the polyphosphate is a weak acid the concentration which was determined by conductometric back-titration with NaOH. The concentration of the polyion was determined by conductometric titration with a strong polycation. However the concentration of weak acid is so low that it could not be determined precisely, and the degree of polymerization was inferred to be 200–300. Sodium polyphosphates (NaPP) with low degrees of polymerization were the same as used previously.[15] The polyphosphate had been purified twice by fractionation from water with acetone, and the number-average degrees of polymerization were 16 and 56. Tri- and tetraphosphate were commercial samples. These NaPP were dried at 120 °C in vacuo for 2 days, and their solutions were stored at 0 °C and used within 10 h to avoid hydrolysis.

The complex $[Co(NH_3)_5Br](ClO_4)_2$ was prepared in a manner similar to that described in ref 9, using 70% $HClO_4$ instead of HNO_3. The salt had an ϵ_{MAX} value of 1.74×10^4 M^{-1} cm^{-1} at 254 nm and was in agreement with the literature. A solution containing $Hg(ClO_4)_2$ and $HClO_4$ was prepared by dissolving HgO (reagent grade) in an excess of $HClO_4$. Cadmium hydroxide was precipitated from a cadmium nitrate solution by treatment with NaOH and was washed exhaustively with water. A solution containing Cd^{2+} and $HClO_4$ was prepared by dissolving the cadmium hydroxide in an excess of $HClO_4$. A solution containing Pb^{2+} and $HClO_4$ was prepared in the same manner as the Cd^{2+} solution. The concentration of Hg^{2+} was determined by conductometric titration with 0.01 N NH_4SCN, and those of Cd^{2+} and Pb^{2+} with 0.01 M EDTA (ethylenediaminetetraacetic acid). $NaClO_4$ and Na_2SO_4 were reagent grade.

Rate Measurement. (1) *Hg^{2+} Induced Aquation.* The reaction is written as

$$Co(NH_3)_5Br^{2+} + Hg^{2+} + H_2O \rightarrow Co(NH_3)_5H_2O^{3+} + HgBr^+$$

As the reaction proceeds, the divalent ions decrease and trivalent ions appear, displacing the divalent reactants in the polyion domain. For this reason, k_2 was obtained from the initial slope. The reaction was followed on a Union stopped-flow spectrophotometer (RA1100).

(2) *Cd^{2+} or Pb^{2+} Induced Aquation.* The decrease of $Co(NH_3)_5Br^{2+}$ was due to both spontaneous and Cd^{2+} or Pb^{2+} induced aquation in the presence of NaPES. The spontaneous aquation accounted for 5–50% of the observed rate. The decrease of the complex due to Cd^{2+} or Pb^{2+} induced aquation was obtained by subtracting the decrease due to the spontaneous reaction from the total decrease. A second-order rate constant for the reactions was calculated from the corrected initial slope. The reactions were followed on a Union high sensitivity UV spectrophotometer (SM401). In the absence of NaPES, Cd^{2+} or Pb^{2+} induced aquation was much slower than spontaneous aquation. Therefore, the second-order rate constant for these reactions could not be measured in the absence of NaPES, and the acceleration factor could not be evaluated.

In all reactions, the initial slope was determined before the conversion of $Co(NH_3)_5Br^{2+}$ to $Co(NH_3)_5H_2O^{3+}$ had reached 5%. The initial concentration of $Co(NH_3)_5Br^{2+}$ was less than a factor of 0.1 lower than those of Hg^{2+}, Pb^{2+}, and Cd^{2+}. Accordingly, the concentration of the triply charged reaction product was so low in this conversion that we could safely ignore the reactive inhibition caused by it.

III. Comparison of the Theoretical Values of the Acceleration Factor with Experimental Data

Theoretical Calculations. The acceleration factor of a reaction between ions A and B in a polyion solution can be represented according to Morawetz et al.[4,5] by

$$k_2/k_{20} = \frac{\int_V C_A(R) \exp(-Z_i\phi) C_B(R) \exp(-Z_A\phi)\, dV}{\bar{C}_A \bar{C}_B} = \frac{C_A(R)}{\bar{C}_A}\frac{C_B(R)}{\bar{C}_B}\int_V \exp(-(Z_A + Z_B)\phi)\, dV \quad (1)$$

$$\phi = \frac{e}{kT}\psi(r)$$

where k_2 is a rate constant for the polyion solution, k_{20} a limiting rate constant at zero ionic strength, $\bar{C}_i$ the average concentration of ion i, $C_i(R)$ the concentration of ion i at the surface of the free volume per polyion (V), r a spatial coordinate, Z_i the signed valency of ion i, $\psi(r)$ the electrostatic potential of the polyion, e the electronic charge, k the Boltzmann constant, and T the absolute temperature. In order to calculate the electrical potential of a rodlike polyion, we must solve the Poisson–Boltzmann equation which can be done analytically only in the absence of added salts. Divalent ions are concentrated in the polyion domain in preference to monovalent ions. Accordingly, even if monovalent ions coexist, $C_i(r)$ of a divalent counterion in the vicinity of the polyion can be approximately estimated from the analytical solution under the following conditions: (1) the concentration of

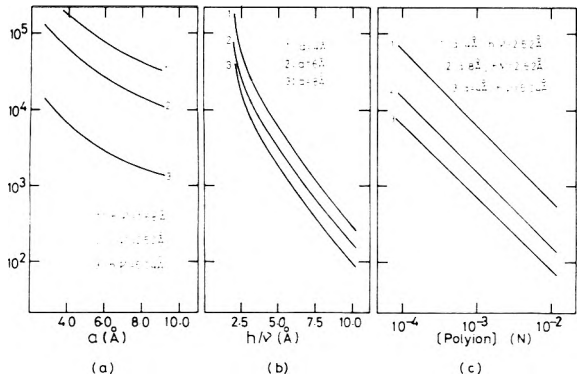

Figure 1. Dependence of the theoretical acceleration factor on (a) the radius of the polyion rod, [polyion] = 10^{-4} N; (b) the charge spacing of the polyion [polyion] = 10^{-4} N; and (c) the polyion concentration, $[A^{2+}] + [B^{2+}]$ = [polyion].

monovalent ions is not much higher than that of the polyion, and (2) the equivalent concentration of divalent reactants is equal to that of the polyion. The acceleration factor calculated from the analytical solution also provides approximate values for the acceleration factor if monovalent ions coexist under the above conditions. Therefore, the author roughly estimated the acceleration factor using the values calculated from the analytical solution.

According to the Lifson–Katchalsky's theory, the polyion carrying ν negative charges is represented by a cylinder of radius a and length h. The counterions are distributed symmetrically around the polyion in a cylinder with radius R. The solution of the Poisson–Boltzmann equation is written as[16]

$$\psi(r) = \frac{kT}{Ze} \ln \left\{ \frac{2}{\beta^2} \frac{C(R)}{\bar{C}} \frac{r^2}{R^2 - r^2} \times \sin^2 (|\beta| \ln Ar) \right\} \quad (2)$$

with λ, $|\beta|$, and A given by

$$\lambda = \nu e^2 / D_0 kTh$$

$$\ln A = -\ln R - (1/|\beta|) \arctan |\beta|$$

$$Z\lambda = \frac{1 + |\beta|^2}{1 + |\beta| \cot \left(|\beta| \ln \frac{R}{a} \right)} \quad (3)$$

where D_0 is the dielectric constant in the bulk phase. The value $C(R)/\bar{C}$ can easily be calculated from the boundary condition ($r = R$, $\psi(R) = 0$). By use of eq 1 and 2, we can calculate the acceleration factor. Equation 1 was transformed as follows:

$$k_2/k_{20} = \alpha = \frac{2}{R^2 - a^2} \left(\frac{C(R)}{\bar{C}} \right)^2 \int_a^R r \exp(-4\phi)\, dr \quad (4)$$

where the acceleration factor was defined as α. A computer was used for the integration using the Newton–Cotes method. The acceleration factor calculated by the above method was denoted by $\alpha_{theo,0}$. The experimental and theoretical values of α are listed in Table II.

Comparison with Experiment. (1) *The Dependence of α on the Radius of the Rodlike Polyion.* In Figure 1a $\alpha_{theo,0}$ is plotted as a function of the radius of the polyion at three constant charge spacings. The concentration of the polyion is 10^{-4} N. It is shown that $\alpha_{theo,0}$ decreases with increasing radius of the rodlike polyion. Morawetz and Vogel[6] studied the effect of NaPES and sodium polymethacryloxyethylsulfonate (NaPMES) on the Hg^{2+} induced aquation of $Co(NH_3)_5Cl^{2+}$. The experimental ratio of α_{NaPES} to α_{NaPMES} was 7.5:1. When the radii of rods of NaPES and NaPMES are taken as 2.5 and 8 Å, respectively, on the basis of their molecular structure, the theoretical ratio is about 8.8:1. Ise and Matsuda[8] reported the effect of NaPP, NaPES, and NaPSS on the Hg^{2+} induced aquation of $Co(NH_3)_5Br^{2+}$. The experimental ratio was 4.2:3.5:1, and the theoretical ratio was 8.9:7.4:1, when the radii of rods were taken as 2, 2.5, and 6.8 Å, respectively. In the author's experiment α_{NaPES}:α_{NaPSS} was 2.3:1 or 2.0:1, while the theoretical ratio was 7.4:1. The agreement between these experimental and theoretical values was qualitative but not quantitative.

TABLE I: Dependence of Acceleration Factor on Polyion Concentration under the Conditions $[A^{2+}] + [B^{2+}]$ = [NaPES] and $[B^{2+}]/[A^{2+}] = 10$

10^4·[NaPES], N	$10^4 k_2$, M^{-1} s^{-1}	k_2/k_2*	$(k_2/k_2)_{theor}$
1.1	17	13	16[a]
2.2	8.8	6.7	8.0[a]
4.4	5.5	4.2	4.0[a]
8.8	2.5	1.9	2.0[a]
17.6	1.3	1.0	1.0[a]
4.6	1.3	6.8	8.0[b]
19	0.38	2.0	2.0[b]
37	0.19	1.0	1.0[b]

[a] A^{2+}, $Co(NH_3)_5Br^{2+}$; B^{2+}, Hg^{2+}, $[H^+] = 5 \times 10^{-3}$ N, this work, at 20.0 °C. [b] A^{2+}, $Co(NH_3)_5N_3^{2+}$; B^{2+}, V^{2+}, $[H^+] = 10^{-4}$ N, by Kim.

(2) *The Dependence of α on the Charge Spacing of the Polyion.* In Figure 1b, $\alpha_{theo,0}$ is plotted as a function of the charge spacing of the polyion (h/ν) at three constant radii of rodlike polyions. The result shows that $\alpha_{theo,0}$ decreases with increasing charge spacing, for example, $\alpha_{theo,0}$ decreases by a factor of 0.1 as the charge spacing is doubled. Since there are no experimental data concerning the effect of the charge spacing on the reactions between divalent cations, theoretical and experimental values could not be compared in this case.

(3) *The Dependence of α on the Polyion Concentration.* In Figure 1c, $\alpha_{theo,0}$ is plotted as a function of polyion concentration under the condition that the equivalent concentration of cationic reactants was equal to that of the polyion. In all cases, $\alpha_{theo,0}$ varies inversely with polyion concentration. A comparison of the experimental and theoretical values of k_2/k_2* for two different reactions is presented in Table I, where k_2* is the rate constant at the concentration marked by an asterisk in the table. The data for the electron transfer reaction were supplied by Kim,[7] and the rate constants were determined under the same condition as described in his paper.[7] The theoretical and experimental values agreed favorably.

(4) *A Comparison of $\alpha_{theo,0}$ with Experiment.* In calculating the theoretical values of α, we used k_{20} for a rate constant in the absence of polyions at a nonzero ionic strength. Accordingly, in order to treat the experimental values of α reported by other authors, we must call attention to the ionic strength, μ, at which k_{20} used by them was measured. Patel[12] used k_{20} determined at very low ionic strength ($\mu \rightarrow 0$) or extrapolated to zero ionic strength using an equation from ref 17. On the other hand, Gould[13] and Shikata,[7] among others, adopted k_{20} determined at high ionic strength ($\mu^{1/2} = 1.0$ or 1.2), since it was experimentally difficult to measure the rate constant of their reactions at low ionic strength. Endicott[17] studied the effect of ionic strength on some electron transfer reactions,

TABLE II: Comparison of Theoretical and Experimental Values of Acceleration Factor

Polyion	10^4-[polyion], N	α_{expt}	$(\alpha_{expt})_{cor}$	$\alpha_{theo,0}$	$\alpha_{theo,II}$
		Hg^{2+} Induced Aquation of Cobalt Complexes			
NaPES	2.2	2.5×10^4	5.0×10^4	6.9×10^4	2.4×10^4 [a]
NaPES	4.4	1.3×10^4	2.6×10^4	3.5×10^4	1.2×10^4 [b]
NaPSS	2.2	1.1×10^4	2.2×10^4	9.5×10^3	9.5×10^3 [a]
NaPSS	4.4	6.7×10^3	1.3×10^4	4.8×10^3	4.8×10^3 [b]
NaPES	11	3.3×10^3	8.3×10^3	1.4×10^4	4.7×10^3 [c]
NaPSS	11	9.5×10^2	2.4×10^3	1.9×10^3	1.9×10^3 [c]
NaPP	11	4.0×10^3	1.0×10^4	1.7×10^4	4.7×10^3 [c]
NaPMES	1.1	2.4×10^4	6.0×10^4	1.6×10^4	1.6×10^4 [d]
NaPES	1.1	1.8×10^5	4.5×10^5	1.4×10^5	4.7×10^4 [d]
		Electron Transfer Reactions			
NaPES	1.1	2.5×10^4	9.3×10^4	1.4×10^5	4.7×10^4 [e]
NaPES	30	7.0×10^2	7.0×10^3	5.1×10^3	1.7×10^3 [f]
NaPES	33	4.1×10^2	4.1×10^3	4.6×10^3	1.6×10^3 [g]
NaPMES	11	2.3×10^3	2.3×10^3	1.6×10^3	1.6×10^3 [h]
NaPES	10	9.5×10^2	9.5×10^3	1.5×10^4	5.2×10^3 [i]

[a] This work, $[Hg^{2+}] = 1.0 \times 10^{-4}$ M, $[Co(NH_3)_5Br^{2+}] = 1.0 \times 10^{-5}$ M, $[H^+] = 5 \times 10^{-3}$ N, at 25.0 °C. [b] This work, $[Hg^{2+}] = 2.0 \times 10^{-4}$ M, $[Co(NH_3)_5Br^{2+}] = 2.0 \times 10^{-5}$ M, $[H^+] = 5 \times 10^{-3}$ N, at 25.0 °C. [c] $Hg^{2+} + Co(NH_3)_5^{2+}$, by Matsuda, ref 8. [d] $Hg^{2+} + Co(NH_3)_5Cl^{2+}$, by Morawetz, ref 6. [e] $Fe^{2+} + Co(NH_3)_5Cl^{2+}$, by Morawetz, ref 1. [f] $Fe^{2+} + Co(NH_3)_5Br^{2+}$, by Shikata, ref 7. [g] $V^{2+} + Co(NH_3)_5N_3^{2+}$, by Kim, ref 7. [h] $Ru(NH_3)_6^{2+} + cis\text{-}Co(en)_2NH_3Cl^{2+}$, by Patel, ref 3. [i] $Cr^{2+} + Co(NH_3)_5C_2H_5COO^{2+}$, by Gould, ref 13.

e.g., between $Co(NH_3)_5Br^{2+}$ and $Ru(NH_3)_6^{2+}$. According to his report, the acceleration factors were 8 at $\mu^{1/2} = 0.2$ and 13 at $\mu^{1/2} = 0.4$. It is inferred that the rate constant at $\mu^{1/2} = 1.0$ or 1.2 is dozens of times as large as that at $\mu = 0$ for reactions of two divalent cations. Therefore, in these cases (f, g, and i in Table II) the experimental values of α were compared roughly with the theoretical values multiplied by 10. In other cases, the reported values of α were corrected by use of k_{20} at $\mu = 0$ which were calculated from the Brønsted and Debye–Hückel equation ($\log (k_2/k_{20}) = 4.08\mu^{1/2}$ at 25 °C). The reported values of α are denoted by α_{expt} and the corrected values by $(\alpha_{expt})_{cor}$. These values are also listed in Table II. The corrected experimental values are in rough agreement with the theoretical values.

IV. The Effect of the Radii of the Counterions on the Acceleration Factor

(1) Gregor and Kagawa[24] solved the Poisson–Boltzmann equation assuming that counterions were rigid spheres of specific size, and the dielectric constant was assigned its bulk value. The electrostatic potential was expressed as

$$\psi(r) = \frac{kT}{Ze} \ln \left\{ \frac{2}{|\beta|^2} \frac{C(R)}{C} Z \frac{r^2}{R^2 - r^2} \times \sin^2 (|\beta| \ln Ar) \right\} \quad (5)$$

$$Z\lambda = \frac{1 + |\beta|^2}{1 + |\beta| \cot \{|\beta| \ln [R/(a + p)]\}} \quad (6)$$

where p is the radius of the counterion. When we substitute a with $a + p$ in eq 2 and 3, coincidence with eq 5 and 6 is obtained. Accordingly, we can consider the effect of the radii of the counterions by estimating the appropriate values of a. In the above section, the author used the values calculated from the molecular structures of charged groups as the radii of rodlike polyions. The radius adopted in this section is denoted by a_p.

The relationship between a, a_p, and p and the estimation of the appropriate radius of the counterions is discussed in Appendix I (supplementary material, see paragraph at end of text regarding supplementary material). When the mean radius of the counterions was taken as 2.9 Å, a_p was 4.3 Å (2.9 + 1.4) for PES and PP. With the use of this value, α_{theo} was again calculated and denoted by $\alpha_{theo,II}$. The corrected value was also listed in Table II. For ref a and b in Table II, α_{NaPES}:α_{NaPSS} = 2.3:1 or 2.0:1, and the theoretical ratio is 2.5:1. For ref c in Table II, α_{NaPP}:α_{NaPES}:α_{NaPSS} = 4.2:3.5:1, and the theoretical ratio is 2.5:2.5:1. For ref d in Table II, α_{NaPSS}:α_{NaPMES} = 7.5:1, while the theoretical ratio is 2.9:1. For the dependence of α on the radius of a rodlike polyion, the agreement between the experimental and theoretical values improved the in the author's experiment (ref a and b in Table II, see section 2). However, the agreement between $(\alpha_{expt})_{cor}$ and $\alpha_{theo,II}$ was less than that between $(\alpha_{expt})_{cor}$ and $\alpha_{theo,0}$. Furthermore, the experimental values of α were often several times larger than $\alpha_{theo,II}$, although they were of the same order of magnitude as $\alpha_{theo,II}$. Alexandrowicz[32,33] pointed out that real polyions do not have the simple geometrical form of the theoretical models and that theoretical values agreed with the experimental values of some thermodynamic quantities when using an effective charge density parameter (λ^*) instead of the charge parameter corresponding to the fully extended chain of polyions (λ). According to Alexandrowicz[33] and Dolar,[21] $\lambda^*/\lambda = 1.3 \sim 2.0$. With this effective charge density parameter, the theoretical values of α became several times larger than the values based on λ (see Figure 1a), bringing them into agreement with the experimental values. It is concluded that the theoretical values of α based on the Lifson–Katchalsky theory agree well with the experimental values when taking account of the effective length of the polyions.

(2) The second-order rate constants for the Pb^{2+} and Cd^{2+} induced aquation of $Co(NH_3)_5Br^{2+}$ were plotted as a function of NaPES in Figure 3. The results showed that the dependence of k_2 on polyion concentration was less in Cd^{2+} induced aquation than in Pb^{2+} induced aquation. This was explained as follows: When the concentration of polyion is less than that of the reactant divalent ions, the two reactant ions compete with each other for the polyion domain. As Dolar et al.[19,20] reported, the lead ion is absorbed more strongly than the cadmium ion since the radius of hydrated lead ion is smaller than that of hydrated Cd^{2+}. Accordingly, the bromopentaminecobalt ion is bound more strongly in Cd^{2+} induced aquation than in Pb^{2+} induced aquation at low polyion concentration, and

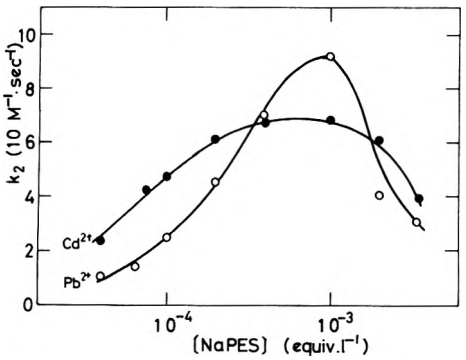

Figure 3. Comparison of the polyion effect for the Cd^{2+} and Pb^{2+} induced aquation of $Co(NH_3)_5Br^{2+}$: $[Pb^{2+}] = 4.4 \times 10^{-4}$ M; $[Cd^{2+}] = 4.6 \times 10^{-4}$ M; $[Co(NH_3)_5Br^{2+}] = 2.2 \times 10^{-4}$ N.

the dependence of k_2 on the polyion concentration is, therefore, less in Cd^{2+} than in Pb^{2+} induced aquation.

V. Relationship beween α and the Local Concentration of Reactants in the Polymer Domain

The discussion in this section was described in Appendix II (supplementary material).

VI. Effect of α on a Change in the Dielectric Constant around the Rodlike Polyion

In order to examine the influence of a change of the dielectric constant in the vicinity of the polyion on α, the acceleration factor was calculated using Conway's method.[14] The differential dielectric constant (D_d) and the integral one (D_i) were expressed as a function of the electric field intensity (E) by Graham[28,29] and Laidler[30] as

$$D_d = \frac{dQ}{dE} = \frac{D_0 - n^2}{1 + mE^2} + n^2 \tag{10}$$

$$D_i = \frac{Q}{E} = \frac{D_0 - n^2}{m^{1/2}E} \arctan (m^{1/2}E) + n^2 \tag{11}$$

where Q was the electric displacement, the square of the optical refractive index n^2 was equal to 1.78, the constant m was found to be equal to 1.08×10^{-8} esu^{-2}, and the dielectric constant in the bulk phase D_0 was taken as 78.54 at 25 °C. The Poisson–Boltzmann equation was transformed to

$$\frac{d^2\psi}{dt^2} = \frac{1}{D_d}\left\{-4a^2\pi\sigma \exp 2t - (D_i - D_d)\frac{d\psi}{dt}\right\} \tag{12}$$

where $t = \ln (r/a)$ and $\sigma = Ze\bar{C} \exp(-Z\phi)$, and the boundary conditions were written as

$$\left(D_i\frac{d\psi}{dt}\right)_0 = -\frac{2ev}{h}\left(\frac{d\psi}{dt}\right)_{\ln(R/a)} = 0$$

Equation 12 was solved approximately by computer using the Runge–Kutta–Gill method. The unknown parameter, $\psi(R)$, was obtained by Conway's[14] method. The acceleration factor was calculated by use of the Lagrange interpolation formula through three points. The interval $0 \leq t \leq \ln (R/a)$ was divided into 1000 subdivisions, and α was expressed as

$$\alpha = \frac{2a^2}{(R^2 - a^2)} \frac{\ln (R/a)}{12000} \sum_{i=1}^{1001} A_i t_i \exp(-2\phi_i + 2t_i) \tag{13}$$

where the integration coefficient A_i is given as follows: $A_i = 4(i = 1, 1001)$, $A_i = 8(i = 1, 3, 5, \ldots, 999)$, $A_i = 16(i = 2, 4, 6, \ldots, 1000)$. The acceleration factor calculated in this way was denoted by $\alpha_{theo,I}$. The reference value of α was calculated using the same method under the condition $D_i = D_d = D_0$. This value was denoted by $\alpha_{theo,R}$. $\alpha_{theo,R}$ was less than 3% larger than the value calculated using eq 2 and the Newton–Cotes method($\alpha_{theo,0}$). $\alpha_{theo,I}$ and $\alpha_{theo,R}$ are listed in Table III. $\alpha_{theo,I}$ was always larger than $\alpha_{theo,R}$, but the difference between them was not large. Furthermore, the difference between $\alpha_{theo,I}$ and $\alpha_{theo,R}$ became smaller as a or h/ν increased. From these results, it was concluded that the effect of a change in the dielectric constant was sufficiently small to estimate α roughly. The dielectric constant, the electric field intensity, the electrostatic potential, and the ratio of counterion condensation (b) is shown as a function of r in Figure 5. The electrostatic potential was corrected for the condition of $\psi(R) = 0$. The ratio of counterion condensation was calculated from

$$b = 1 - \frac{rD_i(r)E(r)}{aD_i(a)E(a)} \tag{14}$$

The dielectric constant decreases considerably with decreasing r in the immediate vicinity of the rod. On the other hand, the field intensity increases with decreasing r more than the reference field intensity. The two effects largely cancel each other in eq 14. Accordingly, only a small increase in the acceleration factor was found when the change in the dielectric constant was taken into account. Of course, the conclusion of this section has a limitation because of the smeared charged model and neglect of the microscopic aspects of the mediums, such as their orientation in the vicinity of the polyion and "hydrophobic hydration". These factors would still affect the acceleration factor, however, their magnitude would

TABLE III: Effect of Dielectric Constant in Polymer Domain on Acceleration Factor

a, A	h/ν, A	[Polyion], N	$\alpha_{theo,I}$[a]	$\alpha_{theo,R}$[b]	$\alpha_{theo,I}/\alpha_{theo,R}$
4	2.52	10^{-4}	8.36×10^4	6.10×10^4	1.37
4	2.52	10^{-3}	8.39×10^3	6.15×10^3	1.36
4	5.04	10^{-4}	7.36×10^3	6.77×10^3	1.09
8	2.52	10^{-4}	1.63×10^4	1.53×10^4	1.07

[a] $D = D(E)$. [b] $D = D_0$.

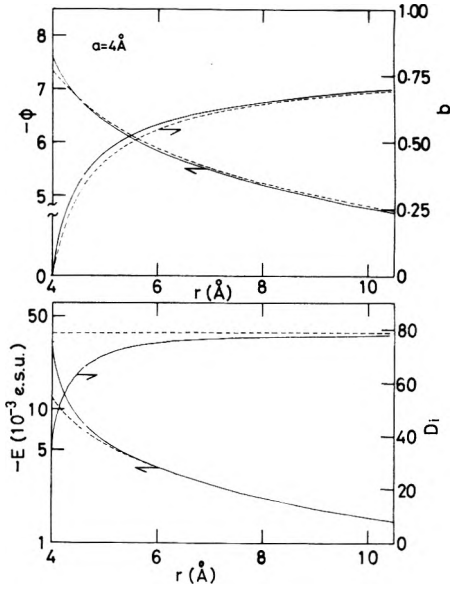

Figure 5. Dielectric constant, field intensity, ratio of counterion binding, and electrostatic potential near a polyion: (——) $D = D(E)$; (---) $D = D_0$. [Polyion] = 10^{-4} N.

TABLE IV: Theoretical Values of Increment of Activation Parameters in the Presence of Polyions at 25 °C

	[Polyion], N	$\Delta(\Delta H^{\ddagger})$, kcal mol^{-1}	$\Delta(\Delta S^{\ddagger})$, eu	$\Delta(\Delta G^{\ddagger})$, kcal mol^{-1}
a = 4 Å	10^{-4}	0.89	24.7	−6.49
h/ν = 2.52 Å	10^{-3}	0.88	20.2	−5.14
	10^{-2}	0.87	15.6	−3.76
a = 4 Å	10^{-4}	1.23	21.5	−5.19
h/ν = 5.04 Å	10^{-3}	1.30	17.3	−3.87
	10^{-2}	1.18	12.6	−2.57
a = 8 Å	10^{-4}	0.90	22.1	−5.68
h/ν = 2.52 Å	10^{-3}	0.87	17.4	−4.33
	10^{-2}	0.92	13.1	−2.98

be smaller than the electrostatic factor when considering the conclusions of section IV and the results of this section.

VII. The Interpretation of Activation Parameters

The activation parameters were calculated considering only the electrostatic interactions between reactants and polyions by use of the Lifson–Katchalsy theory. The increase of thermodynamic activation parameters was calculated as follows:

$$\Delta H = R^* \frac{\mathrm{d} \ln f}{\mathrm{d}(1/T)}$$

$$\Delta(\Delta H^{\ddagger}) = -R^* \frac{\mathrm{d} \ln (f_A f_B / f_X)}{\mathrm{d}(1/T)} \qquad (15)$$

where R^* is the gas constant and ΔH is the relative partial molar heat content. Insertion of eq 1 into eq 15 gives

$$\Delta(\Delta H^{\ddagger}) = -R^* \frac{\mathrm{d} \ln (k_2/k_{20})}{\mathrm{d}(1/T)} = -R^* \frac{\mathrm{d} \ln \alpha}{\mathrm{d}(1/T)} \qquad (16)$$

In addition

$$\Delta(\Delta G^{\ddagger}) = -R^* T \ln \alpha \qquad (17)$$

The acceleration factor was calculated at various temperatures using eq 2 and the Newton–Cotes method. The charge parameter, $\lambda = e^2\nu/D_0kTh$ varies with temperature and dielectric constant. The dielectric constant also depends on temperature and is expressed over a considerable range at t °C by

$$D(t) = D(25) \exp\{-0.0046(t - 25)\} \qquad (18)$$

$\alpha_{\mathrm{theo},0}$ increase gradually with increasing temperature, e.g., 5.50×10^{-4} at 10 °C, 5.78×10^{4} at 20 °C, 6.09×10^{4} at 30 °C, for a = 4 Å, h/ν = 2.52 Å, and $C = 10^{-4}$ N. As λ increases slightly with increasing temperature, the concentration of counterions also increases in the vicinity of the polyion. This tendency is also predicted by Manning's theory,[34] e.g., 82.32% of the divalent counterions are condensed at 15 °C and 82.75% at 35 °C for h/ν = 2.52 Å.

Plots of ln α vs. $1/T$ were approximately linear. From the slope, eq 16 and 17, $\Delta(\Delta H^{\ddagger})$ and $\Delta(\Delta S^{\ddagger})$ were calculated. The results are listed in Table IV about which the following points may be made: (i) The activation enthalpy increased slightly and $\Delta(\Delta H^{\ddagger})$ was found to be about 1. This enthalpy increment depressed the acceleration effect. Furthermore, the increase in enthalpy scarcely varied with polyion concentration since the acceleration factor varied inversely with the polyion concentration (as seen in Figure 1c), (ii) The activation entropy increased to a large extent. $\Delta(\Delta S^{\ddagger})$ decreased with increasing polyion concentration and decreasing acceleration factor. This means that the acceleration effect was due theoretically to the entropy increment. This conclusion had also been found theoretically and experimentally by the addition of simple salts to interions between similarly charged ions.[31]

TABLE V: Thermodynamic Quantities of Interdivalent Cationic Reactions in the Presence of Polyions

[Polyion], N	$\Delta H^{\ddagger}$, kcal mol^{-1}	$\Delta S^{\ddagger}$, eu	$\Delta(\Delta H^{\ddagger})$, kcal mol^{-1}	$\Delta(\Delta S^{\ddagger})$, eu
Hg^{2+} Induced Aquation of Cobalt Complexes				
0	10.5	−20.6	0	0[a]
4×10^{-5}	12.6	4.3	2.2	25[a]
4×10^{-4}	13.4	8.1	2.9	29[a]
4×10^{-3}	12.2	3.1	1.7	22[a]
1.9×10^{-3}	4.5	−23	−9.6	−15[b]
5×10^{-5}	12.6	−26	−6.4	−10[c]
5×10^{-4}	15.4	−15	−3.6	1[c]
Electron Transfer Reactions Proceeding by the Inner-Sphere Mechanism				
3.4×10^{-3}	16.8	9	3.5	37[d]
1.5×10^{-4}	18.0	6	4.2	32[e]
Electron Transfer Reactions Proceeding by the Outer-Sphere Mechanism				
3.7×10^{-3}	2.9	−24	−8.8	−10[f]
1.2×10^{-3}	1.6	−30	−8.6	−18[g]

[a] This work, $[Hg^{2+}] = 2.0 \times 10^{-4}$ M, $[Co(NH_3)_5Br^{2+}] = 2.0 \times 10^{-5}$ M, $[H^+] = 5 \times 10^{-3}$ M, at 25.0 °C. [b] Hg^{2+} + $Co(NH_3)_5Br^{2+}$, by Matsuda, ref 8. [c] Hg^{2+} + $Co(NH_3)_5Cl^{2+}$, by Morawetz, ref 6. [d] Fe^{2+} + $Co(NH_3)_5Br^{2+}$, by Shikata, ref 7. [e] Fe^{2+} + $Co(NH_3)_5Cl^{2+}$, by Morawetz, ref 1. [f] V^{2+} + $Co(NH_3)_5N_3^{2+}$, by Kim, ref 7. [g] $Ru(NH_3)_6^{2+}$ + $Co(NH_3)_5Br^{2+}$, by Kunugi, ref 36.

Some experimental activation parameters listed in Table V were measured mainly when the equivalent concentration of the polyion was roughly equal to those of reactant cations. For the Hg^{2+} induced aquation of $Co(NH_3)_5X^{2+}$, good agreement between theoretical and experimental values was found in the author's result, but there was no agreement in Matsuda's and Morawetz's. The experimental and theoretical values roughly agreed with the inner-sphere electron transfer reactions between Fe^{2+} and cobalt complexes, however, no agreement was found for the outer-sphere electron transfer reactions, such as V^{2+}–$Co(NH_3)_5N_3^{2+}$ or $Ru(NH_3)_6^{2+}$–$Co(NH_3)_5Br^{2+}$. The disagreement could be due to three causes: (i) the methods by which the data were analyzed; (ii) a limitation in the theory; and (iii) specific interaction between reactants, the polyion, and the ion-solvation effect.

(i) The tendencies as well as the absolute values were quite different in the author's and Matsuda's results for the same reaction. The author calculated k_2 from the initial slope in order to avoid the reactive inhibition by the triply charged reaction product, while Matsuda calculated his rate constant from the entire kinetic curve, which does not follow pseudo-first-order kinetics.

(ii) Theoretical problems may result if the influence of monovalent ions, the change in the ionic composition during the reaction, and the dependence of the polyion conformation on temperature are not taken into account. Patel[12] interpreted the activation parameters in terms of a multiple equilibrium model. The ions are subject to a multiple equilibrium, but divalent ions are concentrated by the polyion in preference to monovalent ions. Accordingly, the calculated results should be at least qualitatively reliable. The second problem is avoided if initial rate constants are used in the analysis. As mentioned in section IV, the effective length of polyions is smaller than the fully extended length. Since the dielectric constant

TABLE VI: Influence of $NaClO_4$ on Activation Parameters for Hg^{2+} Induced Aquation of $Co(NH_3)_5Br^{2+}$ in the Presence of NaPES[a]

[NaPES], N	[$NaClO_4$], N	$\Delta H^{\ddagger}$, kcal mol^{-1}	$\Delta S^{\ddagger}$, eu	$\Delta G^{\ddagger}$, kcal mol^{-1}
4×10^{-5}	0	12.9	4.3	11.6
	5×10^{-2}	11.3	−3.2	11.9
	2×10^{-1}	12.1	−6.7	14.1
4×10^{-4}	0	13.4	8.1	11.0
	5×10^{-2}	12.8	5.3	11.2
	2×10^{-1}	12.8	0.2	11.3
4×10^{-3}	0	12.3	3.1	11.3
	5×10^{-2}	12.9	5.4	11.2
	2×10^{-1}	12.0	0.2	12.1

[a] $[Hg^{2+}] = 2.0 \times 10^{-4}$ M, $[Co(NH_3)_5Br^{2+}] = 2.0 \times 10^{-5}$ M, $[H^+] = 5 \times 10^{-3}$ M, at 25.0 °C.

decreases with temperature, the repulsion between the charges fixed on the polyion increases with temperature. On the other hand, the ion-shielding effect by counterions also increases since the counterion binding increases with temperature. The competing effects may influence the effective length of the polyion and the activation parameters, but it is difficult to evaluate the effects quantitatively.

(iii) There may be some specific interactions between reactants and polyions and the ion-solvation effect which are difficult to discuss theoretically. The difference between the outer- and inner-sphere electron transfer reactions may be partly due to these effects.

(3) *The Influence of $NaClO_4$ on Activation Parameters.* It has been established that the acceleration factor in the presence of polyions decreases on addition of simple salts.[6,8] However, the way in which the activation parameters vary with added simple salts has not been made clear. Table VI shows the influence of $NaClO_4$ on the activation parameters of Hg^{2+} induced aquation of $Co(NH_3)_5Br^{2+}$. The following points may be made: (i) As seen in the activation energy, the acceleration factor became more sensitive to the added salt as the polyion concentration decreased. As Morawetz[6] pointed out, this is because the amount of bound divalent ions decreases with increasing ratio of the added salts to polyion. (ii) The activation enthalpy is little affected by addition of salt. (iii) The decrement of the acceleration factor on addition of salt is an entropy effect. The amount of bound reagent ions decreases with an excess of $NaClO_4$. Decreasing binding of reagent ions should result in a decrease of the activation entropy, as is observed.

VIII. The Effect of Molecular Charge on the Acceleration Factor and Activation Parameters

The effect of the molecular charge (MC) of oligo- and polyphosphates on the Hg^{2+} induced aquation of $Co(NH_3)_5Br^{2+}$ was examined. The sulfate ion was used as a divalent anion since the divalent phosphate does not exist at the pH used.

(1) Figure 6 is a double logarithmic plot of α vs. the concentration of the oligo and polyions. When no oligo and polyions were added, the ionic strength of the solution and k_2 were 5.6×10^{-3} and 4.4 s^{-1} M respectively. Accordingly, k_{20} was inferred to be 2.2 s^{-1} M by the Brønsted and Debye–Hückel theories. When only a small amount of these salts, 10^{-4} N, was added, α was small ($\alpha < 5$) for MC < 4, whereas large values ($\alpha > 20$) were observed for MC > 5. The increment of ionic strength resulting from the addition of these salts was so small that the large values for MC > 5 could not be explained by the Brønsted and

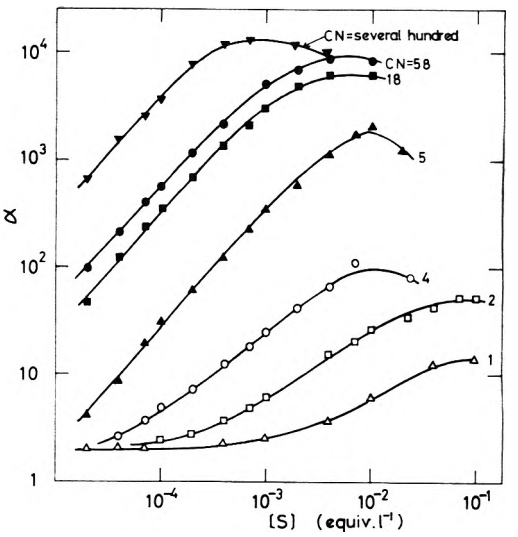

Figure 6. Dependence of α on the concentration of polyphosphate with various MC: $[Hg^{2+}] = 2.0 \times 10^{-4}$ M, $[Co(NH_3)_5Br^{2+}] = 2.0 \times 10^{-5}$ M, $[H^+] = 5 \times 10^{-3}$N. S = polyphosphate or sulfate ion.

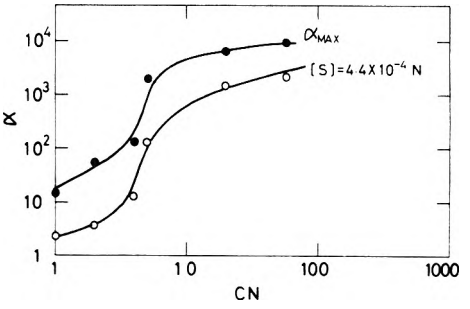

Figure 7. Dependence of α on the molecular charge of polyphosphate for Hg^{2+} induced aquation of $Co(NH_3)_5Br^{2+}$: $[Hg^{2+}] = 2.0 \times 10^{-4}$ M, $[Co(NH_3)_5Br^{2+}] = 2.0 \times 10^{-5}$ M, $[H^+] = 5 \times 10^{-3}$ N.

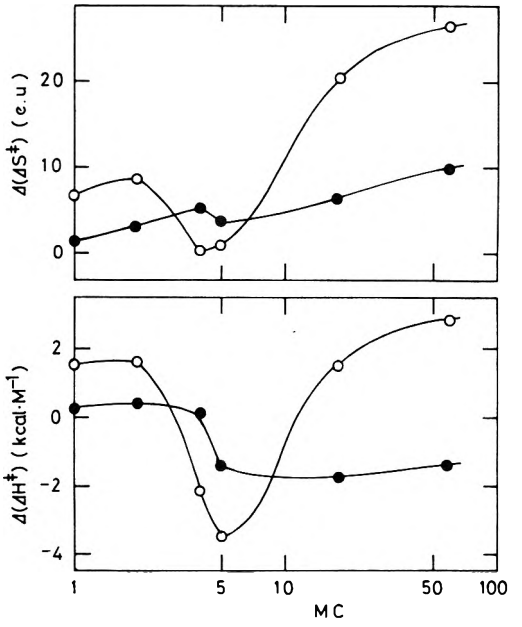

Figure 8. Dependence of $\Delta(\Delta S^{\ddagger})$ and $\Delta(\Delta H^{\ddagger})$ on the molecular charge of polyphosphate for Hg^{2+} induced aquation: (A) [added salt] = 4×10^{-4} N; (B) [added salt] = 4×10^{-3} N. $[Hg^{2+}] = 2.0 \times 10^{-4}$ M, $[Co(NH_3)_5Br^{2+}] = 2.0 \times 10^{-5}$ M, $[H^+] = 5 \times 10^{-3}$ N.

Debye–Hückel theories. This means that the counterion binding effect on oligo and polyions was effective above MC = 5. The slope of the curves increased with MC for MC < 4, but became constant and about 1 for MC > 5. For MC = 4, the slope was due to both effects, i.e., the ion

binding and ion atmospheric effect. Figure 7 showed the dependence of α on MC. In both of the curves, an inflection appeared at about MC = 5. After the inflection, α increased slowly with MC. The theoretical values of α was 1.2×10^{-4} at 4.4×10^{-4} N, when a was taken as 4.3 Å. At MC = 200–300, the experimental value reached the theoretical one. Accordingly, it was concluded that the polyion effect appeared at MC = 5 and was completed at an MC of several hundred in this system.

(2) The activation parameters are shown in Figure 8. $\Delta(\Delta S^{\ddagger})$ was always positive, although an abnormal change was found at MC = 4 and 5. For any simple and poly salts, the acceleration was theoretically due to an increment of activation entropy. The experimental results coincided with the theoretical prediction. On the other hand, $\Delta(\Delta H^{\ddagger})$ showed a complicated change, for example, it was negative at MC = 4, 5, which was opposite to the theoretical prediction. This unexpected result suggests that the binding of ions on oligoions is governed by a complicated equilibrium.

Acknowledgment. The author is grateful to reviewer X for his useful comments and the kind check of my English. The author also thanks Professor N. Ise and Professor M. Nagasawa for useful criticism and discussion.

Supplementary Material Available: (Appendices I and II) A discussion of the relationship between a, a_p, and p and an estimation of the appropriate radii of the counterions and the relationship between α and the local concentration of reactants in the polymer domain (5 pages). Ordering information is available on any current masthead page.

References and Notes

(1) H. Morawetz and G. Gordimer, *J. Am. Chem. Soc.*, **92**, 7532 (1970).
(2) H. Morawetz, *J. Polym. Sci.*, **42**, 125 (1960).
(3) H. Morawetz and J. A. Shafer, *J. Phys. Chem.*, **67**, 1293 (1963).
(4) H. Morawetz, "Macromolecules in Solution", 1st ed, p 435.
(5) H. Morawetz, "Macromolecules in Solution", 2nd ed, p 482.
(6) H. Morawetz and B. Vogel, *J. Am. Chem. Soc.*, **91**, 563 (1969).
(7) M. Shikata, S. Kim, and N. Ise, *Proc. R. Soc. London, Ser. A*, **351**, 233 (1976).
(8) N. Ise and Y. Matsuda, *J. Chem. Soc., Faraday Trans. 1*, **69**, 99 (1973).
(9) N. Ise and F. Matsui, *J. Am. Chem. Soc.*, **90**, 4242 (1968).
(10) K. Mita, S. Kunugi, T. Okubo, and N. Ise, *J. Chem. Soc., Faraday Trans. 1*, **71**, 936 (1975).
(11) K. Mita, T. Okubo, and N. Ise, *J. Chem. Soc., Faraday Trans. 1*, **72**, 1033 (1976).
(12) R. Patel, G. Atkinson, and E. Baumgartner, *Bioinorg. Chem.*, **3**, 1 (1973).
(13) E. Gould, *J. Am. Chem. Soc.*, **92**, 6797 (1970).
(14) B. E. Conway, J. E. Desnoyers, and A. C. Smith, *Phil. Trans. R. Soc. London, Ser. A*, **256**, 389 (1964).
(15) K. Yamaoka, M. Takatsuki, K. Yaguchi, and M. Miura, *Bull. Chem. Soc. Jpn.*, **47**, 611 (1974).
(16) S. Lifson and A. Katchalsky, *J. Polym. Sci.*, **13**, 43 (1954).
(17) J. F. Endicott and H. Taube, *Inorg. Chem.*, **4**, 437 (1965).
(18) Y. Tanito, Y. Saito, and H. Kuroya, *Bull. Chem. Soc. Jpn.*, **25**, 188 (1952).
(19) S. Oman and D. Dolar, *Z. Phys. Chem. (Frankfort Am. Main)* **56**, 1 (1967).
(20) S. Oman and D. Dolar, *Z. Phys. Chem. (Frankfort Am Main)*, **56**, 13 (1967).
(21) D. Kozak, J. Kristan, and D. Dolar, *Z. Phys. Chem. (Frankfort am Main)*, **76**, 85 (1971).
(22) D. Kozak, J. Kristan, and D. Dolar, *Z. Phys. Chem. (Frankfort am Main)*, **76**, 93 (1971).
(23) M. Eigen, *Pure Appl. Chem.*, **6**, 97 (1963).
(24) I. Kagawa and H. Gregor, *J. Polym. Sci.*, **23**, 477 (1957).
(25) I. Miller, F. Bernstein, and H. Gregor, *J. Chem. Phys.*, **43**, 1783 (1965).
(26) H. Ohtaki, M. Maeda, and S. Ito, *Bull. Chem. Soc. Jpn.*, **47**, 2217 (1974).
(27) H. Ohtaki and M. Maeda, *Bull. Chem. Soc. Jpn.*, **47**, 2197 (1974).
(28) C. D. Grahm, *J. Chem. Phys.*, **18**, 903 (1950).
(29) C. D. Grahm, *J. Chem. Phys.*, **21**, 1054 (1953).
(30) J. K. Laidler, *Can. J. Chem.*, **37**, 138 (1959).
(31) V. K. Lamer and M. E. Kamner, *J. Am. Chem. Soc.*, **57**, 2662 (1935).
(32) Z. Alexandrowicz, *J. Polym. Sci.*, **56**, 97 (1962).
(33) Z. Alexandrowicz and A. Katchalsky, *J. Polym. Sci., Part A*, **1**, 3231 (1963).
(34) G. Manning, *J. Chem. Phys.*, **51**, 924 (1969).
(35) T. Alfrey, P. W. Berg, and H. Morawetz, *J. Polym. Sci.*, **7**, 543 (1951).
(36) S. Kunugi and N. Ise, Z. Phys. *Chem. (Frankfort am Main)*, **91**, 174 (1974).

Far-Infrared Study of Cation Motion in Dry and Solvated Mono- and Divalent Cation Containing Zeolites X and Y

Wayne M. Butler,[†] Charles L. Angell,[‡] Warren McAllister,[ϕ] and William M. Risen, Jr.*[†]

Metcalf Research Laboratory, Department of Chemistry, Brown University, Providence, Rhode Island 02912; Tarrytown Technical Center, Union Carbide Corporation, Tarrytown, New York 10591; and Department of Chemistry, East Carolina University, Greenville, North Carolina 27834 *(Received April 14, 1977)*

Publication costs assisted by Brown University and the Union Carbide Corporation

Far-infrared ion motion bands have been observed and assigned in the spectra of dry synthetic zeolites X and Y containing Li^+, Na^+, K^+, Rb^+, Cs^+, Ag^+, Ca^{2+}, Sr^{2+}, and Ba^{2+} cations. The site I′ and site II cation vibrational bands overlap and form the strongest feature in the spectra of samples exchanged with monovalent ions. The site I cation band appears at lower frequency than the site II envelope in these samples, but in divalent ion exchanged zeolites the opposite order occurs. A very low frequency site III cation band, typical of monovalent X zeolites, has been observed in CsY. For a given cation, the frequency on X is higher than on Y due to the higher framework charge of X zeolites. The vibrational frequencies also follow an approximate $m^{-1/2}$ dependence for the two types of cation and the two forms of the zeolite. Solvation of the monovalent zeolites with H_2O, THF, Me_2SO, pyridine, and CH_2Cl_2 results in the appearance of a new band at higher frequency than the ion-framework modes which concurrently diminish in intensity, especially the site III band. The high frequency band is due to ion motion in a solvation shell which is unsymmetric at low hydration levels and at all solvation levels with organic adsorbates. In addition to a cation mass dependence, the ion–solvent frequencies are also dependent on the adsorbent's effective dielectric constant which is greater in X than Y zeolites. Increasing solvation shifts the ion–framework vibrations to lower frequency, but this shift with the organic adsorbates is primarily an indirect effect due to solvent delocalizing the framework charge. The implications of the cation vibrational frequencies for the mechanism of ionic conduction are considered in terms of a simple free-ion model. Ion transport in Y zeolites which have a large number of vacant cation sites so that each jump may be considered an independent event is adequately explained by this model, but ion transport in X zeolites is best interpreted in terms of cooperative effects.

Introduction

Molecular sieve zeolite structures have been intensively studied in recent years not only to relate pore size and molecular sieve behavior, but also to determine the active sites in heterogeneous catalysis. The catalytic sites fall into three classes: framework hydroxyl groups acting as either Brønsted acids[1] or Brønsted bases,[2] Lewis acid sites within the framework such as three-coordinate Al,[3] and the exchangeable cations themselves.[4,5] Of these, hydroxylated zeolites originate upon the hydrolysis of the cations of high electric field strength (or the deammination of ammonium exchanged zeolites), and the Lewis acid sites occur in conjunction with the hydroxylated sites (more so upon thermal dehydroxylation[6]), so the catalytic site problem directly involves locating exchangeable cations.

This task has proven difficult even in fully dehydrated zeolites since there are invariably fewer cations than available sites. Furthermore, the distribution of mobile cations over several crystallographically distinct types of sites varies from sample to sample since the cation distribution is dependent on the negative charge distribution of the aluminosilicate framework, the cation size and charge, directional bond and coordination preference of the cation, and the solvation state of the zeolite.

In previous work on polyelectrolytic salts of copolymers, such as those of polyethylenemethacrylic acid, ionic oxide glasses,[7] and various cation exchanged forms of β-alumina,[8] we have observed mass- and site-dependent cation-site vibrations in the far-infrared spectra. On the basis of this, we may expect such ion motion bands in the far-infrared spectra of zeolites, and for them to be sensitive to solvation and other interactions involving the cations. Indeed, several interionic vibrations have been observed in monovalent exchanged zeolites X and Y[9] and the effect of hydration on the band structure studies.[10] In this work we examine cation interactions with several organic adsorbates to determine whether these molecules affect cation migration and examine the monovalent cation exchanged zeolites to assign the cation motion bands in greater detail. The spectra of divalent ion-exchanged zeolites are also reported in conjunction with the relation between ionic vibrations and ionic conductivity.

The framework topology of zeolites X and Y, isotypical with the mineral faujasite, has been well characterized[11] and is distinguished by the largest known cavities and channels of all zeolites. With unit cell composition $M_x(AlO_2)_x(SiO_2)_{192-x}$ (x = 48–90), the aluminosilicate framework is a cross-linked crystalline macromolecule where each aluminum and silicon atom is tetrahedrally bonded to four bridging oxygen atoms. Twentyfour of these tetrahedrally bonded atoms make up each of the cubooctahedra (sodalite cages) which are in turn stacked in a tetrahedral diamond array so that adjacent Al,Si six-rings of the sodalite cages are joined via six shared oxygen atoms forming a hexagonal prism. The cavities enclosed by the lattice of sodalite cages are called supercages which also interconnect in a tetrahedral manner through channels consisting of 12-rings of Al,Si tetrahedra.

The designation of favorable cation sites and framework oxygens (Figure 1) follows that of Smith.[12] Cations on site I are centered in the hexagonal prisms and are coordinated octahedrally to six O_3 oxygens. The 16 sites of this type per unit cell are inaccessible to species larger than 2.8 Å diameter such as H_2O and Cs^+. Sites I′, II, and II′ all

[†] Brown University
[‡] Union Carbide Corporation
[ϕ] East Carolina University

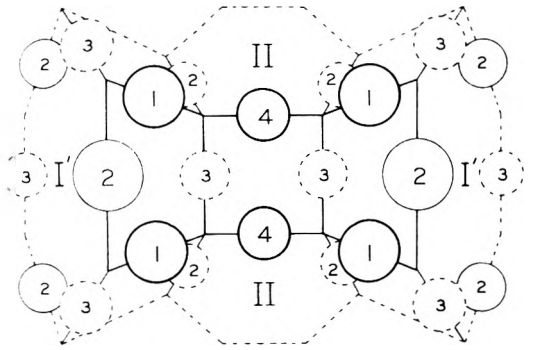

Figure 1. Designation of cation and framework oxygen sites following Smith.[12]

provide one-sided threefold coordination to oxygens of the sodalite cage six-rings. I′ is within the sodalite cage but shares three O_3's of the bridging hexagonal prisms so that simultaneous cation occupancy of I and I′ is unlikely. Sites II and II′, within the supercage and the sodalite cage, respectively, are also mutually exclusive to cation occupancy since both share the same three O_2 oxygens of the free six-rings of the sodalite cages.

There are 32 of each of the asymmetric bonding sites per unit cell so that, depending on the occupancy of site I, 48–64 cations can be accomodated. This number is sufficient for the Y zeolites but not for X type zeolites. To account for these additional cations, various sites, collectively referred to as site III, have been proposed on the walls of the supercage. Mortier et al.[13] proposed a site affording one-sided square-planar coordination to two O_4 oxygens of the sodalite cage and two O_1 oxygens which bridge the cubooctahedra through hexagonal prisms. These squares come in pairs which share an edge of O_4's, therefore, only 48 of the 96 possible sites may be occupied due to steric as well as electrostatic reasons.

No monovalent cations have actually been located at such sites by x-ray structural studies not simply because of a low occupancy factor but probably because of large vibrational and static displacements of the ions. Highly unsymmetric bonding sites in hydrated and dehydrated CuY zeolites place some Cu^{2+} either on the edge of the square bonded unequally to O_1 and O_4 in natural faujasite[14] or in distorted threefold coordination to an O_1, O_2, and O_4 which share the same T atom in synthetic faujasite.[15] Even if monovalent ions larger than Cu^{2+} do not mimic its asymmetric bonding, the possibility of large anisotropic vibrations smearing the electron density remains. An intense high-frequency dielectric relaxation in X zeolites has been attributed to cation motion over neighboring sites III with an activation energy in NaX of only 30 kJ mol^{-1}.[16] This value is considerably lower than the activation energy for ionic conduction which involves a jump from site II to site III.

Upon hydration, a redistribution of cations is observed[12,13] in which the population of sites I, I′, and II decreases and the number of unlocated cations in the supercage increases. A similar migration occurs in the presence of other adsorbents,[17] but different cations have specific preferences for extraction by either small polar molecules or larger π-bonding ligands. Adsorbents can effect migration by delocalizing the framework charge, thus weakening the cation–framework attraction, and by directly bonding to or solvating the cations. Both direct and indirect cation–adsorbent interactions have been inferred through changes in the stretching frequency of adsorbed carbon monoxide[18] and changes in the EPR line shape of Mn^{2+} doped zeolites.[19] In this work, we have been able to associate far-infrared bands with cations on specific sites and through a study of the effects of adsorbents on these bands have been able to distinguish between direct and indirect cation–adsorbent interactions.

TABLE I: Composition of Zeolites

Zeolite	SiO_2/Al_2O_3	% cation analysis
LiY	4.83	47
NaY	4.95	92
KY	4.91	97
CsY	4.89	66
AgY		95
MgY		72
CaY		77
SrY		76
BaY		79
NaX	2.43	100
KX		73
CaX		75

Experimental Section

The zeolites used in this study were supplied in exchanged form by the Linde Division of Union Carbide Corp. and were analyzed as presented in Table I. The balance of cations in each case is predominantly sodium although hydrolysis has been shown to occur to some extent under all aqueous exchange conditions.[20]

Two far-infrared sampling techniques were used with equal success. In one a petroleum jelly mull was held between low density polyethylene plates, and in the other the zeolite powder was supported on a transparent substrate in a vacuum IR cell. In both cases all zeolite powder samples were dehydrated by evacuating them under 10^{-4} Torr vacuum for 6 h and then slowly heating to 400 °C (500 °C for divalent zeolites) for 12 h or until the pressure was less than 10^{-4} Torr. With the mull process, the hot flask containing the zeolite was separated from the line, allowed to cool, then opened in a glove bag filled with dry nitrogen, and immediately mulled with some previously dried petroleum jelly. When pressed between two polyethylene windows, such mulls may be exposed to air at little risk of becoming hydrated.

A silicon wafer mounted in a steel ring served as a substrate to an aqueous slurry of zeolite. After drying, the zeolite powder (ca. 0.2 mm thick) adhered reasonably well to the wafer during magnetic manipulation of the steel ring between the furnace portion of the vacuum cell and the spectral window portion. Since some sample was inevitably lost between runs, conclusions based on adsorbance changes are not quantitative. The windows were ca. 0.5 mm thick polyethylene disks affixed with epoxy cement.

The absorbates, tetrahydrofuran (THF), dimethyl sulfoxide (Me_2SO), pyridine (py), CH_2Cl_2, and D_2O, were reagent grade and, except for the last, were freshly distilled over sodium or calcium hydride then vacuum degassed before use. Dehydrated zeolites were cooled to room temperature before exposure to the solvents. The amount adsorbed was controlled by varying the temperature of the solvent, thus its vapor pressure, as well as the time of exposure, but gas analyses were not performed since it was our goal to simply induce spectral changes. For substrate mounted samples, the zeolites were exposed to 0.05 Torr of the adsorbate for 5 min then reevacuated at room temperature for 5 min.

Infrared spectra were recorded on a Digilab FTS-14 interferometer at a resolution of 4 cm^{-1}. A smoothing function was used occasionally to reduce noise but resolution was never degraded below 8 cm^{-1}. Mull samples were referenced against air while a spectrum of the substrate sample cell with the silicon wafer out of the beam was stored as a reference for these samples.

TABLE II: Far-Infrared Bands of Monovalent Cation Y Zeolites

Assignment	LiY	Int	NaY	Int	KY	Int	CsY	Int	AgY	Int
III							*30*	w sh		
I			*167*	m sh	*107*	m sh			*50*	w
II	*380*	sh	*180*	s	*133*	s	*62*	s	*82*	m
	100	w	122	m			109	m	122	w
									150	w
	164[a]	w			160	w sh	174[a]	m	168	vw
	212	w					210	w sh	228	w sh
	296	sh	273	m	270	w sh	280	w sh	270	w sh
	311	m			310	w sh	317	w sh	320	vw sh
Ring def	396	s	392	s	385	s	383	s	380	s

[a] Due to residual sodium.

TABLE III: Far-Infrared Bands of X Zeolites

Assignment	NaX	Int	KX	Int	RbX	Int	CsX	Int
III	*67*	wm	*58*	m	*48*	wm	*39*	wm
I	*160*	w sh						
II	*190*	ms	*156*	s	*108*	ms	*86*	m
	91	w	77	vw	83	w sh	64[a]	w sh
	109	w	106	wm	118	w sh	126	m
					182[a]	m	188[a]	m
					204[a]	m	199[a]	m
	218	vw	230	w				
	263	w	277	vw sh	259	vw sh	254	w
	295	w	308	w sh	296	w	295	w
	321	w sh	322	m sh				
			357	w sh				
Ring def	382	s	373	s				

[a] Due to residual sodium.

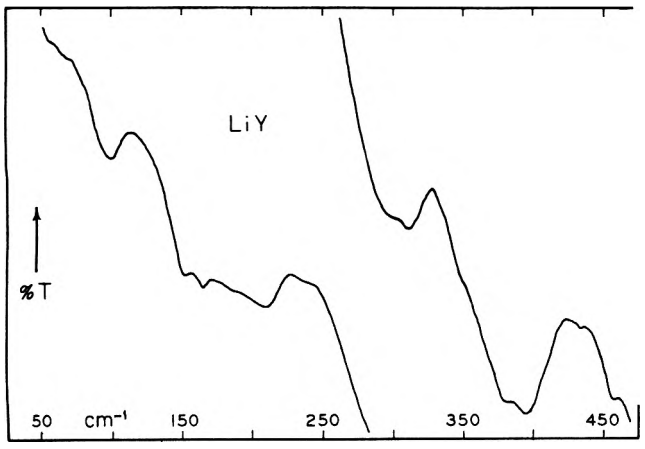

Figure 2. Far-infrared transmittance of LiY zeolite.

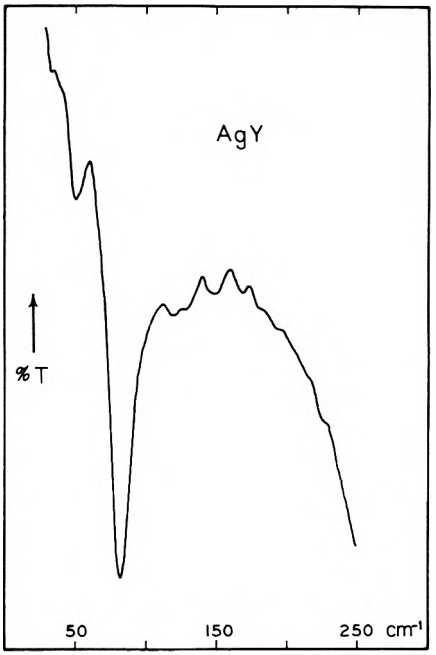

Figure 3. Far-infrared transmittance of AgY zeolite.

Results

A. *Monovalent Cation Containing Dehydrated Zeolites.* The far-infrared spectra of LiY and AgY shown in Figures 2 and 3 are reported for the first time and the spectra of the remaining alkali metal zeolites summarized in Tables II and III are similar to those reported by Brodskii et al.[9] Minor differences in band shapes and positions are expected due to differing synthetic histories of the samples which result in variations in Si, Al ordering and in the Si/Al ratio. The higher resolution of our spectra, however, has permitted the identification of a number of bands not observed by Brodskii.

Various bands have been assigned as interionic vibrations of cations on specific sites by considering the occupancy factors of the sites, the potential energy differences between sites, and the behavior of the bands in the presence of adsorbed gases. Site II is the most highly populated in dry monovalent cation Y zeolites and should give rise to the most intense band. A similar band at slightly higher frequency is expected in the corresponding X zeolites due to their more highly charged framework. There is little chance of site II cations in X being obscured by the more numerous site III cations since the latter are so weakly bonded that the frequencies at the two sites will be far from coincidence.

Site II′ is vacant in these samples so there is no problem of accidental degeneracy from this source, but potential energy calculations by Dempsey[21] and Mortier[22] indicate that site I′, which has a population comparable to site II, lies at only slightly higher energy. Since the strength of the threefold bonding to a six-ring at I′ is nearly indis-

TABLE IV: Far-Infrared Bands of Divalent Cation Zeolites

Assignment	MgY	Int	CaY	Int	SrY	Int	BaY	Int	CaX	Int
II			*227*	m	*150*	w	*107*	s	*273*	m
I			*256*	m	*189*	ms	*137*	s	*287*	wm
			40	w	53	w sh	50	w sh	50	w sh
	64	w sh	65	vw sh	67	w sh	60	w sh	65	w
	84	w	90	w sh	100	m	90	w sh	85	w
									100	w
	132	w	131	ms	122	w			132	w sh
	157	m	162	vw	165	w sh	157	wm	152	w
			170	vw	177	vw sh	182	w sh	168	wm
	190[a]	w	202[a]	w	204[a]	w sh	200[a]	w sh	200[a]	w sh
			211	vw	220	w			210	w
	249	w sh			250	wm	227	w sh	220	wm
	275	m	267	w sh	266	w	270	w sh		
			308	w sh	304	wm	310	m	321	m
	332	wm			330	wm	343	w	359	w sh
Ring def	401	s	385	m	385	s	375	s	380	s

[a] Due to residual sodium.

tinguishable from that at site II, the two vibrational bands will overlap considerably. The highest intensity low frequency band in these zeolites is therefore assigned in Tables II and III as representing cations on sites I′ and II.

Potential energy calculations[21,22] also indicate that site I is at a higher energy than site II in these samples. This does not necessarily mean that cation vibrations at this site will occur at a lower frequency than at site II since the octahedral coordination at site I may place a steric strain on the ion so that the vibrational frequency is higher. The fact that repulsions are dominant in raising the energy of site I is evident in zeolites exchanged with rubidium or cesium which are excluded from the hexagonal prisms. Since x-ray results indicate that the cation–oxygen distance at site I is greater than at site II in dry sodium and potassium zeolites, we conclude that steric repulsions are unimportant for these two ions and that the site I frequency should lie lower than the site II frequency. Furthermore, since the hexagonal prisms in sodium and potassium zeolites never contain more than ten cations per unit cell,[13,23] the site I vibrational bands will be relatively low intensity as reported in Tables II and III.

AgY is anomalous in that its site I is more stable than site II. Due to its high polarizability (2.4 Å^3), the large silver ion is stabilized in the prisms through the formation of covalent bonds. In silver β-alumina,[24] the mobile ions occupy what would normally be considered a high energy site. Likewise in AgX and AgY, silver fills the hexagonal prisms in preference to other sites.[12,25] Nevertheless, the band arising from silver in the prisms will be weaker than the site II band since the amount on fully occupied site I is still only one third of the total and also because the very covalency that stabilizes silver there will lower the infrared intensity.

From the cation distribution, bands assigned to site III cations in X zeolites should not appear in Y zeolites. In the CsY sample, however, there are 37 cesium ions per unit cell which are more than can be accomodated on site II. The band at 30 cm^{-1} is accordingly assigned to the five or more Cs^+ ions per unit cell occupying site III. This means that even at the temperature of dehydration of these samples cesium is excluded from the sodalite cage in contrast to the x-ray results for CsA zeolite[26] which found cesium in the small cavities. Apparently the higher silica content of Y reduces the six-ring opening sufficiently to maintain the exclusion of large ions. Considering the reduced framework charge of CsY relative to CsX, the frequency of the assigned band is reasonable and lends further support to this first indication of site III occupancy in a Y zeolite.

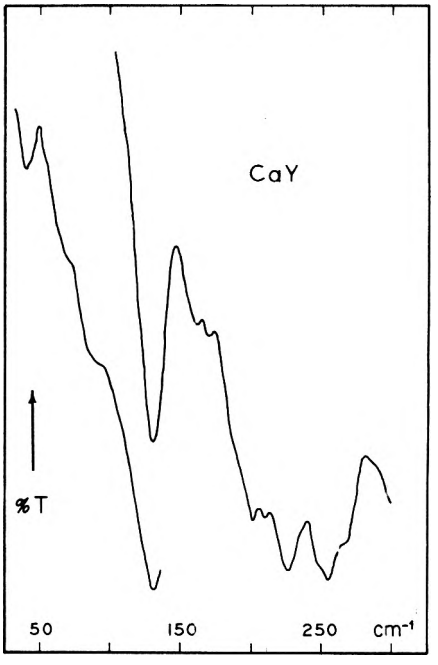

Figure 4. Far-infrared transmittance of CaY zeolite.

B. *Divalent Cation Containing Dehydrated Zeolites.* Because of their high charge/radius ratio, the ionic vibrations of divalent cations on the zeolite framework are expected to occur at significantly higher frequency than monovalent cations of similar mass. The spectra of alkaline earth exchanged Y and Ca exchanged X zeolites summarized in Table IV and illustrated in Figures 4 and 5 with CaY and BaY confirm this expectation.

From either Madelung potential calculations[21] or a consideration of cation site occupancy factors,[12] site I is clearly the most stable in the dry zeolites, and cations at this location will have the highest vibrational frequency. In Y zeolites, the total population at the 16 sites I is nearly equal to that on all other sites combined, while in X zeolites, cations at I account for only one fourth of the total.

The ion motion band assignments for CaY and BaY fit the above prescription: a pair of bands of near equal intensity separated by 30 cm^{-1} with the higher frequency band assigned to ions on site I. In divalent cation zeolites, the band assigned to site II encompasses not only ions on I′ as in monovalent cation zeolites but also II′ which is

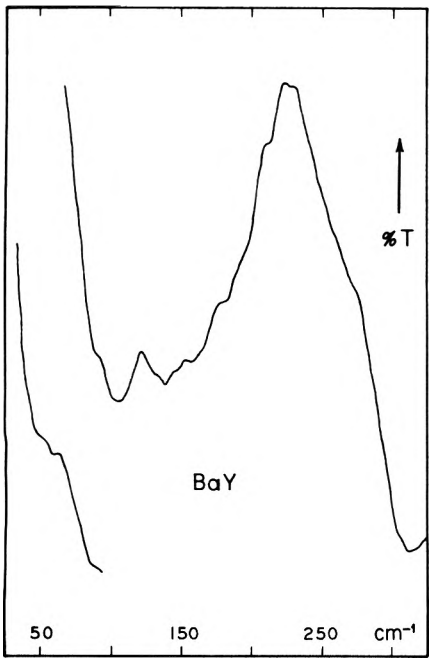

Figure 5. Far-infrared transmittance of BaY zeolite.

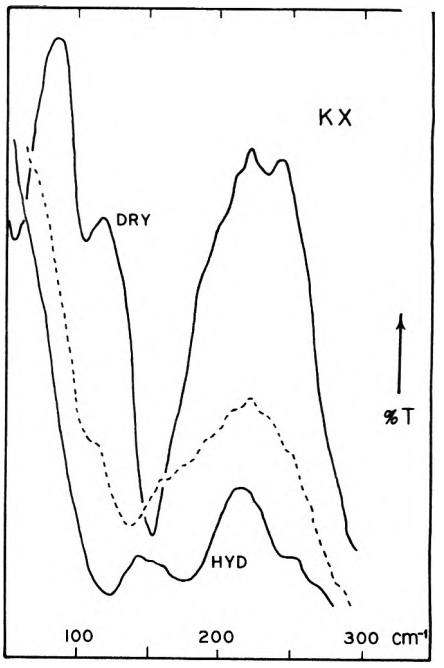

Figure 6. Far-infrared transmittance of KX zeolite dry, hydrated, and approximately 50% hydrated.

found to be occupied in polyvalent cation zeolites due to the presence of tightly bound residual water in the sodalite cage. The pair of bands in CaX is more closely spaced than in CaY, but the lower energy absorption is more intense as expected. The two band pattern is not evident in SrY which has a single strong, broad absorption centered at 189 cm^{-1}. Ions at all sites are probably under this band envelope, so the assignment of site II strontium as the weak 150 cm^{-1} band on the side of this major peak is tenuous.

Unique among these zeolites is MgY since we have been unable to identify its cation motion bands. It is known that the small size and high field of Mg^{2+} enable it to substitute for aluminum in spinel-like structures, and although such replacement is unlikely at the dehydration temperature of 500 °C, the Mg–O vibrational modes will be strongly coupled with those of the framework. The interionic vibrations of Mg^{2+}, therefore, will be evident only in the shifted frequencies of framework modes.

C. *Interactions with Adsorbed Molecules.* Upon adsorption of polar solvents, zeolites are able to approach their equilibrium state in which the framework charge is delocalized by the adsorbent. This charge delocalization will reduce the force constants and vibrational frequencies of nonsterically constrained cations. These exposed cations may also be partially solvated resulting in a further reduction of the vibrational frequency. Both processes, solvation and charge delocalization, operate concurrently so that a steady decrease in the frequency assigned to site II cations is observed upon increasing the degree of hydration. This is illustrated in Figure 6 and 7 with KX and KY in which the site II vibrations shift from 156 to 122 cm^{-1} and from 133 to 114 cm^{-1}, respectively.

The site III vibration observed in X zeolites shifts negligibly in frequency at low degrees of hydration, but its apparent intensity declines dramatically. It is no longer observable in KX zeolites more than 50% hydrated. The disappearance of this band is matched by the growth of a new band at 177 cm^{-1} which had been attributed[10] to liquid water. We believe, however, that this high frequency band is due to ion motion of hydrated potassium ions and is analogous to ion motion bands observed in THF, Me_2SO, and pyridine solutions of the alkali metal salts of $Co(CO)_4^-$ and $Mn(CO)_5^-$.[27] Nearly as large a fraction of the ions in

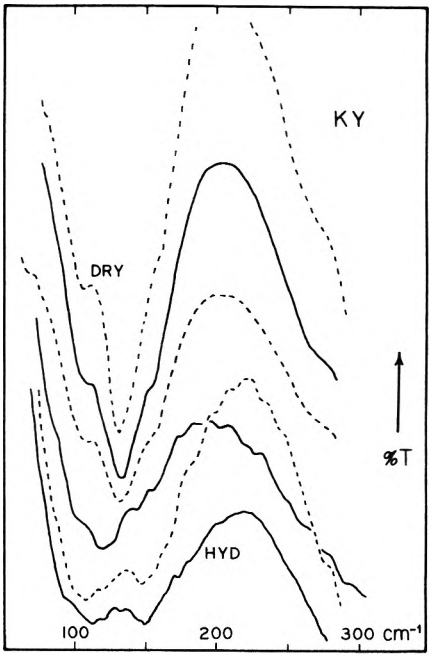

Figure 7. Far-infrared transmittance KY zeolite at various degrees of hydration.

hydrated KY zeolite as in hydrated KX zeolite are unlocated by x-ray diffraction[13] and may be presumed to be "in solution" in the supercage. A similar high frequency band is therefore observed in KY at 149 cm^{-1} due to hydrated potassium.

There is no apparent change in the site I frequency in KY despite the increasing charge delocalization with hydration level. This is probably due to a relaxation of strong lattice distortions that result in a K(I)–O_3 distance that is shorter in hydrated than dehydrated samples.[13] The spectra of Figure 7 provide no evidence for solvent extraction of ions from site I because of the increased overlap of this band with the shifting site II band.

D. *Polar Organic Adsorbates.* On the basis of complete volume filling of the large cavities, the limiting adsorption values for the large molecules studied here, pyridine,

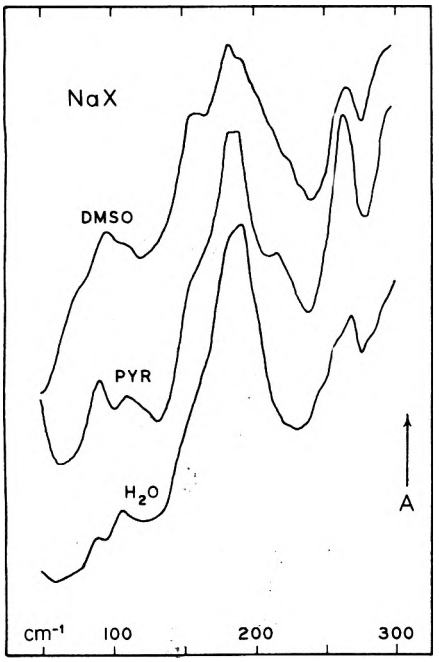

Figure 8. Absorbance spectra of dry NaX zeolite exposed to 0.05 Torr of H_2O, pyridine, and dimethyl sulfoxide.

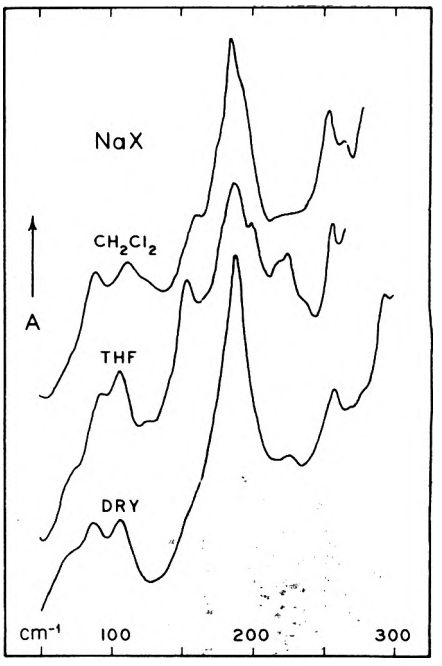

Figure 9. Absorbance spectra of dry NaX zeolite exposed to 0.05 Torr of tetrahydrofuran and dichloromethane.

tetrahydrofuran, dimethyl sulfoxide, and dichloromethane, will be considerably less than the limiting value for water. The void volume of Y zeolites is nearly as great as in NaX which can hold a maximum of six of these large molecules per supercage compared to over 30 water molecules per supercage.[28] This inherently low coverage by the organic compounds will affect the cation vibrations in two ways. First, delocalization of the framework charge will not be as effective as in hydrated zeolites resulting in a less pronounced low energy shift of the site II cation band. Second, direct cation–adsorbate interaction involving all supercage ions is possible only in Y zeolites. Two of the eight ions per supercage in dry NaX and KX will be affected only indirectly and the number of unaffected ions will be even greater if some ions achieve a solvent coordination number greater than one.

As can be seen from the absorbance spectra of Figures 8–10 in which zeolites NaX and KX have been exposed to 0.05 Torr of the various adsorbents, the expected shift of the site II band to lower frequencies is less pronounced with sodium than with potassium. The 190-cm^{-1} band of dehydrated NaX shifts to only 180 cm^{-1} even in fully solvated or hydrated samples. On the other hand, corresponding levels of solvation in KX samples produce a shift in the site II potassium band more than twice as great as in NaX samples. This contrasting behavior reflects the extent of cation exposure to the supercage. Sodium ion, due to its smaller size, resides almost in the plane of the six-ring and is thereby screened to a large extent from direct interaction with adsorbed molecules in the supercage while the larger potassium ions are held well above the plane in trigonal pyramidal coordination to the O_2 oxygens. The shielding nature of planar or near-planar coordination is in agreement with a vibrational analysis of alkali metal ions encaged in a planar cyclic polyether[29] in which the cation motion frequencies are unperturbed by the presence of various organic molecules or anions. An alternative explanation of the more pronounced shift of potassium vs. sodium ion frequencies in X zeolites is that the solvent interacts only indirectly with site II ions and that delocalization of the framework charge has the least effect on cations held in near-planar coordination. This model of solvent behavior is supported by the results for solvated

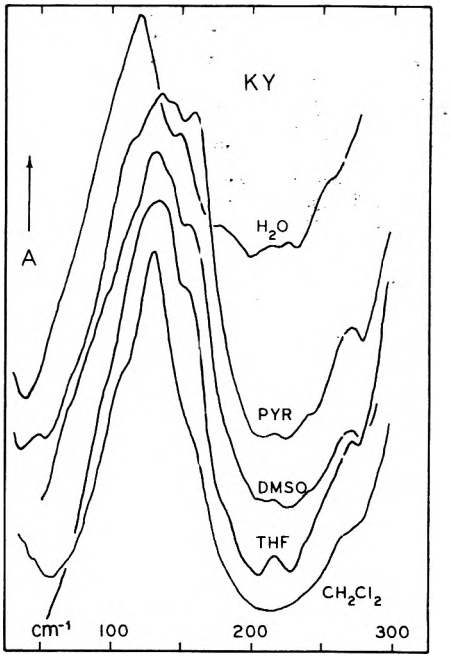

Figure 10. Far-infrared absorbance of dry KX zeolite exposed to 0.05 Torr of the indicated adsorbents.

KY zeolites discussed at the end of this section.

The most symmetric geometry of the solvated ion, ML_n^+, where n = 2, 3, or 4, will be linear, trigonal planar, and tetrahedral, respectively. Assuming that the local symmetry about the cation, $D_{\infty h}$, D_{3h}, or T_d, dominates the spectral selection rules, only the asymmetric stretching mode will be infrared active while the symmetric stretching mode is Raman active only. However, if these three structures are distorted, the symmetry is lowered and both the symmetric and asymmetric vibrations become infrared active. In the NaX spectra of Figures 8 and 9, a new band appears at higher and lower frequency than the site II band. The lower frequency band which grows in near 155 cm^{-1} is coincident with the weak shoulder already assigned to site I sodium, and the higher frequency band near 215 cm^{-1} is almost coincident with a weak framework mode at 220 cm^{-1}. Together, these two bands are assigned as the

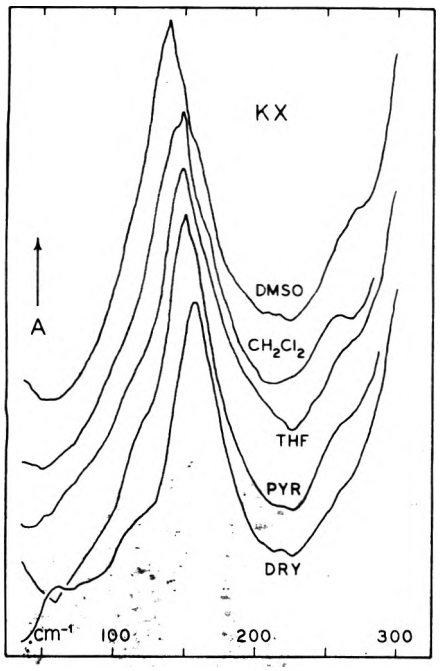

Figure 11. Far-infrared absorbance of dry KY zeolite exposed to 0.05 Torr of the indicated reagents.

symmetric and antisymmetric vibrations, respectively, of cations with distorted solvent coordination.

The presence of a solvated ion motion band at higher frequency than the site II mode is consonant with the results for hydrated zeolites, but the assignment of the lower frequency band as another mode of the same species requires further explanation. It would be tempting, for example, to assign this band to sodium ions migrating into site I, but this is contrary to the observation that migration, if it does occur, is out of site I.[17] Another alternative would be to assign the 155-cm^{-1} band to a sodium vibration on site II weakened by direct interaction with the adsorbate. This would mean that the main site II band is shifted only slightly from 190 cm^{-1} due to charge delocalization effects alone. Although attractive, this last explanation is not tenable because the low-frequency band disappears in moderately hydrated samples. The 155-cm^{-1} band grows in at low hydration levels as with the organic solvents but then completely disappears at moderate to full hydration leaving only the site II band at 180 cm^{-1} and the solvated ion band at 215 cm^{-1}. This indicates that at low hydration levels and at all solvation levels with the organic adsorbates, the limited amount of solvent bonds unsymmetrically to cations considered in solution in the supercage. Of the solvents studied, only water molecules can occupy the supercages in sufficient number to provide a high symmetry field around each cation which causes the symmetric stretching vibration to disappear.

The two modes of the same solvated species appear in the KX spectra as shoulders on the site II band at 120 and 165 cm^{-1}. As in the NaX samples, the growth of these bands is accompanied by a decrease in the intensity of the site III band. The symmetric and antisymmetric modes also appear in the spectra of KY zeolite at 115 and 155 cm^{-1} as shown in Figure 11. In fully solvated samples, these two shoulders become almost as intense as the site II band.

At low solvation levels, the site II band of KY at 133 cm^{-1} shifts two to three wavenumbers higher in frequency and at full solvation moves only three to four wavenumbers lower in frequency. A direct adsorbent–site II cation interaction should result in a more dramatic low energy shift, so this result indicates that the adsorbates preferentially solvate ions in the supercage. There are 20 cations per unit cell unlocated by x-ray of hydrated KY and 20 cations on site II, and if a similar distribution obtains in solvated zeolites, the maximum of 48 large molecules per unit cell will leave the free supercage ions well below the optimum coordination of four ligands. With all the adsorbates molecules thus involved in solvating free supercage cations, the site II vibrational frequency will be affected only indirectly by charge delocalization, and since there is less site charge to be delocalized in Y than in X, the frequency shift is less.

TABLE V: Cation–Rigid Framework Vibrational Force Constants (mdyn/Å)

Zeolite	Site II	Zeolite	Site II
LiY	0.59	CaX	1.76
NaY	0.44	CaY	1.22
AgY	0.43	SrY	1.16
KY	0.41	BaY	0.93
CsY	0.30		

Zeolite	Site II	Site III
NaX	0.49	0.06
KX	0.56	0.08
RbX	0.59	0.12
CsX	0.58	0.12

Discussion

Among the dehydrated zeolites, several bands are observed in each case and attributed to cations on different crystallographic sites. Our confidence in the band assignments is buttressed by the fact that there is a nearly linear relation between the frequencies of site II or site III vibrations in each zeolite and $m^{-1/2}$ for each cation. The deviation from linearity shows an interesting relation between the cation–framework force constant and the cation size and framework charge: in Y zeolites, the force constant decreases slightly with increasing cation size, but in X zeolites, the force constant increases slightly with cation size indicating that secondary electrostatic interactions become significant in the more highly charged zeolite. The force constants, calculated assuming a symmetric vibration and a rigid framework with the expression $k = 4\pi^2\nu^2\mu$ and $\mu \simeq M$, are listed in Table V. The anomalously high value for LiY is probably due to the fact that lithium ion is six-coordinate at site II rather than three-coordinate.

The site II cation–framework force constants in Y zeolites should be related to the activation energy of ionic conduction if the rate-determining step is a jump from site II to site III. This relation is evident in the Rice and Roth model of ionic transport in superionic conductors,[30] which presumes that the conducting ions may be thermally excited from their ionic sites above an energy gap, ϵ_0, so that they propagate through the lattice with a velocity, v_m, and a mean free path, l_m, to another localized ionic site. By relating[31] their expression for ionic conductivity to that of conventional hopping models, the energy gap, ϵ_0, is equal to the activation energy required to effect an ionic hop and

$$E = {}^1/_2 M\nu_0{}^2 a_0{}^2$$

where M is the cation mass, ν_0 is the vibrational frequency of the ion at a localized site, and a_0 is the hopping distance between a cation and a vacant neighboring site. The dependence of the activation energy on the rigid lattice force constant and the hopping distance was recently applied to inorganic oxide glasses.[31]

The most probable hopping distance in Y zeolites, site II–site III, varies with the size of the cation in the same

TABLE VI: Activation Energy of Ionic Conductivity

Zeolite	E_a^{expt} (ref 16), kJ mol^{-1}	a_0 (ref 16), A	ν_0, cm^{-1}	E_a^{calcd}, kJ mol^{-1}
LiY	90.3	5.02	380	113
NaY	74.2	4.62	180	71.6
KY	54.9	4.09	133	50.5
CsY	58.0	3.76	62	33
AgY		4.19	82	57

TABLE VII: Calculated Free Path for III → III Transition

Zeolite	E_a (ref 16), kJ mol^{-1}	ν_0, cm^{-1}	Free path (calcd), A
NaX	52.3	67	10.6
KX	54.7	58	9.6
RbX	67.4	48	8.7
CsX	55.5	37	8.2

way as the force constant and tends to lower the activation energy. The calculated energies listed in Table VI are in reasonable agreement with experimental values and require far fewer approximations than electrostatic calculations.

The observed activation energies of LiX and NaX are lower than those of the corresponding Y zeolite but the energies of K, Rb, and CsX are the same as in Y[16] due to cation–cation repulsions between sites II and III. (Such repulsions also account for the large observed E_a in CsY.) The rate-determining step does not appear to be the same in X zeolites as the simple II → III jump in Y zeolites because the higher force constants in X will make E_a systematically too high. Likewise, a jump for III → II involving the site III force constants results in activation energies systematically too low and leads to a dead end since site III must ultimately be repopulated. Although there are other possible single jump mechanisms to calculate, they are all suspect, since all of the supercage ions contribute to the conductivity and only one activation energy has been observed. A more likely approach is the intersticialcy pair mechanism invoked by Wang et al.[32] to explain transport in β-alumina in which the movement of one ion displaces another. Since the Rice and Roth free-ion model is only approximate at best and is only suited for cases in which there are readily available sites, it should not be expected to apply to a pair mechanism. It appears to apply usefully only when the motion of each ion may be considered to be an approximately independent event.

Another factor affecting the conductivity is the presence of residual sodium in Li, Rb, and Cs exchanged samples. The total number of supercage ions is greater in the last two cases than in the sodium zeolites resulting in the framework charge in the small cages being not as effectively neutralized. Accordingly, the site I Na frequency increases as noted in Tables II and III. In RbX and CsX, about 2/5 of the residual sodium is in the supercages and will have the effect of increasing the activation energy if cooperative interactions are predominant.

Most of the residual sodium in divalent exchanged samples is at site II. Exchange with divalent ions inevitably leaves some of the negatively charged aluminum tetrahedra only indirectly compensated. As a consequence, the local framework charge experienced by the remaining Na will be greater and the site II Na vibrational frequency is seen in Table IV to increase relative to pure sodium zeolite. The smaller number of ions and the larger number of vacancies in divalent zeolites is well suited to the free ion model of ionic conduction but the only conductivity measurements on these zeolites pertain to hydrated samples[23] or organic solvents.[33]

Acknowledgment. We are grateful for the valuable assistance of Mr. Carl Chalek in this work. This work was supported in part by the Office of Naval Research. We gratefully acknowledge that support and the support and use of facilities of the Materials Science Program of Brown University.

References and Notes

(1) (a) P. A. Jacobs and J. B. Uytterhoeven, *J. Catal.*, **26**, 175 (1972); (b) P. A. Jacobs, B. K. G. Theng, and J. B. Uytterhoeven, *ibid.*, **26**, 191 (1972).
(2) A. Bielanski and J. Datka, *J. Catal.*, **32**, 183 (1974).
(3) P. E. Riley and K. Seff, *J. Phys. Chem.*, **79**, 1594 (1975).
(4) P. Pichat, J. C. Vedrine, P. Gallezot, and B. Imelik, *J. Catal.*, **32**, 190 (1974).
(5) D. J. C. Yates, *J. Phys. Chem.*, **70**, 3693 (1966).
(6) G. T. Kerr, *Adv. Chem. Ser.*, **No. 121**, 219 (1973).
(7) (a) A. T. Tsatsas, J. W. Reed, and W. M. Risen, Jr., *J. Chem. Phys.*, **55**, 3260 (1971); (b) G. J. Exarhos, P. J. Miller, and W. M. Risen, Jr., *ibid.*, **60**, 4145 (1974).
(8) W. M. Butler and W. M. Risen, Jr., submitted for publication.
(9) I. A. Brodskii, S. P. Zhdanov, and A. E. Stanevich, *Sov. Phys. Solid State*, **15**, 1771 (1974).
(10) I. A. Brodskii, S. P. Zhdanov, and A. E. Stanevich, *Opt. Spektrosk.*, **30**, 58 (1971).
(11) W. M. Meier and D. H. Olson, *Adv. Chem. Ser.*, **No. 101**, 155 (1971).
(12) J. V. Smith, *Adv. Chem. Ser.*, **No. 101**, 171 (1971).
(13) (a) W. J. Mortier and H. J. Bosmans, *J. Phys. Chem.*, **75**, 3327 (1971); (b) W. J. Mortier, H. J. Bosmans, and J. B. Uytterhoeven, *ibid.*, **76**, 650 (1972).
(14) I. E. Maxwell and J. J. deBoer, *J. Phys. Chem.*, **79**, 1874 (1975).
(15) J. Marti, J. Soria, and F. H. Cano, *J. Phys. Chem.*, **80**, 1776 (1976).
(16) F. J. Jansen and R. A. Schoonheydt, *J. Chem. Soc., Faraday Trans. 1*, **69**, 1338 (1973).
(17) (a) P. Gallezot, Y. Ben Taarit, and B. Imelik, *J. Catal.*, **26**, 295 (1972); (b) *J. Phys. Chem.*, **77**, 2556 (1973).
(18) C. L. Angell and P. C. Schaffer, *J. Phys. Chem.*, **70**, 1413 (1966).
(19) N. N. Tikhomirova, I. V. Nikolaeva, E. N. Rosolovskaya, V. V. Demkin, and K. V. Topchieva, *J. Catal.*, **40**, 61 (1975).
(20) A. Maes and A. Cremers, *Adv. Chem. Ser.*, **No. 121**, 230 (1973).
(21) E. Dempsey, *J. Phys. Chem.*, **73**, 3660 (1969).
(22) W. J.Mortier, *J. Phys. Chem.*, **79**, 1447 (1975).
(23) M. L. Costenoble cited by R. A. Schoonheydt, W. DeWilde, and F. Velghe, *J. Phys. Chem.*, **80**, 511 (1976).
(24) W. L. Roth, *J. Solid State Chem.*, **4**, 60 (1972).
(25) L. P. Aldridge and C. G. Pope, *J. Inorg. Nucl. Chem.*, **36**, 2097 (1974).
(26) P. E. Riley and K. Seff, *J. Phys. Chem.*, **79**, 2163 (1975).
(27) W. F. Edgell, J. Lyford, IV, R. Wright, W. Risen, Jr., and A. T. Watts, *J. Am. Chem. Soc.*, **92**, 2240 (1970).
(28) M. M. Dubinin and V. A. Astakhov, *Adv. Chem. Ser.*, **No. 102**, 69 (1971).
(29) A. T. Tsatsas, R. W. Stearns, and W. M. Risen, Jr., *J. Am. Chem. Soc.*, **94**, 5247 (1972).
(30) M. J. Rice and W. L. Roth, *J. Solid State Chem.*, **4**, 294 (1972).
(31) G. J. Exarhos, P. J. Miller, and W. M. Risen, Jr., *Solid State Commun.*, **17**, 29 (1975).
(32) J. C. Wang, M. Gaffari, and S. Choi, *J. Chem. Phys.*, **63**, 772 (1975).
(33) A. Dyer and R. B. Gettins, *J. Inorg. Nucl. Chem.*, **32**, 2401 (1970).
(34) J. W. Ward, *Adv. Chem. Ser.*, **No. 101**, 380 (1971).
(35) (a) A. V. Kiselev, V. I. Lygin, and R. V. Starodubceva, *J. Chem. Soc., Faraday Trans. 1*, **68**, 1793 (1972); (b) V. K. Chuikina, A. V. Kiselev, L. V. Mineyeva, and G. G. Muttik, *ibid.*, **72**, 1345 (1976).

Thermochemistry of the Copper Fluorides

T. C. Ehlert* and J. S. Wang†

Chemistry Department, Marquette University, Milwaukee, Wisconsin 53233 *(Received March 25, 1977)*

Identification of the solid phases and vapor species of the copper–fluorine system at high temperatures and the measurement of their thermochemical properties were performed by the application of mass spectrometry, x-ray diffraction, and thermal analysis. Solid CuF_2 is stable in the presence of Cu or Pt up to its melting point at 1109 ± 5 K. The heat of fusion is 13 ± 2 kcal mol^{-1}. The heat of the sublimation at 298 K is 65.0 ± 0.5 kcal mol^{-1}. The vapor pressure of $CuF_2(c)$ is given by $R \ln P_{atm} = -(62.17 \pm 0.67)10^3/T + 39.64 \pm 0.72$. $\Delta H_f°_{298}(CuF_2, g)$ was found to be −63.8 ± 1.3 kcal mol^{-1}. The thermal expansion coefficients of CuF_2 between 300 and 1000 K were found to be $\alpha_a = (1.9 \pm 0.6)10^{-5}$ K^{-1}, $\alpha_b = (0.7 \pm 0.5)10^{-5}$ K^{-1}, $\alpha_c = (1.2 \pm 0.8)10^{-5}$ K^{-1}, and $\alpha_v = (3.9 \pm 0.9)10^{-5}$ K^{-1}. The thermal expansion of the unit cell is therefore anisotropic. $(CuF)_{1-5}(g)$ form when CuF_2 is heated in the presence of Cu but no evidence for CuF(c) was found. At 298 K $\Delta H_f(CuF, g)$ is 1.1 ± 3 kcal mol^{-1}. At 900 K the heats of formation of $Cu_2F_2(g)$, $Cu_3F_3(g)$, $Cu_4F_4(g)$, and $Cu_5F_5(g)$ are −48.8 ± 1.4, −112.7 ± 1.6, −177.2 ± 1.7, and −229 ± 3 kcal mol^{-1}, respectively. D(Cu–F) and D(FCu–F) are 98.8 ± 3 and 84 ± 4 kcal mol^{-1}, respectively. No evidence was found for the formation of CuF_3 by the reaction of CuF_2 and F_2 at temperatures ranging from ambient to 1200 K. At 900 K $\Delta H_f(CaCuF_4, c)$ is −241.9 ± 3 kcal mol^{-1}.

Introduction

Our original objective was to prepare CuF_3 in situ in our mass spectrometer-effusion apparatus described previously[1] by allowing F_2 and CuF_2 to react. Hope for success was drawn chiefly from a prediction that the solid is stable[2] and could be detected as $CuF_3(g)$ or by its decomposition product, F_2. However, reduction of the CuF_2 by one of the effusion cells used led to the formation of CuF and its polymers. Since gaseous CuF polymers had not been observed previously we attempted to learn their stabilities. Considerable attention was devoted to the study of the monomer CuF since the ionization potential (IP) and dissociation energy reported by Hildenbrand[3] were not in agreement with the values given by Margrave and co-workers.[4] An examination of the solid phase formed when CuF_2 is heated under reducing conditions also seemed worthwhile since a patent[5] has been issued for the preparation of CuF(c) even though von Wartenberg[6] found CuF to be a metastable solid and several other attempts[7] to produce CuF(c) failed. Consequently, thermal analysis and x-ray diffraction methods were used to study CuF_2 under reducing as well as neutral conditions from ambient temperature to over 1100 K.

Method

Anhydrous, high purity CuF_2 was used[8] as received. Our analyses showed all impurities amounted to less than 0.1% by weight. CuF_2 was handled under dry N_2 only to prevent absorption of water. This is quite important because CuF_2 hydrates to form $CuF_2 \cdot 2H_2O$ which is decomposed to CuO and Cu_2O on heating. The mass spectrometer-effusion apparatus used differed from that described previously[1] in that the electron multiplier was moved to a paraxial location.[9]

For in situ fluorination of CuF_2 the effusion cell and its gas inlet were made of machined, sintered CaF_2.

Reducing conditions were obtained by using a copper effusion cell having a knife-edge orifice and a sample area 360 times larger than the orifice area.

Neutral conditions were obtained by using a cell of 0.01 cm platinum foil, having a sample area 900 times larger than the orifice area and a cell of CaF_2, having a sample area/orifice area ratio of 50. As before, the cell was made isothermal (±3 K) by using two, independent heating filaments.

Appearance potentials (AP) and ionization potentials (IP) were obtained by the automatic semilog plot method described previously[1] using the known[10] IP of CO_2, HCl, O_2, H_2O, C_6H_6, and Hg to calibrate the electron energy scale. Linear ion current vs. electron energy plots were also made and deconvoluted[11] to help distinguish fragment and parent ions.

Absolute pressures were derived from time, temperature, ion current, and weight loss data using the internal calibration procedure described previously.[12] The essentials are repeated here for clarity. The procedure employs the equation

$$\Delta w = 44.33 a C \sum_i k_i M_i^{1/2} \left(\sum_n \Delta t_n T_n^{1/2} I_{i,n}\right) \quad (1)$$

where Δw is the total weight loss in grams due to the effusive escape from a cell of orifice area a cm^2 and Clausing factor C[13] by vapor species of molecular weight M_i, and is accumulated while the sample was held at a series of temperatures T_n for time intervals Δt_n. $I_{i,n}$ is the ion current in amperes derived from ionization of the ith vapor species and 44.33 is the units-conversion constant needed to give the sensitivity constants k_i units of atm K^{-1} A^{-1}. The sum over i accounts for all vapor species contributing to weight loss. The sum over n accounts for the time spent at various temperatures while making measurements of the temperature dependences of the various ion currents. When more than one vapor species was present eq 1 was solved by relating all the k_i to that for one species through the well-known relation[14]

$$k_i = k_j \frac{G_j \sigma_j \Delta E_j \tau_j}{G_i \sigma_i \Delta E_i \tau_i} \quad (2)$$

where G, σ, and ΔE represent the detector gain, ionization cross section, and the electron energy in excess of the AP or IP, and where τ is the relative ion transmission efficiency, a factor which is needed to account for the discrimination in the mass analyzer.[15]

Thermal analyses were performed under dry Ar on a Mettler thermoanalyzer. The temperature scale was calibrated at the transition in $BaCO_3$ (NBS standard reference material 760) for the heating rates used, 6 and 8 K min^{-1}. Both Pt and Cu sample containers were used.

† Taken in part from the Ph.D. Dissertation of J. S. Wang, Marquette University, 1976.

TABLE I: Relative Ion Abundances in the 70-eV Mass Spectrum of CuF_2 Sublimed from Different Containers[a]

Species	Pt cell at 981 K	Cu cell at 964 K	CaF_2 cell at 903 K
Cu^+	34	31	40
CuF^+	100	100	100
CuF_2^+	28	34	25
Cu_2^+		3	
Cu_2F^+		35	
$Cu_2F_2^+$		2	
$Cu_3F_2^+$		20	
$Cu_3F_3^+$		4	
$Cu_4F_3^+$		0.6	
$Cu_4F_4^+$		5	
$Cu_5F_5^+$		0.14	

[a] Total intensity of all isotopic varieties, uncorrected for analyzer discrimination, F^+ not measureable due to high background.

An empty container served as the reference material.

For purposes of identifying residues from experiments, x-ray powder patterns were taken using a 115 mm Debye–Scherrer camera. High temperature studies were performed on a GE diffractometer equipped with a Rigaku-Denki furnace. Lattice parameters at different temperatures were obtained by a least-squares computation.[16] Cu Kα radiation was used in all cases.

Results

For CuF_2 vaporized under neutral conditions, the mass spectrum consists of F^+, Cu^+, CuF^+, and CuF_2^+. Table I gives the relative abundances at 981 K. Although our APs, Table II, are not in good agreement with those of Margrave's group,[4] our interpretation is the same. Namely, CuF_2 sublimes without decomposition to the monomer so that CuF^+ and Cu^+ are merely fragments of CuF_2, as suggested by the high APs for these ions. CuF_2^+ was therefore used to monitor the sublimation process, the data for which are given in Table III. The least-squares equation for the sublimation of CuF_2 using Table III data is

$$R \ln P_{atm} = \frac{-(62.39 \pm 1.05)10^3}{T} + 40.00 \pm 1.12 \quad (3)$$

Using CuF^+ to monitor the sublimation process gives

$$R \ln P_{atm} = \frac{-(63.17 \pm 0.67)10^3}{T} + 39.64 \pm 0.72 \quad (4)$$

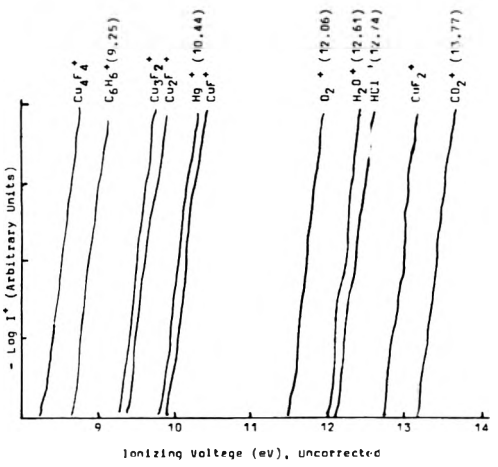

Figure 1. SL plot determination of the first APs in the Cu–F system.

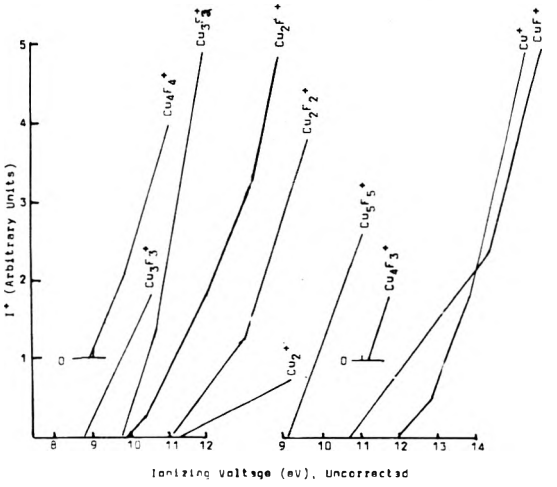

Figure 2. Deconvoluted ionization efficiency curves for Cu–F species.

As shown in Table I, the mass spectrum obtained when CuF_2 was heated in a copper effusion cell differed considerably from that obtained when a platinum cell was used. The only logical interpretation for the difference is the formation of CuF and its polymers. Masses, isotopic varieties, and shutter effects confirmed the identities of the ions observed. Figure 1 shows the semilog plots of the threshold ion currents used to find the lowest APs and Figure 2 shows the deconvoluted threshold ion currents

TABLE II: Appearance Potentials in the Cu-F System in eV

Ion	CuF_2-Pt at 981 K	CuF_2-Cu at 948 K	CuF_2-CaF_2 at 903 K	Lit. Ref 4	Lit. Ref 3
Cu^+	14.8 ± 0.3	12.0 ± 0.3	12.2 ± 0.3	16.5 ± 0.3	
		12.8 ± 0.3	15.2 ± 0.3		
		13.8 ± 0.3			
CuF^+	14.2 ± 0.1	10.5 ± 0.1	10.8 ± 0.3	8.6 ± 0.3	10.5 ± 0.3
		14.2 ± 0.3	14.2 ± 0.3	12.4 ± 0.3	
CuF_2^+	13.4 ± 0.2	13.3 ± 0.1	13.2 ± 0.1	11.3 ± 0.3	
Cu_2^+		11.2 ± 0.3			
Cu_2F^+		10.0 ± 0.1			
		10.5 ± 0.3			
		13.2 ± 0.3			
$Cu_2F_2^+$		11.1 ± 0.3			
		13.0 ± 0.3			
$Cu_3F_2^+$		9.9 ± 0.1			
		10.7 ± 0.3			
$Cu_3F_3^+$		8.8 ± 0.3			
$Cu_4F_3^+$		Intensity too low to measure			
$Cu_4F_4^+$		8.9 ± 0.1			
		9.8 ± 0.3			
$Cu_5F_5^+$		9.1 ± 0.1			

TABLE III: The Sublimation Pressure of CuF_2[a]

T/K	CuF_2^+ data P/atm × 10^6	CuF^+ data P/atm × 10^6
874	0.126	0.125
884	0.181	0.181
892	0.258	0.273
907	0.438	0.441
915	0.774	0.704
926	1.14	0.835
937	1.70	1.58
946	2.28	2.18
956	2.88	2.79
963	4.08	3.47
974	5.40	4.48
983	6.64	7.53
993	10.1	11.1
1000	12.3	13.0
986	7.64	7.31
972	4.70	4.22
954	3.10	2.92
938	1.58	1.53
924	1.07	0.95
900	0.348	0.346
886	0.235	0.231
909	0.744	0.558
935	1.31	1.29
956	2.77	2.84
973	4.69	4.42
994	9.12	9.16
1005	13.4	14.4
980	7.09	6.51
959	3.25	3.09
937	1.63	1.38
911	0.660	0.536
897	0.380	0.358
885	0.213	0.227

[a] Pt cell, $a = 2.21 \times 10^{-3}$ cm², $C = 0.91$, $\Delta w = 3.78 \times 10^{-3}$ g.

used to find the higher APs. Considering the high APs and that at the temperatures involved copper's vapor pressure is only of the order of 10^{-12} atm, Cu^+ and Cu_2^+ were taken to be fragment ions. For CuF^+ Figure 2 shows a process which has its threshold at 10.5 eV, the reported[3] IP of CuF, in addition to CuF^+ formation by fragmentation of CuF_2 which begins at 14.2 eV. Thus, below 14.2 eV we have taken CuF to be the precursor of CuF^+. The break in the CuF^+ curve at 14.2 eV plus the agreement of AP-(CuF_2^+) with our IP(CuF_2) shows that CuF_2(g) was also present in the cell. We have taken the low APs for $Cu_3F_3^+$, $Cu_4F_4^+$, and $Cu_5F_5^+$ to indicate that these are parent ions for the trimer, tetramer, and pentamer of CuF, respectively. We have taken $Cu_3F_2^+$ in the threshold region to be a fragment of Cu_3F_3 because of its high AP and because of good evidence[17] that in the Cu–Cl system $Cu_3Cl_2^+$ is almost entirely derived from Cu_3Cl_3 at low electron energies. The interpretations for Cu_2F^+ and $Cu_2F_2^+$ are difficult. On one hand, it had been established that Cu_2Cl_2 is a vapor species in the Cu–Cl system.[18] On the other hand, the APs and temperature dependences, discussed later, do not rule out the possibility that these ions are fragments of a higher polymer. We have treated Cu_2F^+ and $Cu_2F_2^+$ as being fragments of Cu_2F_2 up to the first breaks in the curves, Figure 2. This assumption, fortunately, has essentially no effect on the thermodynamic data derived for the other vapor species since Cu_2F_2 contributes only a few percent to the total vapor pressure here. Cu_4F_4 has been taken to be the precursor of $Cu_4F_4^+$ near the threshold.

To determine the partial pressures of the species in the Cu–CuF_2 system it should be possible to perform a sufficient number of quantitative vaporization experiments, expressed in the form of eq 1, and then to solve these

TABLE IV: Data for Quantitative Vaporization Experiments, Cu + CuF_2 System[a]

Experiment	1	2	3
Temperature, T/K	946	936	948
Total wt loss, Δw/g	0.04083	0.01697	0.01516
Time, Δt/s	1.335×10^5	8.640×10^4	4.440×10^4
Species	P × 10^6/atm[b]	P × 10^6/atm[b]	P × 10^6/atm[b]
CuF	0.95	0.63	1.06
CuF_2	1.47	0.98	1.63
Cu_2F_2	0.18	0.11	0.21
Cu_3F_3	0.84	0.50	0.95
Cu_4F_4	0.26	0.16	0.29
Cu_5F_5	0.014	0.008	0.015

[a] Orifice area = 4.95×10^{-3} cm². Clausing factor = 0.97, 15-eV electron energy. [b] Calculated using eq 3.

equations simultaneously to obtain the sensitivity constant k_i for each vapor species. In practice, however, the accuracy demanded by this method is too great so it became necessary to estimate these constants using eq 2 in order to have some idea as to the vapor composition. To do this it was assumed that the activity of CuF_2(c) was not affected by the presence of copper. This is supported by the agreement between the temperature dependences of CuF_2^+ in the CuF_2–Cu and CuF_2–Pt systems as discussed later. Then, from the CuF_2 vapor pressure equation (eq 3), CuF^+ current, and temperature, k_{CuF_2} was calculated via the $P = kIT$ equation.[19] The constants k_i for CuF and its polymers were then calculated using eq 2 in which the product $G_i\sigma_i$ was taken to be a constant, independent of the species.[20] Alternative methods of estimating $G_i\sigma_i$ do not substantially change the k_i values. Ion currents were either measured below what appeared to be thresholds for fragment contribution given in Table II or, for low intensity signals, were obtained with 15-V electrons and then reduced to the portion attributed to the threshold process, assumed to depend linearly on ΔE. Analyzer discrimination corrections (τ_j/τ_i) were obtained[15] from measurements of the $^{63}Cu^+$ and $^{65}Cu^+$ abundances in the various ionic species. These corrections agreed, ±10%, with those found by operating the quadrupole analyzer at low resolution where total ion transmission is achieved. The pressures thus calculated are summarized in Table IV.

Six other experiments were performed to determine $\Delta H = -R[\mathrm{d} \ln (I_iT)/\mathrm{d}(1/T)]$ for all the ionic species for which a precursor could be estimated with reasonable certainty. These results are summarized in Table V.

The x-ray diffraction patterns of the CuF_2 residues from the several mass spectrometric experiments indicated in all cases only CuF_2 and a trace of Cu_2O when a Pt effusion cell was used. When the effusion cell was Cu, however, a substantial amount of crystalline Cu was found to be dispersed in the CuF_2 residue. The diffraction pattern of CuF_2 as a function of temperature showed only the expected lattice expansion and decreasing intensity as the temperature was increased. The lattice parameters for each set of interplanar spacing at each temperature were subjected to least-squares analysis and then plotted vs. temperature to give the thermal expansion coefficients. Above 1000 K CuF_2 gives no detectable diffraction pattern.

Thermal analyses were performed on two samples of CuF_2 in Pt containers and two in Cu containers. At least three heating and cooling scans were made on each sample. When heated in a Pt container endothermic transitions were observed at 1028, 1065, and 1109 K. The 1065 and 1109 K transitions were similar in size and shape while the 1028 K transition was much less energetic and appeared

TABLE V: $\Delta H = -R[\mathrm{d} \ln I_i T/\mathrm{d}(1/T)]$ Values for Cu-CuF_2 Reaction Products in kcal mol^{-1}

Run	$\bar{T}$	Ion/precursor							
		CuF_2^+/CuF_2	CuF^+/CuF	Cu_2F^+/Cu_2F_2	$Cu_2F_2^+/Cu_2F_2$	$Cu_3F_2^+/Cu_3F_3$	$Cu_3F_3^+/Cu_3F_3$	$Cu_4F_4^+/Cu_4F_4$	$Cu_5F_5^+/Cu_5F_5$
1	873	62.5 ± 0.9	63.8 ± 0.9	77.0 ± 1.0		79.5 ± 1.1		74.6 ± 1.0	90.4 ± 2.8
2	859	62.7 ± 0.7	64.2 ± 0.7	75.9 ± 0.9		78.4 ± 1.0		75.6 ± 1.0	82.4 ± 1.7
3	870	62.6 ± 1.0	63.9 ± 1.0	78.7 ± 1.5		79.9 ± 1.5		74.9 ± 1.4	90.4 ± 4.3
4	868	64.1 ± 0.9	66.9 ± 0.8	77.3 ± 1.0	73.0 ± 4	81.5 ± 1.1	71.6 ± 1.2	76.8 ± 1.0	91.7 ± 2.8
5	872	65.3 ± 0.8	67.2 ± 0.8	77.9 ± 0.9	78.8 ± 1.7	82.5 ± 0.9	75.1 ± 1.2	77.0 ± 1.0	87.6 ± 2.2
6	888	65.9 ± 0.9	66.9 ± 0.9	79.1 ± 1.1	81.4 ± 1.7	80.4 ± 1.1	73.4 ± 1.0	74.9 ± 1.0	81.4 ± 1.7
Av[a]		63.9 ± 0.9	65.5 ± 0.8	77.6 ± 1.1	77.7 ± 2.5	80.4 ± 1.1	73.4 ± 1.1	75.6 ± 1.1	87.3 ± 2.3

[a] Uncertainties shown are average standard deviations. Differences in median temperatures were ignored in averaging.

TABLE VI: P_{CuF_2} over CuF_2 in CaF_2 Effusion Cell

T/K	P/atm × 10^{6a}	T/K	P/atm × 10^{6b}
948	1.7	812	0.0013
938	1.0	818	0.0027
931	0.725	828	0.0041
925	0.590	841	0.010
920	0.450	849	0.013
912	0.310	850	0.017
904	0.210	861	0.035
895	0.140	873	0.052
886	0.097	884	0.086
878	0.050	892	0.124
867	0.034	886	0.074
858	0.021	875	0.045
847	0.013	875	0.040
837	0.0071	865	0.026
831	0.0053	854	0.016
		843	0.010
		835	0.0048
		826	0.0038
		816	0.0025

[a] Using 14-eV CuF_2^+ data. [b] Using 70-eV CuF_2^+ data.

to vary with the Cu_2O content of the sample. When heated in a Cu container a single endothermic transition at 1040 K was observed and the residue was found to contain of the order of 20% Cu and 10% Cu_2O using x-ray diffraction. The possibility that a Cu_2O–CuF_2 eutectic was responsible for the 1028 and 1040 K endotherms prompted us to obtain heating and cooling curves on the CuF_2 sample in the Cu effusion cell as part of the mass spectrometric analyses where the better vacuum conditions would have nearly eliminated Cu_2O. Four heating curves showed a plateau of 1040 K and four cooling curves showed a plateau at 1030 K. For this purpose, the output of one of the cell's thermocouples was recorded along with CuF_2^+ ion current using a two-pen recorder to that the plateaus were simultaneously observed on both the thermocouple output and the CuF_2^+ signal.

The pressure of CuF_2 when the CaF_2 effusion cell was used is given as a function of temperature in Table VI. Pressure calibration was based on a separate experiment, using the same cell, in which 3.09×10^{-3} g were vaporized in 1.06×10^5 s from the cell at 911 K. The cell orifice area was 1.11×10^{-2} cm^2 and the Clausing factor was 0.60. Comparison with Table III shows P_{CuF_2} is decidedly lower in the presence of CaF_2. Least-squares analysis of the temperature dependence of the tabulated CuF_2 pressures gave $\Delta\tilde{H}_{889\ K} = 76.8 \pm 1.2$ kcal mol^{-1} which is higher than the heat of sublimation of CuF_2. As the CuF_2 pressures were not time dependent the source of CuF_2 appeared to be a CuF_2–CaF_2 compound. This was supported by our observation that at high temperatures the diffraction pattern of CuF_2 supported by CaF_2 showed peaks not belonging to CaF_2 or to CuF_2. An equal mole mixture of CaF_2 and CuF_2 was heated at 1050 K for 3 h and then subjected to x-ray diffraction analysis. The product was identified as $CaCuF_4$, based on the very good agreement between our diffraction pattern and that reported previously.[21]

TABLE VII: ΔH and ΔS Values for Eq 5 at $\bar{T}$ = 880 K and $\Delta\tilde{H}_f^\circ(Cu_nF_n, g)$

n	$\Delta\tilde{H}_{\bar{T}}$ kcal mol^{-1}	$\Delta\tilde{S}_{\bar{T}}$[a] cal K^{-1} mol^{-1}	$\Delta\tilde{H}_f^\circ(Cu_nF_n, g)$ kcal mol^{-1}	
			Second law at $\bar{T}$	at 298
1	65.5 ± 0.8	41.69 ± 0.05	2.3 ± 1.1	4.6 ± 3
2	77.6 ± 1.1	51.18 ± 0.08	−48.8 ± 1.4	
3	76.9 ± 1.1	53.46 ± 0.09	−112.7 ± 1.6	
4	75.6 ± 1.1	49.77 ± 0.06	−177.2 ± 1.7	
5	87.3 ± 2.3	56.29 ± 0.04	−228.7 ± 3	

[a] Uncertainty is average deviation of the three values of ΔS derived using Table IV pressures and by treating ΔH as exact.

No changes in the Cu^+, CuF^+, or CuF_2^+ abundances occurred when fluorine was introduced to the CaF_2 cell containing CuF_2 nor was there any evidence of fluorine evolution on heating CuF_2 which was first fluorinated at temperatures near ambient.

Conclusions

CuF_3 cannot be prepared by direct reaction of F_2 with CuF_2 at or above room temperature. The sublimation pressures of CuF_2 given by eq 4 are about three times lower than those reported previously and our $\Delta H_{subl}{}^\circ_{950}$ is about 2.7 kcal mol^{-1} higher than reported previously.[4] To find $\Delta H_{subl}{}^\circ_{298}$ via the second law we used $(H^\circ_{950} - H^\circ_{298})$ from a recent calorimetric study[22] on the solid and the JANAF value[23] for the gas. The result is 65.9 ± 1 kcal mol^{-1}. The third law $\Delta\tilde{H}_{subl}{}^\circ_{298}$, based on the same calorimetric and JANAF data, is 65.0 kcal mol^{-1}. The JANAF second and third law values are 62.5 kcal mol^{-1}. If CuF_2 is taken to be nonlinear as reported by Hastie et al.[24] from a matrix isolation study, the second law and third law values of $\Delta H_{subl}{}^\circ_{298}$ differ by 3.3 kcal mol^{-1}. This suggests that the spectrum has been misinterpreted or that the matrix causes CuF_2 to become nonlinear.

With $\Delta H_f{}^\circ_{298}(CuF_2, g)$[25] and $\Delta\tilde{H}_{subl}{}^\circ_{298} = 65.0 \pm 1.0$ we find $\Delta\tilde{H}_f{}^\circ_{298}(CuF_2, g) = -63.8 \pm 1.3$ kcal mol^{-1} and $\Delta\tilde{H}_{atom} = 182.6 \pm 2.6$ kcal mol^{-1}.

Near 950 K the vapors over the Cu–CuF_2 system consist, in order of abundance, of CuF_2, CuF, Cu_3F_3, Cu_4F_4, and Cu_5F_5. Cu_2F_2, if it exists, is a bit more abundant than Cu_5F_5 under these conditions. Assuming the polymer vapors were in equilibrium with the Cu cell and $CuF_2(c)$, the enthalpy changes, Table V, and pressures, Table IV, pertain to equilibria of the form

$$(n/2)CuF_2(c) + (n/2)Cu(c) = Cu_nF_n(g) \quad (5)$$

Table VII gives $P(Cu_nF_n)$ equations which were derived from Table IV data in the form $-R \ln P + \Delta H/T - \Delta S$ and $\Delta\tilde{H}_f{}^\circ_T(Cu_nF_n, g)$ values. For CuF(g) $\Delta\tilde{H}_f{}^\circ_{298} = 4.6$ kcal mol^{-1} using $(H^\circ_{880} - H^\circ_{298})$ values for the gas[23] and for $CuF_2(c)$,[22] compared to the third law value of −0.2 kcal

mol^{-1} using JANAF free energy functions with $R \ln P$ calculated from Table VII. By estimating P_{CuF} to be uncertain by a factor of 2 near 900 K and including ±2 kcal for the uncertainty arising in the free-energy functions the third law result is found to be uncertain to ±4 kcal mol^{-1}. As the second law value is probably uncertain by ±3 kcal mol^{-1} the agreement is satisfactory. Hildenbrand's data[3] for the equilibrium

$$MgF(g) + Cu(g) \rightleftharpoons Mg(g) + CuF(g)$$

give $\Delta\tilde{H}_f°_{298}(CuF, g) = -3.7 \pm 5$ kcal mol^{-1} after recalculation using JANAF data. Until more is known about the molecular constants of gaseous CuF and CuF_2 the best value for the heat of formation of CuF(g) at 298 K appears to be $+1.1 \pm 3$ kcal mol^{-1}. This corresponds to $D°_{298} = 98.8 \pm 3$ kcal mol^{-1} and $D°_{298}(FCu-F) = 83.8 \pm 4$ kcal mol^{-1}. If at the threshold Cu^+ is formed from CuF by dissociative ionization then $AP(Cu^+)$ from Table II, used in the approximation $D(Cu-F) = AP(Cu^+/CuF) - IP(Cu)$, gives $D(Cu-F) = 4.3 \pm 0.3$ eV (99 ± 7 kcal mol^{-1}) which is consistent with the thermochemical data.

Similarly, our IP(CuF) and $AP(CuF^+/CuF_2)$ indicate $D(FCu-F) = 3.64 \pm 0.2$ eV (84 ± 5 kcal mol^{-1}). Together, our electron impact results give $\Delta H_{atom,\bar{T}} = 7.9 \pm 0.5$ eV (182 ± 12 kcal mol^{-1}). Again, the electron impact and thermochemical results are consistent. Hildenbrand has already pointed out[3] the reason why $D(M-F) > D(FM-F)$ for copper, in contrast to the behavior of several other first transition series metals.

The heat of dimerization of CuF, −53 kcal mol^{-1}, seems reasonable when compared to that for KF, −50 kcal mol^{-1}.[23]

The anisotropic behavior previously noted in a low temperature neutron diffraction study[26] is confirmed. The average thermal expansion coefficients of CuF_2, 300–1000 K, are $\alpha_v = (3.9 \pm 0.9) \times 10^{-5}$ K^{-1}, $\alpha_a = (1.9 \pm 0.6) \times 10^{-5}$ K^{-1}, $\alpha_b = (0.7 \pm 0.5) \times 10^{-5}$ K^{-1}, $\alpha_c = (1.2 \pm 0.8) \times 10^{-5}$ K^{-1}. Both x-ray and DTA show there are no transitions in CuF_2 between room temperature and 1000 K in agreement with calorimetric results.[22] The transition observed by DTA at 1028 K is believed to be the formation of a Cu_2O–CuF_2 eutectic so that is energy is limited by the amount of Cu_2O present while the 1040 K transition in Cu containers is believed to be the formation of a Cu_2O–Cu–CuF_2 eutectic. The 1065 K transition is apparently a solid state transition, so that it is melting which occurs at 1109 K, about 60 K higher than the transition observed in a DTA study of a $CuF_2 + SiO_2 + CaF_2$ mixture.[27] The estimated uncertainty in these temperatures is ±10 K. It is interesting to note that recent work[28] has shown that for MnF_2, CoF_2, and ZnF_2 $dT/dP < 0$ for the rutile–fluorite phase boundary. For MnF_2 at 1 atm the rutile → fluorite transition was actually observed at 1023 K while CoF_2 and ZnF_2 melted before the transition occurred. Thus, it seems quite possible that the solid phase transition at 1065 K in CuF_2 is also the rutile → fluorite change. By treating the 20 wt % Cu–10 wt % Cu_2O eutectic formed with CuF_2 as an ideal solution the heat of fusion of CuF_2 can be estimated at 13.2 ± 2 kcal mol^{-1} from the eutectic temperature, 1040 K, and the melting point of CuF_2, taken to be 1109 K. This value seems quite reasonable when compared to the values for CoF_2, 14.1 kcal mol^{-1}, and MgF_2, 13.9 kcal mol^{-1}.[23]

In a CaF_2 effusion cell the source of $CuF_2(g)$ appears to be the process

$$CaCuF_4(c) \rightarrow CaF_2(c) + CuF_2(g) \quad (6)$$

To find $\Delta H_{f,900}(CaCuF_4,c)$ we combined the $\Delta H°_{900}$ (eq 6), 76.8 ± 1.2 kcal mol^{-1}, $\Delta\tilde{H}_f°(CaF_2, c)$, −291.1 ± 1.5 kcal mol^{-1},[23] and $\Delta\tilde{H}_f°(CuF_2, c)$, -126.0 ± 0.3 kcal mol^{-1}.[22,25] The result is -241.9 ± 3 kcal mol^{-1}. Thermal dissociation of $CuF_2(g)$ can account for the presence of CuF(g) in this system, indicated by the AP data in Table II.

None of our observations indicate the stable existence of CuF(c) or CuF(l).

Acknowledgment. The authors thank Drs. Joseph Doninger and James Currier of International Minerals and Chemical Corp. for allowing us to use the Mettler thermoanalyzer and Dr. Dayal Meshri of Ozark-Mahoning Corp. for providing the very pure and dry CuF_2 samples.

References and Notes

(1) T. C. Ehlert and M. Hsia, *J. Fluorine Chem.*, **2**, 33 (1972/1973).
(2) M. Barber, J. W. Linnett, and N. H. Taylor, *J. Chem. Soc.*, 3323 (1961).
(3) D. L. Hildenbrand, *J. Chem. Phys.*, **48**, 2457 (1968).
(4) R. A. Kent, J. D. McDonald, and J. L. Margrave, *J. Phys. Chem.*, **70**, 874 (1966).
(5) D. A. McCaulay, U.S. Patent 2 817 576 (1957).
(6) H. von Wartenberg, *Z. Anorg. Allg.*, **241**, 381 (1939).
(7) J. M. Crabtree, C. S. Lees, and K. Little, *J. Inorg. Nucl. Chem.*, **1**, 213 (1955).
(8) Kindly provided by D. Meshri, Ozark-Mahoning Corp.
(9) Special photomultiplier SPMO3-419, DuMont Corp.
(10) J. L. Franklin, J. G. Dillard, H. M. Rosenstock, J. T. Herron, K. Draxl, and F. H. Field, *Natl. Stand. Ref. Data Ser., Natl. Bur. Stand.*, **No. 26** (1969).
(11) R. E. Winters, J. H. Collins, and W. L. Courchene, *J. Chem. Phys.*, **45**, 1931 (1966).
(12) T. C. Ehlert and M. Hsia, *J. Chem. Eng. Data*, **17**, 18 (1972).
(13) R. P. Iczkowski, J. L. Margrave, and S. M. Robinson, *J. Phys. Chem.*, **67**, 229 (1963).
(14) R. T. Grimley, "The Characterization of High-Temperature Vapors", J. L. Margrave, Ed., Wiley, New York, N.Y., 1967, p 225.
(15) T. C. Ehlert, *J. Sci. Instrum.*, **48**, 237 (1970).
(16) J. K. Boyter and R. M. Brugger, "Introducing Computer Programs for Neutron Diffraction", U.S. Atomic Energy Commission Research and Development Report Issued Under Contract AT(10-1)-1230 (1968).
(17) L. C. Wagner, P. Robert, Q. Grindstaff, and R. T. Grimley, *Int. J. Mass Spectrom. Ion Phys.*, **15**, 255 (1974).
(18) M. Guido, G. Gigli, and G. Balducci, *J. Chem. Phys.*, **57**, 3731 (1972).
(19) W. A. Chupka and M. G. Inghram, *J. Phys. Chem.*, **59**, 100 (1955).
(20) D. L. Hildenbrand, "Some Checks on the Mass Spectrometric Method of Measuring Gaseous Equilibria", 21st Annual Conference on Mass Spectrometry and Applied Topics, San Francisco, Calif., 1973.
(21) D. Dumora, J. Ravez, and P. Hagenmuller, *Bull. Soc. Chim. Fr.*, 1361 (1970).
(22) T. C. Ehlert, *Thermochim. Acta*, submitted for publication.
(23) D. R. Stull and H. Prophet, *Natl. Stand. Ref. Data, Ser., Natl. Bur. Stand.*, **No. 37** (1971).
(24) J. W. Hastie, R. Hauge, and J. L. Margrave, *Chem. Commun.*, 1452 (1969).
(25) V. S. Pervov, V. Ya Leonidov, L. I. Klyuev, and A. G. Muravina, *Dokl. Akad. Nauk SSSR*, **214**, 1088 (1974).
(26) P. Fisher, W. Hälg, D. Schwarzenbach, and H. Gamsjäger, *J. Phys. Chem. Solids*, **35**, 1683 (1974).
(27) H. M. Haendler, L. H. Towls, E. F. Bennett, and W. L. Patterson, Jr., *J. Am. Chem. Soc.*, **76**, 2178 (1954).
(28) L. M. Lityagina, M. F. Kachan, S. S. Kobalkina, and L. F. Vereshchagin, *Dokl. Akad. Nauk, SSSR*, **216**, 1066 (1974).

The Enthalpy of Interaction between Various Amino Acids and Sodium Chloride

John W. Larson,* W. Joseph Plymale, and Albert F. Joseph

Department of Chemistry, Marshall University, Huntington, West Virginia 25701 *(Received June 2, 1977)*

The enthalpies of interaction between aqueous NaCl and aqueous solutions of seven amino acids have been determined calorimetrically. These enthalpies $\Delta H_s°$, are for the reaction amino acid$^{\pm}$(aq) = amino acid$^{\pm}$(ideal, 1 M NaCl). The values obtained for $\Delta H_s°$ are −211 cal/mol for glycine, 3 cal/mol for α-alanine, 112 cal/mol for valine, −120 cal/mol for serine, −78 cal/mol for β-alanine, −16 cal/mol for γ-aminobutyric acid, and 161 cal/mol for ε-aminocaproic acid. These results are discussed in terms of compensation and the influence of the amino acids on the structure making–breaking of water.

Introduction

Biological systems consist largely of highly polar molecules (water, amino acids, etc.) and of ions carrying a net charge. The chemistry of these systems cannot be properly understood without an understanding of the physical interactions in these systems.

In a previous paper,[1] data were presented on the enthalpy of interaction between glycine and NaCl in water. These results indicated that even though electrostatic theories account nicely for the free energy of interaction between dipolar ions and electrolytes, they do not even qualitatively account for the enthalpy of interaction.

In this paper, data are presented on two series of amino acids in order to provide information to answer two fundamental questions: How do the electrostatic theories account for free energy data but not enthalpy data? What information can be obtained from enthalpy data?

In the first series of amino acids studied, the dipole moment of the amino acid increased from 13.5 D for glycine to 24.1 D for ε-aminocaproic acid. Comparable free energy data are also available for this series.[2]

The second series consisted of glycine, alanine, valine, and serine in which the dipole moment remained approximately constant and the side group varied.

Experimental Section

The calorimeter has been described previously.[1,3] Certified ACS sodium chloride was obtained from the Fisher Scientific Co. It was used without further purification. β-Alanine (J. T. Baker Co., mp 199 °C), γ-aminobutyric acid (Nutritional Biochemical Corp., mp 194 °C), ε-aminocaproic acid (Nutritional Biochemical Corp., mp 203 °C), *dl*-α-alanine (Matheson Coleman and Bell, mp 293 °C), *dl*-valine (Eastman Kodak Co., mp 296 °C), and *dl*-serine (Nutritional Biochemicals Corp., mp 233 °C) were used in the measurements. The melting points of all of these were in good agreement with literature values and were used without further purification. β-Alanine was recrystallized from a water–ethanol mixture and dried before using.

Procedure and Calculations

The enthalpy of interaction between the amino acids and NaCl was determined by one of two methods. In method 1, a concentrated aqueous solution of NaCl was made up by weight. Samples of about 5 g were taken from this solution and weighed accurately into thin glass bulbs of 6–12 mL capacity. Sample entry into aqueous amino acid solutions of varying concentrations was effected by breaking the bulb.

By subtracting the heat of solution of the concentrated solution of NaCl into water from its heat of solution into the aqueous amino acid solution, $\Delta H_1(a)$ values were obtained for the reaction

$$\text{NaCl(aq)} = \text{NaCl}(a\text{ M amino acid}) \quad (1)$$

Small corrections for the heat of dilution from the final concentration of the measurements (0.05 M) to infinite dilution were made to both measured heats of solution. Literature values for the heats of dilution in water[4] were used to estimate these corrections. The $\Delta H_1(a)$ values were then fit by linear least squares to

$$\Delta H_1(a)/a = \Delta H_3° + ba \quad (2)$$

The details of these calculations as applied to glycine are reported in ref 1. The resulting enthalpy of interaction, $\Delta H_3°$, corresponds to the enthalpy of the reaction

$$\text{NaCl(aq)} = \text{NaCl(ideal, 1 M amino acid)} \quad (3)$$

Because of the limited solubility of α-alanine and valine, method 1 was used for these amino acids.

The experimental procedure and calculations of method 2 closely follow those of method 1. The enthalpy of solution of a concentrated amino acid solution into aqueous NaCl solutions is measured. The corrections for the heats of dilution in this method were very small (±2 cal/mol), but an additional correction had to be applied to account for the effect of the NaCl on the intermolecular proton transfer reaction. Details of this procedure and calculations are also reported in ref 1.

Equations analogous to eq 1–3 may be written as follows:

$$\text{amino acid}^{\pm}\text{(aq)} = \text{amino acid}^{\pm}(a\text{ M NaCl}) \quad (4)$$

$$\Delta H_4(a)/a = \Delta H_6° + ba \quad (5)$$

$$\text{amino acid}^{\pm}\text{(aq)} = \text{amino acid}^{\pm}\text{(ideal 1 M NaCl)} \quad (6)$$

In these equations a refers to the concentration of NaCl in the solvent system.

Both methods should give the same results for the enthalpy of interaction if the amino acid and the electrolyte are the same (the Gibbs–Duhem relationship must be satisfied[5]). The resulting $\Delta H_3°$ and $\Delta H_6°$ are therefore referred to as $\Delta H_s°$, regardless of the method used. Experimental values of $\Delta H_s°$ are reported in Table I. The uncertainties are the standard deviations in the fit to eq 2 or 5.

In addition to the enthalpy data, Robinson and Schrier[2] have determined values of the interaction coefficient, k_s, for reactions 2 or 5. Their values of k_s for glycine, β-alanine, γ-aminobutyric acid, and ε-caproic acid are given in Table II along with the values of the free energy and entropy of interaction calculated from

$$\Delta G_s° = -2.303RTk_s \quad (7)$$

$$\Delta G_s° = \Delta H_s° - T\Delta S_s° \quad (8)$$

TABLE I: Enthalpy of Interaction between Amino Acids and NaCl

Amino acid	Concn range, M	Method	No. of runs	ΔH_s°, cal/mol
Glycine	0–1.0	1	11	−212 ± 7
Glycine	0–1.0	2	11	−210 ± 3
α-Alanine	0–1.0	1	10	+3 ± 28
Valine	0–0.5	1	4	+112 ± 10
Serine	0–1.0	2	12	−120 ± 22
β-Alanine	0–1.0	2	10	−78 ± 5
γ-Amino-butyric acid	0–1.0	2	10	−16 ± 6
ε-Amino-caproic acid	0–1.0	2	10	+161 ± 10

TABLE II: Thermodynamics of Interaction between Amino Acids and NaCl

Amino acid	k	ΔG_s°, cal/mol	ΔH_s°, cal/mol	ΔS_s°, eu
Glycine	0.127	−173	−211	−0.13
β-Alanine	0.170	−232	−78	0.52
γ-Amino-butyric acid	0.213	−291	−16	0.92
ε-Amino-caproic acid	0.213	−291	+161	1.51

Discussion

Because of the large dipole moment of dipolar ions, the dominant term in the descriptions of the interaction between amino acid and electrolytes was assumed to be the electrostatic term.[1,2,6] The Kirkwood equation (eq 9)

$$k_s = \frac{2\pi^2 z^2 e^2}{2303DkTa}\left(\frac{3\mu^2}{2DkT} - \alpha(\rho)\bar{V}\right) \quad (9)$$

has successfully predicted the variation of k_s with the dielectric constant of the solvent; correlated k_s values with reasonable estimates of μ and a; and with an additional term to account for the salting out of the nonpolar parts of the dipolar ion, quantitatively accounted for the k_s of glycine, β-alanine, γ-aminobutyric acid, and ε-aminocaproic acid.[2]

The corresponding thermodynamics of interaction can be arrived at from eq 9 and result in

$$\Delta G_s^\circ = 2.303RTk_s = 7.47\frac{\mu^2}{a} + 6.36\alpha(\rho)\bar{V} \quad (10)$$

$$\Delta H_s^\circ = RT^2\frac{dk_s}{dT} = \left[-14.94\frac{\mu^2}{a} + 6.36\frac{\alpha(\rho)v}{a}\right]\left(1 + T\frac{\alpha \ln D}{dT}\right) \quad (11)$$

The ΔH_s° values calculated from eq 11 are not even in qualitative agreement with the experimental values (see Table III). If an additional term is added to account for the salting out effect of the nonpolar CH_2 groups, the disagreement becomes worse. We estimate this term to be about +175 cal/mol per CH_2;[1] whereas the experimental difference is negative and not proportional to the number of CH_2 groups.

The origin of this anomaly we believe lies in the unusual properties of liquid water that results from its highly structured nature. Solutes have a highly specific effect on this structure that is reflected in solution thermodynamics, viscosity, etc.[8-10] The magnitude of these effects may be estimated by assuming each of the thermodynamic functions may be written as the sum of three terms: its value in a constant structure water, its additional value from long-range structure making, and its value from short-range structure breaking. (Not included is Frank's very short range structure making region that results from the hydration of the solutes.)

The first two terms constitute Frank's bulk water region and the values are calculated from the Kirkwood equation. The values calculated for the glycine–NaCl system are reported in Table IV. In the first row, the ΔG, ΔH, and ΔS values are calculated from eq 10 and 11 assuming the structure of water does not change. This is done by assuming the dielectric constant of water can be calculated from the Kirkwood–Fröhlich equation in which the structural parameter, g, is assumed constant.[11,12] This results in $d \ln D/dT \sim -1/T$ and a very small enthalpy contribution. The overlapping of regions of ordered water dipoles results in an appreciable entropy increase. The second row of values are the additional contributions due to electrostatic structure making in the outer region and are calculated using the experimental value of $d \ln D/dT$ for water.[13] Whereas the free energy is unchanged, the positive enthalpy and entropy changes result from the overlap of the structured regions of water around the ions and dipolar ions.

The third row values of Table IV (and the last column of Table III) are the additional contributions necessary in order to obtain the experimental values. These values reflect the highly specific structural changes in the water close to the ion and dipolar ions. The dominant term for these charged solutes is the overlap of structure breaking regions of water in the high fields close to the solutes. Hydrophobic structure making (and primary hydration structure making) would show up in this term as a reduction of the amount of structure breaking. The addition of hydrophobic groups, that do not change the dipole moment, as in α-alanine and valine, greatly reduces this term.

Our conclusions are as follows:

(1) The free energy of interaction is determined predominantly by and yields information about the electrostatic interactions of the solute species.

(2) Linear compensation[14,15] between the enthalpy and entropy changes that occur as the result of the solutes effect on the structure of water leads to an almost unchanged free energy term.

TABLE III: Enthalpies of Interaction

Amino acid	μ, D	a, A	V, cm³/mol	$a(\rho)$	ΔH_s°, cal/mol	ΔH_s°, cal/mol	
						Eq	Diff
Glycine	13.5	4.2	57	1.30	−211	195	−406
β-Alanine	16.7	4.45	73.3	1.32	−78	290	−368
γ-Amino-butyric acid	19.9	4.68	92.3	1.34	−16	400	−416
ε-Amino-caproic acid	24.1	5.01	122.2	1.36	161	551	−394
α-Alanine	13.7	4.45	73.3	1.32	3	186	−183
Valine	14.2	4.85	105.9	1.34	112	134	−22
Serine	14	4.45	73.7	1.32	−120	186	−306

TABLE IV: Contributions to the Thermodynamics of Interaction of Glycine and NaCl

	ΔG, cal/mol	ΔH, cal/mol	ΔS, cal/mol K
Constant structure water	−213	+5	0.72
Long-range structure making	0	+190	0.65
Shorter-range structure breaking	+40	−406	−1.50

(3) The enthalpy of interaction is determined predominantly by yields information about the structure making–breaking of the solutes. An exothermic enthalpy of interaction indicates the amino acid is a net structure breaker while an endothermic value indicates a net structure maker.

(4) The difference between the experimental enthalpies of interaction and those calculated by eq 11 indicates the effect of the amino acid on the structure of water close to the amino acid.

Though differing in detail, the above interpretation is consistent with the conclusions reached by other workers examining the enthalpy of interaction data and heats of dilution.[16-18]

Acknowledgment. We thank the Union Carbide Corp. for scholarship support (A.F.J.) and the Marshall University Foundation for financial support.

References and Notes

(1) J. W. Larson and D. G. Morrison, *J. Phys. Chem.*, **80**, 1449 (1976).
(2) E. E. Schrier and R. A. Robinson, *J. Biol. Chem.*, **246**, 287 (1971).
(3) R. N. Goldberg and L. G. Hepler, *J. Phys. Chem.*, **72**, 4654 (1968).
(4) V. B. Parker, *Natl. Stand. Ref. Data Ser., Natl. Bur. Stand.*, **No. 2**, (1965).
(5) J. H. Stern, J. Lazartic, and D. Fost, *J. Phys. Chem.*, **72**, 3053 (1968).
(6) J. T. Edsall and J. Wyman, "Biophysical Chemistry", Vol. 1, Academic Press, New York, N.Y., 1958.
(7) E. J. Cohn and J. T. Edsall, Ed., "Proteins, Amino Acids and Peptides", Reinhold, New York, N.Y., 1943.
(8) H. S. Frank and M. W. Evans, *J. Chem. Phys.*, **13**, 507 (1945).
(9) J. L. Kavanau, "Water and Solute-Water Interactions", Holden-Day, San Francisco, Calif., 1964
(10) R. A. Horne, Ed., "Water and Aqueous Solutions", Wiley-Interscience, New York, N.Y., 1971.
(11) J. B. Hasted, "Aqueous Dielectrics", Chapman and Hall, London, 1973.
(12) H. Fröhlich, "Theory of Dielectrics", Oxford University Press, London, 1949.
(13) H. S. Harned and B. B. Owens, "The Physical Chemistry of Electrolyte Solutions", Reinhold, New York, N.Y., 1958.
(14) R. Lumbry and S. Rajender. *Biopolymers*, **9**, 1125 (1970).
(15) L. G. Hepler, *J. Am. Chem. Soc.*, **85**, 3089 (1963).
(16) G. C. Kresheck and L. Benjamin, *J. Phys. Chem.*, **68**, 2476 (1964).
(17) R. H. Wood, H. L. Anderson, J. D. Beck, J. R. France, W. E. deVry, and L. J. Soltzberg, *J. Phys. Chem.*, **71**, 2149 (1967).
(18) S. Lindenbaum, *J. Phys. Chem.*, **75**, 3733 (1971).
(19) J. H. Stern and J. T. Swearingen, *J. Phys. Chem.*, **74**, 167 (1970).
(20) J. H. Stern and J. D. Kulluk, *J. Phys. Chem.*, **73**, 2795 (1969).

Disregistry Transition in the Krypton Monolayer on Graphite

George D. Halsey

Department of Chemistry, University of Washington, Seattle, Washington 98195 *(Received June 16, 1977)*

Publication costs assisted by the University of Washington

An earlier two-structure model for transition between two Langmuir isotherms with different adsorption maxima is applied to the transition of an adsorbed layer from a substrate-registered lattice structure into a more dense self-determined lattice. This treatment locates the transition but neglects the transition region structure. The latter is described in terms of the interaction of clustered, lattice-dislocated atoms viewed as a large mobile molecule. The Hill–van der Waals isotherm is used to calculate an adequate shape for the transition region. The Gibbs–Eriksson theory of surface tension is used to predict the behavior of the spreading pressure and surface tension during the transition.

Thomy, Regnier, and Duval[1] have presented detailed isotherms for krypton adsorbed on graphite. Similar isotherms have been found by Putnam and Fort.[2] Each of these isotherm show a series of steps which can be identified with "events" on the surface. In particular the A_1''–B_1 or last such "substep" in the monolayer region has been identified with a transition from a triangular lattice of krypton in registry with the graphite surface, to a similar structure out of registry with the substrate. This interpretation has been confirmed by LEED measurements which produce similar steps when the lattice parameter is plotted against pressure.[3] It should be noted that these steps are not vertical, but appear rounded in shape, especially at the upper edge. They amount to about 0.1 monolayer in height, although, because of the general upward slope of the isotherm,[1] it is difficult to estimate the exact extent of the transition itself, as distinguished from vacancy filling and second layer formation.

I. Langmuir–Langmuir Transition

Two-Structure Models. In several earlier papers,[4,5] the author has presented a treatment of the transition between two distinct surface structures, such as the Langmuir and Volmer models of lattice and random structure, respectively. Similar but more complex models have been examined by Price and Venables.[6] Since these theories do not include intermediate structures, they are strongly predisposed to predict stepwise or first-order transitions.

If the adsorption maxima differ for the two structures, they may be otherwise the same and a transition will still be possible. Such a model was proposed[7] to describe the transition between substrate fit to closest packing, or the in registry–out of registry transition, that was suggested by the observations of Lander[8] and the discussion that followed. The model of Price and Venables gives a first-order disregistry transition for essentially the same reason.

High-Coverage Approximation. Since the initial and final states of the transition are at high coverage and of the same triangular structure, they can both be approximated by the Langmuir model. The lower regions of each isotherm will be represented by slightly different Langmuir equations, rather than ones involving lateral interaction. The situation is shown in Figure 1. At the transition,

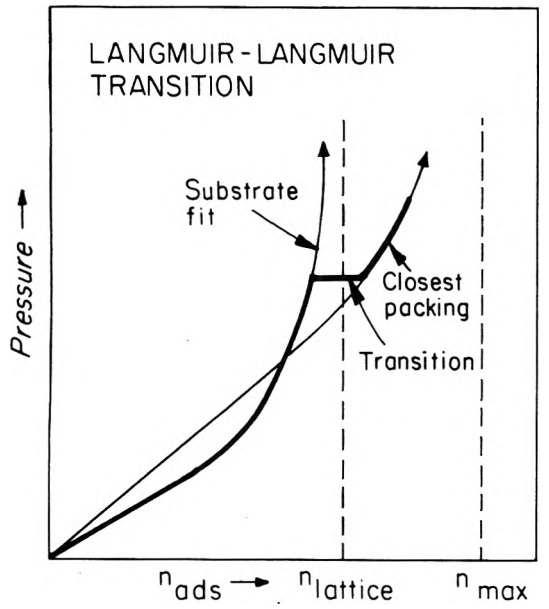

Figure 1. Simple model for the two-structure transition between two Langmuir isotherms with different binding constants and different adsorption maxima.[7]

spreading pressure, chemical potential, and temperature for the two structures must be equal.

These equations are

$$\theta/(1-\theta) = kp$$
$$\theta'/(1-\theta') = k'p \qquad (1)$$

where the prime denotes the denser structure: $k > k'$. The chemical potential, equivalent to the pressure p, is the same in both equations. The spreading pressure π_f is also equated at the transition and is given by the equations[4]

$$-(1/a_0)\ln(1-\theta) = \pi_f/kT$$
$$-(1/a_0')\ln(1-\theta') = \pi_f/kT \qquad (2)$$

where a_0 and a_0' are the areas per site: $a_0 > a_0'$. If we eliminate p, π_f, and θ' with θ and θ' near unity, we find that the transition occurs at θ given by

$$-\ln(1-\theta) = [\ln(k/k')]/[1-(a_0'/a_0)]$$
$$\approx \ln(p_t/p_{1/2}) \qquad (3)$$

where $p_{1/2}$ is the pressure at coverage $\theta = 1/2$, or $1/k$.

Experimental Values. For the isotherm at 77.3 K, the transition pressure p_t is 0.033 Torr, and $p_{1/2}$ is 0.0005 Torr.[1] With a value of a_0'/a_0 of 0.9, the calculated value of k/k' is 1.5. This corresponds to an energy difference between sites ($RT \ln (k/k')$) of 32° or 64 cal/mol. A similar calculation using the data at 96.3 K where the transition pressure is about 5 Torr and $P_{1/2}$ is about 0.06 Torr yields an energy of 42°. Other data in the higher temperature region are similar. The extensive calculations of Steele indicate a maximum difference of about 30° in krypton sites on graphite, and an average difference over the surface of the order of 20°. Since these considerations leave out the Kr–Kr interactions, which presumably operate in the opposite sense of favoring disregistration, our result seems somewhat larger than the calculation of Steele would indicate.

Nevertheless, we can conclude that the Langmuir–Langmuir model, with the aid of suitable energy values obtained by lattice summations over the structures revealed by LEED and other measurements, would serve to approximate the location of the transition, but cannot account for its observed shape.

It has been relatively difficult to devise a model that will produce the observed continuous behavior of the transition; indeed there is the possibility that on a perfect graphite lattice that the transition *may* become discontinuous. In what follows we propose a model that is not structurally different from that proposed by Chinn and Fain,[3] but that is thermodynamic in content rather than mechanical.

II. Cluster Interaction Model

Adsorption into a Nearly Complete Registered Layer. Just prior to the delocalization, the nearly completed layer has a coverage given by the equation $(1-\theta)^{-1} = kp$, a large number of the order 10^2, which yields a coverage of near unity. If the coverage is to increase further to 1.1 in terms of this monolayer measure, the initial interstitial atoms cannot disturb all the registered layer, but only a number of atoms in the vicinity of each interstitial addition. This number of atoms in the disturbed region or cluster would be determined by geometrical factors, but might be expected to be of the order of 10 if the unregistered close-packed structure is 10% denser than the registered structure. If these clusters are widely spaced from each other, they will behave independently, and the coverage will be given by the equation

$$\theta = 1 - (kp)^{-1} + k''p \qquad (4)$$

where the term in reciprocal pressure represents the filling-up of isolated registered vacancies, and the final term the isolated intrusion of extra atoms of krypton, with no evidence of a steplike transition. Soon, however, these clusters must interact, and the nature of this interaction determines the shape of the transition region.

Since the clusters are much larger than the lattice spacing, they may be thought of as large mobile ad-atoms that move nearly continuously over the surface. As the measure of coverage θ goes from 1 to 1.1 the cluster coverage Θ goes from zero to one.

Hill–van der Waals Treatment of Θ. The interaction of the clusters is a sort of virtual interaction, which might be approximated in a variety of ways. The simplest treatment with a Volmer or Langmuir equation is clearly not adequate. The two-dimensional van der Waals equation has been used by Hill[10] to interpret mobile monolayer adsorption. It can be written in terms of an interaction parameter W.

$$\ln(P/P_{1/2}) = \ln[\Theta/(1-\Theta)] + [\Theta/(1-\Theta)] - 1 + W(1-2\Theta) \qquad (5)$$

At $W = 27/8$, there is a critical point, and for W greater than this value there is a phase separation. The parameter $W = a/bkT$ in terms of the two-dimensional molecular van der Waals parameters a and b. It is not expected that the value of W for the interaction of the virtual molecules that represent the clusters would have any such strong dependence on temperature. The interaction is determined more by packing factors rather than energy differences, and may be thought of as largely entropic.

Comparison with Experiment. There are two sets of data, those of Thomy et al.[1] and those of Chinn and Fain.[3] The former are isotherm data and thus include any second layer formation and any vacancies in the first layer. The data at 77 K were chosen because the whole isotherm is shown and the correction can be estimated. A quantity $\Delta\theta = 0.25(P/P_0)$ was subtracted from the data points to obtain an adjusted set of points. No such correction is appropriate for the LEED data of Fain.

The experimental points are compared with a single calculated curve in Figure 2. The total change in ad-

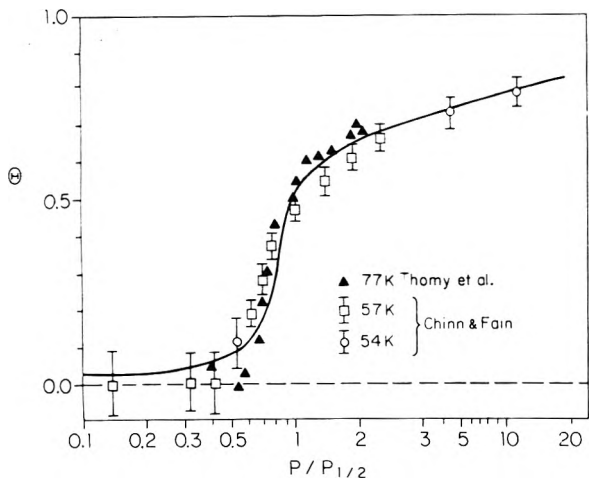

Figure 2. Experimental data from ref 1 and 3 fitted to a Hill–van der Waals isotherm slightly above the critical temperature. The whole range of Θ is only 0.1 of an experimental monolayer of krypton. (Only selected points are shown for the 54 K isotherm. Note that $P_{1/2} \approx P_t$, the transition pressure.)

sorption over the transition, that is the range of between zero and one, was that adopted by Fain and Chinn[11] to compare their data and that of Thomy et al.,[1] with the theory proposed by Chinn and Fain. No further adjustment was made. The parameter W was set at 24/8 = 3, which is very slightly above the critical region. This assignment was suggested by the appearance of the data, and so corresponds to no phase change, but a gradual assumption of close packing of the clusters and thus of the ad-atoms themselves. Fain's data could be better fit with a somewhat smaller value of W, and the data of Thomy et al. would require a larger value. Thomy's points are perhaps not accurage enough to warrant more detailed analysis and Fain's data close to the transition depend on details of the interpretation of the LEED patterns.

It is characteristic of mobile isotherms near condensation[4] that pressure on a log scale changes much more slowly above Θ = 1/2 than below. The steepest part of the curve is below 1/2. For the van der Waals case it is near Θ = 1/3, where the critical density is located. As Steele shows[12] more accurate treatments accent this dissymmetry; the steepest region shifts to the region of Θ = 1/4. This characteristic is shared by the transition region investigated in this paper, and thus supports the idea that the model of mobile clusters of disregistered atoms is appropriate. This point of view is not at all inconsistent with the idea of modulated misfit used by Chinn and Fain. In fact, the one-dimensional analogue of the misfit cluster is clearly visible in Figure 3b of their paper.[3] One could investigate how these one-dimensional misfits interacted or whether they are distributed at random along the chain.

It should be pointed out that the mobile isotherm employed for the clusters implies a further transition to an ordered structure itself. Since this first-order change would involve only about 1% of the whole monolayer at a much higher pressure, it is of no experimental significance.

III. Elastic Deformation of the Substrate

Gibbs–Eriksson Theory. Gibbs pointed out that, contrary to the case of a liquid, the surface of a solid can be extended in two fashions; first, by increase in the amount of surface at constant lattice parameter, and second by stretching.[13] The calculation of spreading pressure from the isotherm using a moving boundary to define π_f is an extension of the first type. A change in the lattice constant of the substrate caused by adsorption is associated with a change in surface tension γ_f. Eriksson[14] has shown that these two pressures are related by an expression

$$(\partial \gamma_f / \partial \pi_f)_T = 1 + A(\partial \ln \Gamma_2 / \partial A)_{TP} \quad (6)$$

where Γ_2 is the surface concentration of the absorbed species. We have assumed here that π_f is the appropriate quantity to equate at the boundary between two disjoint surface phases present at once on the surface of a rigid graphite crystal. If, however, measurements of the distortion of the crystal could be made, the quantity γ_f must be calculated.

Substrate–Lattice Change at the Disregistry Translation. The values of the derivatives in eq 6 might be expected to change drastically as the film comes out of registry. In particular, for mobile adsorption it is possible that $\pi_f = \gamma_f$ while for substrate-determined fixed-site Langmuir adsorption $\gamma_f = 0$. For fixed site adsorption of a layer of ad-atoms somewhat stretched beyond the equilibrium distance γ_f can even be negative while π_f will always be positive.

Above the transition to the unregistered solid, the density of the adsorbed layer will be almost independent of area, while just below the transition the density of the almost completely covered lattice-adsorbed atoms will be inversely proportional to A, the (stretched) area. Thus, dilatation should begin abruptly in the transition region.

IV. Discussion

More Refined Isotherms. Equations 1 and 2 can easily be replaced by the Fowler–Guggenheim isotherm[15] that allows for interaction energy of magnitude w between the atoms of the lattice gas. The results are littled changed, except that the quantity $RT \ln (k/k')$ contains an added factor Δw, which reflects any difference in the interaction energy caused by change in the lattice distance during the transition.

The isotherm equation used for the clusters of unregistered atoms, eq 5, is very crude, but the approximate nature of the theory and the uncertainty in the data do not warrant further refinement. What is clear is that the data indicate a cooperative introduction of added atoms of krypton when the disregistry of the adsorbed layer begins, with a point of inflection. The so-called transition in the isotherm equation used here to represent it is continuous, and so is identified solely by this point of inflection. We are thus in agreement with the observations of Putnam and Fort.[16]

Thermodynamic Considerations. The identification of $RT \ln (k/k')$ with the enthalpy difference neglects the entropy difference between the two phases, which may indeed be of lesser importance. If this quantity is largely an energy difference due to average difference in binding energy in and out of registry, the isosteric heat should reflect the change. The thermodynamic aspects of the relations between the enthalpy of adsorption, the isosteric heat, and the quantities adsorbed have been thoroughly discussed by Larher.[17] If the isosteric heat is constant up to the transition, it should fall by ten times the change in average binding energy, because ~0.1 layer additional changes the binding of the entire layer. The isosteric heats of Thomy et al.[1] (which are not constant) do drop by 600 cal/mol over the transition, superficially consistent with a binding energy change of 60 cal/mol. When the isosteric heats vary with coverage, it is necessary to employ the integral heat of adsorption, which can be estimated from the isosteric heats. In the vicinity of 84 K the integral heat of adsorption just before the transition is about 4.05 kcal/mol and 4.04 afterwards. This result would imply in

turn a change in binding energy of only ~10 cal/mol. At higher temperatures the integral heats differ even less, and the difference may even be slightly negative. We may conclude, then, that there is some difficulty in reconciling the isosteric heats presented by Thomy et al.[1] with the simple picture of a disregistry transition.

Acknowledgment. The author is indebted to Professor S. Fain who kindly made his work available prior to publication.

References and Notes

(1) A. Thomy, J. Regnier, and X. Duval in "Thermochemie", Colloques Internationaux du Centre National de la Recherche Scientifique No. 201, CNRS, Paris, 1972, p 511.
(2) F. A. Putnam and T. Fort, Jr., *J. Phys. Chem.*, **79**, 459 (1975).
(3) M. D. Chinn and S. C. Fain, Jr., *Phys. Rev. Lett.*, **39**, 145 (1977).
(4) J. P. Stebbins and G. D. Halsey, Jr., *J. Phys. Chem.*, **68**, 3863 (1964).
(5) F. Tsien and G. D. Halsey, Jr., *J. Phys. Chem.*, **71**, 4012 (1967).
(6) G. L. Price and J. A. Venables, *Surface Sci.*, **59**, 509 (1976).
(7) G. D. Halsey, Jr. in "Fundamentals of Gas-Surface Interactions", H. Saltsburg, J. N. Smith, Jr., and M. Rogers, Ed., Academic Press, New York, N.Y., 1967 p 334.
(8) J. J. Lander in ref 7, p 25.
(9) W. A. Steele, *Surface Sci.*, **36**, 317 (1973).
(10) T. L. Hill, *J. Chem. Phys.*, **14**, 441 (1946).
(11) S. C. Fain, Jr. and M. D. Chinn, *J. Phys.*, in press.
(12) W. A. Steele, "The Interaction of Gases with Solid Surfaces", Pergamon Press, Oxford, 1974, p 175.
(13) J. W. Gibbs, "Collected Works", Vol. I, Longmans Green, New York, N.Y., 1928, p 315.
(14) J. C. Eriksson, *Surface Sci.*, **14**, 221 (1969).
(15) R. H. Fowler and E. A. Guggenheim, "Statistical Mechanics", Cambridge University Press, Cambridge, England, p 429.
(16) F. A. Putnam and T. Fort, Jr. in "Colloid and Interface Science", Vol. III, Academic Press, New York, N.Y., 1976 p 247.
(17) Y. Larher, *J. Chem. Soc., Faraday Trans. 1*, **70**, 320 (1974).

The Surface Area of Pendant Drops

Philip Anthony Arundel*

Imperial Chemical Industries Ltd., Corporate Laboratory, Runcorn, Cheshire WA7 4QE, England

and Robert David Bagnall

Bioengineering and Medical Physics Unit, Liverpool University, Mount Pleasant, Liverpool, England *(Received February 4, 1977)*

Publication costs assisted by Imperial Chemical Industries Ltd.

A simple technique is described for the estimation of pendant drop surface areas from drop photographs. For certain drop lengths, an error of 0.001% is obtained, while for drops in general the surface area may be estimated to within 0.1%. The mathematical techniques used to develop the method are discussed in detail. Extrapolation procedures accurate to 1.25% are described for use with certain drops not covered by the published tables. A relationship between drop surface area and drop volume is also demonstrated for a fixed fluid system and syringe tip diameter. This enables drops of given surface area to be created by control of drop volume alone. Using the methods described in this paper, the pendant drop technique becomes an alternative to the surface balance for studying adsorption from bulk solution.

Introduction

The state of molecules adsorbed from bulk solution at an interface may be deduced from expansion–compression measurements using a surface balance fitted with a suitable rubber membrane to separate pure solvent from solution.[1] The method is convenient but suffers from leakage problems at the moving surface boundary and the membrane seal. During a study of the adsorption of proteins at liquid–liquid interfaces, we considered that since drops created with an Agla micrometer syringe may be readily expanded and contracted, the pendant drop technique for interfacial tension measurements could represent an ideal alternative to the surface balance, provided only that the surface area of the drop were known.

The pendant drop technique involves the measurement of interfacial tension from a photograph of the drop profile. In this paper we present a simple, accurate method for calculating, from the same photograph, the surface area of the pendant drop. Arising from this, we also demonstrate that in systems of known interfacial tension, drops of known surface area may be created without recourse to any photographic procedure.

Background

The profile of a pendant drop is given by [2,3]

$$1/(\rho/b) + \sin\phi/(x/b) = 2 + \beta(z/b) \quad (1)$$

where x, z, and ϕ are shown in Figure 1, and ρ is the radius of curvature of the profile at the point (x, z). The shape-dependent quantity β is given by

$$\beta = -g\sigma b^2/\gamma \quad (2)$$

where σ is the density difference between the two phases, γ is the interfacial tension, and b is the radius of curvature at the apex of the drop. The unit of length is b, so that x/b and z/b are independent of drop size. Thus b determines drop size and β determines drop shape.

Equation 1 was solved by Bashforth and Adams[3] for selected values of β, by determining the coordinates x/b and z/b for equal increments of s/b, the arc length from the apex of the drop.

Unfortunately, β and b are difficult to estimate, so that the tables cannot be used for determinations of γ. Andreas[4] overcame this difficulty by defining a new variable $S = d_s/d_e$ where d_e is the equatorial diameter and d_s is the diameter at a length d_e from the drop apex (see

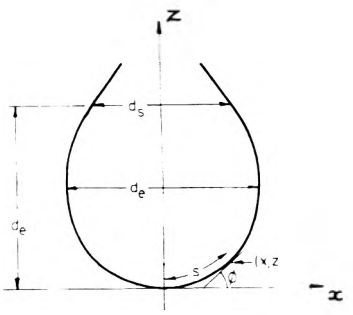

Figure 1. Pendant drop profile, $\beta = -0.25$.

TABLE I: Calculated Shapes of Drops ($\beta = -0.25$)[a]

s/b	ϕ, rad	ϕ, deg	ϕ, min	s	x/b	z/b
0	0		0		0	0
0.1	0.09997	5	43	40	0.09983	0.00500
0.2	0.19975	11	26	41	0.19867	0.01992
0.3	0.29916	17	8	26	0.29554	0.04460
0.4	0.39801	22	48	16	0.38948	0.07875
0.5	0.49614	28	25	35	0.47961	0.12197
0.6	0.59335	33	59	48	0.56510	0.17378
0.7	0.68950	39	30	20	0.64519	0.23360
0.8	0.78442	44	56	39	0.71920	0.30078
0.9	0.87797	50	18	14	0.78657	0.37464
1.0	0.97000	55	34	37	0.84680	0.45442
1.1	1.06038	60	45	20	0.89952	0.53935
1.2	1.14899	65	49	57	0.94443	0.62866
1.3	1.23571	70	48	2	0.98135	0.72156
1.4	1.32041	75	39	14	1.01018	0.81729
1.5	1.40299	80	23	8	1.03091	0.91508
1.6	1.48334	84	59	21	1.04362	1.01425
1.7	1.56134	89	27	28	1.04844	1.11410
1.8	1.63684	93	46	42	1.04559	1.21404
1.9	1.70972	97	57	34	1.03534	1.31349
2.0	1.77979	101	58	29	1.01801	1.41196
2.1	1.84686	105	49	2	0.99398	1.50901
2.2	1.91065	109	28	21	0.96364	1.60428
2.3	1.97084	112	55	16	0.92746	1.69749
2.4	2.02700	116	8	18	0.88592	1.78844
2.5	2.07853	119	5	28	0.83953	1.87702
2.6	2.12467	121	44	4	0.78887	1.96323
2.7	2.16433	124	0	25	0.73455	2.04718
2.8	2.19601	125	49	20	0.67726	2.12913
2.9	2.21758	127	3	29	0.61778	2.20952
3.0	2.22596	127	32	18	0.55709	2.28900
3.1	2.21667	127	0	22	0.49639	2.36847
3.2	2.18323	125	5	24	0.43736	2.44918

[a] Reproduced from ref 2 with the kind permission of the author and the Royal Society.

Figure 1). Since S is also a shape-determining quantity, S and β must be related. Andreas combined β and b by defining instead

$$H = -\beta(d_e/b)^2 \tag{3}$$

so that from eq 2

$$\gamma = \sigma g d_e^2/H \tag{4}$$

The relationship between S and H was then determined experimentally with pendant drops of water.

Fordham[2] pointed out that this empirical relationship was unnecessary, since both S and H for given β values could be calculated from the tables of Bashforth and Adams.[3] Experimentally however, S is normally only measurable for the range $S = 0 \rightarrow 1$, corresponding to β values of $0 \rightarrow (-0.6)$, and Bashforth and Adams[3] list only six values of β within this range. Fordham[2] therefore extended the tables to cover a comprehensive series of β values within these limits, and was able to place the relationship between S, β, and H on a firm theoretical basis with an error of less than 0.01%. This confirmed and

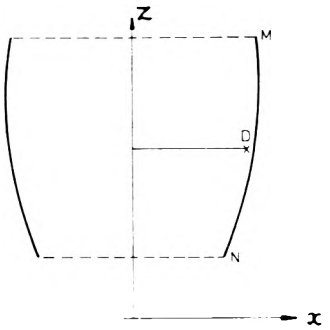

Figure 2. Cross section of a general solid of revolution.

improved upon the experimental data of Andreas. A typical result (for $\beta = -0.25$) is shown in Table I.

Recently, Padday[5-7] solved eq 1 by an alternative procedure, and provided tables for many more values of β within the experimentally determined range of values of S. Unlike the previous data, these tables present x/b and z/b for equal intervals of ϕ rather than s/b, the interval $\Delta\phi$ being 5°. Also tabulated are the drop surface area and drop volume at each interval. The tables of Padday therefore represent one approach to estimation of the surface area of pendant drops.

Use of the tables for any drop photograph involves estimation of β from the measured value of S. Since β is unlikely to correspond exactly to any one table, an interpolation must be made between the two nearest tables. Also, the drop length is unlikely to correspond to any given value of z/b, so that an interpolation must be made between z/b values, and hence between surface area values. A problem is that because the tables are for 5° changes in ϕ, above the drop equator (i.e., z/b at $\phi = 90°$) the change in ϕ for large area changes is so small that only a few data points are listed although Padday also provides a computer program for the generation of extra data. Considerable interpolation is required for normal drops, so that although individual areas in the tables are accurate to ~0.0001%,[8] the accuracy of the interpolated area may be considerably reduced.

In this paper, we present a simple alternative solution to the problem of drop surface area which is of the same order of accuracy and which makes the use of extensive data tables unnecessary. In particular, we show that the tables of Bashforth and Adams,[3] extended by Fordham,[2] which use equal increments of arc length s/b rather than ϕ, are ideally suited to the development of this simple method.

Surface Area of Any Solid of Revolution. Theory

Consider in Figure 2 the curve MN to be rotated about the z axis, creating a solid of revolution. If this curve, of length (arc MN), has its center of gravity at D positioned x_D from the axis, then by Pappus' theorem[9]

$$\text{surface area} = 2\pi x_D (\text{arc MN})$$

or in nondimensional form

$$(\text{surface area}/b^2) = 2\pi x_D/b(\text{arc MN}/b) \tag{5}$$

Although other techniques are available for the surface area determination, eq 5 is particularly suited to the pendant drop problem because the published tables list x/b and s/b as mentioned previously.

Surface Area of Pendant Drops

Method 1. Simple Approach. Consider in Figure 3 the portion of a pendant drop profile of arc length

$$\Delta(s/b) = 0.1$$

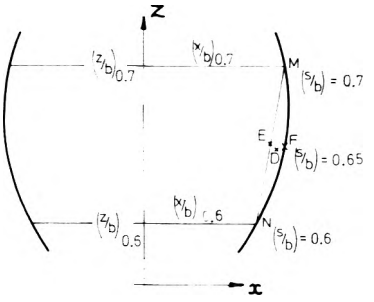

Figure 3. Portion of pendant drop profile, length $\Delta(s/b) = 0.1$.

When this is rotated about the z axis the surface area generated is given by eq 5, in which only (x_D/b) is unknown. Estimation of the position of D is the key problem in this paper. A first approximation for D would be

$$x_D/b \doteqdot x_E/b = {}^1/_2((x/b)_{0.6} + (x/b)_{0.7})$$

Upon substitution into eq 5 this gives

$$\text{surface area}/b^2 \doteqdot 2\pi[{}^1/_2((x/b)_{0.6} + (x/b)_{0.7})0.1]$$

The summation formed for a sequence of arcs from the origin is

$$\text{total surface area}/b^2 = 2\pi[{}^1/_2((x/b)_0 + (x/b)_{3.2} + 2\sum_{\substack{i=0.1 \\ 0.1\ \text{step}}}^{3.1}(x/b)_i)0.1] \quad (6)$$

The accuracy of eq 6 can be checked by applying it to a hemisphere where the surface area is already known.

For a hemisphere of radius b

$$(\text{true surface area}/b^2) = 2\pi$$

by applying eq 6

$$(\text{surface area}/b^2) = (0.9991302)2\pi$$

using an interpolation for the equatorial region $s/b = 1.5 \rightarrow 1.6$. Hence the error = 0.09%. Equation 6 can therefore be used to estimate the surface area of pendant drops from the published tables of drop profiles. Since the hemisphere represents a severe test due to its high curvature, an error of 0.1% is conservative.

However the tables of drop profiles are accurate to 0.001% or better. Such accuracy in surface area determinations would be desirable and as will be shown in method 2 this can be achieved by modifications to eq 6.

Method 2. Advanced Approached. In Figure 3, it can be seen that generally the point D will lie in the region between E and F, where F is the midpoint along the arc (i.e., $(s/b) = 0.65$). Thus a better approximation for D would be

$$x_D/b \doteqdot {}^1/_2((x_F/b) + (x_E/b)) = {}^1/_2[(x/b)_{0.65} + {}^1/_2((x/b)_{0.6} + (x/b)_{0.7})] \quad (7)$$

However data points such as $(x/b)_{0.65}$ are not listed, but by a small rearrangement of the technique this problem can be overcome as follows.

Taking a larger portion of the drop profile, as in Figure 4, we now have F as the midpoint of arc MN such that $(s/b)_F = 0.7$, arc $MN/b = 0.2$, and $(x/b)_{0.7}$ is found from Table I. Thus a better estimate of the position of D is given by

$$x_D/b \doteqdot {}^1/_2[(x/b)_{0.7} + {}^1/_2((x/b)_{0.6} + (x/b)_{0.8})]$$

Unfortunately the summation formed for a sequence of arcs from the origin using this expression produces a result identical with eq 6. In order to successfully improve the

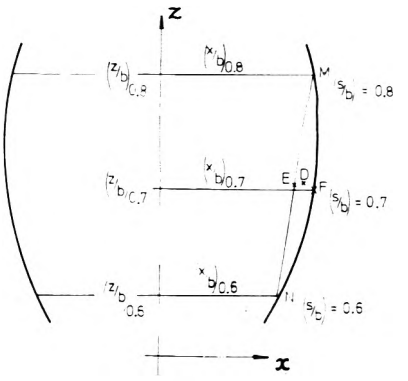

Figure 4. Extended portion of pendant drop profile, length $\Delta(s/b) = 0.2$.

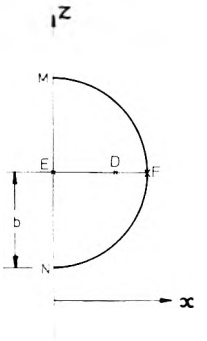

Figure 5. Semicircular arc.

accuracy a further modification is made which leads to the final expression for surface area.

It will be recalled that in eq 7 the following approximation was used

$$x_D/b \doteqdot {}^1/_2((x_F/b) + (x_E/b))$$

When dealing with smooth curved surfaces a better approximation is

$$x_D/b \doteqdot {}^1/_3(2(x_F/b) + (x_E/b)) \quad (8)$$

as will now be shown. Consider a semicircular arc of radius b, center of gravity D, rotated about the z axis as shown in Figure 5.

$$\text{surface area}/b^2 = 4\pi$$

From eq 5

$$4\pi = 2\pi(x_D/b)(\pi b/b)$$

therefore $(x_D/b) = 0.637$. However by eq 8

$${}^1/_3(2(x_F/b) + (x_E/b)) = {}^1/_3(2(1.0) + (0.0)) = 0.667$$

Thus the error in estimation of (x_D/b) using this method is 5%, whereas by using eq 7 it would have been 21%.

For the case of a quadrant the errors can similarly be shown to be 2.3 and 5.2%, respectively. Thus eq 8 is considerably more accurate than eq 7. Applying eq 8 to the solid of revolution shown in Figure 4, we obtain

$$\text{surface area}/b^2 \doteqdot 2\pi/6((x/b)_{0.6} + (x/b)_{0.8} + 4(x/b)_{0.7})0.2$$

The equivalent expression to eq 6 would then become

$$\text{total surface area}/b^2 \doteqdot 2\pi/6((x/b)_0 + (x/b)_{3.2} + 4\sum_{\substack{i=0.1 \\ 0.2\ \text{step}}}^{3.1}(x/b)_i + 2\sum_{\substack{i=0.2 \\ 0.2\ \text{step}}}^{3.0}(x/b)_i)0.2 \quad (9)$$

TABLE II: Values of Area/$2\pi b^2$ and Area/d_e^2 against β and S for Drop Lengths z/d_e = 1.00, 1.05, and 1.10

		z/d_e = 1.00		z/d_e = 1.05		z/d_e = 1.10	
$-\beta$	S	Area/$2\pi b^2$	Area/d_e^2	Area/$2\pi b^2$	Area/d_e^2	Area/$2\pi b^2$	Area/d_e^2
0.250	0.66781	2.1299	3.0433	2.2157	3.1659	2.2927	3.2769
0.275	0.69540	2.1515	3.0402	2.2395	3.1646	2.3196	3.2778
0.300	0.72195	2.1746	3.0377	2.2648	3.1637	2.3479	3.2798
0.325	0.74763	2.1991	3.0356	2.2916	3.1633	2.3779	3.2824
0.350	0.77259	2.2252	3.0338	2.3203	3.1635	2.4097	3.2854
0.375	0.79697	2.2531	3.0324	2.3509	3.1640	2.4436	3.2888
0.400	0.82086	2.2829	3.0312	2.3836	3.1650	2.4799	3.2928
0.425	0.84437	2.3149	3.0303	2.4188	3.1663	2.5187	3.2971
0.450	0.86759	2.3493	3.0296	2.4566	3.1679	2.5606	3.3020
0.475	0.89057	2.3865	3.0289	2.4976	3.1699	2.6060	3.3075
0.500	0.91340	2.4269	3.0282	2.5422	3.1720	2.6555	3.3134
0.525	0.93610	2.4712	3.0272	2.5912	3.1742	2.7098	3.3194
0.550	0.95869	2.5203	3.0255	2.6456	3.1761	2.7703	3.3256
0.575	0.98110	2.5758	3.0225	2.7072	3.1767	2.8390	3.3313
0.600	1.00287	2.6411	3.0158	2.7798	3.1742	2.9200	3.3343

To show the improvement in accuracy obtained using eq 9 the case of the hemisphere is again considered.

true surface area/$b^2 = 2\pi$

By eq 9

surface area/$b^2 = (0.9999891)2\pi$

using an interpolation for the equatorial region as before. Hence the error = 0.0011%. This error is considerably smaller than that obtained by eq 6 and approaches the level of accuracy of the available data. Equation 9 will be used exclusively throughout the following work.

It should be noted that the sphere, because of its high curvature, is a more severe test of the technique than is the pendant drop. An error of 0.001% is therefore conservative.

Application of Method 2

Equation 9 may now be applied to the published tables[2,3] for the experimentally amenable range $-\beta$ = 0.25 → 0.575, for any given drop length z/b. However, the tables are constructed for equal increments of s/b, and the individual values of z/b are unique to each table. For a simple method of surface area estimation applicable to all drops, a termination plane independent of drop shape is introduced.

Considering that any drop length must be at least d_e/b for S to be calculated for interfacial tension purposes, we have chosen to terminate drops at lengths $z/b = d_e/b$, $1.05d_e/b$, and $1.10d_e/b$. Drops of greater length would, strictly, require extension of the available data,[2,3] but as an alternative, this paper also presents a method for approximating the surface area of longer drops with an accuracy within the experimental error of interfacial tension determinations.

Thus eq 9 has been used to create curves of (surface area/$2\pi b^2$) against $-\beta$ for three termination planes as shown in Figure 6 and Table II, individual points being obtained by a linear interpolation. As already mentioned the accuracy of the table should be 0.001% or better. Figure 9 may then be used to obtain the surface area of pendant drops up to any of the three termination planes, provided only that β and b are known.

To estimate β a graph is constructed of S against $-\beta$ from Fordham's data,[2] as shown in Figure 7 and Table II. Since S is readily measured from a drop photograph, β can be read directly from Figure 7.

To estimate b, a graph is constructed of d_e/b against $-\beta$, again from Fordham's data,[2] as shown in Figure 8 and Table III. Since β and d_e are known, b is readily obtained.

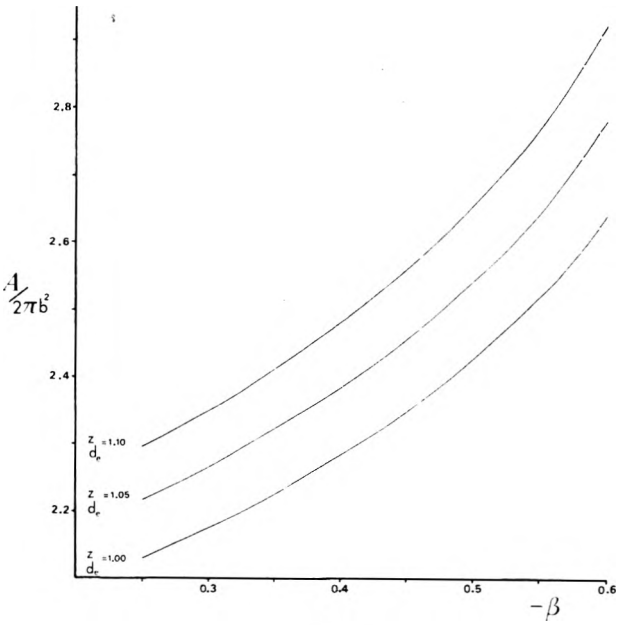

Figure 6. Graph of surface area/$2\pi b^2$ against $-\beta$ for various z/d_e values.

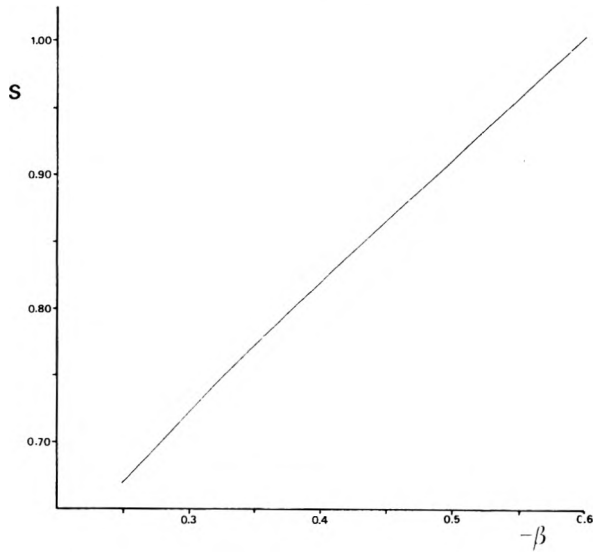

Figure 7. Graph of S against $-\beta$.

Alternatively if γ and σ are known, b may be calculated from eq 2.

Figures 6–8 may usefully be combined into a single graph of (area/d_e^2) against S, as shown in Figure 9 and Table II. This removes the need to estimate β and b, and

TABLE III: Values of x/b and z/b against β at z/d_e = 1.00, 1.05, and 1.10[a]

	z/d_e = 1.00		z/d_e = 1.05		z/d_e = 1.10	
$-\beta$	x'/b	z/b	x'/b	z/b	x'/b	z/b
0.250	0.7002	2.09700	0.6234	2.20185	0.5436	2.30670
0.275	0.7332	2.10866	0.6640	2.21409	0.5925	2.31953
0.300	0.7656	2.12082	0.7034	2.22686	0.6394	2.33290
0.325	0.7975	2.13348	0.7413	2.24015	0.6849	2.34683
0.350	0.8293	2.14674	0.7797	2.25408	0.7294	2.36141
0.375	0.8610	2.16066	0.8172	2.26869	0.7732	2.37673
0.400	0.8928	2.17532	0.8546	2.28409	0.8168	2.39285
0.425	0.9249	2.19084	0.8923	2.30038	0.8603	2.40992
0.450	0.9575	2.20734	0.9303	2.31771	0.9042	2.42807
0.475	0.9908	2.22498	0.9689	2.33623	0.9486	2.44748
0.500	1.0248	2.24402	1.0085	2.35622	0.9940	2.46842
0.525	1.0600	2.26478	1.0491	2.37802	1.0407	2.49126
0.550	1.0966	2.28780	1.0916	2.40219	1.0986	2.51658
0.575	1.1351	2.31400	1.1363	2.42970	1.1410	2.54540
0.600	1.1762	2.34574	1.1840	2.46303	1.1958	2.58031

[a] Note $x/b = x'/b$, see Figure 10.

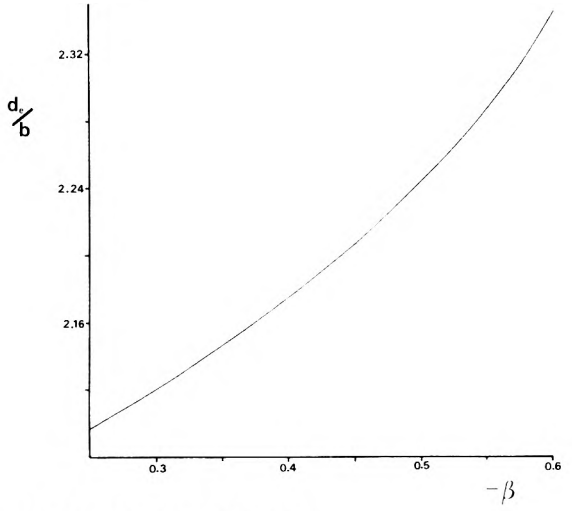

Figure 8. Graph of d_e/b against $-\beta$.

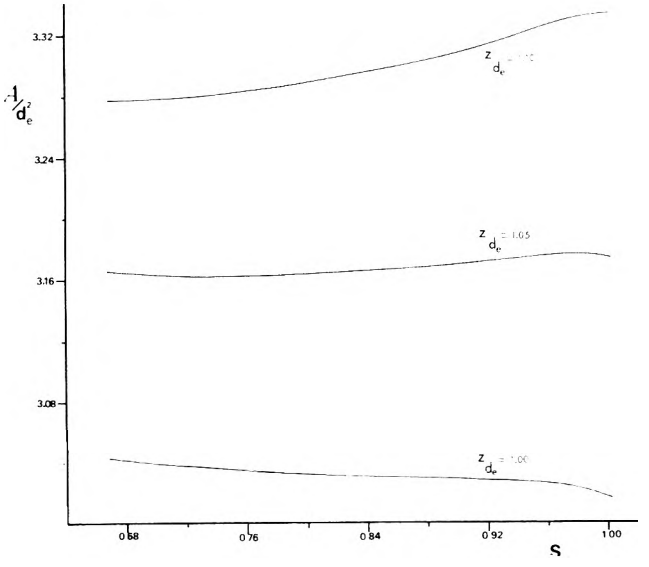

Figure 9. Graph of surface area/d_e^2 against S for various values of z/d_e.

gives the surface area up to any of the three termination planes by two simple measurements (d_s and d_e) on the drop photograph.

A problem now arises concerning the surface area of a drop above $z/b = d_e/b$ when the true termination plane of the drop does not lie at $1.05d_e/b$ or $1.10d_e/b$. In the absence of extended data tables of the Fordham type,[2] we

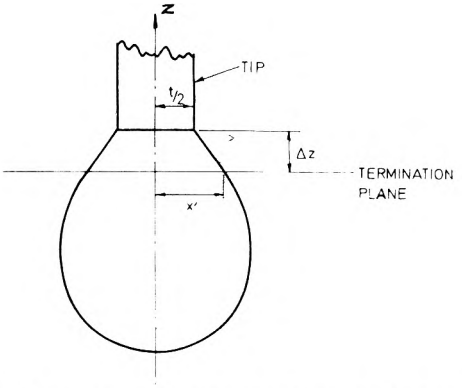

Figure 10. Cross section of drop showing termination plane and the tip.

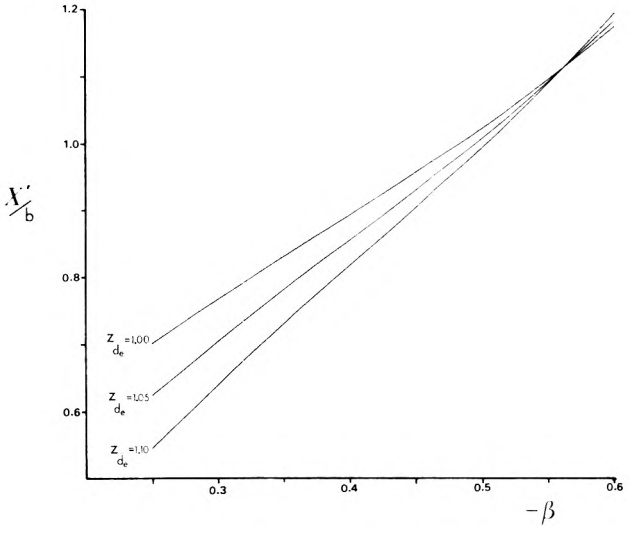

Figure 11. Graph of x'/b against $-\beta$ for various z/d_e values.

propose a simple approximation which is at least as accurate as the determination of interfacial tension from the same photograph, for values of z/b up to $1.6d_e/b$.

First, the area is calculated as described previously up to the nearest termination plane below the tip upon which the drop has formed. The remainder of the drop is then approximated to a truncated right circular cone as shown in Figure 10, the surface area of which is given by

$$\text{area} = \pi(x' + t/2)(\Delta z^2 + [x' - t/2]^2)^{1/2} \qquad (10)$$

where t is the tip diameter, x' is the x coordinate at the nearest termination plane, and Δz is the distance from the

termination plane to the tip.

To facilitate this calculation, Table III gives interpolated values of x'/b against $-\beta$ for the three termination planes, and the relationship is shown graphically in Figure 11. Alternatively, x' can be measured directly from the photograph of the drop.

Example. Consider a drop with the following parameters: $d_e = 3.141$ mm, $d_s = 2.327$ mm, $t = 2.092$ mm, drop length $z = 3.361$ mm $= 1.07d_e$, then

area = (area up to $z/d_e = 1.05$) + (area of remainder)

(i) Area up to $z/d_e = 1.05$:

$S = d_s/d_e = 0.741$

from Figure 7, $\beta = -0.319$; from Figure 8, $b = 1.475$ mm; from Figure 6, area/b^2 (to $z/d_e = 1.05$) = (2.284) 2π so that the area is 31.22 mm^2. Alternatively, from Figure 9, area/d_e^2 (to $z/d_e = 1.05$) = 3.1635 so that the area is 31.21 mm^2.

(ii) Area of the remainder: from Figure 11, x'/b (at 1.05 d_e) = 0.732 from which, $x' = 1.080$ mm. $\Delta z = (1.07 - 1.05)d_e = 0.0628$ mm. Hence from eq 10, the area = $\pi(2.126)(0.0714) = 0.48$ mm^2.

(iii) Total area: Using Figures 6–8, the total area is 31.70 mm^2; using Figure 9, the total area is 31.69 mm^2.

Estimation of Errors

To estimate the errors involved in the truncated cone approximation, consider the following case: $d_e = 2.097$ mm, $d_s = 1.400$ mm, $t = 0.874$ mm, drop length $z = 2.449$ mm, $b = 1.000$ mm (assumed). These are taken from Forham's table[2] for $\beta = -0.25$ (Table I), the drop length being $1.168d_e$. From eq 9, the drop surface area can then be calculated up to $z/b = 1.168d_e/b$ without approximation.

area = $(2.380)2\pi$ mm^2

Using the approximation method, we have (i) area (up to $z/d_e = 1.10$) = $(2.290)2\pi$ mm^2; (ii) area of remainder = $(0.087)2\pi$ mm^2; (iii) total approximated area = $(2.377)2\pi$ mm^2.

The difference between the two methods is 0.15%, indicative of the error in the approximation. For $-\beta$ in the range $0.25 \rightarrow 0.575$ this error is reduced, so that 0.15% is a conservative estimate for the error in approximating up to $z/d_e = 1.17$.

The Problem of Long Drops. For even greater values of z_{max}/d_e, it would be necessary to extend the published tables for given values of β.[2,3] However, it can be shown that the existing data allow an estimation of the surface area of pendant drops up to $z/d_e = 1.6$, with an accuracy approaching that of the determination of interfacial tension.

To demonstrate this, consider the case of $\beta = -0.25$ given in Table I. The largest value of z/d_e is 1.168, and the surface area for this length was given previously as area/b^2 = $(2.380)2\pi$ with minimal error. Alternatively, the area may be estimated by calculating the surface area up to $z/d_e = 0.800$ by eq 9, and considering the remainder as a truncated cone. This is similar to extrapolation of a drop from $z/d_e = 1.10$ to $z/d_e = 1.60$. Thus from Table I (i) area to $z/d_e = 0.800$ ($z/b = 1.679$): from eq 9, area/b^2 (to $z/b = 1.604$) = $(1.645)2\pi$; area/b^2 (from $z/b = 1.604$ to $z/b = 1.679$) = $(0.076)2\pi$ from which, area/b^2 (to $z/d_e = 0.300$) = $(1.721)2\pi$. (ii) Area of remainder to $z/d_e = 1.168$ ($z/b = 2.449$): at $z/b = 1.679$, $x/b = 0.935$, $\Delta z/b = 0.770$, $t/2b = 0.437$ (i.e., x/b at [$z/b = 2.449$]); from eq 10, area/b^2 = $\pi(1.372)(0.917) = (0.629)2\pi$. (iii) Total approximated area/b^2 = $(2.350)2\pi$.

The error involved in the approximation is thus ~ 1.25%, which compares favorably with the experimental error for the determination of interfacial tension from the same photograph. Thus in using the pendant drop technique as an alternative to the surface balance, it would seem acceptable to approximate drop surface areas by this procedure for drop lengths up to $z/d_e = 1.6$, provided only that the drop has not formed a neck (which would invalidate the truncated cone approximation).

Examination of the available tables[2,3] shows that drops in the experimentally amenable range reach a neck at $z/d_e \leq 1.6$, the value of $z/d_e = 1.6$ being reached only for $-\beta$ values less than 0.25. For $-\beta$ in the range $0.25 \rightarrow 0.575$ the error in determining surface area up to the drop neck will be less than 1.25%. Additionally, $\beta = -0.25$ represents the severest test of the truncated cone approximation for this range, so that an error of 1.25% would in any event be conservative.

The Problem of Short Drops ($z_{max}/d_e < 1.00$). The method of estimating surface area (and interfacial tension) given in this paper requires knowledge of S by measurement of d_s and d_e from a drop photograph; S is then used either directly (Figure 9) or indirectly through β (Figures 6–8). A problem arises when $z_{max}/d_e < 1.00$ because d_s cannot be found. However, S is not an absolute quantity but merely an experimentally convenient parameter. For short drops, other shape-dependent parameters S' can be defined provided only that d_e is known. Thus, for example, S' could be d_s'/d_e where d_s' is measured at, for example, $z/d_e = 0.7$. New graphs involving S' could be constructed from the available data,[2,3] so that the surface area and interfacial tension of short drops could be obtained.

Correlation of Drop Volume with Drop Surface Area

An interesting relationship between drop volume and drop surface area now arises. Consider the following: (i) It will be recalled that in eq 4

$$\gamma = \sigma g d_e^2/H$$

so that from the definition of S

$$S^2H = d_s^2\sigma g/\gamma$$

Parameters S and H are shape-dependent quantities related to β, so that the term S^2H must also be related to β. The relationship is readily calculated from Fordham's data[2] as shown in Table IV and Figure 12.

Consider then the case where the tip is at $z/d_e = 1.00$, so that $d_s = t$, then

$$S^2H = t^2\sigma g/\gamma$$

If t, σ, and γ are known for any system, S^2H and hence β may also be calculated for this unique drop. From eq 2 the value of b for the drop is then obtained. (ii) From the available data, values of volume/b^3 against β may be calculated for drops of length $z/d_e = 1.00$ by the method of Bashforth and Adams,[3] as shown in Figure 13 and Table IV. From β and b, the volume of the unique drop may now be calculated. (iii) From Figure 6, the surface area of the drop may now be obtained.

An important conclusion is reached. If, for a system of known γ, σ, and t, a drop is created of volume determined from Figure 13 (by using a volumetric, e.g., agla, syringe) the resulting drop has known surface area from Figure 6, without recourse to any photographic technique. This may be of use in for example hanging mercury electrodes. Similar curves may be created for the cases where $z/d_e = 1.05$ and 1.10, if required.

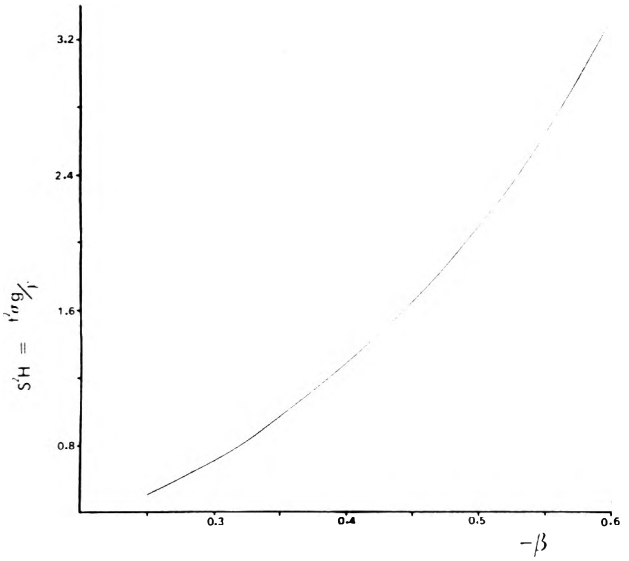

Figure 12. Graph of $S^2H = (t^2\sigma g/\gamma)$ against $-\beta$.

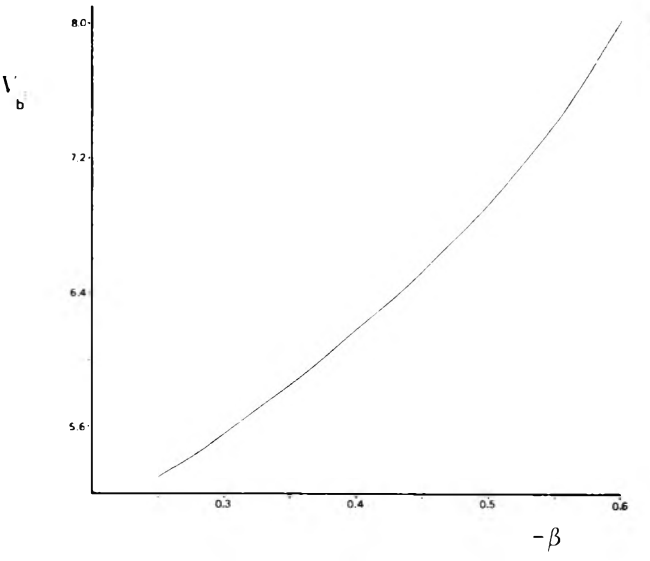

Figure 13. Graph of drop volume/b^3 against $-\beta$ for $z/d_e = 1.00$.

TABLE IV: Values of S, $1/H$, S^2H, and V/b^3 against β[a]

$-\beta$	S	$1/H$	$S^2H = (t^2\sigma g/\gamma)$	V/b^3 at $z/d_e = 1.00$
0.250	0.667 81	0.909 63	0.490 28	5.2914
0.275	0.695 40	0.817 81	0.591 31	5.4213
0.300	0.721 95	0.741 10	0.703 29	5.5572
0.325	0.747 63	0.675 99	0.826 86	5.6990
0.350	0.772 59	0.619 97	0.962 78	5.8479
0.375	0.796 97	0.571 21	1.111 96	6.0042
0.400	0.820 86	0.528 31	1.275 41	6.1690
0.425	0.844 37	0.490 22	1.454 37	6.3426
0.450	0.867 59	0.456 09	1.650 36	6.5259
0.475	0.890 57	0.425 26	1.865 01	6.7222
0.500	0.913 40	0.397 17	2.100 61	6.9336
0.525	0.936 10	0.371 35	2.359 72	7.1624
0.550	0.958 69	0.347 38	2.645 77	7.4129
0.575	0.981 10	0.324 79	2.963 63	7.6907
0.600	1.002 87	0.302 89	3.320 51	8.0113

[a] Taken in part from ref 2 and reproduced with the kind permission of the author and the Royal Society.

Summary

The procedures described in this paper for estimating the surface area of pendant drops may be summarized as follows: (i) The surface area of any drop

(1) From the drop photograph, find d_s, d_e, z/d_e, and Δz (the distance from the termination plane to the tip).
(2) Calculate $S = d_s/d_e$, and hence find from Figure 9 the surface area upto the termination plane nearest the tip (i.e., $z/d_e = 1.0$, 1.05, or 1.10).
(3) Calculate x', the drop radius at the selected termination plane, from Figures 7, 8, and 11, or measure x' directly from the drop photograph.
(4) Use eq 10 to approximate the remaining drop surface area using x', Δz, and t (the tip diameter).
(5) Calculate total surface area.

(ii) The creation of drops of known surface area

(1) Select a system of known t, surface tension (γ), and fluid density difference (σ). Calculate $t^2\sigma g/\gamma$ and hence find β from Figure 12.
(2) Calculate b (the radius of curvature at the apex) from eq 2.
(3) Find volume to be ejected, using Figure 13.
(4) Find area of ejected drop from Figure 6.

Although there are obvious experimental problems in the careful retraction and expansion of pendant drops over extended periods, it is concluded that using the methods described in this paper the pendant drop technique becomes an alternative to the surface balance for studying adsorption from bulk solutions.

Acknowledgment. The authors thank Messrs Imperial Chemical Industries Ltd. for providing the facilities for this work.

References and Notes

(1) A. W. Adamson, "Physical Chemistry of Surfaces", Interscience, 1967, p 183.
(2) S. Fordham, *Proc. R. Soc. London, Ser. A*, **194**, 1 (1948).
(3) F. Bashforth and J. C. Adams, "An Attempt to Test the Theory of Capillary Action", Cambridge University Press, London, 1883.
(4) J. M. Andreas, E. A. Hauser, and W. B. Tucker, *J. Phys. Chem.*, **42**, 1001 (1938).
(5) J. F. Padday, *Phil. Trans. R. Soc. London, Ser. A*, **269**, 265 (1971).
(6) J. F. Padday, *J. Electroanal. Chem.*, **37**, 313 (1972).
(7) J. F. Padday and A. R. Pitt, *Phil. Trans. R. Soc. London, Ser. A*, **275**, 489 (1973).
(8) J. F. Padday, personal communication.
(9) G. W. Caunt, "Infinitesimal Calculus", Oxford University Press, London, 1959, p 331.

Linear Dichroism Spectroscopy as a Tool for Studying Molecular Orientation in Model Membrane Systems

Bengt Nordén,* Göran Lindblom, and Ivan Jonáš

Department of Inorganic Chemistry 1 and Department of Physical Chemistry 2, University of Lund, S-220 07 Lund, Sweden *(Received May 9, 1977)*

Ordinary linear dichroism (LD) spectroscopy with rectangular optics is not applicable to thin uniaxial samples having the optical axis perpendicular to the plane of the sample. A method has been developed to study such samples at inclined optical incidence and a general relation derived between the LD (corrected for polarized reflection) and the average orientation of the absorbing transition dipole. For molecules of C_{2v}, D_{2h}, or higher symmetry the usual order parameters can be obtained. The method has been tested on anthracene in a polyethylene standard slab of perfectly axial symmetry. The estimated orientation agreed with previous reports on anthracene in stretched polyethylene sheets. A number of chromophoric molecules solubilized in macroscopically aligned lamellar mesophases of the systems sodium octanoate/decanol/water and sodium di-2-ethylhexylsulfosuccinate (Aerosol OT)/water have also been studied. In the first system rodlike molecules (diphenylethyne, anthracene, retinal) are oriented with their long axes parallel to the hydrocarbon chains of the amphiphile, while an extremely long molecule (β-carotene) as well as water-soluble planar cationic dyes are on the average oriented parallel to the lamellar planes. In the Aerosol OT system all molecules studied were oriented parallel to the lamellar planes.

Introduction

With water, amphiphilic molecules frequently form liquid crystalline phases with structures depending on temperature and composition. Most notably, they can form lamellar mesophases built up of molecular bilayers separated by water. The resemblance to biological membranes has led to a great interest in the physical properties of lyotropic liquid crystalline phases.[1] Well-known physical methods such as x-ray diffraction and differential scanning calorimetry have given evidence about the structure and the phase stability of such systems. Molecular motion has also been studied by NMR and ESR.[1-3] However, knowledge about the orientation of partly or completely solubilized molecules in the bilayer membrane is still quite limited, probably due to the lack of specific and unambiguous methods for these kinds of studies.

The technique of linear dichroism (LD), nowadays sensitively measured using the phase modulation technique,[4] has been successfully employed in a number of cases where the sample molecules can be given a certain degree of orientation.[5] Since various membranes may themselves be easily aligned (e.g., by "spreading"[6] on a plane, by flow gradients,[7] or magnetic fields[6]) there appear to be possibilities of applying linear dichroism spectroscopy to elucidate the orientation, e.g., of an embedded protein in the lipid matrix, provided the orientation of some chromophore within the protein is known. However, a problem arises since the thin membranes do not permit light of sufficient intensity to be propagated through themselves in the direction parallel to the membrane plane. On the other hand, if the light impinges perpendicularly to the membrane plane, that is, along the optical axis, no dichroism results since the distribution of the molecules around this axis is cylindrically symmetric.

The obvious way to obtain an observable LD of such a sample is to tilt the optical axis with respect to the direction of the incident light. In Figure 1a a sample which is uniaxially symmetric (around the z axis) is tilted around a "hinge", the laboratory-fixed X axis. In this way unequal interaction probabilities can arise between light rays with mutually orthogonal polarizations (X and Z) and an absorbing transition dipole oriented in the sample. Inclined incidence has been employed on several occasions before to study thin uniaxial samples: e.g., Bateman and Covington[8] discussed the orientation of the carbon chains of fatty acid multilayers on the basis of polarized reflection studies, and Yannas et al.[9] estimated elements of the rotivity tensor of collagen from measurements of the optical activity under inclined incidence on a dried collagen film. No detailed analysis has been reported on the method of studying polarized transmission of such samples, but previously employed relations between measureable entities and molecular properties have been based on special assumptions about the orientational distributions and the symmetries of the molecules.[6,10]

Basic Theory

Intrinsic Linear Dichroism Due to Molecular Orientation. The perturbation producing ordinary electronic spectra is an interaction of the electric field, E, of the radiation and the electric dipole moment, μ, of the molecule. The decadic extinction coefficient ϵ (M^{-1} cm^{-1}) due to a single transition o $\rightarrow$ m is

$$\epsilon = \frac{4\pi^2\rho(\lambda)_{om}}{2303hcn}|\hat{\mathbf{E}}\cdot\mu_{om}|^2 = k|\hat{\mathbf{E}}\cdot\mu_{om}|^2 \quad (1)$$

where ρ denotes a normalized band shape function and $\hat{\mathbf{E}}$ is a unit vector along E, the other symbols having their usual meaning.[11] The linear dichroism is defined as

$$\mathrm{LD} \equiv A_\parallel - A_\perp = kCd\{\langle|E\cdot\mu_{om}|^2\rangle_\parallel - \langle|\mathbf{E}\cdot\mu_{om}|^2\rangle_\perp\} \quad (2)$$

(where C is the concentration in mol dm^{-3} and d is the optical path length in centimeters) that is the difference in absorption when the light is polarized parallel and perpendicular, respectively, to the laboratory Z axis in Figure 1 (i.e., $\hat{\mathbf{E}}$ is parallel and perpendicular to Z, respectively). The averages are over the distribution function appropriate to the method of orientation. The averages are conveniently handled by employing a spherical tensor formalism[12] and it is then shown (Appendix, eq A1–A6)

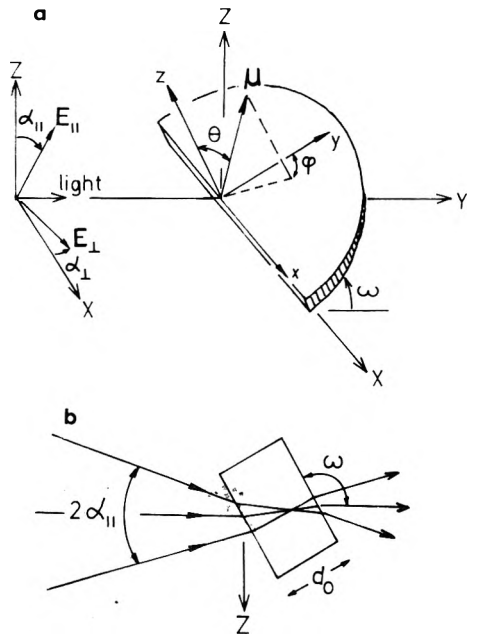

Figure 1. Geometrical parameters of membrane model system and optics: (a) transition dipole μ and its coordinates (ϕ, θ); (b) conical angle of light beam and tilting angle of sample.

that the LD due to the molecular orientation, divided by the absorption of the sample at random orientation, is given by the very simple equation

$$\mathrm{LD}/A_r = 3S\cos^2\omega \tag{3}$$

where ω is the angle between the laboratory Y axis (the direction of light propagation) and the membrane plane, and S is the order parameter[13] representing the average orientation of μ with respect to the director of the uniaxial membrane system (see the Appendix).

If we assume that A_r be determined at normal incidence we have to adjust for the fact that LD refers to a longer pathlength, by the factor $[1 - (\cos\omega/n)^2]^{-1/2}$ (n is the refractive index of the sample). Further, a sample tilt as defined in Figure 1 corresponds to a true angle arcsin $(\sin\omega)/n$ within the sample (Snellius' law). Finally, one may take into account the conicity of the light pencil, implying a tilt ($\alpha_{\parallel}$ or $\alpha_{\perp}$) of the electric vector with respect to the laboratory axes. We assume circular conicity (one angle 2α) and an even intensity distribution. Incorporating these corrections one obtains instead of eq 3:

$$\frac{\mathrm{LD}}{A_r} = 3S\left[\cos^2\omega\Big/n^2\left(1-\frac{\cos^2\omega}{n^2}\right)^{1/2}\right]\left({}^1/_2 + \sin\alpha\frac{\cos\alpha}{2\alpha}\right) \tag{4}$$

Generally an absorbance, A, of the oriented sample with nonpolarized radiation at normal incidence, is more easily obtained than A_r. A relation between A and A_r is, however, easily derived; the absorbance at random orientation is equal to one third of the trace of the absorbance tensor of the sample: $A_r = {}^1/_3(A_{xx} + A_{yy} + A_{zz})$. A_{xx} is the absorption when E is polarized parallel to the x axis, etc. The absorbance of the oriented sample for nonpolarized light is equal to $A = (A_{xx} + A_{yy})/2$. Furthermore, the LD extrapolated to $\omega = 0$ is given according to the definition $\mathrm{LD}^{\omega=0} = A_{zz} - A_{xx}$. The cylindrical symmetry of the sample implies that $A_{xx} = A_{yy}$ and we have

$$A_r = A + \mathrm{LD}^{\omega=0}/3 \tag{5}$$

Since LD/A is approximately linear in $\cos^2\omega$ a preliminary $\mathrm{LD}^{\omega=0}$ is easily obtained (Figure 2e) and the following expression can be used (we have dropped the conicity factor, which is justifiable for small α)

$$\frac{\mathrm{LD}_i}{A + (\mathrm{LD}_i^{\omega=0}/3)} = 3S_i\frac{\cos^2\omega}{n^2(1-(\cos\omega/n)^2)^{1/2}} \tag{6}$$

We stress by the index i that the relation is between the LD from the transition moment μ_i and the average orientation of that direction in the molecule. In the case of overlapping bands with differing polarizations, S_i can be replaced by $(\epsilon_x S_x + \epsilon_y S_y + \epsilon_z S_z)/(\epsilon_x + \epsilon_y + \epsilon_z)$ for a symmetric molecule.[14]

Reflection Dichroism. In the derivation above we have only considered the LD effect from molecular orientation in the membrane. In order to experimentally obtain that LD, however, we shall have to first subtract a generally strong contribution, $\mathrm{LD_R}$, from polarized reflections at the various boundaries. In the present experiments we have thick samples and $\mathrm{LD_R}$ can be extrapolated from the LD level observed in the transparent regions surrounding the absorption band. However, for the sake of completeness when presenting this method, we give the expression which must be used to correct for $\mathrm{LD_R}$ in case of thin ($d < 10^{-5}$ cm) or strongly absorbing (10^4 cm$^{-1} < A$) samples. This point has hitherto been ignored in polarized studies of membranes.

The boundaries are the following: air/supporting plate = 12, supporting plate/membrane = 23. The supporting plate is generally transparent and thick as compared to the wavelength of light. The LD contribution from the two ambient boundaries 12 can be expressed by, e.g., following the outline of ref 15.

$$2\mathrm{LD}_{12} = 2\log[(1 - R_{\perp 12})/(1 - R_{\parallel 12})] \tag{7}$$

where the Fresnel coefficients ($R = rr^*$) are defined as

$$\begin{aligned}R_{\perp ij} &= [(n_i^2\cos^2\phi_i - n_j^2\cos^2\phi_j - k_j^2\cos^2\phi_j)^2 + \\ &\quad 4k_j^2n_i^2\cos^2\phi_i\cos^2\phi_j]/[(n_i\cos\phi_i + \\ &\quad n_j\cos\phi_j)^2 + k_j^2\cos^2\phi_j]^2\\ R_{\parallel ij} &= [(n_j^2\cos^2\phi_i - n_i^2\cos^2\phi_j + k_j^2\cos^2\phi_i)^2 + \\ &\quad 4k_j^2n_i^2\cos^2\phi_i\cos^2\phi_j]/[(n_j\cos\phi_i + \\ &\quad n_i\cos\phi_j)^2 + k_j^2\cos^2\phi_i]^2\end{aligned} \tag{8}$$

$R_{\perp 12}$ and $R_{\parallel 12}$ are obtained by inserting $n_1 = 1$, n_2 = refractive index of the supporting plate at the relevant wavelength, $\phi_1 = \pi/2 - \omega$, $\phi_2 = \arcsin[(\sin\phi_1)/n_2]$ and $k_2 = 0$.

To obtain the contribution from the reflections 23 at the absorbing thin sample we must take into account the effect of interference in the transmitted intensity, and of a complex refractive index $\hat{n}_3 = n_3 + ik_3$. As a reasonable approximation isotropic n_3 and $k_3 = A\ln 10/4\pi\nu d_0$ may be assumed in eq 8 to get $R_{\perp 23}$ and $R_{\parallel 23}$. We insert $\phi_3 = \arcsin[\sin(\pi/2 - \omega)/n_3]$. The effect of interference is governed by the phase coefficient $\cos 2\delta$, where $\delta = 2\pi d n_3\cos\phi_3/\lambda$. By following the derivation methods of any standard textbook on optics[16] one obtains

$$2\mathrm{LD}_{23} = 2\log(1 - R_{\perp 23})/(1 - R_{\parallel 23}) - \log\frac{[1 - R_{\perp 23}\exp(-Ad/d_0)]^2 + 4R_{\perp 23}\exp(-Ad/d_0)\cos\delta}{[1 - R_{\parallel 23}\exp(-Ad/d_0)]^2 + 4R_{\parallel 23}\exp(-Ad/d_0)\cos\delta} \tag{9}$$

For very large absorptions eq 9 has the form of eq 7 and the effect of the interference is negligible. On the other hand, when $A = 0$ and $\delta = (2N + 1)\pi/2$, we have LD_{23} =

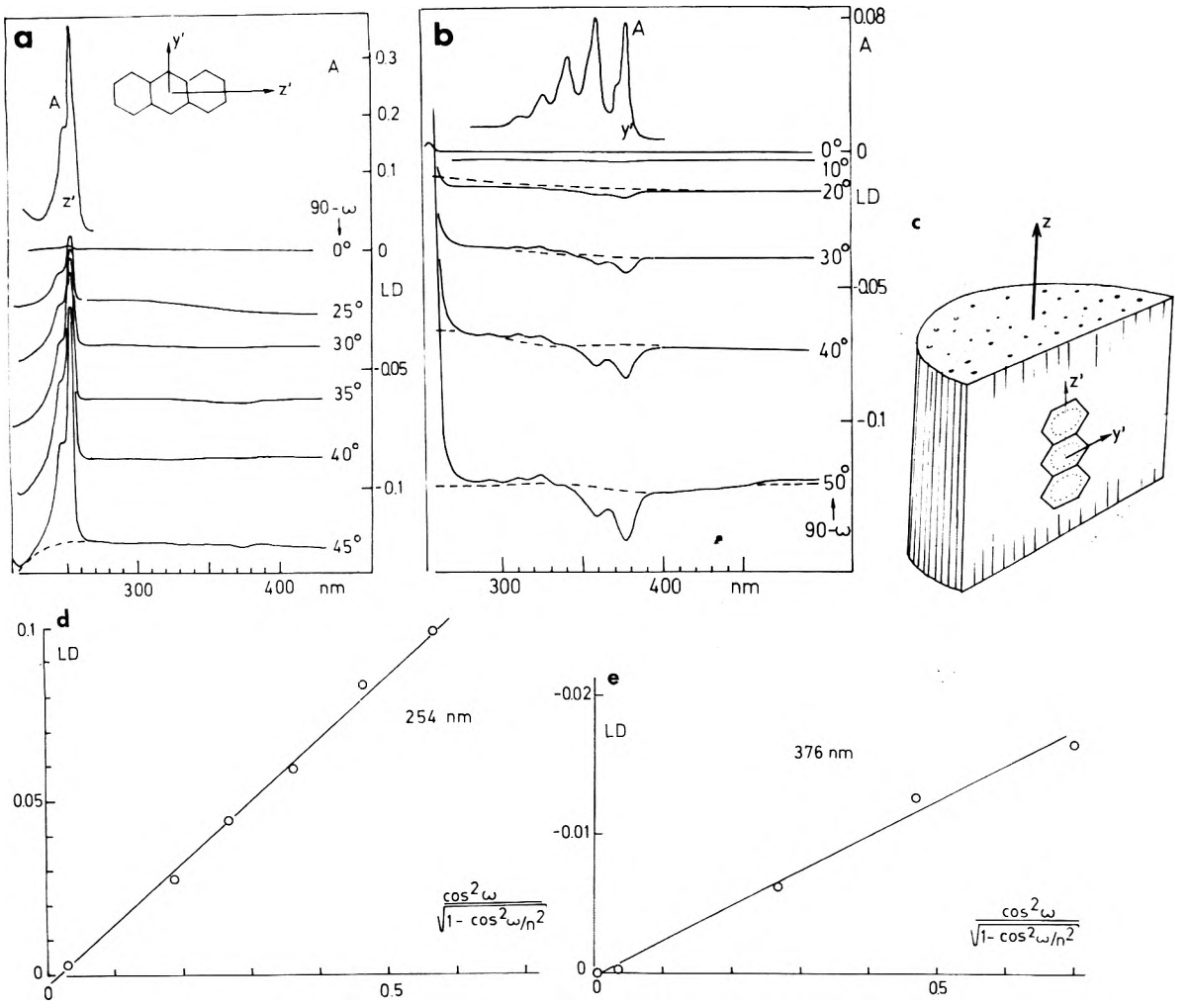

Figure 2. LD and *A* of anthracene in a polyethylene slab (diameter 8 mm, thickness 0.15 mm) in which the hydrocarbon chains are aligned perpendicularly to the plane. The slab was arranged at different incidence angles according to Figure 1: (a) longitudinal band region (concentration 1.4 × 10^{-4} M); (b) transverse band region (concentration 4.6 × 10^{-4} M); (c) sketched preferred orientation of anthracene in the polyethylene slab; (d,e) dependence of LD of the two anthracene bands on the angular factor in eq 8.

0. Thus a varying δ, e.g., due to the wavelength dependence of n_3, can cause large LD_R variations. Since the LD in eq 6 decreases with A, a simultaneously increasing ambiguity in LD_R (due to uncertainty in δ) may prevent the accurate determination of S_i. However, when k_3 is small (k_3 may be neglected in eq 8 when <0.1) we expect only a slow monotonic change in LD_{23} when passing through the absorption band and LD_{23} can then safely be extrapolated from the surrounding transparent region. Effect due to wavelength dependence in δ may otherwise be eliminated by studying a series of samples with suitable d (e.g., $d_\nu = d_0 + \nu\lambda/10$, ν = 1–10).

It should finally be noted that the linear birefringence of the sample, i.e., the fact that $n_z - n_x = n_z - n_y \neq 0$, implies that the rays parallel and perpendicular will have slightly different path lengths. A correction for this effect is provided by eq 10 (a McLaurin expansion of LD/A_r to second order of Δn):

$$\frac{LD}{A_r} = 3S\frac{\cos^2\omega}{n_x^2}\left[1-\frac{\cos^2}{n_x^2}\right]^{-1/2}\left[1-\frac{2\cos^2\omega}{n_x^2}\Delta n\right] - \frac{1-S}{n_x^3}\cos^2\omega\left[1-\frac{\cos^2\omega}{n_x^2}\right]^{-3/2}\Delta n \qquad (10)$$

For LD/A_r of about 0.01 at ω = 45° this corresponds to a correction of about 10%, so this is usually a second-order effect compared to the molecular and reflection dichroisms.

Experimental Section

The polyethylene matrices were manufactured by cutting slices perpendicular to the axis of a polyethylene cylinder which had been previously stretched beyond the yield point. In order to prevent orientational relaxation a water-cooled diamond saw was used with a very long sawing time (12 h). At a thickness below 0.1 mm it was difficult to obtain planar slabs, but a 0.15-mm plate could be made with sufficient optical quality (T = 50% at 400 nm, T = 48% at 360 nm and almost no surface scattering).

A circular dichroism spectrometer (Jasco J-40 A) was converted to LD mode according to earlier methods.[4] The specimen was first mounted at normal incidence (adjustment on the back-scattered light spot) on a goniometer table, rotatable around a vertical axis passing through the focus of the light pencil. A lens (f = 10 cm) was used, condensing the aperture from 10 × 5 to 3 × 1 mm^2. The present specimens could also be run without a lens and it was then shown that the effect of the conicity was negligible here. This was expected from eq 4, since α < 0.2 rd.

The anthracene (blue-fluorescent quality) was diffused into the polyethylene disk by soaking it in a saturated solution in *n*-hexane. To remove crystallites the surface was afterward wiped in the presence of methanol. If this was omitted reflection effects due to high surface concentration frequently emerged. Samples from two lamellar liquid crystalline lipid systems (I and II) were doped with

TABLE I: Dependence of Sample Thickness on Observed LD (Corrected for LD_R), A, and Estimated S_i for Anthracene in System I[a]

	253 nm (z polarized)				377 nm (y polarized)			
d, μm	LD_{45}	A	$(LD/A)_{45}$	$S_{z'}$	10^2LD_{45}	A	$(LD/A)_{45}$	$S_{y'}$
10[b]	0.055	0.29	0.19	0.11	−0.18	0.021	−0.08	−0.05
28[b]	0.12	1.31	0.09	0.05	−0.26	0.058	−0.04	−0.03
50[b]	(0.18)	2.22	0.08	0.05	−0.53	0.105	−0.05	−0.03
120	(0.36)	5.28[b]	0.07	0.04	−0.85	0.250	−0.03	−0.02

[a] 18.2% sodium octanoate, 35.5% decanol, and 46.3% water. [b] Calculated from A at 377 nm.

TABLE II: Dependence of Anthracene Orientation on Lipid Content in System II (d_0 = 40 μm, ω = 0)

% lipid	% H_2O	$(LD/A)_{\omega=0}$	$S_{z'}$
60	40	0.024	−0.008
40	60	0.045	−0.015
30	70	0.075	−0.025
20	80	0.042	−0.014

various chromophoric probe molecules: (system I) the lamellar phase of the system sodium n-octanoate/n-decanol/water;[17] (system II) the lamellar phase of the system sodium di-2-ethylhexylsulfosuccinate/water.[17] The lamellar phases were aligned macroscopically in thin layers between glass plates as described elsewhere.[17] To enable studies in the UV range, quartz plates were used. The best alignment was obtained by heating the sample sandwiched between the plates to 100 °C and then cooling it to room temperature.

Results

Figure 2 shows LD spectra of anthracene in the polyethylene slab at different angles of inclination. After subtracting LD_R, extrapolated from the transparent region, deflections remain at 254 nm (positive) and at 379 nm (negative), bands in anthracene known to have almost pure z' and x' polarizations, respectively. By means of eq 6 the order parameters were calculated: $S_{z'}$ = +0.39 ± 0.1, $S_{y'}$ = −0.30 ± 0.05. In view of the different kinds of sample (a slice from a stretched rod) and measuring technique this is in acceptable agreement with the orientational behavior observed in stretched polyethylene sheets (typically $S_{z'}$ = +0.40, $S_{y'}$ = −0.20, $S_{x'}$ = −0.20[5,18]). The sign change at 340 nm is also in accord with previous observations. The fact that $S_{x'} \approx S_{y'}$ is consistent with the fact that anthracene orients like a rod. In Figure 2 the LD deflections, corrected for LD_R, are plotted vs. the angular factor of eq 6. LD was found to follow the predicted dependence on ω in the range $30° \leq \omega \leq 90°$. That the average alignment of the sample was uniaxial was proven by a zero LD at ω = 90°.

Equations (7 and 8) were found to predict LD_R accurately for well-defined planar boundaries (glass or quartz plates). With the unpolished polyethylene slabs, however, the experimental values at larger angles of incidence, exceeding those predicted (e.g., n = 1.56, ω = 45° should yield LD_R = −0.09, observed −0.12 ± 0.03). For the lamellar liquid crystalline systems one should expect disturbing effects due to LD_{23} contributions from the manifold of thin lamellae (for a layer of 20 Å, δ is typically 0.2 so $\cos\delta \approx 1$ in eq 9). However, LD_R was not found to be significantly changed (±10%) when the sample temperature was raised to 95 °C where most of the anisotropy of the sample had disappeared. This indicates that in practice only the four reflections of eq 7 and 8 need to be considered (e.g., at ω = 70°, $2LD_{12}$ = −0.011 04; n_2 = 1.46; $LD_{23} \approx 0$).

In Figures 3 and 4 some typical LD and A spectra are reproduced from samples of the two lamellar liquid crystalline lipid systems doped with various chromophoric probe molecules. The polarizations of the transitions employed to estimate S_i are shown in the molecular skeletons in Figure 3. The samples were selected to have a high degree of alignment; the orientation depends on the sample thickness, on the composition of the phase, and on the temperature (vide infra). That the samples were uniaxially aligned was supported by the fact that $LD^{90} = 0 \pm 10^{-4}$. The probes studied were unpolar molecules, which are solubilized in the hydrophobic regions of the lamellar liquid crystal, but also ions which are preferentially located in the water layers. Depending on the size and shape of the chromophore molecule and on the type of amphiphile molecule, the chromophores were found to orient themselves with their longest dimension either *parallel* or *perpendicular* to the optical axis (= the z axis = the normal to the surface of the lipid lamellae); in system I short rodlike molecules (such as diphenylethyne, anthracene) were oriented parallel, whereas a long molecule, such as β-carotene, was perpendicularly oriented.[19] The planar cationic dyes were oriented with their planes perpendicular to the optical axis. In system II all molecules investigated were perpendicularly oriented.

It may be noted that for rodlike molecules (diphenylethyne, *trans*-β-carotene) the average orientation is unequivocally determined from the LD/A of a single transition, since $S_x = S_y$ (z = long axis). The observation that $S_z \approx -2S_y$ from the two mutually perpendicularly polarized band in anthracene (system I, Table I) indicates that anthracene also behaves almost like a rod in this liquid crystalline system.

The order parameter (or LD/A) was well reproducible for corresponding samples, at a fixed sample thickness. It was practically independent of the concentration (0.01–0.1%) of the probe molecule. A monotonic decrease in S_i with increasing *total* sample layer thickness appeared to be the rule (see, e.g., Table II). This effect is expected since the macroscopic orientation should be less complete

TABLE III: Observed LD (Corrected for LD_R), A, and Estimated S_i for β-Carotene in System II of Varying Composition (ω = 0)

% NaC_8	% decanol	% H_2O	d_0, μm	$(LD/A)_A$	$S_{z'}$	$(LD/A)_C$	$(LD/A)_B$	Approx lamellae thickness, Å: Lipid	Water
40.2	34.7	25.1	40	−0.21	−0.12	−0.18	0.17	23	7.5
			25	−0.25	−0.14	−0.21	0.17		
18.2	35.5	46.3	40	−0.22	−0.12	−0.24	0.79	25	16
			24	−0.28	−0.16	−0.34	0.81		
12.1	27.9	60.0	40	−0.14	−0.08	−0.21	0.24	24	33

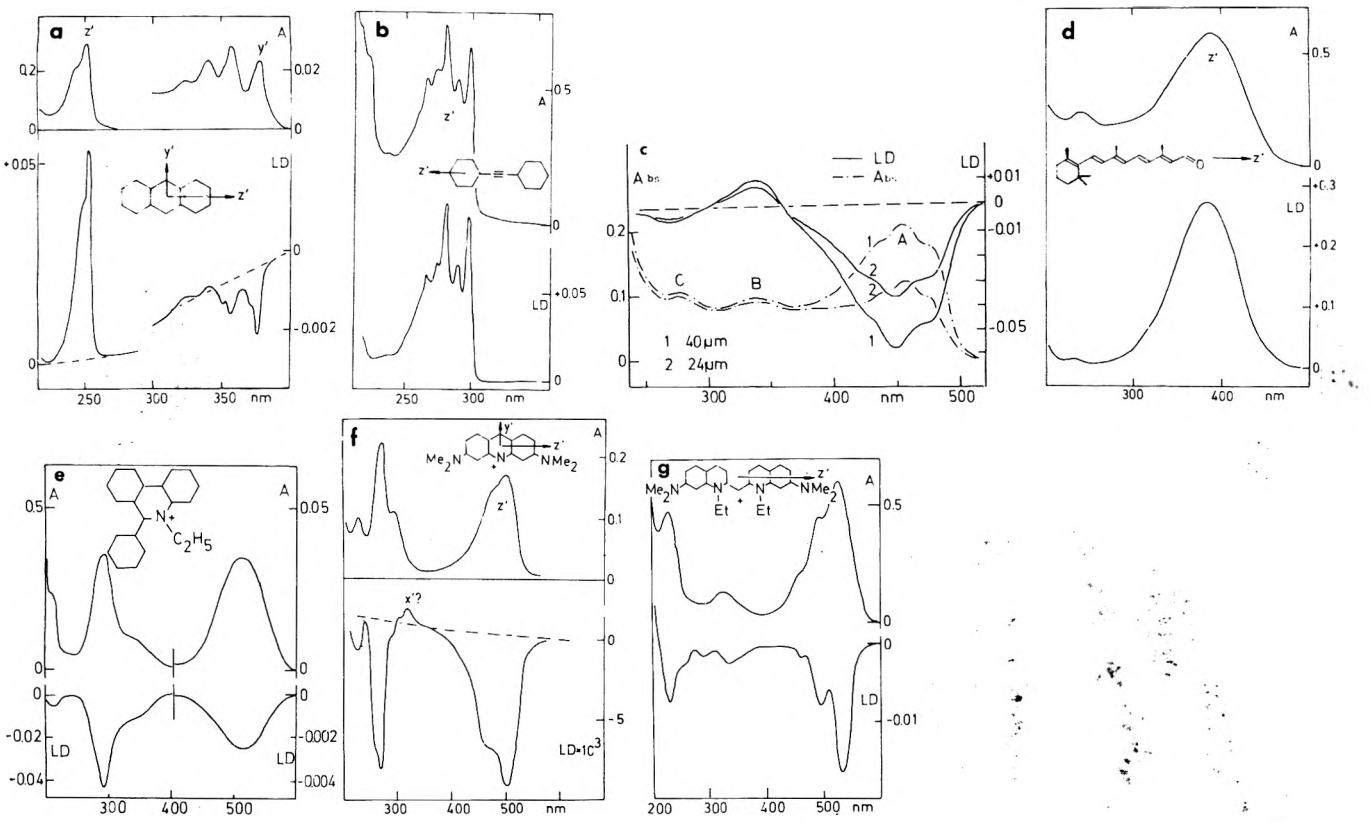

Figure 3. LD and *A* spectra of various chromophoric probes solubilized in the lamellar mesophase of sodium octanoate (p %), decanol (q %), water (r %). Chromophore concentrations around 0.1%; $\omega = 45°$: (a) anthracene ($p = 18.2$, $q = 35.5$, $r = 46.3$; $d_0 = 20$ μm); (b) diphenylethyne ($p = 24.0$, $q = 43.0$, $r = 33.0$; $d_0 = 40$ μm); (c) β-carotene ($p = 18.2$, $q = 35.3$, $r = 46.3$); (d) retinal ($p = 18.2$, $q = 35.5$, $r = 46.3$; $d_0 = 20$ μm); (e) ethidium bromide ($p = 18.2$, $q = 35.5$, $r = 46.3$; $d_0 = 20$ μm); (f) acridine orange ($p = 40.2$, $q = 34.7$, $r = 20.1$; $d_0 = 20$ μm); (g) 1,1′-diethyl-2,2′-cyanine iodide ($p = 18.2$, $q = 35.5$, $r = 46.3$; $d_0 = 20$ μm).

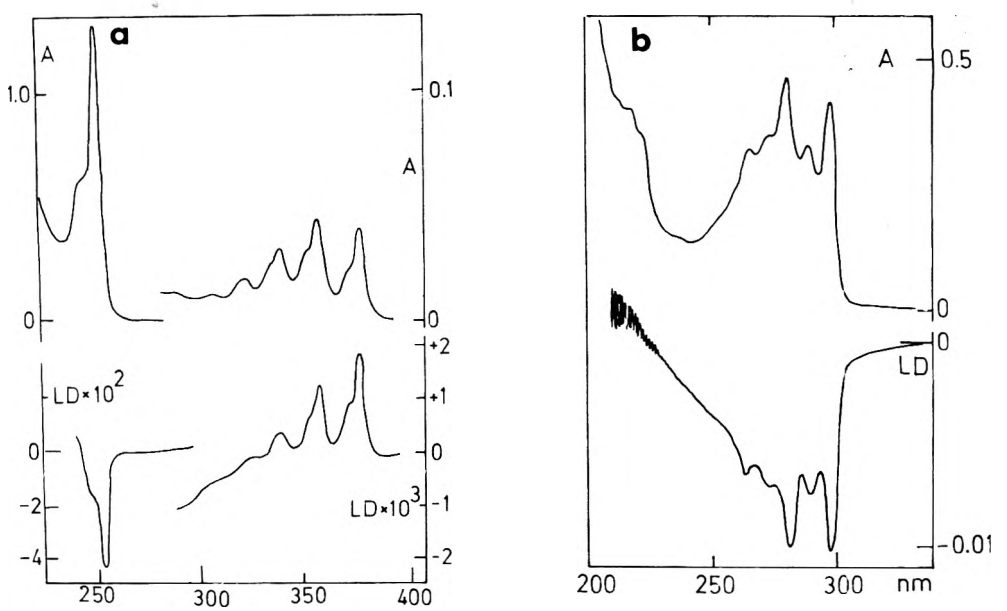

Figure 4. LD and *A* spectra of anthracene [(a) 50.2% lipid, 49.8% water] and diphenylethyne [(b) 20.0% lipid, 80.0% water] in the lamellar mesophase of sodium di-2-ethylhexylsulfosuccinate and water ($d_0 = 20$ μm, $\omega = 45°$). For assignments, see Figure 3a–b. The LD and *A* spectra of β-carotene in this system have been omitted as they are almost identical with those in Figure 3c.

at large distances from the supporting plates.

With the aim of estimating to what extent the dimensions of the amphiphile and water lamellae influence the solute orientations we also studied a few samples of different composition (Table III). For system II there appeared to be a maximum in orientation at 30–40% lipid content. For system I no significant difference in orientation was observed between some samples with different water contents.

In Figure 5 the dependence of LD/*A* on ω is shown and it is found to be in good agreement with eq 6.

Discussion

It is inferred that short rodlike and nonpolar molecules such as anthracene and diphenylethyne tend to orient themselves parallel to the amphiphile carbon chains in the lamellar liquid crystal, system I. This may be understood in terms of repulsion and dispersion forces (the latter

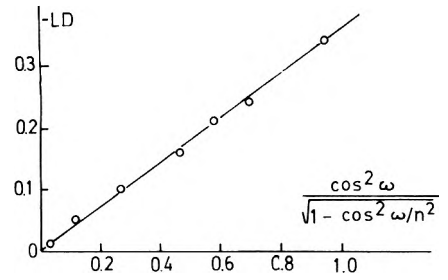

Figure 5. LD vs. the angular factor of eq 6 for β-carotene as in Figure 3c. (Band A, $A = 1$, $d_0 = 40$ μm).

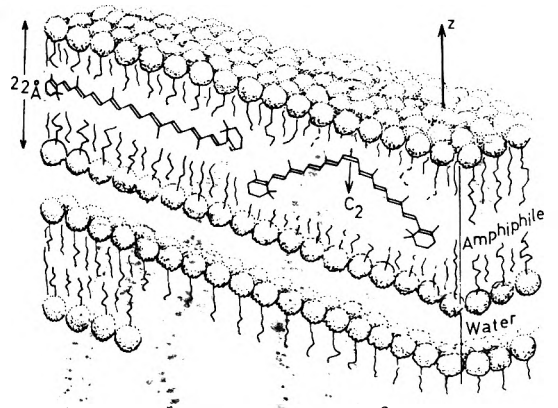

Figure 6. Sketched preferred orientation of β-carotene in system I.

favoring the molecular axis of maximum polarizability).[20] On the other hand a long rodlike molecule such as *trans*-β-carotene, which has a length of about 2.2 nm, cannot adopt such a parallel orientation, since the amphiphilic lamellae are to thin (Figure 6). However, retinal, a rodlike molecule with a polar head group (aldehyde), was not unexpectedly aligned along the amphiphile carbon chains and probably with the aldehyde group anchored at the polar surface.

The negative LD of the planar cationic dyes (Figure 3e–g), with $\pi \rightarrow \pi^*$ transitions polarized in their molecular planes, implies that these molecules are aligned with their planes parallel to the lamellar surfaces. It is reasonable to assume that such an orientation is due to an ion binding to the polar amphiphilic surface.

In the case of system II the branched hydrocarbon implies a less regular order inside the amphiphilic lamellae and this causes a less effective net probe orientation.

We have finally tried to characterize the temperature dependence of the orientation in a few cases. Generally the degree of orientation was decreased by raising the temperature but it regained rapidly its initial value upon returning to the initial temperature. As is shown in Figure 7a, different types of alignment vs. cooling curves are observed for system I depending on the choice of probe molecule. We have interpreted these variations in terms of the temperature dependencies of the different environments; diphenylethyne (or anthracene) is believed to reflect the intrinsic orientation of the lipid hydrocarbon chains. When raising the temperature their thermal motion is continuously increased, leading to a decreased orientation in the interior of the membrane. A retained orientation at the lamellar surfaces is indicated by the fact that, e.g., retinal seems not to be randomized even at 95 °C (for a sample of 18% sodium octanoate, 36% decanol, and 46% water). This is probably due to the fact that retinal has its polar aldehyde group anchored at the polar surface. Therefore retinal reflects mainly the macroscopic orientation of the lamellae. Similar behavior was observed with other probe molecules directed by the surfaces of the lamellae (acridine orange and *trans*-β-carotene).

Some interesting observations were made when lowering the temperature below the gel-to-liquid crystalline phase transition of the sodium octanoate/decanol/water system. Probes of the macroscopic orientation of the lamellae indicated a decreased order on decreasing the temperature to 9 °C and the original orientation was not immediately

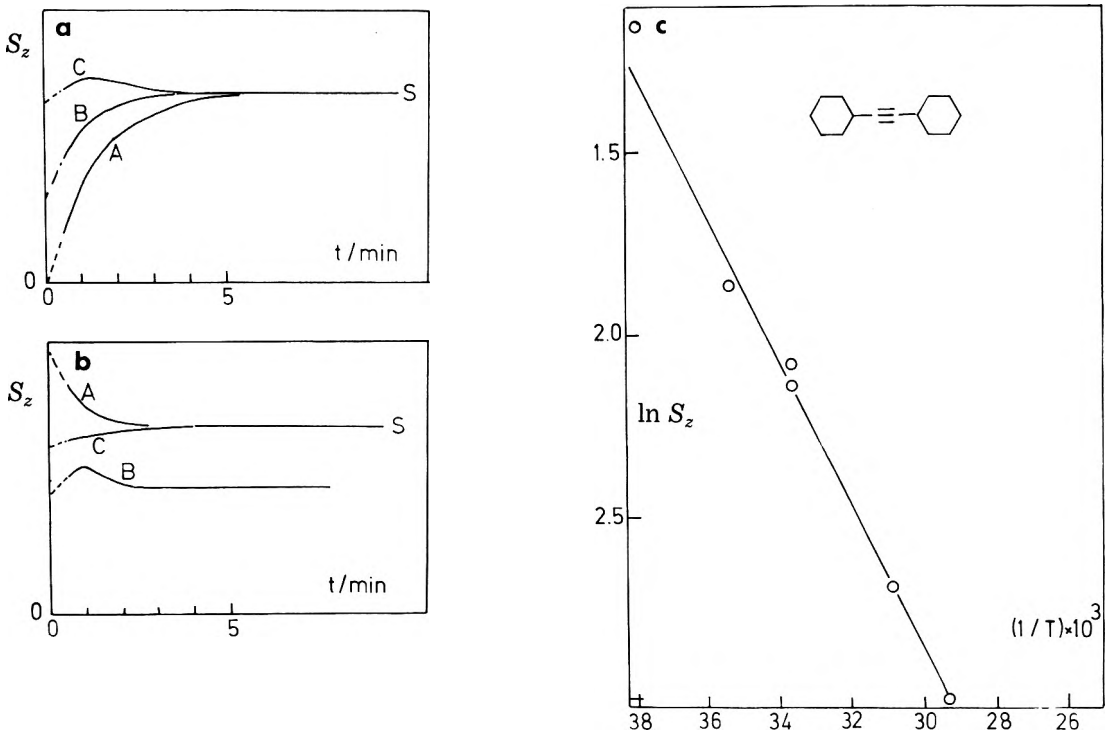

Figure 7. Temperature effects on the probe orientations in system I. (a) cooling curves, S_z in arbitrary units on the vertical axis from 95 °C to room temperature, time on horizontal axis (A = diphenylethyne, B = retinal, C = acridine orange, S = orientation at the standard procedure); (b) corresponding relaxations to room temperature of samples A, B, and C after cooling to 9 °C; (c) orientation of diphenylethyne (ln S_z, on the vertical scale as a function of temperature).

regained when returning to room temperature (Figure 7b). This may be due to the formation of more than one phase (several gel phases have been observed in similar systems[21]) at low temperature and that the attainment of the equilibrium is slow. Further studies are necessary to clarify this point.

Although the arguments are fairly fragmentary they strongly indicate that the observed anisotropy in system I is a product of two effects: one "macroscopic" due to the alignment of fairly large lamellae domains, the other "microscopic" due to the degree of regularity in the packing of the hydrocarbon chains in the amphiphile phase. It was thus observed that even a very small mutual displacement of the supporting quartz plates at room-temperature generally resulted in an irreversible randomization. On the other hand, the complete randomization at elevated temperature occurred at the distinct point at which the lamellae structure disintegrated. In contrast to this behavior, the second ("microscopic") anisotropy is as expected continuously dependent on the temperature. The reorientation after a temperature cycle is immediate and well reproducible. A linear dependence of log $S_{z'}$ vs. $1/T$ was observed for diphenylethyne in system I (Figure 7c), which can be understood in terms of activation parameters of the interactions between the hydrocarbon chains.

Concluding Remarks

The results make us feel optimistic about the possibility of determining the orientation of a chromophoric compound, such as a protein, in a biomembrane by using this linear dichroism spectroscopic method. One great advantage of this method is that very small concentrations of the solubilized chromophore can be used, so that the risk of disturbing the original structures can be minimized. Another positive point is the apparently negligible interference from absorption statistics. For instance in a recent study in this laboratory of β-carotene in egg lecithin liposomes which could be oriented by Couette flow, serious absorption statistics, due to the necessarily small volume fraction of the liposomes, obscured any evaluation.

It is our hope that the method can also be used for studies of orientations of ionophores in membranes. One such compound, gramicidine A, about which there is considerable controversy as regards how it spans the membrane, is currently being studied by LD in a lamellar liquid crystal.

Acknowledgment. The cost of the dichroism spectrometer was defrayed by the Knut and Alice Wallenberg Foundation. This work was supported by grants from the Swedish Natural Science Research Council (Project No. K 3216-008, K 3500-004. We thank Drs. H. Wennerström and D. Burton for valuable discussions.

Appendix

Derivation of Eq 3. Referring to Figure 1 the elements of the diagonal electric field tensor can be written $E_{+1} = -(E_x + iE_z)/\sqrt{2}$, $E_{-1} = (E_x - iE_z)/\sqrt{2}$, $E_0 = E_y$. To form its interaction with μ, E (in the laboratory system XYZ, below denoted L) has to be transformed into the molecular coordinate system (below denoted M) via the sample coordinate system xyz (below denoted D; the z axis is frequently called the director in liquid crystals). One may then write[12]

$$(E^{M}\cdot\mu^{M}) = \sum_{qq'} E^{L}_{q'}\mu^{M} D^{(1)}_{q0}(\Omega_{MD}) D^{(1)}_{q'q}(\Omega_{DL})$$

and

$$(E^{M}\cdot\mu^{M})^2 = \sum_{qq'q''q'''} E^{L}_{q'}E^{L}_{q'''}(\mu^{M})^2 D^{(1)}_{q0}(\Omega_{MD}) D^{(1)}_{q'q}(\Omega_{DL})/ D_{q''0}(\Omega_{MD}) D^{(1)}_{q'''q''}(\Omega_{DL}) \quad (A.1)$$

where $D^{(k)}_{q'q}(\Omega)$ is a Wigner rotation matrix element[12] and Ω_{MD} represents the three eularian angles $(\alpha\beta\gamma)$ specifying the transformation from the coordinate system D to system M. Ω_{DL} similarly specifies the transformation between the L and D systems.

By using the relation[12]

$$D^{(j_1)}_{m_1'm_1}(\Omega) D^{(j_2)}_{m_2'm_2}(\Omega) = \sum_{Jm} (-1)^{q+q'+q''+q'''}(2J+1)\begin{bmatrix} j_1 & j_2 & J \\ m_1' & m_2' & m' \end{bmatrix} \times \begin{bmatrix} j_1 & j_2 & J \\ m_1 & m_2 & m \end{bmatrix} D^{(J)}_{-m'-m}(\Omega)$$

where

$$\begin{bmatrix} j_1 & j_2 & J \\ m_1 & m_2 & m \end{bmatrix}$$

is a Wigner 3-j symbol, eq A.1 becomes

$$(E^{M}\cdot\mu^{M})^2 = \sum_{qq'q''q'''} E^{L}_{q'}E^{L}_{q'''}(\mu^{M})^2 \sum_{J} \begin{bmatrix} 1 & 1 & J \\ q & q'' & -(q'+q'') \end{bmatrix} \times \begin{bmatrix} 1 & 1 & J \\ 0 & 0 & 0 \end{bmatrix} D^{(J)}_{q+q'',0}(\Omega_{MD})(2J+1)(-1)^{q+q''} \times \sum_{J'} \begin{bmatrix} 1 & 1 & J' \\ q' & q''' & -(q'+q''') \end{bmatrix} \begin{bmatrix} 1 & 1 & J' \\ q & q'' & -(q+q'') \end{bmatrix} \times D^{(J)}_{(q'+q''')(q+q'')}(2J'+1)(-1)^{q+q'+q''+q'''} \quad (A.2)$$

We can now formulate the average of $\langle|E\cdot\mu|^2\rangle$ by noting that the cylindrical symmetry around the z axis implies that $\langle D^{(k)}_{q'q}(\Omega_{MD})\rangle = \delta_{q0}\langle D_{q'0}(\Omega_{MD})\rangle$. Then eq A.2 becomes

$$\langle|E^{M}\mu^{M}|^2\rangle = \sum_{q'q'''} E^{L}_{q'}E^{L}_{q'''}(\mu^{M})^2(-1)^{q'+q'''} \left\{ \left(-\frac{1}{\sqrt{3}}\right) \times \begin{bmatrix} 1 & 1 & 0 \\ q' & q''' & -(q'+q''') \end{bmatrix} D^{(0)}_{q'+q''',0}(\Omega_{DL})\langle D^{(0)}_{00}(\Omega_{MD})\rangle + \frac{10}{\sqrt{30}} \begin{bmatrix} 1 & 1 & 2 \\ q' & q''' & -(q'+q''') \end{bmatrix} \times D^{(2)}_{q'+q''',0}(\Omega_{DL})\langle D^{(2)}_{00}(\Omega_{MD})\rangle \right\} \quad (A.3)$$

and so follows

$$\langle|E^{M}\cdot\mu^{M}|^2\rangle = (\mu^{M})^2\{(E^{L}_{1})^2(2/\sqrt{6})D^{(2)}_{20}(\Omega_{DL})\langle D^{(2)}_{00}(\Omega_{MD})\rangle + (E^{L}_{-1})^2(2/\sqrt{6})D^{(2)}_{-20}(\Omega_{DL})\langle D^{(2)}_{00}(\Omega_{MD})\rangle + E^{L}_{1}E^{L}_{-1}[(2/3)D^{(2)}_{00}(\Omega_{DL})\langle D^{(2)}_{00}(\Omega_{MD})\rangle - (2/3)D^{(0)}_{00}(\Omega_{DL})\langle D^{(0)}_{00}(\Omega_{MD})\rangle] + (E^{L}_{0})^2[(1/3)D^{(0)}_{00}(\Omega_{DL})\langle D^{(0)}_{00}(\Omega_{MD})\rangle + (2/3)D^{(2)}_{00}(\Omega_{DL})\langle D^{(2)}_{00}(\Omega_{MD})\rangle]\} \quad (A.4)$$

Remembering that $\parallel$ and $\perp$ denoted light with E polarized along the Z axis and X axis, respectively, we have the

following expression for the ratio between the linear dichroism and the absorption of the sample at random orientation:

$$LD/A_r = (Cd\langle|E^M|^2\rangle_{E_X=E,E_Z=0} - \langle|E^M|^2\rangle_{E_Z=E,E_X=0})/(Cd(1/3)[\langle|E^M|^2\rangle_{E_X=0,E_Z=E} + \langle|E^M|^2\rangle_{E_Z=0,E_X=E} + \langle|E^M|^2\rangle_{E_Y=E}]) \quad (A.5)$$

Using the definition of the electric field tensor in eq A.4 and A.5, one obtains:

$$LD/A_r = \langle D^{(2)}_{00}(\Omega_{MD})\rangle[D^{(2)}_{-20}(\Omega_{DL}) - (2/\sqrt{6})D^{(2)}_{20}(\Omega_{DL})] \quad (A.6a)$$

where

$$\langle D^{(2)}_{00}(\Omega_{MD})\rangle = (3\langle\cos^2\beta_{MD}\rangle - 1)/2 \quad (A.6b)$$

$$D^{(2)}_{\pm 2}(\Omega_{DL}) \doteq \sqrt{(3/8)}\sin^2\beta_{DL}e^{2i\gamma_{DL}} \quad (A.6c)$$

For uniaxial systems, as we are dealing with here, one usually defines an order parameter[13] $S = \langle D^{(2)}_{00}(\Omega_{MD})\rangle$ representing the average orientation of μ with respect to the z axis (the director). If a molecule has a D_{2h} or C_{2v} symmetry, each transition must be polarized parallel to any of the symmetry axes. Then one should, from the LD of an absorption band with pure polarization, directly obtain the average orientation of the appropriate molecular coordinate axis. Furthermore, since $\Sigma_{i=1}{}^3S_i = 0$, i is the molecular coordinate axes (x', y', z'), the validity of the assumption about cylindrical symmetry of the sample can be checked from the linear dichroism of two bands, mutually perpendicularly polarized in a molecule with $C_{\infty v}$ or $D_{\infty h}$ symmetry (then $S_{x'} = S_{y'}$). An independent check is provided by the criterion that LD = 0 for $\beta = 0$.

Equation A.6 can be simplified by noting that the eularian angle γ_{DL} can be arbitrarily set to zero and we obtain $LD/A_r = 3S\sin^2\beta_{DL}$, i.e. eq 3.

References and Notes

(1) S. Friberg, *Adv. Chem. Ser.*, **No. 152** (1976).
(2) H. Wennerström and G. Lindblom, *Q. Rev. Biophys.*, **10**, 67 (1977).
(3) G. Lindblom and H. Wennerström, *Biophys. Chem.*, **6**, 167 (1977).
(4) Å. Davidsson and B. Nordén, *Chem. Scr.*, **9**, 49 (1976).
(5) E. Fredericq and C. Houssier, "Electric Dichroism and Electric Birefringence", Clarendon Press, Oxford, 1973; J. Michl, E. W. Thulstrup, and J. H. Eggers, *J. Phys. Chem.*, **74**, 3878 (1970); E. W. Thulstrup, J. Michl, and J. H. Eggers, *ibid.*, **74**, 3868 (1970); A. Yogev, L. Margulies, B. Strasberger, and Y. Mazur, *ibid.*, **78**, 1400 (1974); B. Nordén and F. Tjerneld, *Biophys. Chem.*, **4**, 191 (1976); **6**, 31 (1977); B. Nordén, "Proceedings of Nobel Workshop on Linear Dichroism Spectroscopy", Lund, 1976.
(6) J. Breton, M. Michel-Villaz, and G. Paillotin, *Biochim. Biophys. Acta*, **314**, 42 (1973).
(7) B. Nordén and F. Tjerneld, "Proceedings of Nobel Workshop on Linear Dichroism Spectroscopy", Lund, 1976.
(8) J. B. Bateman and E. J. Covington, *J. Colloid Sci.*, **16**, 531 (1961).
(9) I. V. Yannas, N. H. Sung, and C. Huang, *J. Phys. Chem.*, **76**, 2935 (1972).
(10) R. J. Cherry, K. Hsu, and D. Chapman, *Biochim. Biophys. Acta*, **267**, 512 (1972); A. J. Hoff, *Photochem. Photobiol.*, **19**, 51 (1974); H. Akatsu, Y. Kyogoku, H. Nakahara, and K. Fukuda, *Chem. Phys. Lipids*, **15**, 222 (1975); U. P. Fringeli, M. Schadt, P. Rihak, and H. H. Güthard, *Z. Naturforsch. A*, **31**, 1098 (1976).
(11) J. A. Schellman, *Chem. Rev.*, **75**, 323 (1975).
(12) A. R. Edmonds, "Angular Momentum in Quantum Chemistry", Princeton University Press, Princeton, N.J., 1960.
(13) A. Saupe, *Mol. Cryst.*, **1**, 527 (1966).
(14) Å. Davidsson and B. Nordén, *Chem. Phys. Lett.*, **28**, 221 (1974); *Chem. Scr.*, **8**, 95 (1975).
(15) Å. Davidsson and B. Nordén, *Chem. Phys.*, **8**, 223 (1975).
(16) A. Schulster and J. W. Nicholson, "The Theory of Optics", Edward Arnold, London, 1924.
(17) G. Lindblom, *Acta Chem. Scand.*, **26**, 1745 (1972).
(18) H. Inoue, R. Hoshi, T. Masamoto, J. Shiraishi, and Y. Tanizaki, *Berichte*, **75**, 441 (1971).
(19) According to Eckert and Kuhn, only two of the observed absorption bands of β-carotene (A and C in Figure 3c) derive from *trans*-β-carotene, while the third band (B) is due to a small amount of the cis isomer. The latter band is assigned to be polarized along the C_2 axis of this planar molecule. The positive sign of $(LD/A)_B$ (Table I) thus indicates that this axis is aligned parallel to the optical axis (i.e., parallel to the hydrocarbon chains). R. Eckert and H. Kuhn, *Z. Electrochem.*, **64**, 356 (1960).
(20) E. Sackmann and H. Möhwald, *Chem. Phys. Lett.*, **12**, 467 (1972).
(21) M. J. Janiak, D. M. Small, and G. G. Shipley, *Biochemistry*, **15**, 4575 (1976); J. Ulmius, H. Wennerström, G. Lindblom, and G. Arvidson, *ibid.*, in press.

Study of Inclusion Complex Formation by Positron Annihilation Techniques[1]

Yan-Ching Jean and Hans J. Ache*

Department of Chemistry, Virginia Polytechnic Institute and State University, Blacksburg, Virginia 24061

(Received June 9, 1977)

Publication costs assisted by the Petroleum Research Fund

The positron annihilation technique was applied to determine the complex formation constants for a series of inclusion complexes of *p*-nitrophenol, nitrobenzene, and *p*-benzoquinone with cyclohexaamylose. The formation constants, K_c, were found to be 341, 48.6, and 6.8 M^{-1}, respectively.

Introduction

In previous papers[2,3] we have demonstrated and discussed the positron annihilation technique as a method to study the molecular association phenomena in a series of conventional molecule complexes, such as nitrobenzene–hexamethylbenzene, and in biological systems, such as vitamin K_1–indol. We found this method particularly suitable to determine the formation constants in systems where spectroscopic measurements are difficult to perform. More recently this technique was applied to study the position of probe molecules, such as nitrobenzene in micelles.[4]

Another series of interesting compounds, where intermolecular forces and complex formation are of great importance, are the so-called inclusion compounds.[5] Cyclic oligosaccharides have a toroid shape with a central void of a few angstroms diameter with an internal hydrophobic surface and external hydrophilic face. They are known for their ability to complex a variety of molecules in the cavity. This phenomenon was also observed when the cyclic ol-

igosaccharides were dissolved in water.[6-9] The stability of the complexes was found to vary with the size of the guest and host molecule, i.e., if the substrate is too small it will pass in and out of the cavity with little binding, whereas if the substrate is too large, it will not fit into the cavity and therefore will not bind to the cyclic oligosaccharides. These inclusion compounds play an important role by virtue of their capability of catalyzing or inhibiting many chemical and biochemical reactions. Particularly interesting appears the application of cycloamyloses as enzyme active site models. While most of the previous studies of inclusion compounds in solution were carried out by NMR and fluorescence probe techniques, we report in the following some results obtained by employing the positron annihilation techniques to the study of inclusion complexes in aqueous solutions.

The usefulness of the ortho-positronium atom, o-Ps,[10] which is the bound state of a positron and an electron (parallel spin orientation), in probing molecular association phenomena is based on the fact that it reacts very rapidly with certain compounds, such as nitroaromatics, quinones, and iodine, under Ps–molecule complex formation.[11-13] These compounds, however, lose most of their reactivity toward Ps when they are already in a complexed form.[2,3,14-15] Thus by observing the difference in the reactivities of these compounds in their complexed and uncomplexed state it is possible to determine the molecular association constants of the systems under investigation.

In the present study, the inclusion complexes of nitrobenzene, *p*-nitrophenol, and *p*-benzoquinone with cyclohexaamylose (α-cyclodextrin) in aqueous solution were studied and their molecule association constants determined.

Experimental Section

The experimental techniques employed were similar to those described previously.[2,3] Various amounts of cyclohexaamylose in the form of its tetrahydrate (Aldrich Chemical Co., highest available purity) were dissolved in a buffer solution of pH 3.5 and ionic strength 0.5, prepared from triple-distilled water and appropriate amounts of phosphoric acid and sodium hydroxide, which contained small amounts of the guest molecules, nitrobenzene, *p*-nitrophenol, or *p*-benzoquinone, respectively. All of the latter compounds were purified by suitable methods until subsequent tests showed a purity of better than 99.5%. The solutions, 2 mL each, were transferred to sample vials, 100 mm long, 10 mm i.d., which contained the positron source, 3–5 μCi of ^{22}Na in a thin glass foil, positioned in the center of the liquid sample. The samples were thoroughly degassed under vacuum by freeze–thaw techniques and subsequently sealed off.

The positron lifetime measurements were carried out by conventional fast–slow γ–γ coincidence techniques.[16] The resolution as measured by the fwhm of the prompt ^{60}Co spectrum was less than 0.4 ns. The lifetime spectra were analyzed as previously reported, by computational techniques using the PAL[17] decay analysis program and source corrections were made.

Results and Discussion

In a solution consisting of a host molecule such as cyclohexaamylose (D) and the guest molecule (nitrobenzene, etc.) in its uncomplexed form, Q, and in its complexed form QD, the following equilibrium exists:

$$Q + D \rightleftarrows QD \qquad (1)$$

Thus, the situation is identical with that previously[3] described. The same equations apply (as outlined in ref 3), which correlate the decay constants λ_2 of the long-lived component in the positron lifetime spectra, with K_c, the molecular association constant, and $K_{Q(obsd)}$ and $K_{QD(obsd)}$, the rate constants for the reaction of Ps with the guest molecule in its complexed and uncomplexed form, respectively. The results are shown in Figure 1, where $-1/(\tilde{\lambda}_2 - \tilde{\lambda}_2^0)$ is plotted as a function of $1/[D]$. $\tilde{\lambda}_2$ and $\tilde{\lambda}_2^0$ are the decay constants associated with the long-lived component in the lifetime spectra, corrected for the contribution made by the solvent and host molecule to the overall annihilation rates (see ref 3). [D] and [Q] are the concentrations of the host and guest molecule, respectively.

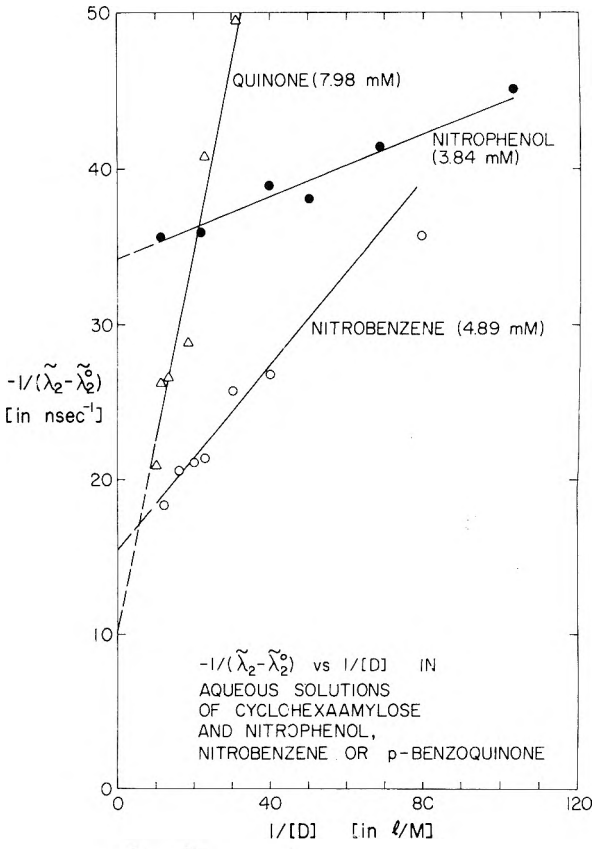

Figure 1. $-1/(\tilde{\lambda}_2 - \tilde{\lambda}_2^0)$ vs. $1/[D]$ in aqueous solutions of cyclohexaamylose containing 7.88 mM *p*-benzoquinone, 4.89 mM nitrobenzene, or 3.84 mM *p*-nitrophenol, respectively: pH 3.5, ionic intensity 0.5, temperature 22 °C.

Since[3]

$$\frac{1}{\tilde{\lambda}_2 - \tilde{\lambda}_2^0} = \frac{1}{K_c[Q][D][K_{QD(obsd)} - K_{Q(obsd)}]} + \frac{1}{[Q][K_{QD(obsd)} - K_{Q(obsd)}]} \qquad (2)$$

from the slope and intercept of the plot of $(\tilde{\lambda}_2 - \tilde{\lambda}_2^0)^{-1}$ against $1/[D]$ K_c and $K_{QD(obsd)}$ can be determined. ($K_{Q(obsd)}$ is the rate constant of the guest molecule in H_2O and has been determined separately.) The results are summarized in Table I. As expected, the reactivity of the guest molecules in their complexed form is reduced by a factor of 10 or more, thus facilitating the determination of the molecular association constant. *p*-Nitrophenol was found to exhibit a rather strong tendency to complex with cyclohexaamylose under the experimental conditions, as indicated by a K_c of 341 M^{-1} which is in excellent agreement with the value obtained by spectroscopic methods.[7] The molecular association constants for nitrobenzene and *p*-benzoquinone are significantly smaller,

TABLE I: Inclusion Complex Formation Constants, K_c, and Rate Constants, $K_{QD(obsd)}$, for the Interaction of the Inclusion Complexes of Nitrobenzene, *p*-Nitrophenol, and *p*-Benzoquinone with Cyclohexaamylose (CD) at pH 3.5, Ionic Intensity 0.5, in Aqueous Solution at 22 °C

Compound	$K_{QD(obsd)}$, 10^{10} M^{-1} s^{-1}	K_c, M^{-1}	K_c(spectrosc), M^{-1}
p-Nitrophenol	0.88		
p-Nitrophenol-CD	0.11	341	385[a]
Nitrobenzene	1.38		
Nitrobenzene-CD	0.09	48.6	
p-Benzoquinone	1.37		
p-Benzoquinone-CD	*b*	6.8	

[a] From ref 7. [b] Not detectable. The reactivity of the molecular complex toward Ps is below the detectable limit ($K < 0.05 \times 10^{10}$ M^{-1} s^{-1}) inherent to method of evaluation.

48.6 and 6.8 M^{-1}, respectively.

This result is somewhat surprising, since previous measurements of the Ps–molecular complex formation[11] with these three compounds have shown that it occurs at rates which show a trend opposite to that observed here for the inclusion complex formation. (K_{obsd} for Ps reaction with *p*-nitrophenol, nitrobenzene, and *p*-benzoquinone are 1.3×10^{10}, 2.7×10^{10}, and 5×10^{10} M^{-1} s^{-1}.) If one assumes that similar forces are responsible for the complexation of the nitrobenzene etc. with Ps or with cyclohexaamylose, the drastic differences observed in K_c would have to be explained in terms of geometric or steric requirements. In these terms it would appear that *p*-nitrophenol has the best fit to penetrate into the cycloamylose cavity, while nitrobenzene and *p*-benzoquinone might be too small to undergo efficient binding. On the other hand, if the nature of the binding forces is significantly different from those found in conventional molecular complexes,[11] and consists of so-called "hydrophobic" interactions[5] involving mostly entropy changes the observed different trend may result. Unfortunately very little is known about the latter interactions so that no final conclusions can be reached.

It is interesting that in all cases studied so far (see Table I, and ref 2) the complex formation resulted not only in a reduced reactivity toward Ps, but this reduction in reactivity was more pronounced if a weaker complex, with a smaller K_c, was formed than when strong complexing occurred. It seems that in the former case most of the complexing capability of the guest molecule is used for binding and very little is left to interact with Ps, whereas a strong complex can itself complex with Ps.

Summarizing, it can be said that the positron annihilation technique allows an accurate determination of inclusion complex formation constants. Furthermore it appears that by systematically studying the trends which lead to a reduction of the reactivity of the complexed guest molecule toward Ps, valuable information about the type of intermolecular interactions could be obtained.

References and Notes

(1) Acknowledgment for financial support is made to the Donors of the Petroleum Research Fund administered by the American Chemical Society and the U.S. Energy Research and Development Administration.
(2) Y.-C. Jean and H. J. Ache, *J. Phys. Chem.*, **80**, 1693 (1976).
(3) Y.-C. Jean and H. J. Ache, *J. Am. Chem. Soc.*, **99**, 1623 (1977).
(4) Y.-C. Jean and H. J. Ache, *J. Am. Chem. Soc.*, in press.
(5) For recent reviews on inclusion compound, see, e.g., (a) R. J. Bergeron, *J. Chem. Ed.*, **54**, 204 (1977); (b) D. W. Griffiths and M. L. Bender, *Adv. Catal.*, 209–261 (1973).
(6) H. Schlenk and D. M. Sand, *J. Am. Chem. Soc.*, **83**, 2312 (1961).
(7) F. Cramer, W. Saenger, and H.-Ch. Spatz, *J. Am. Chem. Soc.*, **89**, 14 (1967); see also previous papers in this series.
(8) R. L. Van Etten, J. F. Sebastian, G. A. Clowes, and M. L. Bender, *J. Am. Chem. Soc.*, **89**, 3242, 3253 (1967).
(9) D. J. Wood, F. E. Hruska, and W. Saenger, *J. Am. Chem. Soc.*, **99**, 1735 (1977).
(10) For general references, see (a) J. Green and J. Lee, "Positronium Chemistry", Academic Press, New York, N.Y., 1964; (b) V. I. Goldanskii, *At. Energy Rev.*, **6**, 3 (1968); (c) J. D. McGervey in "Positron Annihilation", A. T. Steward and L. O. Roellig, Ed., Academic Press, New York, N.Y., 1967, p 143; (d) J. A. Merrigan, S. J. Tao, and J. H. Green, "Physical Methods of Chemistry", Vol. 1, Part III D, A. Weissberger and B. W. Rossiter, Ed., Wiley, New York, N.Y., 1972; (e) H. J. Ache, *Angew. Chem., Int. Ed. Engl.*, **11**, 179 (1972); (f) J. H. Green, *MTP Int. Rev. Sci., Radiochem.*, **8**, 251 (1972); (g) V. I. Goldanskii and V. G. Virsov, *Annu. Rev. Phys. Chem.*, **22**, 209 (1971).
(11) For Ps-molecule complex formation, see, e.g., W. J. Madia, A. L. Nichols, and H. J. Ache, *J. Am. Chem. Soc.*, **97**, 5041 (1975), where also additional references can be found.
(12) W. J. Madia and H. J. Ache, *J. Phys. Chem.*, **80**, 451 (1976).
(13) E. Hall, W. J. Madia, and H. J. Ache, *Radiochem. Radioanal. Lett.*, **23**, 283 (1975).
(14) P. Jansen, M. Eldrup, B. Skytte-Jensen, and O. Mogensen, *Chem. Phys. Lett.*, **10**, 303 (1975).
(15) B. Levay and P. Hautojarvi, *J. Phys. Chem.*, **76**, 1951 (1972).
(16) T. L. Williams and H. J. Ache, *J. Chem. Phys.*, 50, 4493 (1969).
(17) PAL is a version of the CLSQ nuclear decay analysis program (J. B. Cummings, BNL report no. 6470), modified by A. L. Nichols in this laboratory.

Structure of Water–Hydrochloric Acid Complexes in Argon and Nitrogen Matrices from Infrared Spectra

A. Schriver, B. Silvi, D. Maillard, and J. P. Perchard*

Laboratoire de Spectrochimie Moléculaire, Université Pierre et Marie Curie, 8 Rue Cuvier, 75005 Paris, France

(Received April 8, 1977)

The infrared spectra of water–hydracid (HCl, HBr, DBr) mixtures in argon or nitrogen matrices reveal evidence of several complexes, the structures of which are discussed from both HX and H_2O frequencies. The HCl frequency shifts are discussed according to two models: the Lippincott–Schroeder potential and the MINDO/3 semiempirical method. In both cases a relation between HCl frequency and O···Cl distance is obtained but lead to noticeable discrepancies which are discussed in the limiting case of proton transfer for short O···Cl distances.

It is well established that the matrix isolation technique applied to vibrational spectroscopy provides a powerful tool for studying intermolecular forces between the crystalline matrix and the doping molecules, or between the dopant molecules themselves. According to the nature and the magnitude of the intermolecular potential, there are two ways to get into the discussion of the spectra: for weak interactions an analytical development of intermolecular potential, taking into account electrostatic, induction, dispersion, and repulsion forces allows the

determination of interaction energy, geometrical configuration, and spectral perturbation of the impurity molecules embedded in the matrix crystal; for stronger interactions between doping molecules leading to the formation of super molecules the matrix effects are supposed to be negligible and quantum chemistry methods must be applied. The first method has been mainly used to discuss the weakly perturbed spectra ($\Delta\nu/\nu_{gas} < 3\%$, where $\Delta\nu = \nu_{gas} - \nu_{matrix}$) of diatomic molecules such as hydracids, either for monomers[1] or for aggregates;[2] the second method is the only one to be used for reactive species as metal–ligand complexes and for hydrogen bonded systems A–H···B characterized by noticeable electronic perturbations in the space between the two molecules.

We have recently applied the first method to the interpretation of HCl and HBr aggregate spectra in argon or nitrogen matrices,[3] but the extension to the study of water–hydracid systems we shall discuss here is made impossible by strong HX spectral perturbations ($\Delta\nu/\nu_{gas}$ = 5–10%) typical of a weak hydrogen bond between lone electron pairs of the oxygen atom and the HX molecule. Such specific interaction prevents one from considering the water molecule as a whole and thus from defining it by its multipolar moments and its Lennard-Jones parameters. There is another limitation to the theoretical approach, tied to the electronic complexity of the Cl or Br atoms. Except for the HF–H_2O system studied by ab initio SCF LCAOMO,[4] the only nonexpensive methods to be used are the semiempirical methods.

Spectroscopic study of the water–hydracid system has already been undertaken previously by two groups of researchers: Ault and Pimentel[5] have analyzed infrared spectra of the water–hydrochloric acid (HCl and DCl) complex in nitrogen matrices and more recently, Ayers and Pullin[6] have discussed the spectrum of the same complex in argon matrices. In both cases the authors agree upon the existence of a weak hydrogen bond O···H–Cl, but in a nitrogen matrix the ν(HCl) vibration of the complex is related to two bands at 2540 and 2650 cm^{-1} while in an argon matrix a band at 2663 cm^{-1} is the only one observed in the same spectral range. Thus there is an important matrix effect upon the hydrogen bond and an unexplained splitting in the nitrogen matrix. Furthermore the spectral perturbation of the water molecule in nitrogen matrices has not been discussed by Ault and Pimentel and, according to Ayers and Pullin, in argon matrices remains questionable in the ν_3 region. We tried to solve these important questions. The presentation of our work is divided into three parts, the first one related to the presentation of the experimental data, the second to the discussion of the spectra, and the third is a description of some semiempirical calculations on the HCl–H_2O system allowing the determination of the spectral shifts for both parts of the complex.

Experimental Section

We used a conventional helium Dewar equipped with two deposition inlets and a cesium iodide cold window. The matrix sample was deposited at 10 mmol/h on the window maintained at 17 K for nitrogen and at 20 K for argon matrices. The infrared spectra were scanned with a Perkin-Elmer Model 225 spectrophotometer. The frequency accuracy is ±0.3 cm^{-1} for narrow bands, the resolving power being of the order of 0.9 cm^{-1} whatever the spectral region.

For HCl(HBr)/H_2O/matrix experiments, the deposition was obtained from a one jet inlet, the mixture being prepared in a 0.5- or 1-L bulb according to the matrix/dopant concentration ratio, hereafter refered to as M/R.

TABLE I: HX Absorption Frequencies of H_2O/HX Mixtures in Nitrogen or Argon Matrices and Attribution

		N_2[a]	Ar[a]	Attribution[b]
HCl/H_2O	C_2	2647+	2754+	1-2 complex
			2740+	HP
		2599–		
	C_1	2545	2663	1-1 complex
HBr/H_2O		2390+		HP
	C_2	2375+	2438+	1-2 complex
		2366+		
			2416+	HP
	C_1	2282	2395	1-1 complex
DBr/H_2O		1726+		HP
	C_2	1713+		1-2 complex
		1702+		
	C_1	1657		1-1 complex

[a] A plus sign indicates that the absorption grows in on annealing. A minus sign indicates that the absorption disappears on annealing. [b] HP = H_2O/HX aggregates other than 1-1 and 1-2 complexes.

For DBr/H_2O/N_2 experiments we used two inlets and no H/D exchange between H_2O and DBr has been observed.

Liquid H_2O was degassed under vacuum before use. The HCl and HBr were Matheson gas products (>99% purity); the DBr was prepared by the action of D_2O on PBr_5 and its isotopic purity is higher than 90% but decreases to 70–80% in the matrix. Nitrogen and argon (Air Liquide Products) are of the highest purity available (less than 10 ppm impurity).

Results

A. *Nitrogen Matrices.* We have already published an accurate spectrum of HCl in a nitrogen matrix in the polymer region (2810–2720 cm^{-1});[7] addition of H_2O does not give rise to any change in the spectral range 2900–2700 cm^{-1}; in the same way HBr and DBr polymer spectra are not perturbed by water addition. In agreement with Ault and Pimentel we observe that the H_2O perturbed hydracid features lie at lower frequency than the one corresponding to polymers and are mainly constituted of two groups of bands, 100 cm^{-1} apart, hereafter refered to as C_1 and C_2, the first one being the low frequency group (Table I). Systematic dilution and annealing experiments lead to the conclusion that these bands behave differently, and thus must be assigned to different kinds of H_2O–HX complexes. The main result can be summarized in the following way: the C_1 band is the only one to appear at high M/R ratio while the C_2 group is observed for M/R values less than 200 and strongly increases upon warming the sample. As the fine structure of the C_2 bands is slightly different from HCl to HBr we shall present successively the results for each of them.

$N_2/H_2O/HCl$. The evolution of HCl spectra at constant $N_2/(HCl + H_2O)$ ratio but for several HCl/H_2O values is displayed in Figure 1 in the range 2700–2500 cm^{-1}. For a ratio greater than 500 the C_1 band at 2545 cm^{-1} is the only one to appear, even after annealing; for lower values a second band appears at 2599 cm^{-1} which vanishes upon warming the sample, then comes a third one called C_2 at 2647 cm^{-1}, the intensity of which increases if there is an excess of HCl relatively to water and after annealing. The bandwidth of the C_1 component varies noticeably according to the samples, the lowest value being 10 cm^{-1}; one of the two other bands at 2599 and 2647 cm^{-1} generally does not exceed 10 cm^{-1}.

$N_2/H_2O/HBr$. Before annealing and for high M/R values the C_1 band is observed (Figure 2) at 2282 cm^{-1}; for M/R of the order of 200 and an excess of HBr, the C_2

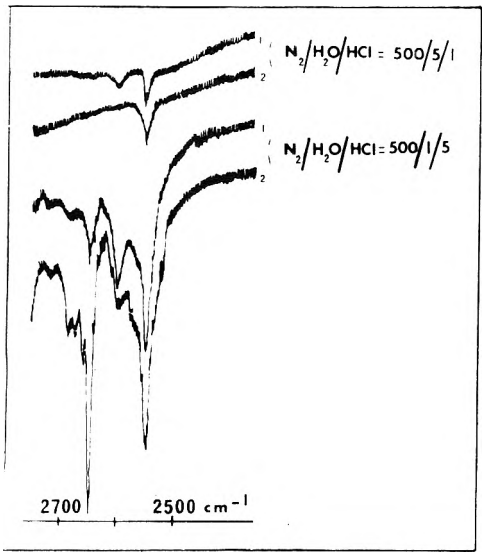

Figure 1. Infrared spectra of nitrogen matrices doped by HCl and H_2O over the spectral range 2700–2500 cm^{-1}: (1) before annealing, (2) after annealing at 33 K for 10 min.

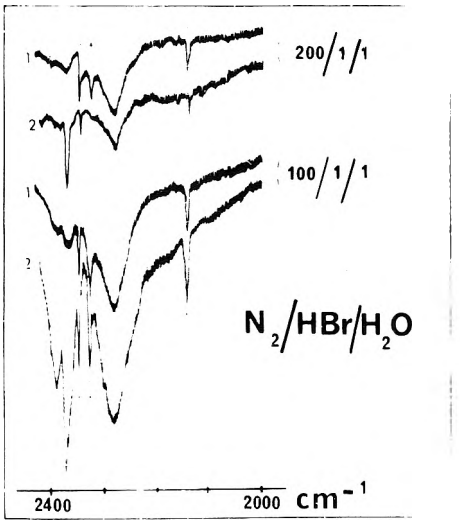

Figure 2. Infrared spectra of nitrogen matrices doped by HBr and H_2O over the spectral range 2200–2450 cm^{-1}: (1) before annealing, (2) after annealing. The starred bands are due to impurities (CO_2 or N_2).

bands are measured at 2366 and 2375 cm^{-1}. After annealing these two bands increase while for M/R less than 100 a new band is observed at 2390 cm^{-1}. Furthermore, taking advantage of the presence of HBr in DBr samples, we observed spectra of isotopically diluted HBr; all the features previously described for the pure species are still observed in these dilution experiments, except for the 2366-cm^{-1} band.

$N_2/H_2O/DBr$. The results are similar to those observed for HBr (Figure 3): the C_1 band is measured at 1657 cm^{-1} while the three C_2 bands lie at 1702, 1713, and 1726 cm^{-1}, this last one being observed at a M/R ratio less than 100.

In order to discuss the water spectra in the complexes we first recorded spectra of N_2/H_2O mixtures for various M/R ratios. These spectra are in good agreement with those previously published by Tursi–Nixon[8] and Huong-Cornut.[9] Addition of hydracid (Figure 4) gives rise in the stretching region to new bands around 3710, 3680, 3620, and 3600 cm^{-1}, the second and the last ones being split into several components. The same concentration and annealing studies as described for the HX bands lead to the conclusion that the 3710- and 3620-cm^{-1} bands are the only ones observed at high M/R ratios and high H_2O/HX

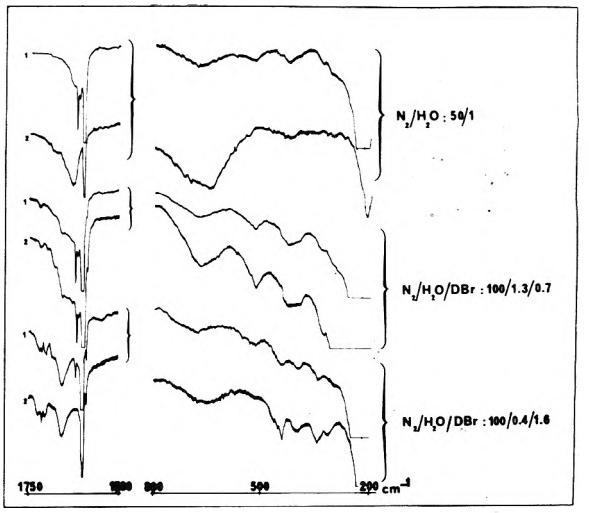

Figure 3. Infrared spectra of nitrogen matrices doped by DBr and H_2O: (1) before annealing, (2) after annealing.

values and these bands behave as the C_1 absorption of HX. On the contrary two other absorptions around 3680 and 3600 cm^{-1} occur at the same time as the C_2 bands of HX, for the previously described conditions.

In the ν_2 region, the addition of HBr or DBr causes two noticeable changes of the water spectra (Figure 5): before annealing, a well-resolved band at 1594 cm^{-1} close to the monomer band at 1597.5 cm^{-1}; after annealing another band at 1604 cm^{-1} grows in in the same time as the C_2 bands. For $N_2/HCl/H_2O$ mixtures the first band at 1594 cm^{-1} is not resolved and exists as a shoulder to the monomer band while the other is measured after annealing at 1606 cm^{-1}.

In the low frequency region (800–200 cm^{-1}) the identification of the bands due to HX–H_2O complexes is made difficult by the existence of several absorptions due to water, the intensity of which strongly varies with concentration. These bands are measured at about 218, 430, and 520 cm^{-1} for a N_2/H_2O ratio of 100 (Figure 3); at higher dilution another band at 320 cm^{-1} is also observed while after annealing two new broad bands appear at 640 and 700 cm^{-1}. All these bands are due to OH···O bending vibrations of different kinds of water polymers, except the 218-cm^{-1} component which correspond to the librational mode of the H_2O monomer.

Addition of hydracids changes only slightly the whole pattern. Even though the relative intensity of the different bands is not easily reproducible because of variations in the relative concentration of the various $(H_2O)_n$ and H_2O–HX polymers, we propose the following tentative attribution: the weak bands around 460 cm^{-1} which appear before annealing in the spectra of HCl–H_2O and HBr–H_2O mixtures and the band at 340 cm^{-1} in DBr–H_2O spectra correspond to an intermolecular mode of the complex responsible for the C_1 band; after annealing a narrow band at 275 cm^{-1} is observed in the HBr–H_2O spectra and grows in in the same time as the C_2 bands.

B. *Argon Matrices.* As already mentioned by Ayers and Pullin,[6] addition of water to Ar–HCl mixtures gives rise to a new absorption at 2663 cm^{-1} (Figure 6). At low water concentration this band is very narrow, reaching a bandwidth of 3 cm^{-1} for ^{35}Cl isotope enriched hydrochloric acid and an Ar/H_2O ratio of the order of 1000. Above 2700 cm^{-1} in the HCl polymer region, appear under some conditions new absorptions due to water–HCl complexes which have not been discussed by Ayers and Pullin. Typical spectra of HCl over the spectral range 2800–2650 cm^{-1} are displayed in Figure 6; the upper spectrum cor-

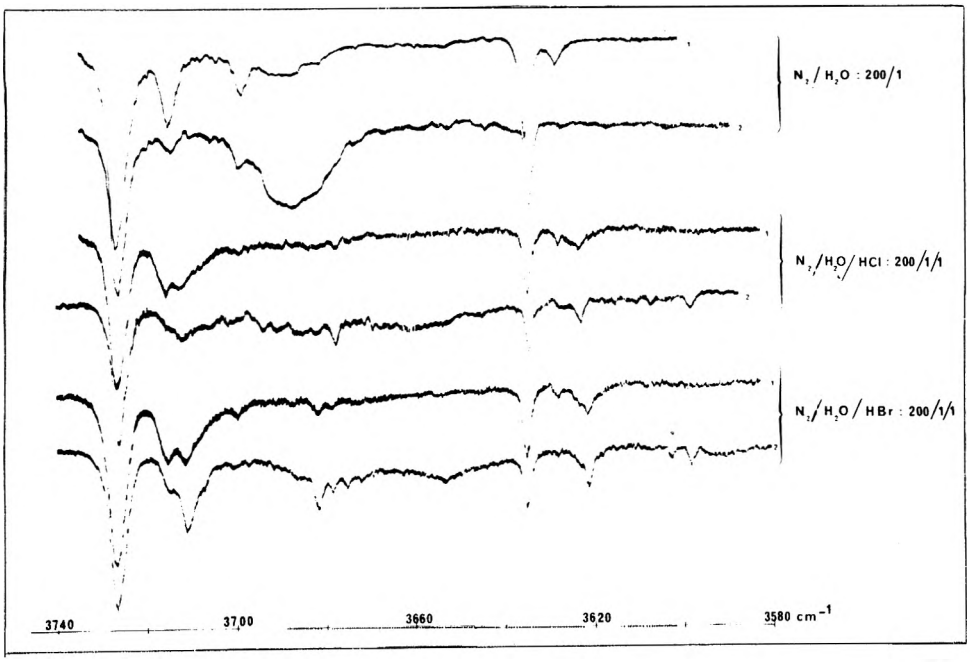

Figure 4. Infrared spectra of nitrogen matrices doped by HBr (or HCl) and H_2O over the spectral range 3730–3550 cm^{-1}: (1) before annealing, (2) after annealing.

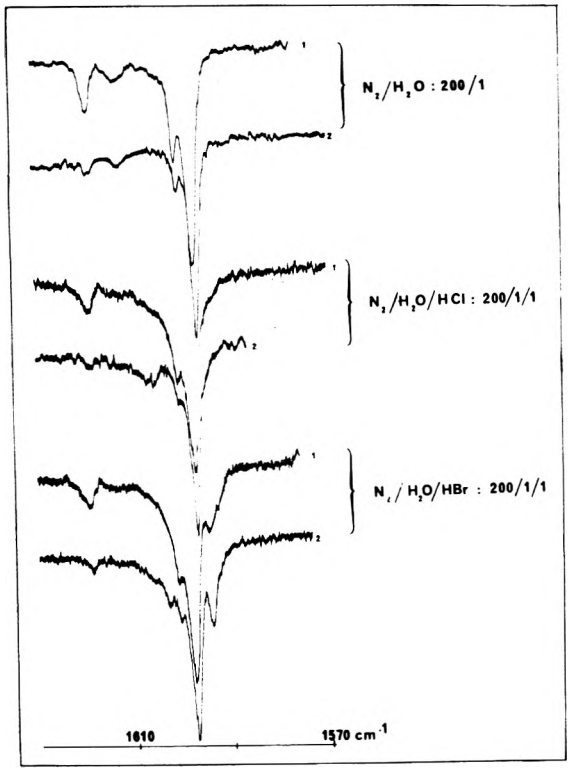

Figure 5. Infrared spectra of nitrogen matrices doped by HBr (or HCl) and H_2O over the spectral range 1630–1550 cm^{-1}.

responds to a binary mixture Ar/HCl and the others to $Ar/H_2O/HCl$ mixtures before annealing. Beyond the 2663-cm^{-1} band, addition of H_2O gives rise to new bands at 2754 and 2740 cm^{-1}, the intensity of which has been carefully studied as a function of HCl/H_2O ratio and annealing cycles. From these experiments one concludes that the 2663/2754 cm^{-1} intensity ratio decreases when the HX concentration increases relative to that of water in the matrix; furthermore the 2740-cm^{-1} band is very weak before annealing but increases appreciably after warming to 42 K for several minutes. For $Ar/H_2O/HBr$ mixtures the observations are similar. At high M/R values the main band characteristic of the $HBr-H_2O$ system is observed at 2395 cm^{-1} (Figure 7). When M/R decreases two news band appear at 2438 and 2416 cm^{-1}; the first is the stronger as the HBr/H_2O ratio increases and the second only appears after annealing.

In the water region, as pointed out by Ayers and Pullin, the spectral features due to H_2O–HX complexes are difficult to observe for two reasons, namely, the complexity of the pure water spectrum and the weakness of the new bands, especially in the ν_3 region, around 3700 cm^{-1}. As shown in Figure 8, there appear two groups of bands in the ν_1 region: the first at 3630 and 3628.5 cm^{-1} on doping with HCl or HBr, respectively, and the second at 3607–3604.5 or 3600 cm^{-1} according to the hydracid (Table II). The 3630-cm^{-1} band is the only band observed by Ayers and Pullin probably because the 3604.5–3607-cm^{-1} doublet is weaker and grows in after annealing, mainly with an excess of HCl relatively to water. In the ν_3 region the situation is far from being clear. Ayers and Pullin suggested assigning the corresponding band in the complex around 3711 cm^{-1}. We did not observe the broadening of the monomer band at 3711 cm^{-1} discussed by these authors but the appearence of a new band at 3721.5 cm^{-1} very close to another band at 3724 cm^{-1} which, in our opinion, could correspond to the ν_3 band of the oxygen perturbed molecule of the open dimer $(H_2O)_2$. Below 3700 cm^{-1} exist several weak features; two of them, at about 3700 and 3695 cm^{-1} appear in binary A/H_2O matrices and have been observed by Ayers and Pullin. Two others, near 3690 cm^{-1} seem to occur only in presence of HCl or HBr.

Finally, in the ν_2 region, addition of hydracid gives rise (Figure 9), close to the nonrotating monomer frequency, to a new band at 1590 cm^{-1} which has been already identified by Ayers and Pullin. This band is the only one we are able to attribute to H_2O–HX complexes in this region.

Analysis of Spectra

As Ault and Pimentel for N_2 and Ayers and Pullin for argon matrices previously concluded, the new low frequency absorptions in the ν(HX) region are a proof that the H_2O–HX complex involves a weak hydrogen bond.

TABLE II: H_2O Absorption Frequencies of H_2O/HX Mixtures in Nitrogen or Argon Matrices and Attribution

	H_2O/HX/N_2[a]			H_2O/HX/Ar[a]		
	HCl	HBr	DBr	HCl	HBr	Attribution[b]
ν_3	3711.5	3711	3710	3721.5?	3721?	1-1 complex
	3677+	3681+	3677+	3690+	3690.5+	
	3674+	3678+	3672+			1-2 complex + HP
		3672+				
ν_1	3622	3621	3620	3629.5	3628.5	1-1 complex
	3607+	3603+	3606+	3607+		
	3600+	3598+	3601+	3604+	3600+	1-2 complex + HP
	3595.5+	3593.5+	3591+			
ν_2	1594 sh	1594	1590	1590	1588.5	1-1 complex
	1606+	1604+				1-2 complex

[a,b] See the corresponding footnotes to Table I.

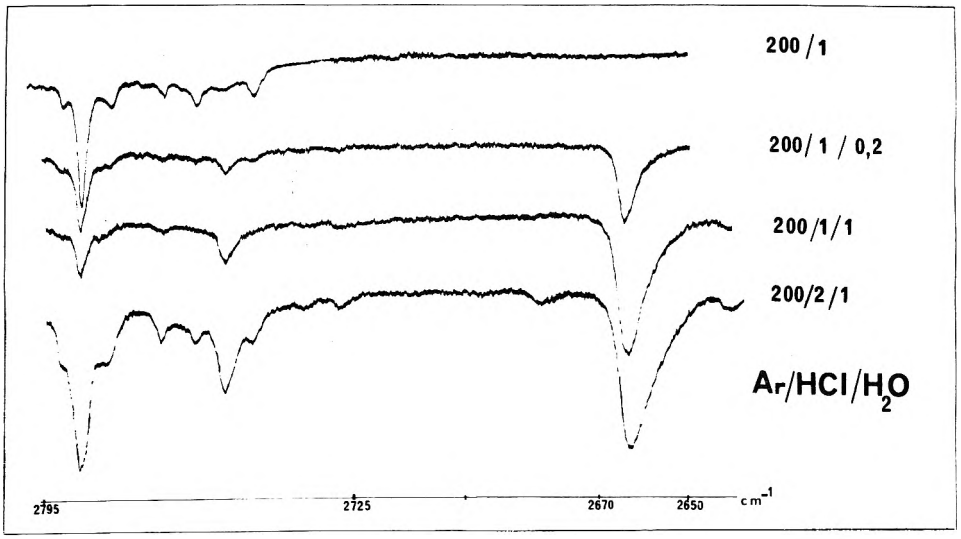

Figure 6. Infrared spectra of argon matrices doped by HCl and H_2O over the spectral range 2800–2650 cm^{-1}.

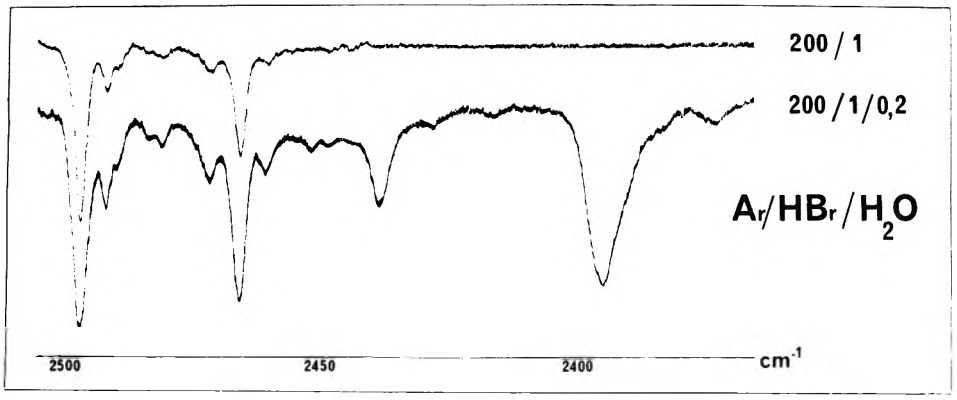

Figure 7. Infrared spectra of argon matrices doped by HBr and H_2O over the range 2500–2350 cm^{-1}.

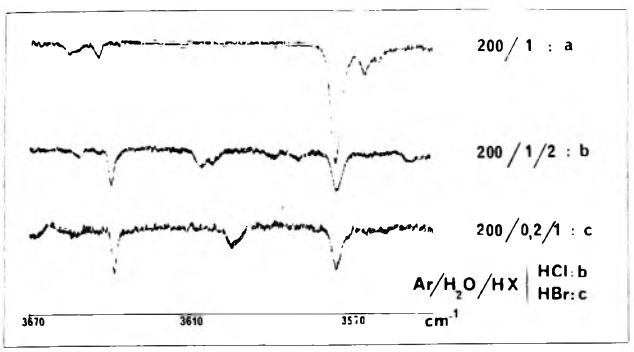

Figure 8. Infrared spectra of argon matrices doped by HBr (or HCl) and H_2O over the spectral range 3640–3570 cm^{-1}.

From our results two new questions arise, one related to the band multiplicity, the other to the strong matrix shift from argon to nitrogen.

At high dilution of both doping species, the water–hydracid interaction is characterized by only one band in the HX region and two bands in the OH stretching region; these three bands are attributed to ν(HX), ν_3(···OH_2), and ν_1(···OH_2) of the one-to-one complex H_2O···HX. In N_2 matrices ν_3 and ν_1 are respectively observed at 3710 and 3620 cm^{-1} and are very close to the corresponding vibration of the oxygen perturbed molecule in the $(H_2O)_2$ dimer (3714 and 3627 cm^{-1}, according to Tursi and Nixon[8]). This analogy is strong support for the existence of open water dimers in nitrogen matrices. In argon matrices the cor-

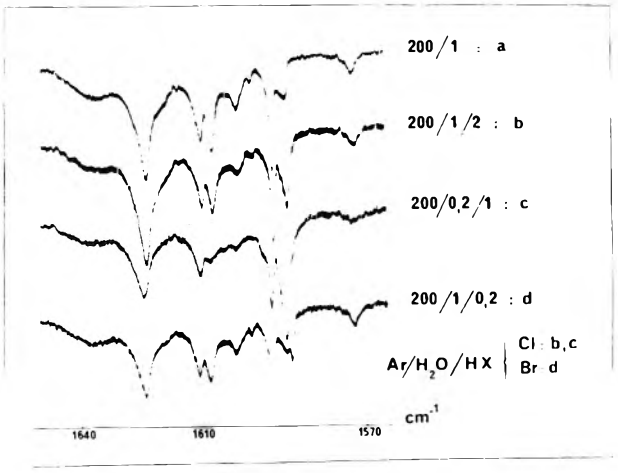

Figure 9. Infrared spectra of argon matrices doped by HBr (or HCl) and H_2O over the spectral range 1630–1570 cm^{-1}.

responding ν_3 and ν_1 bands of the complex lie at 3721 and 3630 cm^{-1} (Table II).

The appearence of new bands after annealing or at low M/R ratios clearly means there exist other possibilities of interaction between water and hydracid molecules, leading to higher states of aggregation. The sharpness of the corresponding bands, sometimes sharper than the 1–1 complex, allows one to conclude that other well-defined complexes $(H_2O)_m(HX)_n$ can be obtained in matrices, m or n being greater than one. The discussion of the respective values of m and n is based upon the experimental observation that the corresponding bands occur for H_2O/HX ratios less than one. This remark suggests that n is greater than m and the simplest formula is $H_2O(HX)_2$, for which one can imagine three different structures: a linear $H_2O\cdots HX\cdots HX$, a cyclic

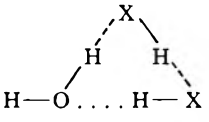

or a bifid structure

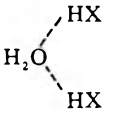

In the linear case the water perturbation is expected to stay in the same range of magnitude as in the 1–1 complex; on the other hand, it is likely that the end of chain HX frequency will be found in the HCl polymer range 2800–2700 cm^{-1} and that of central HX at lower frequency than in the 1–1 complex since this molecule is perturbed on both ends. This last remark eliminates such a model since one does not observe any absorption below that of the 1–1 complex.

In the cyclic form of the trimer, which corresponds to the structure of $(HCl)_3$ in an argon matrix[10] one OH bond of the water molecule is involved in a hydrogen bond as a hydrogen donor and acceptor at the same time, which would lead to a strong perturbation of this vibrator; this situation does not correspond to the description of the spectrum where only weak perturbations in the ν_3 and ν_1 regions have been detected.

In the last 1–2 complex model, the water perturbation is expected to be slightly stronger than in the 1–1 complex and quantum chemistry calculations (see below) show that the HCl perturbation is weaker. Experimental data are in good agreement with the third model which, however, cannot explain the fine structure of the corresponding ν_3 and $\nu_1(H_2O)$ bands.

The second question which is raised by the comparison between nitrogen and argon results is the strong matrix effect on the HX frequencies of the different complexes; indeed for HCl the relative frequency shifts $\Delta\nu/\nu_{gas}$ are 11.7 and 7.6% for the 1–1 and 8.2 and 4.8% for the 1–2 complex for N_2 and Ar matrices, respectively. Thus the nature of the surroundings plays an important role on the properties of the complexes. Two explanations can be invoked: (i) steric constraints are stronger in N_2 than in Ar lattice and impose a shorter O···X distance in the first case, and thus a greater ν(HX) shift; (ii) specific HX–N_2 interaction increases the HX perturbation.

The second explanation has been experimentally checked by adding a few percent of N_2 to an argon matrix containing 0.5% HCl and 0.5% H_2O. The HCl spectrum is strongly modified in the range 2700–2800 cm^{-1}, as already discussed;[11] furthermore the 2663-cm^{-1} band of the complex HCl–H_2O in argon is accompanied by a second band at 2640 cm^{-1} due to some kind of trimer H_2O–H-Cl–N_2. Thus it is clear that there is a specific interaction in HCl–N_2 modifying the spectroscopic properties of the HCl molecule in the H_2O–HCl complex.

Semiempirical Calculations on the HCl–H_2O and $(HCl)_2H_2O$ Complexes

A quantitative analysis of these experimental data has been undertaken following two different methods: the use of the Lippincott–Schroeder potential,[11] in order to relate frequency shift and intermolecular distance R(O···Cl) of the 1–1 complex; the use of the semiempirical quantum chemistry MINDO/3 method to discuss both the geometry and ν(HCl) frequency in the 1–1 and 1–2 complexes.

The Lippincott–Schroeder potential has already been used by Lassègues et al.[12] to study dimethyl ether–HCl complexes in various physical states. We kept the Lassègues values of the parameters; the variation with the intermolecular distance R(O···Cl) of the HCl force constant ratio K/K_0, where K_0 is the gas force constant (5.15 mdyn $Å^{-1}$), is shown in Figure 10. From this graph the O···Cl distance of the 1–1 complex in the argon matrix, which corresponds to a ν(HCl) frequency of 2663 cm^{-1}, is found equal to 3.14 Å.

In a recent study on the hydrogen chloride dimer[13] we have shown that the MINDO/3 semiempirical method[14] provides satisfactory predictions of molecular properties such as intramolecular distances and intermolecular angles, though it fails to reproduce the experimental equilibrium distance. In order to find an interpretation of the important ν(HX) frequency shifts observed in the spectra of the 1–1 and 1–2 complexes we have calculated relevant geometries and force constants by this method.

The calculation technique has already been described[15] and stretching force constants computed in this way agrees generally within 15% with the experimental values. In the present case we first computed the force constant K_e of an isolated HCl molecule and found 4.97 mdyn $Å^{-1}$; then, for each complex, geometry optimization and force constant calculation were carried out for selected O···Cl intermolecular distances in the range 3.0–3.2 Å. The 1–1 complex is found pyramidal, with a C_s symmetry, and the following geometrical parameters: H–Cl distance of 1.24 Å (instead of 1.23 Å for the monomer), angle θ between the H_2O plane and HCl of 117°; furthermore the H_2O geometry remains unchanged. The 1–2 complex is found to have the highest possible symmetry, i.e., C_{2v}, with the same parameters as for the 1–1 complex. We calculated OH and HCl stretching force constants for the two

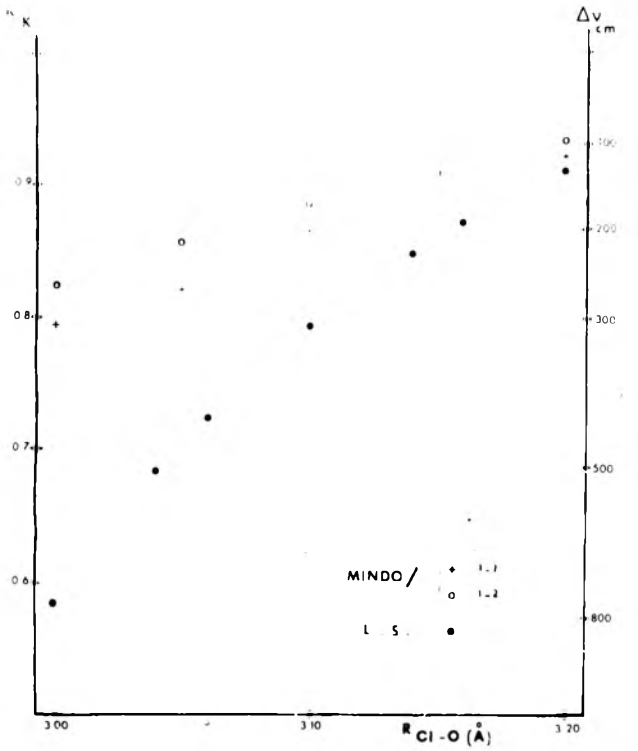

Figure 10. Relative changes of the force constant and frequency of HCl with O···Cl distance as calculated by the Lippincott–Schroeder potential and the MINDO/3 method.

complexes. In both cases the OH force constant is found very slightly perturbed and corresponding to a frequency red shift of about -15 cm^{-1}, which is the correct range of magnitude, while the evolution of the HCl force constant relative to the gas value as a function of the O···Cl distance is shown in Figure 10.

The discussion of these results is divided in two parts: the first related to the geometry and the second to the HX frequency of the complexes.

(i) *Geometry of the Complexes.* The results related to the 1–1 complex appear somewhat contradictory with the ab initio calculation of Kollman and Allen[4] on hydrogen fluoride–water dimer for which the equilibrium geometry is planar. Indeed the substitution of HF by HCl is expected not to strongly modify the structure of the complex and one can wonder what the reason for this difference is. In the same paper Kollman and Allen, using the same basis set (10s, 5p GLF on O and F, 5s, 1p on H) predict for $(HF)_2$ an angle between HF molecular axes of 160° instead of 120° as found experimentally.[16] It has been shown in the case of NH_3[17] and H_3O^+[18] that molecular geometries may be considerably improved when the basis set involves d functions for the second row atom and a recent calculations on the HF dimer[19] support this conclusion. On the other hand, minimal basis set calculations and semiempirical methods using ZDO approximation satisfactorily predict angle values in the preceding examples. For these reasons we believe that the pyramidal structure found for the 1–1 H_2O–HX complex by the MINDO/3 method is realistic.

(ii) *HCl Frequency.* The MINDO/3 calculations qualitatively agree with our experimental analysis on the following point: the HCl frequency is higher in the 1–2 than in the 1–1 complex; but the frequency difference is calculated 2.5 times smaller than observed. The discrepancy could be explained by an increase in the O···Cl distance from the 1–1 to the 1–2 complex.

On the other hand, Figure 10 clearly shows the discrepancy between the results of the Lippincott–Schroeder and MINDO/3 methods to relate HCl frequency and O···Cl distance. For instance the O···Cl distance in the 1–1 complex imbedded in an argon matrix is found equal to 3.09 Å by MINDO/3 instead of 3.14 Å by the LS potential. The situation is still worse for stronger HCl perturbations; for instance, for an O···Cl distance of 3 Å, the predicted ν(HCl) shift is of the order of 350 cm^{-1} by MINDO/3 and 800 cm^{-1} by the LS potential; according to Lassègues[12] this last value corresponds to the possibility of proton transfer, i.e., to the formation of an O–H$^+$···Cl$^-$ structure. The occurence of proton transfer at 3 Å can be discussed in the light of x-ray data on hydrogen chloride hydrates extensively studied by Lundgren and Olovsson.[20,21] In the case of the trihydrate for instance these authors observe the formation of the ion pair $H_5O_2^+Cl^-$ with O···Cl distances equal to or greater than 3.01 Å. Thus possibility of proton transfer for O···Cl distances of 3 Å seems to be realistic and suggests that the Lippincott–Schroeder potential gives a better correlation (ν(HCl) shift–O···Cl distance) than the MINDO/3 calculation.

Conclusion

IR spectra of H_2O–HCl and H_2O–HBr complexes in argon and nitrogen matrices have been extensively reinvestigated; annealing and concentration effects lead to the conclusion that there are several kinds of complexes; two of them are identified: the one, H_2O–HX, already described by Ault[5] and Ayers[6] is mainly observed before annealing; after annealing another one is observed, which corresponds to a higher state of aggregation. The corresponding frequency and intensity evolution with HX/H_2O concentration ratio are compatible with the structure of a 1–2 complex, in which each oxygen electron lone pair is involved in an hydrogen bond with an HX molecule. For both species a strong matrix effect is observed, the nitrogen being more perturbing than the argon. From mixed Ar–N_2 matrix experiments one concludes that there exist a specific interaction between N_2 and HCl molecules, as already analyzed in a previous publication.[3]

The structure of the complexes and the correlation between the O···Cl distance and HCl frequency have been discussed according to two semiempirical methods: MINDO/3 calculation which concludes a pyramidal shape with C_s symmetry for the 1–1 and a C_{2v} symmetry for the 1–2 complex, the ν(HCl) frequency being higher in the 1–2 than in the 1–1 complex. The correlation between HCl frequency and O···Cl distances has been studied using both Lippincott–Schroeder and MINDO/3 techniques. The first seems to give better results, with the possibility of proton transfer for a O–Cl distance around 3 Å.

Acknowledgment. The authors are grateful to Pr M. L. Josien for valuable discussions on the present work and for critical readings of the manuscript.

References and Notes

(1) H. Friedmann and S. Kimel, *J. Chem. Phys.*, **43**, 3925 (1965).
(2) C. Girardet and D. Robert, *J. Chem. Phys.*, **59**, 5020 (1973).
(3) D. Maillard, J. P. Perchard, A. Schriver, C. Girardet, and D. Robert, *J. Chem. Phys.*, in press.
(4) P. A. Kollman and L. C. Allen, *J. Chem. Phys.*, **52**, 5085 (1970).
(5) B. S. Ault and G. C. Pimentel, *J. Phys. Chem.*, **77**, 57 (1973).
(6) G. P. Ayers and A. D. E. Pullin, *Spectrochim. Acta, Part A*, **32**, 1641 (1975).
(7) D. Maillard, A. Schriver, J. P. Perchard, C. Girardet, and D. Robert in "Molecular Spectroscopy of Dense Phases", Elsevier, 1976, p 337.
(8) A. J. Tursi and E. R. Nixon, *J. Chem. Phys.*, **52**, 1521 (1970).
(9) P. V. Huong and J. C. Cornut, *J. Chim. Phys.*, **72**, 534 (1975).
(10) J. B. Davies and H. E. Hallam, *Trans. Faraday Soc.*, **67**, 3176 (1971).
(11) E. R. Lippincott and R. Schroeder, *J. Phys. Chem.*, **61**, 921 (1957).
(12) J. Lascombe, J. C. Lassègues, and P. V. Huong, *J. Phys. Chem.*, **77**, 2779 (1973). See also J. C. Lassègues, Thèse de doctorat es Sciences, Bordeaux, 1972.

(13) D. Maillard and B. Silvi, to be submitted for publication.
(14) R. C. Bingham, M. J. S. Dewar, and D. H. Lo, *J. Am. Chem. Soc.*, **97**, 1285 (1975).
(15) B. Silvi, *Spectrochim. Acta*, in press.
(16) T. R. Dyke, B. J. Howard, and W. Klemperer, *J. Chem. Phys.*, **56**, 2442 (1972).
(17) J. D. Petke and J. L. Whitten, *J. Chem. Phys.*, **59**, 4855 (1973).
(18) M. Allavena and E. Leclech, *J. Mol. Struct.*, **22**, 265 (1974).
(19) D. R. Yarkony, S. V. O'Neil, H. F. Schaefer, C. P. Baskin, and C. F. Bender, *J. Chem. Phys.*, **60**, 855 (1974).
(20) J. O. Lundgren and J. Olovsson, *Acta Crystallogr.*, **23**, 966 (1967).
(21) J. O. Lundgren and J. Olovsson, *Acta Crystallogr.*, **23**, 971 (1967).

Water and OH Groups in Zeolite ZK-5, Studied by Nuclear Magnetic Resonance

Wolf D. Basler

Institute of Physical Chemistry of the University of Hamburg Laufgraben 24, 2000 Hamburg 13, West Germany *(Received May 13, 1977)*

Proton NMR relaxation times and intensities have been measured from −70 to 100 °C for water and OH groups in original and sodium-exchanged ZK-5 zeolite. In original ZK-5 two-phase behavior of the transverse relaxation has been observed. Assuming fixed OH groups and mobile water molecules, calculated intensities and relaxation times are in agreement with the observed values. Proton exchange takes place within 1 ms at room temperature; the activation energy of the exchange reaction is roughly 3 kcal/mol. In NaZK-5 there are less than two OH groups per unit cell, if any at all, as only one single exponential relaxation was found after ion exchange. The temperature dependence of the relaxation times (T_1 and T_2) shows that water in the cages of NaZK-5 behaves similarly to water in the supercages of faujasites and A-type zeolites. These results confirm earlier conclusions that the two-phase behavior in faujasites and zeolite A originates from water inside the sodalite units.

Introduction

Recent NMR studies of water in faujasite-type zeolites showed two-phase behavior of the proton magnetic resonance, indicating two different species of protons, which were attributed to water molecules in the two different intracrystalline cavities of the faujasite framework (supercages and sodalite cages).[1-3] Furthermore, it was observed that partial hydrolysis of the alumosilicate framework produced a NMR signal of comparable intensity and about twice as long as the transverse relaxation time of water molecules in the sodalite cages.[1] Thus the proton NMR signal of faujasites exposed to water can be composed of three parts, two of which are quite similar, i.e., those originating from the OH groups of the hydrolysis products and of the water molecules in the sodalite cages.

By further investigation of sodium–faujasites we found that the water molecules are penetrating relatively slowly from the supercages into the sodalite cages (half-times up to several months), which allowed preparation of faujasites, which contained water exclusively in the supercages. The proton NMR relaxation of these zeolites was only one single exponential; a possibly superimposed signal of water in the sodalite cages or of OH protons could not be observed at a detection limit of 1%.[4,5]

From this one can conclude that the usual pretreatment of outgassing at 400 °C until the pressure is less 10^{-5} Torr for 12 h, followed by sorption using water vapor, leaves the alumosilicate framework of sodium–faujasites essentially unchanged and the fraction of protons in OH groups and products of hydrolysis must be less the experimental upper limit of 1%.

If one removes sodalite cages from zeolite structures, one should eliminate the NMR relaxation of water occluded in sodalite cages and the NMR relaxation of those zeolites is expected to be a single exponential, if they are intact after sorption of water. On the other hand, those zeolite structures without sodalite cages should be well suited to study OH groups and hydrolysis in large-pore zeolites by proton NMR, as the disturbing signal from the water molecules in the sodalite cages is absent. This work was done to test and to verify this thesis.

Zeolite structures containing large cavities but no sodalite cages are those of zeolite Rho and of ZK-5. In this paper we report NMR studies of protons in ZK-5 loaded with water after various pretreatments.

The structure of zeolite ZK-5, first synthesized by Kerr,[6,7] was determined by Meier and Kokotailo.[8] It is related to zeolite A, as it is composed of the same large cavities (α cages or truncated cubooctahedra) as zeolite A, but they are joined through double six-membered rings in a body-centered array. The remaining volume is occupied by smaller cavities (γ cages) which are entered from the larger cavities by near planar eight-membered rings. The whole pore system consists of two independent three-dimensional channel systems, where the access is restricted by the eight-membered rings of 3.9 Å free diameter.

In contrast to zeolite A and faujasites, where the access from the large cavities into the sodalite units is controlled by the smaller six-membered rings, the whole intracrystalline channel system (α and γ cages) of ZK-5 can be compared with that of the large cavities of zeolite A, for in both cases the accessibility is given by the eight-membered rings.

As that fraction of water, which is sorbed in the large cavities of NaA, behaves like a mobile intracrystalline fluid and shows a single exponential proton NMR relaxation, the same is expected for all the water in NaZK-5.

Experimental Section

The original ZK-5 powder was synthesized by the method of Kerr[7] with a composition $(0.55R, 0.45Na_2)$-$OAl_2O_3 4.81SiO_2$, where R is the double-charged organic cation 1,4-dimethyl-1,4-diazoniabicyclo[2.2.2]octane. The iron content was about 80 ppm.

To obtain a zeolite with only sodium ions (NaZK-5), the following treatments were done: (1) burning the organic cation by heating to 450 °C for 24 h with access to air; (2) rehydration by storing several days over saturated ammonium chloride solution of 80% relative humidity; (3) outgassing at 400 °C until the pressure was less 10^{-5} Torr

for 12h; (4) rehydration; (5) cation exchange by stirring 1 g of ZK-5 in 1 L of 0.1 N NaOH for 12 h at room temperature; (6) rehydration. After each step x-ray powder measurements were done and compared with the data from Meier and Kokotailo.[8] All listed diffraction lines and only these were found. Treatments 1–6 only slightly changed the relative intensities; no loss of crystallinity was observed.

The pulsed proton NMR measurements were done at 60 MHz using a Bruker B-KR 322 spectrometer and conventional pulse sequences. The amount of sorbed water is given in milligrams of water per gram of outgassed zeolite or in molecules per unit cell (uc) which is four α and four γ cages.

Results and Discussion

By thermal treatment (step 1) essentially all the organic cations were removed. The loss of weight by outgassing after rehydration (steps 2 and 3) was ~298 mg/g and the water uptake after outgassing was found to be the same within an experimental error of 1 mg/g.

By steps 1–4 the organic cations are replaced by protons giving OH groups. This product will be called (H,Na)ZK-5 and contains 12 sodium ions and 16 OH groups per unit cell.

By step 5 these OH groups were effectively exchanged with sodium ions, giving NaZK-5. By chemical analysis the ratio Na/Al was found to be 0.985 ± 0.03. Therefore, NaZK-5 has less than one OH group/uc if any at all. By pulsed proton-NMR the following results were obtained:

A. *(H,Na)ZK-5 Outgassed.* After burning and outgassing (steps 1–3) a remaining proton NMR signal was observed, the intensity of which corresponded to 2 ± 0.5 OH groups/uc. This means that under the outgassing conditions (400 °C, pressure less 10^{-5} Torr for 12 h) 90% of the OH groups were removed.

B. *(H,Na)ZK-5 with Water.* The outgassed (H,Na)-ZK-5 was loaded with 100 mg of water/g while any heating was avoided by slow sorption (30 min) and cooling with a water–ice bath. Ten minutes after the end of sorption the transverse relaxation showed two-phase behavior. Beside a slow decaying signal of the more mobile water molecules with relative intensity I_A = 74 ± 3% and transverse relaxation time T_{2A} = 0.5 ± 0.1 ms, a second fast decaying signal was observed with I_B = 26 ± 3% and T_{2B} = 50 ± 10 μs.

The same was found for full water loading (298 mg/g for p/p_0 = 0.80) with I_B = 8 ± 2%. As the longitudinal relaxation was a single exponential with T_1 = 14 ± 1 ms, the exchange between the two species of protons must be in the range of milliseconds.

To prove that the fast decaying signal originates from the protons of the OH groups, we calculated intensity I_B and relaxation time T_{2B} under the following assumptions: (1) The concentrations of OH groups is equal to the deficit of sodium ions for Na/Al = 1. This means that burning the organic cation gives two OH groups. It follows from the chemical composition that there are 16 OH/uc. (2) The OH groups are immobile on the NMR time scale (10^{-5} s) and the transverse relaxation time T_{2B} is given by static dipole–dipole interaction of the proton with the aluminum nuclei and other OH groups:

$$1/T_{2B} = 1/T_{H-Al} + 1/T_{H-H}$$

The influence of the water molecules is neglected since this effect will be of the same order of magnitude as the intramolecular relaxation time of these water molecules, which is 10–100 ms by motional averaging. As the OH groups are immobile, relaxation by paramagnetic centers (Fe^{3+}) can be neglected, too.

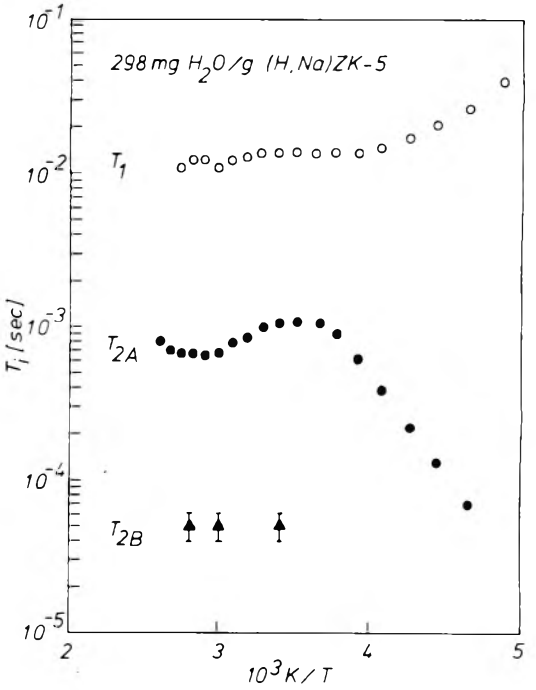

Figure 1. Arrhenius plot of the transverse relaxation times T_{2A} of water protons (●), T_{2B} of OH groups (▲), and of the longitudinal relaxation time T_1 (○) of all protons. Zeolite (H,Na)ZK-5 with 298 mg of water/g.

Taking a proton–aluminum separation of 2.2 Å used by Resing[1] gives T_{H-Al} = 70 μs. T_{H-H} is calculated to be 210 μs, using the formula of Oehme et al. for a statistical distribution of the OH groups.[9] This results in T_{2B} = 52 μs.

Both the experimental values for concentration (17 ± 2 OH/uc) and relaxation time T_{2B} (50 ± 10 μs) are in agreement with the calculated values.

A first inspection of the sample with 100 mg of H_2O/g showed that for temperatures up to 80 °C the transverse relaxation still showed two-phase behavior. To obtain further information about the exchange rate between the water molecules and the OH groups, the transverse (T_{2A}) and the longitudinal (T_{1A}) relaxation time of the water protons were measured for full loading (298 mg/g) in the temperature range from −70 to 110 °C. The results are shown in Figure 1 as the usual Arrhenius plot of log T_i against the reciprocal absolute temperature. The temperature dependence of T_{2A} shows a maximum at about 10 °C and a minimum at about 80 °C indicating exchange with the rapidly relaxing OH groups. Applying the NMR theory of relaxation of two phases[10] to this case with an only small, but fast relaxing fraction (e.g., the protons of the OH groups)[1,11] we can draw the following conclusions:

(1) In the region of slow exchange below 10 °C the observed T_{2A} is the true intrinsic relaxation time of the protons of the more mobile water molecules. As the relaxation is essentially given by diffusion to the paramagnetic Fe^{3+} ions in zeolites with 80 ppm iron content[3] an energy of activation of the motional correlation time, which is roughly that of the diffusion, of 5.8 kcal/mol can be deduced from the slope of log T_{2A} with reciprocal temperature. Assuming equal jump lengths, the diffusion coefficient is about the same as in faujasites and A-type zeolites, for the absolute values can be compared, given the same concentration of paramagnetic Fe^{3+}.

(2) In the region of intermediate exchange (10–80 °C) T_{2A} is the mean lifetime of a proton the phase of the water molecules. It follows from Figure 1 that the mean lifetime is 1 ms at room temperature and an energy of activation of the exchange reaction of roughly 3 kcal/mol (with an

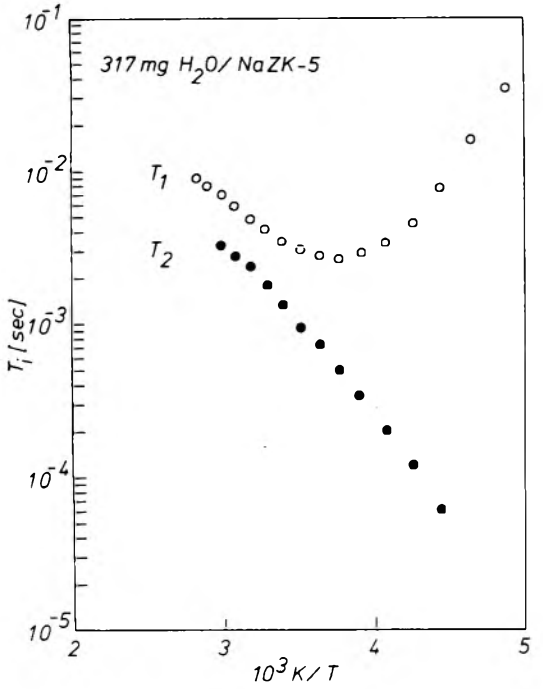

Figure 2. Arrhenius plot of the transverse T_2 (●) and longitudinal T_1 (○) relaxation times of water protons in zeolite NaZK-5 with 317 mg of water/g.

error up to 50% as the slope is not well defined) is found. By extrapolation it is seen that the mean lifetime is always shorter than T_{1A} which means that there is rapid exchange on the T_1 time scale. This is in agreement with the observation of a single exponential T_1 in the whole range from −70 to 110 °C.

(3) The T_{2A} values above 80 °C indicate the beginning of fast exchange on the T_2 time scale, but it is not reached fully and the transverse relaxation is still composed of two parts at 110 °C.

C. *NaZK-5 Outgassed.* After ion exchange of (H,Na)ZK-5 giving NaZKk-5 with Na/Al = 0.985 ± 0.03 this zeolite was outgassed under the same conditions. No proton signal was observed at a detection limit of 0.1 OH/uc. This is less than 5% of the intensity found in (H,Na)ZK-5 and complete replacement of OH groups by sodium ions can be assumed under mild conditions of ion exchange (0.1 N NaOH, 22 °C).

D. *NaZK-5 with Water.* The proton NMR relaxation of NaZK-5 with full water loading (317 ± 5 mg/g at p/p_0 = 0.80) was, as expected, a single exponential with relaxation times T_1 and T_2 similar to those of water in the large cavities of faujasites and A-type zeolites and to T_{1A} and T_{2A} of (H,Na)ZK-5. The temperature dependence is shown in Figure 2. A T_1 minimum is observed at −10 °C which is close to the temperature found for water in faujasites. Thus water in faujasites and NaZK-5 have the same mobility. The Arrhenius plot of T_2 shows a nearly straight line. No maximum and minimum are present.

The ratio $T_1/T_2 = 5$ at the minimum of T_1 shows that the motion of the water molecules cannot be described by a single correlation time, but a distribution of correlation times must be used.[12] By this, the slope of log T_2 vs. reciprocal temperature is changed less than the slope of log T_1 and from the slope of T_2 a mean activation energy of 5.7 ± 0.5 kcal/mol is found for the motional correlation time and hence for the diffusion. Similar values were found for water in faujasites.[13,14]

TABLE I: Effect of Ion Exchange on Number and Relaxation Times of OH Groups and Water Molecules as Studied by Proton NMR of ZK-5 (T = 295 K)

Zeolite	(0.45Na,0.55H)ZK-5		NaZK-5
Sorption of Water			
Rel. pressure p/p_0	$<10^{-6}$ at 400 °C	0.80	0.80
Amount, mg/g	100 ± 5	298 ± 3	317 ± 5
H_2O/uc	34 ± 2	25.3 ± 0.3	114 ± 2
Fraction of Immobile Protons			
% of NMR signal	100	26 ± 3	8 ± 2	<1
OH/uc (calcd)		16	16	<1
(expt)	2 ± 0.5	17 ± 2	17 ± 4	<2
T_{2B}, μs (calcd)	70	52	52	
(expt)	70 ± 20	50 ± 10	50 ± 10	
Fraction of Mobile Protons			
% of NMR signal		74 ± 3	92 ± 2	>99
H_2O/uc		25 ± 2	93 ± 3	114 ± 2
T_{2A}, ms		0.5 ± 0.1	1.1 ± 0.1	1.4 ± 0.1
T_{1A}, ms			14 ± 1	3.5 ± 0.2
Activation energy for diffusion kcal/mol			5.8 ± 0.5	5.7 ± 0.5

As a possible fast decaying component must have an intensity of less than the experimental error of 1%, we conclude that NaZK-5 has less than two OH groups per unit cell, in agreement with the ratio Na/Al = 0.985 ± 0.03 and the assumption that all aluminum belong to the zeolite framework.

All results are summarized in Table I.

Conclusions

By the purely exponential proton NMR relaxation of water in NaZK-5 it is proven that the fast decaying signal observed in faujasites and NaA originates from water in the sodalite units, since the conditions of outgassing and loading were the same and the structures of the alumosilicate framework are closely related.

Further, it is proposed that zeolites such as ZK-5 and probably Rho are well suited to study of OH groups and hydrolysis in large-pore zeolites, especially by NMR, since the otherwise disturbing signal from the water molecules in the sodalite units of faujasites and A-type zeolites is absent here.

Acknowledgment. The author thanks Dr. G. Kerr, Mobil Oil, Princeton, N.J., for helpful discussions and the "Deutsche Forschungsgemeinschaft" for its support of this work.

References and Notes

(1) J. S. Murday, R. L. Patterson, H. A. Resing, J. K. Thompson, and N. H. Turner, *J. Phys. Chem.*, **79**, 2674 (1975).
(2) H. Pfeifer, *Surface Sci.*, **52**, 434 (1975).
(3) W. D. Basler, H. Lechert, and H. Kacirek, *Ber. Bunsenges. Phys. Chem.*, **80**, 451 (1976).
(4) W. D. Basler, *ACS Symp. Ser.*, **No. 34**, 291 (1976).
(5) W. D. Basler, *ACS Symp. Ser.*, **No. 40**, 335 (1977).
(6) G. T. Kerr, *Science*, **140**, 1412 (1963).
(7) G. T. Kerr, *Inorg. Chem.*, **5**, 1539 (1966).
(8) W. M. Meier and G. T. Kokotailo, *Z. Kristallogr.*, **121**, 211 (1965).
(9) W. Oehme, D. Freude, and H. Schmiedel, *Z. Phys. Chem. (Leipzig)*, **255**, 566 (1974).
(10) J. R. Zimmerman and W. E. Britten, *J. Phys. Chem.*, **61**, 1328 (1957).
(11) D. E. Woessner and J. R. Zimmerman, *J. Phys. Chem.*, **67**, 1590 (1963).
(12) H. A. Resing, *J. Chem. Phys.*, **43**, 669 (1965).
(13) H. Pfeifer, A. Gutsze, and S. P. Shdanov, *Z. Phys. Chem. (Leipzig)*, **257**, 721 (1976).
(14) J. Kärger, *Z. Phys. Chem. (Leipzig)*, **248**, 27 (1971).

The Role of Site Mobility in Determining Potentiometric Selectivity of Liquid Ion-Exchange Membranes

Frederick S. Stover and Richard P. Buck*

William R. Kenan Jr. Laboratories of Chemistry, University of North Carolina, Chapel Hill, North Carolina 27514 *(Received May 11, 1977)*

Results of digital stimulation of partially associated liquid ion-exchange membranes with varying site mobility are presented. The membrane is assumed to be ideally permselective and completely electroneutral. The bathing solutions correspond to the biionic case with one complexing and one noncomplexing counterion. Selectivity toward the associated counterion, as computed from biionic potentials, is compared with changes in the site and complex mobility. The decrease in the selectivity with decreasing site mobility is found to arise from changes in both interfacial and diffusional potential components. Examination of concentration profiles and internal electric field strengths leads to descriptions of the process by which the selectivity is altered.

Introduction

To evaluate the factors which affect potentiometric selectivities of liquid ion exchangers, we have investigated the role of site mobility and effects of complexation equilibria involving mobile sites. It is a well known theoretical result[1] that steady state membrane potentials for completely dissociated, liquid ion-exchange membranes are independent of site mobilities. The response function has the same form as that derived for fixed site membranes. Site mobility affects the selectivity only when the sites are mobile and are ion paired to some degree with at least one of the counterions. Ion pairing introduces a dependence of selectivity not only on site mobility, but also on the mobility of the complex.[2,3]

Over the last 10 years, major developments have been made in the theory for relating electrical properties of mobile site ion-exchange membranes to measurable physicochemical parameters. Studies by Conti and Eisenman,[1] and Sandblom, Eisenman, and Walker[2,3] have given analytical descriptions of effects of system parameters (single ion extraction coefficients, mobilities, and complex formation constants) on potentiometric selectivities. By solving the Nernst–Planck transport equations for ions with the same absolute charge, they derived expressions for the steady state membrane potential of completely dissociated and strongly associated systems in terms of bathing solution activities and system parameters. Mathematical complexities prevent the attainment of completely general, closed form solutions. In this laboratory, we have turned to techniques of digital simulation[4-6] to characterize fully the potentiometric behavior of ion-exchange membranes, over a wide range of ion pairing conditions.

Recently, we developed an algorithm which can simulate the electrical response of permselective liquid ion-exchange membranes for all degrees of ion pairing between a trapped, mobile site and up to two counterions.[7] All ions must be univalent and obey ideal chemical equilibrium laws for ion pair formation. The membrane is assumed to be completely electroneutral and thus static, diffuse space charge is eliminated inside the membrane. Proper accounting of interfacial potentials is taken by using a Nernstian calculation.

Model

Input to the computer program includes total site concentration, complex formation constants for each counterion, activities of each counterion in the test and reference bathing solutions, mobilities and charges of all species, and the current density. Single ion extraction coefficients, k, and activity coefficients, γ, are taken to be unity to simplify the results. The bathing solution activities conform to the biionic case. The test solution is composed of pure salt N^+Y^- at an activity of 1, while the reference solution is composed of equal activity in the pure salt M^+Y^-. The membrane is assumed to be ideally permselective so that only cations may cross the interfaces. The mobile ion-exchange site is designated X^-. Counterion N^+ is completely dissociated but M^+ may form ion pair complexes with the sites according to

$$M^+ + X^- \rightleftarrows MX \qquad (1)$$

Formation of MX is taken to be at equilibrium at all times and is governed by the ion pair formation constant K, where

$$K = C_{MX}/C_M C_X \qquad (2)$$

While this study does not consider complexation between N^+ and X^-, the principles discussed here apply to any system where there is a difference in levels of ionic association between the counterions.

Results obtained from the simulation include the total membrane potential, electric field profiles, and concentration profiles. These are depicted schematically in Figure 1 for a case of moderate ion pairing, $K = 1$. Steady state concentration and field profiles are never precisely linear and may become quite curved as K and mobilities are varied. The electric field, E, is integrated to obtain the potential drop through the membrane. Thus in Figure 1, the electric field changes from negative to positive and the potential profile exhibits a maximum. This diffusional potential is added to the calculated interfacial potentials to give V, the total membrane potential.

Previously, it was found for a membrane composed of site X^-, counterion N^+, counterion M^+, and complex MX, that the potential is dependent upon all species reduced mobilities,[7] u_i (i = X, M, N, MX). For common liquid ion-exchange membranes, the site is a large, hydrophobic ion and the counterion is often a more mobile, inorganic species. An ion pair between these two is likely to reflect the mobility characteristics of the site. For this reason, the study reported here is limited to membranes with equal mobilities for site and complex ($u_X = u_{MX}$).

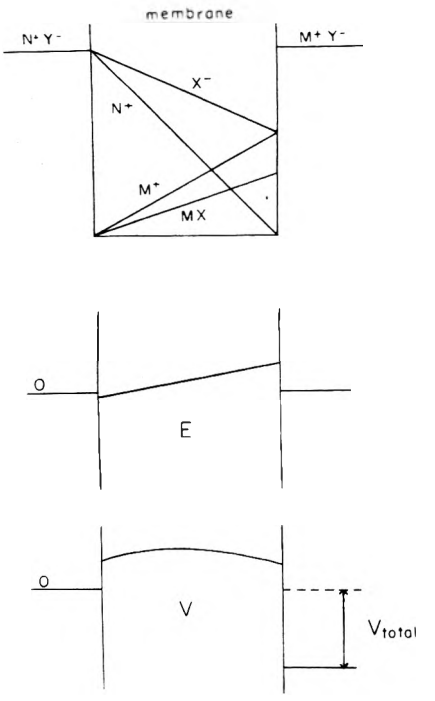

Figure 1. Schematic of electrostatic characteristics of a permselective liquid cation exchange membrane for a case of moderate ion pairing. At top is the general appearance of concentration profiles for biionic bathing solutions with a complexing reference counterion. E is the reduced electric field profile and V is the reduced potential profile from which selectivities are computed.

Results

The reported selectivity coefficients apply to the reduced potential equation of an ion-exchange membrane with two counterions, M^+ and N^+, which can be expressed by

$$\frac{VF}{RT} = \ln\left[\frac{a_N' + K_{N,M}^{pot} a_M'}{a_N'' + K_{N,M}^{pot} a_M''}\right] \tag{3}$$

where the primed activities indicate the left or test bathing solution, the double primes indicate the right or reference bathing solution, and $K_{N,M}^{pot}$ is the selectivity of the membrane to M^+ over N^+. This form of the Horovitz–Nicolsky–Eisenman equation[8] is also known as a form of the Hodgkin–Goldman–Katz equation. By substituting the biionic activities into eq 3, the selectivity coefficient can be calculated using

$$K_{N,M}^{pot} = e^{-(VF/RT)} \tag{4}$$

A consequence of the form of the response function derived in the Sandblom, Eisenman, and Walker analysis[2] is that complex formation by species M^+ should improve membrane response to M^+, i.e., $K_{N,M}^{pot}$ should increase with complex formation constant K. It is clear that the dependence of $K_{N,M}^{pot}$ on K should disappear when $u_X = 0$; but it by no means is clear how the dependence should appear when u_X is varied. To investigate this, calculations were performed and the results are given in Figure 2. It is shown that the selectivity coefficient, for various degrees of ion pairing as measured by K, decreases nonlinearly as the log of the site–complex mobility becomes more negative. Ion pairing increases the selectivity of the membrane toward M^+ for all nonzero values of site–complex mobility. Also, for any value of the complexation constant, the membrane becomes less selective for M^+ as the site–complex mobility decreases. In the limit of a fixed site membrane, the selectivity becomes that of a dissociated, mobile site membrane. For a dissociated membrane (K = 0 in Figure 2), the selectivity coefficient is known from theory and is found to be $u_M k_M / u_N k_N$, or 1.33 in our case.

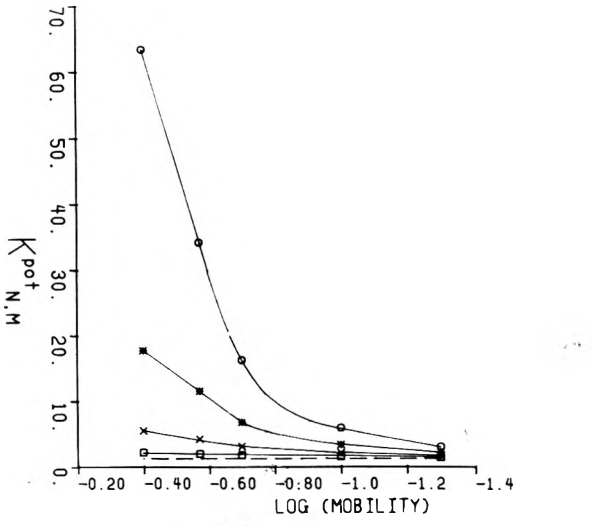

Figure 2. Selectivity coefficient $K_{N,M}^{pot}$ of a liquid membrane vs. an equal site–complex mobility for various values of the ion pair association constant, K, between site and counterion whose selectivity is shown. Values for all cases are as follows: complexing counterion mobility = 0.4, noncomplexing counterion mobility = 0.3, total site concentration = 1.0. Ion pair association constants for (—) K = 0, (□) K = 1, (×) K = 10, (•) K = 100, (○) K = 1000.

Discussion

By examining the fields, concentrations, and potentials, one can gain insight into concomitant changes or possible causes for the decrease in selectivity coefficient $K_{N,M}^{pot}$ with decreasing site and complex mobility. First, some relations between interfacial concentrations, potentials, and selectivity need to be qualitatively discussed. The general subdivision of membrane potential into interfacial and diffusion components

$$V = \underbrace{(\bar{V}' - V')}_{\text{left interface}} + \underbrace{(\bar{V}'' - \bar{V}')}_{\text{diffusion}} + \underbrace{(V'' - \bar{V}'')}_{\text{right interface}} \tag{5}$$

is for this system

$$VF/RT = \ln(a_N'/\bar{a}_N') + (\bar{V}'' - \bar{V}') + \ln(\bar{a}_M''/a_M'') \tag{6}$$

Interfacial and diffusion potential components have different origins, but both depend on log activity of species at the inner surfaces. Deducing relative contributions on an intuitive level requires prior knowledge of the inner surface concentrations of exchangeable ions which are related to the site profile. The magnitude and sign of average concentration gradients (concentration profiles) for simple noncomplexing mobile site, biionic membranes can be rigorously derived; but for membranes with complexation, some provisional generalizations, based on the scanning of many computer-simulated results, can be stated.

For noncomplexing membranes: (1) Mobile site profiles are constant (flat) only when $u_M = u_N$ (independent of u_X). (2) Site profiles are high at the interface where the less mobile ion enters the membrane and low at the interface where the more mobile ion enters. For our case with M^+ on the right, N^+ on the left, and $u_M > u_N$, the site profile tips downward from left to right. Ion pairing increases the slope of the site concentration profile.

For complexing membranes: (3) An independent decrease in mobility of any species causes an increase in the

TABLE I: Simulated Interfacial Concentrations, Fields, and Potentials for Values of Complexation Constant and Site-Complex Mobility[a]

$K = 1$	$U = 0.4$	$U = 0.3$	$U = 0.2$	$U = 0.1$	$U = 0.05$
C_X', C_X''	1.07, 0.585	1.04, 0.596	1.01, 0.607	0.978, 0.619	0.960, 0.625
C_{MX}''	0.342	0.355	0.369	0.383	0.391
E', E''	0.016, 0.027	0.009, 0.019	0.000, 0.011	−0.01, 0.004	−0.15, −0.00
V'	−0.070	−0.043	−0.013	0.022	0.041
V(diff)	−0.185	−0.120	−0.051	0.026	0.068
V''	−0.538	−0.518	−0.499	−0.479	−0.470
V(total)	−0.791	−0.681	−0.562	−0.431	−0.361
$K = 10$	$U = 0.4$	$U = 0.3$	$U = 0.2$	$U = 0.1$	$U = 0.05$
C_X', C_X''	1.07, 0.258	1.02, 0.266	0.945, 0.274	0.860, 0.281	0.810, 0.284
C_{MX}''	0.667	0.707	0.749	0.789	0.805
E', E''	0.016, 0.057	0.002, 0.030	−0.02, 0.004	−0.06, −0.02	−0.09, −0.03
V'	−0.072	−0.015	0.057	0.150	0.211
V(diff)	−0.278	−0.096	0.118	0.374	0.521
V''	−1.35	−1.33	−1.30	−1.27	−1.26
V(total)	−1.70	−1.44	−1.12	−0.745	−0.528
$K = 100$	$U = 0.4$	$U = 0.3$	$U = 0.2$	$U = 0.1$	$U = 0.05$
C_X', C_X''	1.08, 0.091	1.00, 0.095	0.915, 0.098	0.802, 0.101	0.726, 0.102
C_{MX}''	0.833	0.894	0.959	1.02	1.03
E', E''	0.017, 0.128	0.000, 0.051	−0.02, −0.02	−0.07, −0.07	−0.13, −0.07
V'	−0.073	−0.003	0.089	0.221	0.321
V(diff)	−0.407	−0.080	0.330	0.859	1.18
V''	−2.39	−2.36	−2.32	−2.29	−2.28
V(total)	−2.87	−2.44	−1.90	−1.21	−0.786
$K = 1000$	$U = 0.4$	$U = 0.3$	$U = 0.2$	$U = 0.1$	$U = 0.05$
C_X', C_X''	1.07, 0.030	1.00, 0.031	0.909, 0.032	0.793, 0.034	0.713, 0.034
C_{MX}''	0.894	0.965	1.05	1.13	1.15
E', E''	0.017, 0.213	0.000, 0.051	−0.02, −0.13	−0.06, −0.24	−0.11, −0.19
V'	−0.074	−0.001	0.095	0.232	0.338
V(diff)	−0.516	−0.056	0.551	1.39	1.94
V''	−3.51	−3.47	−3.43	−3.39	−3.38
V(total)	−4.10	−3.53	−2.78	−1.77	−1.11

[a] K = ion pair formation constant of MX; $U = u_X = u_{MX}$ = site and complex mobility; C_X = site concentrations at left and right interface; C_{MX} = complex concentration at right interface; E = electric fields at left and right side of membrane; V' = left interfacial potential; V(diff) = diffusional potential; V'' = right interfacial potential; V(total) = total membrane potential. The above quantities are reduced, dimensionless variables.

slope of the concentration profile for that species. (4) The combined effect when $u_X = u_{MX}$ is that the site's concentration profile flattens out and the complex's profile steepens when the site–complex mobility is decreased. This site leveling causes a decrease in the site concentration at the left interface and an increase at the right. Both of these processes cause a decrease in the membrane's selectivity.

From the form of eq 4, it can be seen that more positive simulated potentials lead to less selective membranes toward the complexing counterion, M^+. The decrease in the site concentration (and simultaneously $\bar{a}_N'$) at the left interface causes the left interfacial potential to increase positively and to decrease the selectivity. Conversely, the concomitant increase in the site concentration (since total sites are conserved) at the right interface also decreases the selectivity. Finally, both of these changes are accompanied by the electric fields within the membrane becoming more negative, the diffusion potential (negative integral of the field) becoming more positive, and the selectivity decreasing.

Interpretation of Selectivity Loss by Decrease of Site and Complex Mobility

In Figure 3a,b are illustrated the concentration profiles for values of the site–complex mobility for a typical case, $K = 1$. The profile is less steep for smaller u_X and the change of site concentration at the left interface for the two cases is greater than the change at the right. This effect is to be expected, since changes in site concentration at the right side of the membrane are "buffered" by the ion pairing reaction. Inspection of the interfacial potentials in Table I shows that the positive shift with changing u_X in the left interfacial potential is greater than in the right. Thus, the decrease in the membrane's selectivity, resulting from changing interfacial site concentrations, is caused mainly by the positive potential shift at the left interface. This result contrasts with the increase in selectivity with degree of ion pairing, a case in which the decrease in the site concentration at the right interface is the dominant factor.[7]

A second contribution to the decrease in the membrane's selectivity with decreasing site–complex mobility is the shift in the diffusion potential. For all cases, it is found that the fields are originally positive for a mobility of 0.4. As the site–complex mobility is lowered, the fields decrease, change sign, and become increasingly negative. This causes a positive shift in the diffusion potential, and a decrease in selectivity. The reason for the negative shift in the fields is apparent from the equation for the total site (i.e., free site plus complex) flux

$$J_X^* = -u_X\left[RT\frac{dC_X}{dx} + C_XFE + RT\frac{dC_{MX}}{dx}\right] \qquad (7)$$

which in the steady state must be zero. The first term on the right is the site diffusion term, the second is the site migration term, and the third is the complex diffusion term. Solving for the field in the steady state gives

$$\frac{FE}{RT} = -\left[\frac{dC_X}{dx} + \frac{dC_{MX}}{dx}\right]\Big/C_X \qquad (8)$$

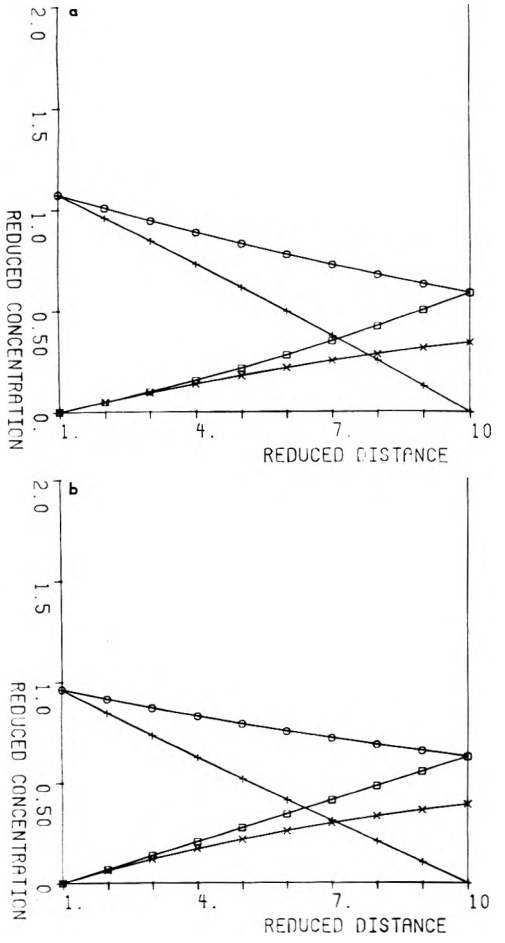

Figure 3. Concentration profiles for case where $K = 1$: (O) site, (+) noncomplexing counterion, (□) complexing counterion, and (×) complex. Site–complex mobility values: (a) 0.4; (b) 0.05.

The field is dependent on the difference between the slope of the site's profile and that of the complex. Recall that dC_X/dx becomes a smaller negative quantity and dC_{MX}/dx a larger positive quantity as the site–complex mobility decreases. As the site profile becomes less steep, the contribution to its flux from diffusion decreases, and the fields change negatively so that migration can maintain a balance with the complex's increased diffusional flux. The effect is more pronounced at higher degrees of ion pairing since C_X decreases and both the site and complex profiles become steeper. Comparison of the magnitudes of the diffusion potentials with interfacial potentials shows that the diffusion potential effect is greater than, though comparable to, the effect of changing interfacial concentrations.

Conclusion

Digital simulation provides data and leads to an intuitive description of the role of the site mobility in determining the selectivity of liquid ion-exchange membranes. In this case digital simulation provides data that cannot be obtained by analytical means. For liquid ion-exchange membranes with complex formation, decreased site mobility decreases the potentiometric selectivity for the complexed counterion; the effect is greatest for *high* degrees of ion pairing. As the mobilities decrease, the selectivity is leveled, regardless of complexation, to that of a fixed site membrane. There are two causes of this effect. Total site flux balance is maintained more strongly by migration and less strongly by diffusion for lower values of the site–complex mobility. The concurrent change in the internal electric fields creates a diffusion potential which decreases the selectivity. In addition, the decrease in the diffusional flux of the site leads to a leveling of the site concentration profile and more nearly equal site concentrations at the interfaces. This factor also contributes to the decreased selectivity.

Acknowledgment. This study was supported by National Science Foundation Grant No. CHE-7500970-AO1.

References and Notes

(1) F. Conti and G. Eisenman, *Biophys. J.*, **6**, 227 (1966).
(2) J. Sandblom, G. Eisenman, and J. Walker, *J. Phys. Chem.*, **71**, 3862 (1967).
(3) J. Sandblom, G. Eisenman, and J. Walker, *J. Phys. Chem.*, **71**, 3871 (1967).
(4) S. W. Feldberg in "Electroanalytical Chemistry", Vol. 3, A. J. Bard, Ed., Marcell Dekker, New York, N.Y., 1969.
(5) J. R. Sandifer and R. P. Buck, *J. Electroanal. Chem.*, **49**, 161 (1974).
(6) J. R. Sandifer and R. P. Buck, *J. Phys. Chem.*, **79**, 384 (1975).
(7) F. S. Stover and R. P. Buck, *Biophys. J.*, **16**, 753 (1976).
(8) IUPAC Recommendation, *Pure Appl. Chem.*, **48**, 127 (1976).

Pressure Dependence of Shear Viscosity in *n*-Alkane + Dimethylsiloxane Mixtures

Eric Dickinson[†]

Physical Chemistry Laboratory, South Parks Road, Oxford OX1 3QZ, England *(Received June 23, 1977)*

The shear viscosity (η) has been measured near room temperature up to a pressure (p) of 3–5 kbar for the liquids *n*-hexane, *n*-octane, hexamethyldisiloxane (HMDS), and octamethylcyclotetrasiloxane (OMCTS), and the three mixtures *n*-hexane + HMDS, *n*-octane + HMDS, and *n*-hexane + OMCTS. The Enskog smooth hard-sphere theory overestimates $d\eta/dp$, but reasonable agreement is obtained up to 2 kbar either by (i) allowing for coupling of rotational and translational motion (rough hard-sphere model) or (ii) introducing a simple attractive potential (square-well model). At higher densities no approach based on the hard-sphere model is applicable.

Introduction

Of all the bulk properties of a molecular fluid, the shear viscosity is probably the most density dependent. Until recently, however, there has been little attempt to predict this density dependence theoretically, apart from the use of semiempirical models based on the "free-volume" concept.[1] With the recognition that the structural and thermodynamic properties of a fluid are determined mainly by the repulsive forces, it is of interest to ask as to how far the transport properties, and notably the shear viscosity, can be represented by a hard-core model. Pre-

[†] Present address: Department of Food Science, University of Leeds, Leeds L52 9JT, England.

liminary work on the smooth and rough hard sphere fluids by Chandler[2] and Dymond[3,4] would seem to suggest that the repulsive forces are dominant here also.

While the viscosities of pure fluids have received much attention, there are few measurements of mixture viscosities at pressures above atmospheric. In this paper experimental viscosities are reported for three *n*-alkane + dimethylsiloxane mixtures as well as for the four pure fluids comprising them. The *n*-alkane + dimethylsiloxane systems exhibit small deviations from thermodynamic ideality,[5-7] and were therefore not expected to show anomalous viscosity behavior. The results are compared with predictions from two modifications to the simple hard-sphere theory: the first takes account of the coupling between rotational and translational degrees of freedom, and the second introduces attractive forces.

Experimental Section

The viscometer was an adaptation of that used by Cappi[8,9] in the Department of Chemical Engineering at Imperial College, London.

A close-fitting, stainless-steel, cylindrical, "guided" sinker is allowed to fall under gravity inside a vertical, precision-bore tube (length 20 cm, diameter 7.7 mm), and the time for it to pass between two fiducial points is recorded. At one end of the tube, a stainless-steel bellows assembly transmits pressure to the test liquid and accommodates any volume changes; at the other end are connections for filling and a silver-foil bursting disk (0.0175 mm). The electronic timer is triggered as the sinker passes a point midway between pairs of matched, wire-wound coils forming part of a sensitive bridge circuit: the soft-iron core induces an out-of-balance voltage which rapidly changes sign near the midpoint of the coils.

The pressure vessel containing the viscometer tube is immersed in an oil bath whose temperature is controlled to within ±0.1 K. A hand-operated intensifier (piston area ratio 14:1) generates the pressure. A mixture of silicone oil (Hopkin and Williams, 5 cSt) and standard handpump oil is used as hydraulic fluid. Pressure is measured by a resistance strain gauge transducer (Coleraine Instruments, Type 8615/7) and is displayed on a compatible digital indicator (Type 8656). The gauge was calibrated against a Harwood deadweight piston gauge in the Department of Mechanical Engineering of the Queen's University of Belfast; a further calibration toward the end of the work indicated negligible drift in the readings. The full performance characteristics of this type of transducer are discribed in ref 10.

The sources and purities of the liquids were as follows: *n*-hexane, *n*-decane, *n*-dodecane, octan-1-ol (BDH, 99%); *n*-heptane, *n*-octane (BDH, 99.5%); butan-1-ol (BDH, 99.9%); hexamethyldisiloxane (HMDS) (Fluka, puriss., 99%); octamethylcyclotetrasiloxane (OMCTS) (Fluka, purum.). The liquids were partially degassed before introduction into the viscometer tube. The sinker was calibrated at 302.8 K using the known viscosities of the hydrocarbons and alcohols at atmospheric pressure,[11-13] and in Figure 1 the product of the fluidity η^{-1} and the corrected falltime t_8^* (adjusted to the density of *n*-octane) is plotted against the logarithm of the uncorrected falltime t. Times in the two directions differed by less than 0.5% for *n*-hexane and *n*-heptane, but for octan-1-ol the discrepancy was as much as 4% (as has been observed previously[9]). For the longest falltimes, $t_8^*\eta^{-1}$ appears to follow the theoretical behavior described below.

Under ideal conditions (a perfectly round sinker falling concentrically in a perfectly round and parallel tube), the buoyancy-corrected weight of the sinker balances the

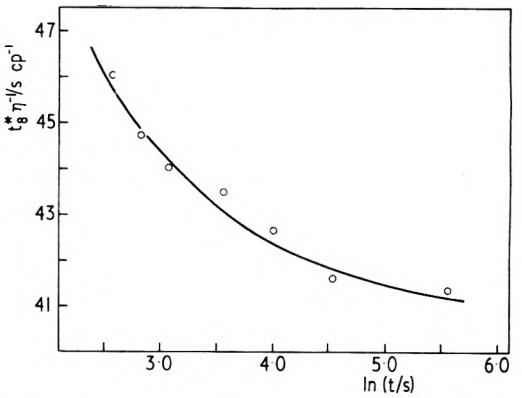

Figure 1. Calibration of viscometer at 1 bar and 302.8 K. The quantity $t_8^*\eta^{-1}$, where t_8^* is the corrected falltime relative to *n*-octane and η is the literature viscosity value (ref 11-13), is plotted against the logarithm of the uncorrected falltime t.

effects of a shear stress from fluid-flow through the annulus and a force due to the pressure difference across the sinker. Assuming laminar flow and neglecting sinker end effects

$$\eta = \varkappa mgt^*/2\pi lL \tag{1}$$

where mg and l are the weight and length of the sinker, L is the length of the tube, and

$$\kappa = \ln (R/r) - (R^2 - r^2)(R^2 + r^2)^{-1} \tag{2}$$

r and R are the radii of sinker and tube, respectively.

In a real viscometer, however, the ends and guiding pins of the sinker disturb both the viscous drag and the pressure difference, and $\varkappa$ must be treated as a constant of the apparatus. Using an effective value of r in eq 2, an allowance was made for the variation of the constant $\varkappa$ with temperature and pressure. Where unavailable in the literature, densities for the buoyancy correction were estimated from a generalized van der Waals equation of state

$$p = (RT/V_m)\,\phi(y) - (a/V_m^2) \tag{3}$$

where p, T, V_m, and R are pressure, temperature, molar volume, and gas constant, respectively. The density-dependent function $\phi(y)$ was taken as[14]

$$\phi(y) = (1 + y + y^2 - y^3)/(1 - y)^3 \tag{4}$$

where $y = b/4V_m$. The constants a and b were estimated from experimental densities and compressibilities at 1 bar.[15-18] (Compressibilities were obtained from ratios of the more precise expansivities and thermal pressure coefficients.) Table I shows calculated densities of *n*-hexane, *n*-octane, HMDS, and OMCTS at pressures up to 5 kbar together with Bridgman's experimental results for *n*-octane.[19] Mixture densities were estimated using excess volumes, where available,[6] and compressibilities were taken as volume fraction averages of pure component values.

Results

Table II shows relative viscosity data for *n*-hexane + HMDS and *n*-octane + HMDS at 303.2 K and *n*-hexane + OMCTS at 323.2 K together with data for the pure liquids at the same temperatures. Each quoted result corresponds to the mean of 8–10 falltimes.

For graphical illustration, it is convenient to consider the logarithm of the relative viscosity, ln (η/η_0), where η_0 is the viscosity at 1 bar. Figures 2 and 3 show that $\{\partial \ln (\eta/\eta_0)/\partial T\}_p$ is very slightly positive up to 1.5 kbar for

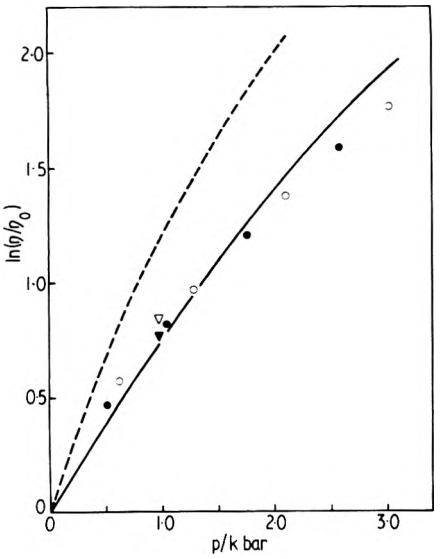

Figure 2. Pressure dependence of viscosity for *n*-hexane. The logarithm of the relative viscosity η/η_0 is plotted against the pressure p: (●) experiment, 303.2 K, this work; (○) experiment, 323.2 K, this work; (▼) experiment, 303 K, Bridgman (ref 19); (▽) experiment, 348 K, Bridgman (ref 19); (—) rough hard-sphere model; (- - -) smooth hard-sphere model.

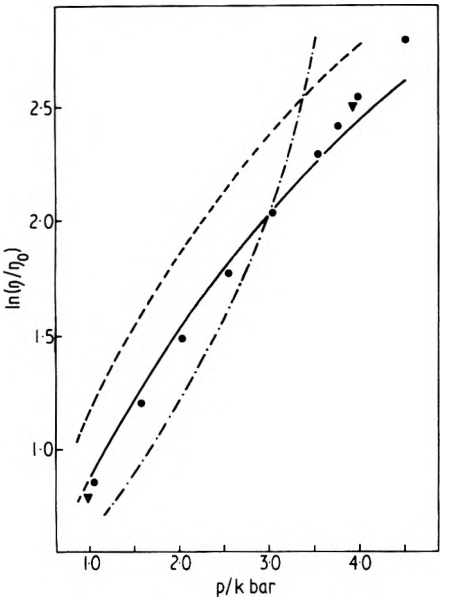

Figure 3. Pressure dependence of viscosity for *n*-octane at 303.2 K. The logarithm of the relative viscosity η/η_0 is plotted against the pressure p: (●) experiment, this work; (▼) experiment, Bridgman (ref 19); (—) rough hard-sphere model; (- - -) smooth hard-sphere model; (-·-) Hildebrand's theory (eq 16).

n-hexane and *n*-octane, but it becomes increasingly negative at higher pressures. Even so, the apparent change in sign is not conclusive, since the two sets of data lie within the combined maximum experimental uncertainty (2%). A comparison with Bridgman's *n*-octane results[19] shows better agreement at 4 kbar than at 1 kbar (within 1%).

Results for the mixtures are illustrated in Figures 4–6. The pressure range is determined by the position of the solid–liquid phase boundary. The range is especially short for *n*-hexane + OMCTS, since, like most other pseudo-spherical molecules, OMCTS has a low freezing pressure. A general feature of these results is that the value of the derivative $\{\partial \ln (\eta/\eta_0)/\partial p\}_T$ increases with the degree of molecular complexity and tends toward constancy at the highest pressures.

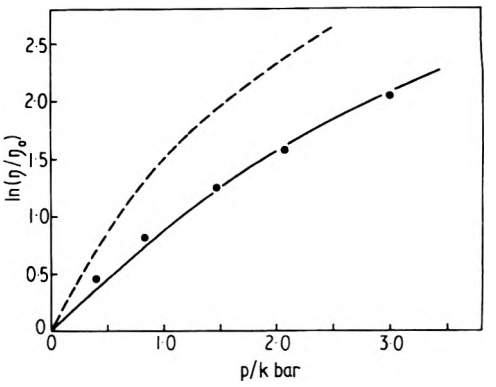

Figure 4. Pressure dependence of viscosity for *n*-hexane ($x_1 = 0.5$) + HMDS ($x_2 = 0.5$) at 303.2 K. The logarithm of the relative viscosity η/η_0 is plotted against the pressure p: (●) experiment, this work; (—) rough hard-sphere model; (- - -) smooth hard-sphere model.

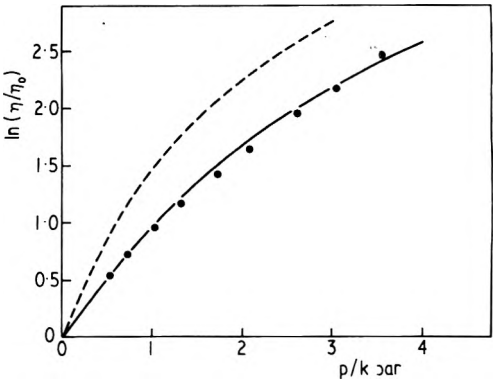

Figure 5. Pressure dependence of viscosity for *n*-octane ($x_1 = 0.5$) + HMDS ($x_2 = 0.5$) at 303.2 K. The logarithm of the relative viscosity η/η_0 is plotted against the pressure p: (●) experiment, this work; (—) rough hard-sphere model; (- - -) smooth hard-sphere model.

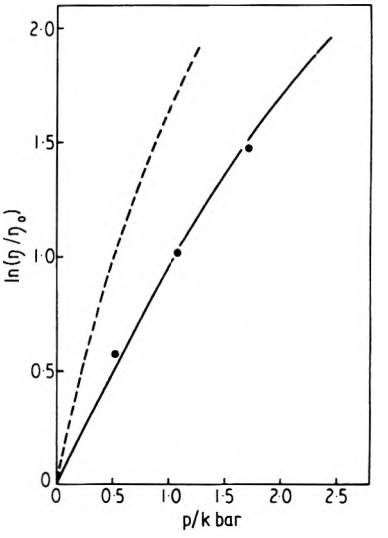

Figure 6. Pressure dependence of viscosity for *n*-hexane ($x_1 = 0.297$) + OMCTS ($x_2 = 0.703$) at 323.2 K. The logarithm of the relative viscosity η/η_0 is plotted against the pressure p: (●) experiment, this work; (—) rough hard-sphere model; (- - -) smooth hard-sphere model.

Smooth Hard-Sphere Model

According to Enskog,[20] the shear viscosity of a dense fluid of smooth hard spheres of mass m and diameter σ is given by

$$\eta_E = \eta^0\{g(\sigma)^{-1} + 3.2y + 12.176\, g(\sigma)y^2\} \qquad (5)$$

where $\eta^0 = (5/16\sigma^2)(mkT/\pi)^{1/2}$ is the zero density limit, and $g(\sigma)$ is the radial pair distribution function at contact. Computer simulation has shown[21] that the "molecular

TABLE I: Densities of Pure Liquids from Modified van der Waals Equation of State

Substance	T, K	p, kbar	ρ, g cm^{-3}	Substance	T, K	p, kbar	ρ, g cm^{-3}
n-Hexane	303.2	0	0.650	HMDS	303.2	0	0.757
		1	0.724			1	0.852
		2	0.765			2	0.901
		3	0.793			3	0.934
		4	0.815			4	0.958
		5	0.833			5	0.978
n-Hexane	323.2	0	0.632	OMCTS	323.2	0	0.921
		0.5	0.683			0.5	0.987
		1	0.716			1	1.028
		1.5	0.740			1.5	1.058
		2	0.760			2	1.082
		2.5	0.776			2.5	1.101
n-Octane	303.2	0	0.694				
		1	0.758	(0.746[a])			
		2	0.795	(0.782[a])			
		3	0.821	(0.811[a])			
		4	0.841	(0.833[a])			
		5	0.858	(0.855[a])			

[a] Experiment (ref 19).

TABLE II: Experimental Viscosities (Relative to Those at 1 bar)

System	T, K	p, kbar	η/η_0	p, kbar	η/η_0
n-Hexane	303.2	0.51_5	1.60_6	1.75_5	3.35_0
		1.03_5	2.27_3	2.57	4.90_1
	323.2	0.62_5	1.77_8	2.09_5	3.96_2
		1.27_5	2.63_8	3.01_5	5.84_9
n-Octane	303.2	0.52_5	1.63_8	3.03_5	7.63_8
		1.03_5	2.35_6	3.54	9.92_1
		1.56_5	3.34_1	3.76_5	11.17
		2.04	4.42_0	3.98_5	12.72
		2.55_5	5.86_8	4.52	16.41
	323.2	0.51	1.63_7	2.56_5	5.62_9
		1.04_5	2.40_2	3.38	8.32_1
		1.78	3.71_6	4.03_5	11.18
HMDS	303.2	0.50_5	1.84_5	2.09_5	5.99_4
		1.04_5	2.94_7	3.05_5	10.62
	323.2	0.52	1.93_8		
OMCTS	323.2	0.30	1.79_3	0.52	2.43_6
n-Hexane + HMDS	303.2	0.38_5	1.57_8	2.06_5	4.85_4
		0.82_5	2.25_9	2.98_5	7.74_8
		1.47	3.48_9		
n-Hexane + OMCTS	323.2	0.52	1.78_4	1.71	4.38_7
		1.07_5	2.76_7		
n-Octane + HMDS	303.2	0.52	1.71_4	2.07_5	5.18_7
		0.72_5	2.06_9	2.60_5	7.07_5
		1.02_5	2.61_5	3.01_5	8.82_1
		1.31_5	3.22_3	3.54	11.80
		1.72_5	4.16_2		
	323.2	0.72_5	2.10_1		

chaos" approximation of the Enskog theory leads to errors which are large at high density, and Dymond[4] has represented such deviations by the expressions

$$\eta_S = \eta_E\{1.02 + 15(y' - 0.35)^3\} \quad 0.427 < y' \leq 0.575$$
$$\eta_E\{1.02 + 15(y' - 0.35)^3 + 900(y' - 0.575)^3\} \quad 0.575 < y' \leq 0.66 \qquad (6)$$

where $y' = (3\sqrt{2}/\pi)y$. Distribution functions are also available from simulation studies, but for computational convenience an analytic expression derived from eq 4 is used, i.e.

$$g(\sigma) = (1 - {}^1/_2 y)(1 - y)^{-3} \qquad (7)$$

The above equations are strictly valid only for a pure fluid, and Thorne[22] has developed the theory to include binary mixtures. Unfortunately, however, there is little to be gained by using the more complex mixture expressions unless the two separate collision diameters can be fitted independently and relations can be formulated for the three pair distribution functions. Such a full analysis is not feasible here and so, since the aim is to study the dependence on pressure rather than composition,[36] it seems reasonable to represent each mixture as a pure fluid having characteristic mean collision diameter $\langle\sigma\rangle$ and pair distribution function $g(\langle\sigma\rangle)$, i.e., to assume that it can be represented by the "one-fluid" approximation.

Predictions from the Enskog hard-sphere theory are shown in Figures 2–6. Except for *n*-hexane and *n*-octane, where experimental values were used,[19] densities were calculated from eq 3 and 4. Hard-core diameters were obtained by fitting η_0 to the experimental low-pressure viscosities.[11-13] For each system studied (including HMDS and OMCTS, not shown) the relative viscosity (η/η_0) from the smooth hard-sphere theory is larger than found experimentally. Although part of the *n*-alkane discrepancy may be attributable to departures from molecular spherical symmetry, since OMCTS and carbon tetrachloride[2] also exhibit similar behavior, it would appear not to be the major factor. In any case, transport theory in fluids of nonspherical particles is insufficiently developed for us to

TABLE III: Values of Rough Hard-Sphere Viscosity Constants

System	T, K	C_η
n-Hexane	303	0.5_4
n-Octane	303	0.9_1
HMDS	303	1.4_6
OMCTS	323	2.2
n-Hexane + HMDS	303	1.1_0
n-Octane + HMDS	303	1.2_7
n-Hexane + OMCTS	323	1.2_0

make any satisfactory correction for this factor, and it will not be discussed further.

In what follows, we consider three improvements to the smooth hard-sphere model, each of which leads to better agreement with experiment: (i) the introduction of "roughness", i.e., coupling of translational and rotational degrees of freedom at collision; (ii) the introduction of an attractive contribution to the pairwise interaction energy; and (iii) the introduction of "softness" into the repulsive potential.

Rough Hard-Sphere Model

Chandler has shown[2] that the viscosity η_R of a rough hard-sphere fluid is given by

$$\eta_R = (1 + C_\eta)\eta_S \tag{8}$$

where C_η is a positive constant. The logic behind eq 8 follows along similar lines to an analysis of diffusion in the rough hard-sphere fluid,[2] where an approximation is introduced[24] for the limiting behavior of the Laplace transform of the velocity autocorrelation function. The constant C_η can be treated as an adjustable parameter, equal to zero if, as with smooth spheres, binary collisions do not allow transfer of rotational and translational energy.

Figures 2–6 show how adjusting C_η leads to good agreement up to about 2 kbar. At higher pressures, the predicted values of $\ln(\eta_R/\eta_0)$ deviate from experiment, but the densities here generally correspond to the metastable hard-sphere fluid region where the extrapolated form of eq 6 is unreliable ($y' > 0.66$). As before, collision diameters were determined from literature values of η_0.[11-13] The "best-fit" values of C_η are listed in Table III.

We find that eq 8 is able to reproduce $\{\partial \ln(\eta/\eta_0)/\partial p\}_T$ for the pure and mixed fluids within the density range of thermodynamic stability of the hard-sphere fluid. As expected, the coupling constant increases with the degree of molecular complexity and for a mixture lies between its pure component values. However, that agreement is improved by the introduction of an adjustable parameter is not in the least surprising, and in the next section an alternative perturbation is examined: the inclusion of attractive forces.

Square-Well Model

There is no explicit expression for the viscosity coefficient in a fluid with a realistic attractive potential such as the Lennard-Jones (12–6). However, by reducing the problem to an average over four different collision types, a solution has been obtained for the particular case of the dense square-well fluid.[25] Although the square-well potential (eq 9) is not physically realistic, it does provide,

$$\begin{aligned} u(r) &= \infty & r &< \sigma \\ &= -\epsilon & \sigma &\leq r < \lambda\sigma \\ &= 0 & \lambda\sigma &\leq r \end{aligned} \tag{9}$$

through the parameter ϵ, a useful indicator of the influence of attractive forces on the transport coefficients. Moreover, it has been studied extensively in the past,[26] and distribution functions are available over a wide density range.[27]

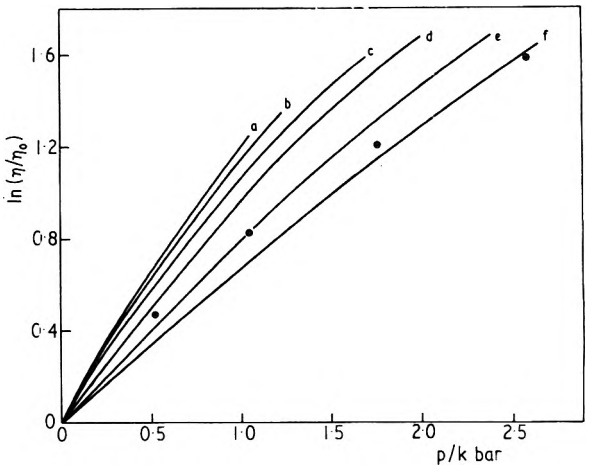

Figure 7. Viscosity of *n*-hexane at 303 K from square-well theory. The logarithm of the relative viscosity η/η_0 is plotted against the pressure p for various values of the reduced well-depth $\tilde{\epsilon}$: (a) 0.0; (b) 0.2; (c) 0.4; (d) 0.6; (e) 0.8; (f) 1.0; (●) experiment.

According to Davis and Luks,[28] the shear viscosity of a square-well fluid is given by

$$\eta_{SW} = \eta^0 \left[\frac{\{1 + 1.6y(g^{sw}(\sigma) + \lambda^3 g^{sw}(\lambda\sigma)\Psi)\}^2}{g^{sw}(\sigma) + \lambda^2 g^{sw}(\lambda\sigma)\{\Xi + (\tilde{\epsilon}^2/6)\}} + 9.778y^2\{g^{sw}(\sigma) + \lambda^4 g^{sw}(\lambda\sigma)\Xi\} \right] \tag{10}$$

where $\tilde{\epsilon}$ is the reciprocal of the reduced temperature $\tilde{T} = kT/\epsilon$, $g^{sw}(r)$ is the square-well distribution function, and

$$\Psi = 1 - \exp\tilde{\epsilon} + {}^1/_2\tilde{\epsilon}\{1 + 4\pi^{-1/2} \times \exp\tilde{\epsilon} \int_{\tilde{\epsilon}^{1/2}}^{\infty} \exp(-x^2)x^2\,dx\} \tag{11}$$

$$\Xi = \exp\tilde{\epsilon} - {}^1/_2\tilde{\epsilon} - 2\int_0^{\infty} x^2(\tilde{\epsilon} + x^2)^{1/2} \times \exp(-x^2)\,dx \tag{12}$$

Figure 7 shows the viscosity of *n*-hexane predicted at 303.2 K by the square-well model for several values of $\tilde{\epsilon}$. The well-width parameter is set equal to 1.75, and $g^{sw}(r)$ is calculated from first-order perturbation theory, i.e.

$$g^{sw}(r) = g(r) + \tilde{\epsilon}\, g_1(r) \tag{13}$$

where $g(r)$ refers to hard spheres and $g_1(r)$ is the correction term. For each $\tilde{\epsilon}$, the collision diameter σ was adjusted as before to fit the viscosity at $p = 1$ bar, and the correction from the simulation results (eq 4) was applied at each density.

The effect of including attractive forces is to reduce $\{\partial \ln(\eta/\eta_0)/\partial p\}_T$ and thus improve agreement with experiment. The optimum well-depth is $\epsilon \sim 0.9kT$, which compares favorably with the value of $1.1kT$ necessary to fit the second virial coefficient of *n*-hexane[29] calculated from

$$B = b\{1 - (\lambda^3 - 1)(\exp\tilde{\epsilon} - 1)\} \tag{14}$$

Hence, the introduction of attractive forces in the form of the square-well potential modifies the pair distribution functions in such a way that the hard-sphere pressure dependence is reduced, and so brought into moderate but reasonable agreement with experiment. *Mutatis mutandis*, the other systems behave in a similar manner.

Discussion

It has been shown that the hard-sphere theory of Enskog is inadequate for describing the pressure dependence of

shear viscosity in a pure or mixed fluid composed of simple oligomeric molecules. Chandler's proposal[2] that this is due to the absence of translational–rotational coupling is consistent with the better agreement found with the rough hard-sphere model, although even here agreement is not perfect. We find that the square-well model is equally successful if, instead of C_η, the well-depth ϵ is treated as the adjustable parameter. As for the possibility of including a "softness" into the repulsive part of the potential, this would be equivalent to reducing the effective hard-core diameter with increasing density. Again this would reduce $(\partial\eta/\partial p)_T$ and improve agreement with experiment.

Hence, while the neglect of translational–rotational coupling is undoubtedly an important reason behind the failure of Enskog's theory, it is perhaps not the *only* reason. In addition, since its degree of importance cannot be assessed from viscosity data alone, we require an estimate of C_η from an independent experimental source. A promising quantity in this regard is the molecular reorientational correlation time as derived from pulsed NMR or Raman scattering studies. It has been shown[30] that experimentally determined values of the Kivelson parameter K,[31] which measures the extent of intermolecular anisotropy (and therefore the effective degree of coupling between translational and rotational modes), are inversely proportional to a parameter which reflects molecular shape

$$S = \sum_i \rho_i^2 \qquad (15)$$

where ρ_i $(i = x, y, z)$ is the axial ratio for rotation about the ith axis. The good correlation between K and S suggests that it might also be possible to relate C_η to the molecular structure, but whether S is the most appropriate shape parameter for oligomers is not clear.

The aim of this work has been to discuss the dependence of viscosity on pressure in a molecular fluid without resort to the more traditional free-volume[32] or rate-theory[33] approaches. While useful predictively either together[34] or separately, the two approaches suffer from the serious physical defect being associated with the assumption of a quasi-crystalline liquid structure. This means that they are not suitable for refinement in a systematic manner. Worthy of consideration because of its simplicity, however, is Hildebrand's semiempirical representation of the fluidity:[35]

$$\eta^{-1} = B(V_m - V_0)/V_0 \qquad (16)$$

where B is a constant, and $V_m \to V_0$ as $\eta^{-1} \to 0$. It is not linked to a lattice model, and Figure 3 shows that it gives a moderately accurate prediction of (η/η_0) for n-octane up to about 3 kbar. Like the hard-sphere based theories, it diverges substantially from experiment at higher pressures. It seems likely that only a model which allows for molecular flexibility will be successful in the high density region.

Acknowledgment. I am greatly indebted to Dr. K. E. Bett for the loan of high-pressure viscometry equipment from the Department of Chemical Engineering, Imperial College, London. I also thank Professor W. R. Smith for making available unpublished square-well distribution functions, Professor J. S. Rowlinson and Dr. C. J. Danby for providing laboratory space, and Messrs A. J. Whiting and C. J. V. Jones for technical assistance. Financial support from Imperial Chemical Industries is gratefully acknowledged.

References and Notes

(1) S. G. Brush, *Chem. Rev.*, **62**, 513 (1962).
(2) D. Chandler, *J. Chem. Phys.*, **62**, 1358 (1975).
(3) J. H. Dymond, *Physica*, **75**, 100 (1974).
(4) J. H. Dymond, *Chem. Phys.*, **17**, 101 (1976).
(5) E. Dickinson and I. A. McLure, *J. Chem. Soc., Faraday Trans. 1*, **70**, 2313 (1974).
(6) E. Dickinson, I. A. McLure, and B. H. Powell, *J. Chem. Soc., Faraday Trans. 1*, **70**, 2321 (1974).
(7) E. Dickinson and I. A. McLure, *J. Chem. Soc., Faraday Trans. 1*, **70**, 2328 (1974).
(8) K. Bett and J. B. Cappi, *Nature (London)*, **207**, 620 (1965).
(9) J. B. Cappi, Ph.D. Thesis, University of London, 1964.
(10) A. W. Birks and C. A. Gall, *Strain*, **9**, 60 (1973).
(11) Selected Values of Properties of Hydrocarbons and Related Compounds, American Petroleum Institute Research Project 44, Thermodynamic Research Center, Texas A & M University, College Station, Tex., 1965, extant.
(12) J. Timmermans, "Physico-Chemical Constants of Pure Organic Compounds", Elsevier, New York, N.Y., 1950.
(13) P. Dakshinamurty, K. Veerabhadra, P. Venkatesawara Rao, and C. Chiranjira, *J. Chem. Eng. Data*, **18**, 39 (1973).
(14) N. F. Carnahan and K. E. Starling, *J. Chem. Phys.*, **51**, 635 (1969).
(15) R. A. Orwoll and P. J. Flory, *J. Am. Chem. Soc.*, **89**, 6814 (1967).
(16) I. A. McLure, A. J. Pretty, and P. A. Sadler, *J. Chem. Eng. Data*, in press.
(17) C. B. Hurd, *J. Am. Chem. Soc.*, **68**, 364 (1946).
(18) M. Ross and J. H. Hildebrand, *J. Phys. Chem.*, **67**, 1301 (1963).
(19) P. W. Bridgman, "The Physics of High Pressures", Bell and Sons, London, 1949.
(20) S. Chapman and T. G. Cowling, "The Mathematical Theory of Non-Uniform Gases", Cambridge University Press, New York, N.Y., 1953.
(21) B. J. Alder, D. M. Gass, and T. E. Wainwright, *J. Chem. Phys.*, **53**, 3813 (1970).
(22) H. H. Thorne, quoted in ref 20, p 292.
(23) W. A. McElhannon, Jr., and E. McLaughlin, *Mol. Phys.*, **32**, 1349 (1976).
(24) D. Chandler, *J. Chem. Phys.*, **60**, 3500, 3508 (1974).
(25) H. T. Davis, S. A. Rice, and J. V. Sengers, *J. Chem. Phys.*, **35**, 2210 (1961).
(26) J. A. Barker and D. Henderson, *Rev. Mod. Phys.*, **48**, 587 (1976).
(27) W. R. Smith, D. Henderson, and J. A. Barker, *J. Chem. Phys.*, **55**, 4027 (1971).
(28) H. T. Davis and K. D. Luks, *J. Phys. Chem.*, **69**, 869 (1965).
(29) J. H. Dymond and E. B. Smith, "The Virial Coefficients of Gases", Clarendon, Oxford, 1968.
(30) M. Fury and J. Jonas, *J. Chem. Phys.*, **65**, 2206 (1976).
(31) R. E. D. McClung and D. Kivelson, *J. Chem. Phys.*, **49**, 3380 (1968).
(32) M. H. Cohen and D. Turnbull, *J. Chem. Phys.*, **31**, 1164 (1959).
(33) S. Glasstone, K. J. Laidler, and H. Eyring, "The Theory of Rate Processes", McGraw-Hill, New York, N.Y., 1941.
(34) P. B. Macedo and T. A. Litovitz, *J. Chem. Phys.*, **42**, 245 (1965).
(35) J. H. Hildebrand, *Science*, **174**, 490 (1971).
(36) The composition dependence of viscosity in hard sphere mixtures has been discussed in detail recently by McElhannon and McLaughlin (ref 23).

Electrokinetic Studies on Ion-Exchange Membranes. 5. Streaming Potentials

R. P. Rastogi,* Kehar Singh, Raj Kumar, and S. A. Khan

Department of Chemistry, Gorakhpur University, Gorakhpur-273001, India *(Received October 28, 1976)*

Streaming potentials developed during streaming of methanol, water, and methanol–water mixtures through Zeokarb 225 membranes have been measured. Experiments have been repeated with H^+, Na^+, Ba^{2+}, and Al^{3+} forms of the resin. The dependence of the streaming potential on pressure differences is markedly nonlinear. With the H^+ form of the ion exchanger it changes sign when the pressure exceeds 50 cm of liquid column. Multiple sign reversals are observed in ion exchangers of a different form. An attempt has been made to fit the results by a nonlinear equation similar to that used for fitting the electroosmotic data by Rastogi et al.

Introduction

Out of all electrokinetic phenomena, electroosmosis has been most extensively studied.[1-10] Studies on streaming potentials have not been so extensive.[11-15] Streaming potential studies in biological systems have also been demonstrated in the case of the gall bladders of fishes[16] and in the rat small intestine.[17] Rastogi et al.[18] recently observed that for weakly charged membranes, e.g., the quartz and pyrex membranes, streaming potentials depend linearly on pressure. Ion-exchange membranes display peculiar electrokinetic properties. For example, it has been reported[19] that the direction of electroosmotic velocity of 10% water–alcohol mixtures through Zeokarb 226 (H^+ form) is reversed when $\Delta\Phi > 300$ V is applied. Change in the direction of the electrophoretic velocity has also been observed to occur at the same time $\Delta\phi$ for Zeokarb 226 (H^+ form) water–alcohol mixtures. This behavior has been ascribed to the high charge of the ion-exchange membrane. Streaming potential measurements were not made for the system. It was, therefore, decided to study the phenomenon of streaming potential for highly charged ion-exchange membranes. In the present investigation Zeokarb 225 membranes in different ionic forms have been used. Water, methanol, and their mixtures have been used as permeants. The results show that there is a complex nonlinear relationship between the streaming potential and the streaming pressure. A reversal in the sign of the observed streaming potential occurs when streaming pressure, ΔP, changes higher than a certain value are applied. The results have been examined from the point of view of the theory of nonequilibrium thermodynamics.

Experimental Section

Materials. Zeokarb 225, Na^+ form (>200 mesh, 8% DVB having an exchange capacity of 4.8 mequiv/g by weight and a water content of 45–50%) obtained from Permutit Co., London, was used in the present investigation. It was converted into H^+, Ba^{2+}, and Al^{3+} forms by equilibrating it with 1 M hydrochloric acid, barium chloride, and aluminum chloride solutions, respectively, for over 24 h. Ordinary distilled water was redistilled over $KMnO_4$ before use. BDH methyl alcohol was used as such without further purification.

Membranes. The membranes were prepared by mechanical compression. A small quantity of araldite cement was mixed with a certain quantity of the ion exchanger and the mixture was compressed in a glass tube by using a mechanical arrangement reported earlier.[20] The ion exchanger was kept compressed for about 24 h. The membrane was then kept in the experimental solution for over 24 h for equilibration.

The cross-sectional area and the thickness of the membrane were 2.82×10^{-1} cm^2 and 0.90 cm, respectively. The average pore radius estimated from hydrodynamic and electroosmotic permeability[21] was found to be 1.74×10^{-4} cm.

Measurement of Streaming Potentials. Streaming potentials were measured with a Lindemann electrometer. Two coiled platinum electrodes were kept in contact with the two faces of the membrane. The permeant was streamed through the membrane under the action of a known difference of pressure applied by maintaining a constant difference in the level of the liquid across the membrane. Constancy of the applied pressure differences was ensured by using a constant pressure head.[22] A steady streaming potential was developed in about 4 min which was measured by the Lindeman electrometer calibrated earlier. The deflection in scale division was plotted against the potential difference. This curve was used for calibration purposes. The uncertainty in the measurement of streaming potential was of the order of ±1 mV.

Measurement of Membrane Conductivity. The resistance of the membrane equilibrated with permeant was measured with a Toshniwal conductivity bridge. Alternating current (frequency 50 Hz) was used. Platinum electrodes were used which were placed in contact with the two faces of the membrane. The conductivity of the membrane in the absence of streaming is different from that when streaming occurs, i.e.

$$(I/\Delta\phi)_{J_V=0} \neq (I/\Delta\phi)_{\Delta P=\text{constant}}$$

For the estimation of L_{22}/T, only the values of $(I/\Delta\phi)_{\Delta P=0}$ are needed since

$$(I/\Delta\phi)_{\Delta P=0} = L_{22}/T$$

From this the membrane conductivity or L_{22} was estimated.

Measurement of Electroosmotic Permeability. For checking the thermodynamic consistency of the data, electroosmotic permeability measurements were also carried out. The experimental procedure was the same as described elsewhere.[4] A known magnitude of electrical potential difference was applied across the equilibrated membrane through platinum electrodes with an electronically regulated power supply. The rate of the volume flux was estimated by noting the movement of the permeant in a horizontally placed graduated capillary tube of known cross-sectional area. All the measurements were taken at 30 ± 1 °C.

Measurement of pH. The pH of the solution before and after the experiment was measured with a pH meter obtained from Electronic & Industrial Instrument Co. Pvt.

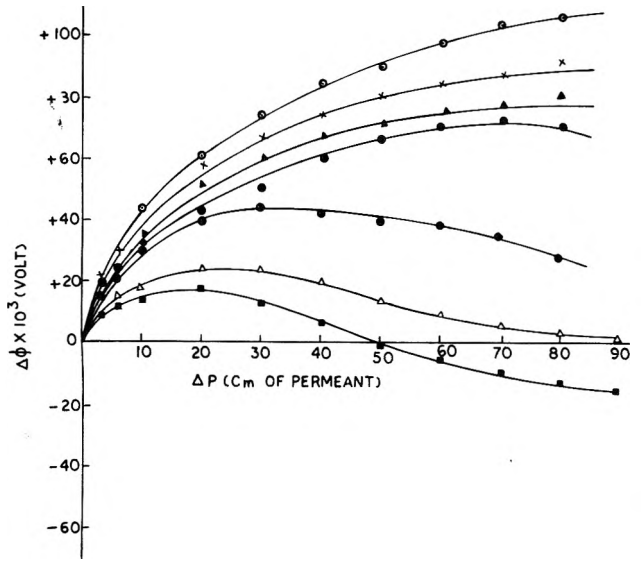

Figure 1. Dependence of streaming potential, $\Delta\phi$, on pressure difference, ΔP, for Zeokarb 225 (H^+ form)/methanol–water system: (⊙) 0.00 mole fraction of water; (×) 0.20 mole fraction of water; (▲) 0.40 mole fraction of water; (●) 0.60 mole fraction of water; (⊗) 0.80 mole fraction of water; (△) 0.95 mole fraction of water; (■) 1.00 mole fraction of water.

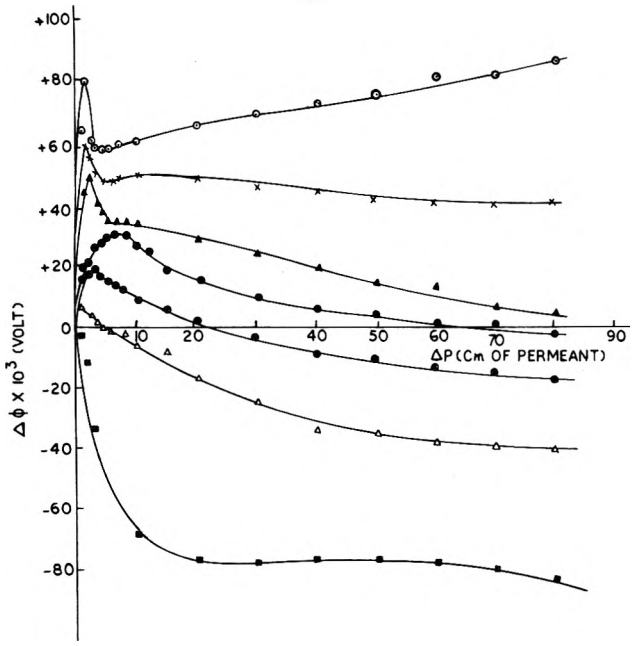

Figure 2. Dependence of streaming potential, $\Delta\phi$, on pressure difference, ΔP, for Zeokarb 225 (Na^+ form)/methanol–water system: (⊙) 0.00 mole fraction of water; (×) 0.20 mole fraction of water; (▲) 0.40 mole fraction of water; (●) 0.60 mole fraction of water; (⊗) 0.80 mole fraction of water; (△) 0.95 mole fraction of water; (■) 1.00 mole fraction of water.

Ltd. Hyderabad, which had a precision of ±0.05 pH units.

Results and Discussion

The results on streaming potentials are plotted in Figures 1–3 for Zeokarb 225 membranes in H^+, Na^+, and Ba^{2+} forms, respectively. A typical curve showing the buildup of streaming potential with time is shown in Figure 4. The buildup of streaming potential in almost all cases was found to obey the relation

$$\Delta\phi = (\Delta\phi)_0 e^{-\tau/t} \qquad (1)$$

$(\Delta\phi) = (\Delta\phi)_0$ when t is infinity. τ is the relaxation time. Figure 5 gives a typical result when log $(\Delta\phi)$ is plotted

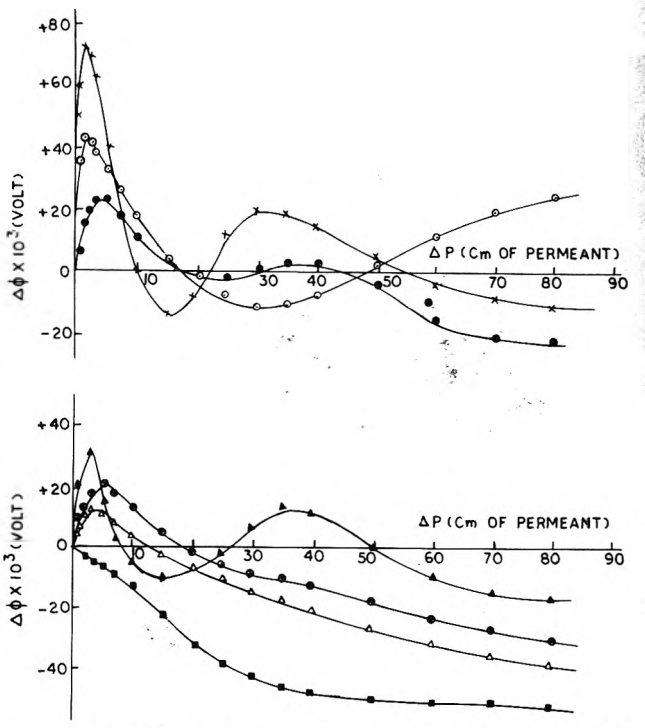

Figure 3. Dependence of streaming potential, $\Delta\phi$, on pressure difference, ΔP, for Zeokarb 225 (Ba^{2+} form)/methanol–water system: (⊙) 0.00 mole fraction of water; (×) 0.20 mole fraction of water; (▲) 0.40 mole fraction of water; (●) 0.60 mole fraction of water; (⊗) 0.80 mole fraction of water; (△) 0.95 mole fraction of water; (■) 1.00 mole fraction of water.

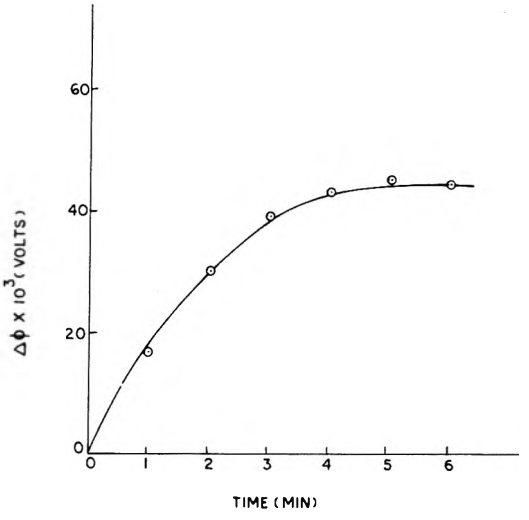

Figure 4. Build up of streaming potential, $\Delta\phi$, with time, t, for a typical result.

against the reciprocal of time; straight lines are obtained in all cases, confirming the validity of eq 1. The relaxation time for each case was determined from the slope. For streaming potentials between 10 and 100 mV, the value of was of the order of 0.5 min.

Figures 1–3 show that sign reversals and multiple sign reversals occur when streaming potentials are plotted against the streaming pressure. The behavior is exactly reproducible since the experiments were repeated a number of times and the measurements were made for increasing magnitudes of pressure differences, as well as decreasing magnitudes of pressure differences for the same direction of flow. The internal consistency of the data was further checked by releasing the pressure occasionally so that $\Delta P = 0$. The streaming potential returned to zero value. For the Ba^{2+} and Al^{3+} forms of resin, multiple sign

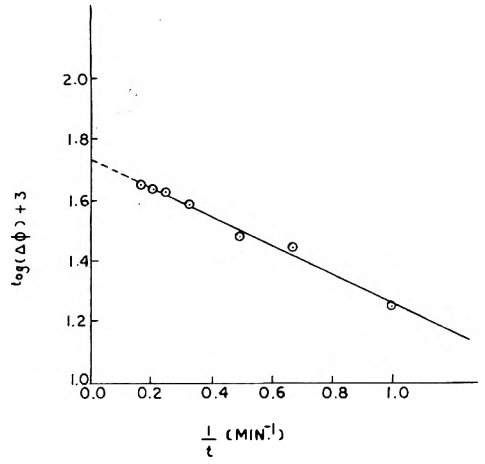

Figure 5. Test of validity of eq 1 for a typical result.

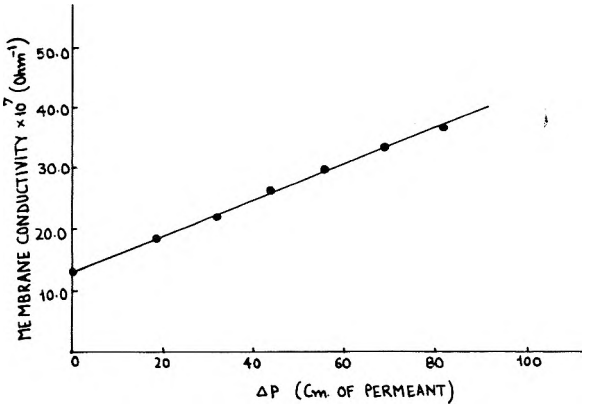

Figure 6. Dependence of membrane conductivity on streaming pressure for an Amberlite I.R.C.-50/methanol system.

reversals are observed. With the Na^+ form of the ion exchanger sign reversal for the streaming potential is observed for aqueous mixtures having mole fractions of water equal to 0.60, 0.80, and 0.95. However, the behavior of the H^+ form is simplest. Only one sign reversal is observed with the permeation of water. With alcohol–water mixtures no sign reversal is observed.

The observed electrokinetic behavior of the ion exchanger may be due to any one of the following factors:

(1) The heteroporous nature of the membrane.
(2) The swelling pressure of the membrane might be affected by the streaming pressure.
(3) Exchange of Na^+ and Ba^{2+} ions of the ion exchanger by hydrogen ions of the permeant.
(4) Changes in the ionization of the pore liquid on account of polarization effects.
(5) Changes in the dipole orientation in the electrical double layer.

It may be thought that the observed effects might be due to the heteroporous nature of the membrane. However, this does not seem to be the case since these effects are not observed with other heteroporous membranes.[18]

Regarding the swelling properties of the membrane, it is obvious that swelling may depend on the alcohol–water composition but it will not depend on ΔP. Swelling equilibria are a balance of opposing forces. The tendency of the polar and ionic constituents of the resin to surround themselves with solvent and thus to stretch the matrix meets with an increasing resistance by the latter. Equilibrium is attained when the elastic forces of the matrix balance the dissolution tendency. Swelling pressure, π, is defined as[23]

$$\pi = \bar{P} - P \tag{2}$$

where $\bar{P}$ is the pressure in the resin and P is the pressure in the external solution. The swelling pressure is of the order of tens of atmospheres and the streaming pressures are of the order of hundreds of centimeters of permeant, hence the swelling pressure is not likely to be affected in the streaming potential experiments.

Regarding the third alternative, it is known that a membrane tends to prefer counterions of high charge density and small size for electrostatic reasons and for steric reasons. The selectivity sequence of ions, particularly for a strong acid ion exchanger would be as follows:[24] $Ba^{2+} > Na^+ > H^+$. Accordingly, hydrogen ions cannot replace Na^+ or Ba^{2+} in the ion exchanger.

pH measurements of the permeating solution before and after the experiments show that the changes in pH are negligible and hence the observed electrokinetic effects cannot be ascribed to the ionization of the pore liquid on account of polarization effects.

Considering all the above alternatives, it follows that the observed streaming potential behavior would depend on the nature of the electrical double layer. It should be noted that Schmid's model[25] is a good approximation for ion-exchange membranes when the pore size is smaller than or equal to the thickness of the double layer. The average pore radius of the membrane under investigation here was found to be of the order of 10^{-4} cm, which is much larger than the double layer thickness. Hence, for the present case the double layer model is adequate enough. It has been pointed out earlier[19] that the orientation of dipoles affects the electroosmotic and electrophoretic properties of the ion exchanger. In the present case, it seems that the streaming pressure influences the orientation of the dipoles.

The measurements on electrical conductivity of an equilibrated membrane during streaming reveals that it depends on the applied streaming pressure. This is shown in Figure 6. This may be due to a change in the surface conductivity as a result of alteration in the double layer characteristics when the pressure is varied.

Analysis of the results of the H^+ form of the ion exchanger shows that the following nonlinear phenomenological equation for streaming current, I:

$$I = L_{21}\left(\frac{\Delta P}{T}\right) + L_{22}\left(\frac{\Delta\phi}{T}\right) + \frac{1}{2}L_{211}\left(\frac{\Delta P}{T}\right)^2 + L_{212}\left(\frac{\Delta\phi}{T}\right)\left(\frac{\Delta P}{T}\right) \tag{3}$$

holds good, where L_{21}, L_{22}, L_{211}, and L_{212} are phenomenological coefficients. Further, from electroosmosis data, one finds that[18] the following equation satisfies the data:

$$J_v = L_{11}\left(\frac{\Delta P}{T}\right) + L_{12}\left(\frac{\Delta\phi}{T}\right) + L_{112}\left(\frac{\Delta P}{T}\right)\left(\frac{\Delta\phi}{T}\right) + \frac{1}{2}L_{122}\left(\frac{\Delta\phi}{T}\right)^2 + \frac{1}{2}L_{1112}\left(\frac{\Delta P}{T}\right)^2\left(\frac{\Delta\phi}{T}\right) + \frac{1}{2}L_{1122}\left(\frac{\Delta P}{T}\right)\left(\frac{\Delta\phi}{T}\right)^2 \tag{4}$$

where J_v is the volumetric flux and L_{11}, L_{12}, L_{112}, L_{122}, L_{1112}, and L_{1122} are phenomenological coefficients. Since, except for $L_{12} = L_{21}$, all coefficients in eq 3 and 4 are independent, we cannot expect any correspondence of electroosmotic

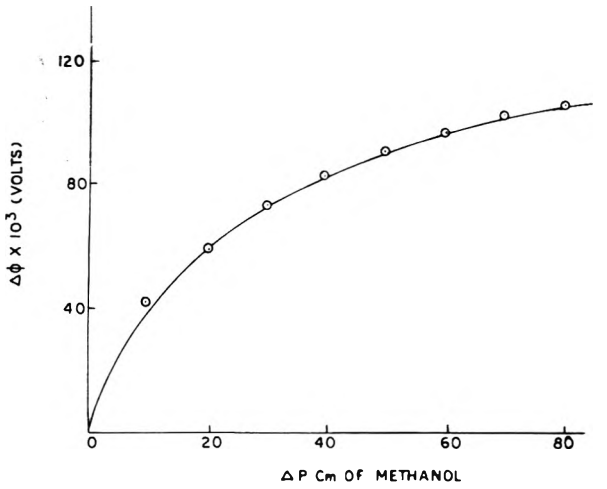

Figure 7. Test of the validity of eq 3 for Zeokarb 225 (H^+ form)/methanol system: (—) calculated curve; (⊙) experimental values.

and streaming potential data in the nonlinear region. When $\Delta P = 0$, we have from eq 3

$$L_{22}/T = I/\Delta\phi \tag{5}$$

L_{22} was estimated from the conductance of the membrane measured with a conductivity bridge. The other three phenomenological coefficients L_{21}, L_{211}, and L_{212} were obtained[26] from streaming potential data, by solving a set of simultaneous equations when the appropriate values for the variables were substituted into eq 3 when $I = 0$. Values of $(\Delta\phi)_{I=0}$ calculated by using these sets of coefficients have been compared with the experimental values of the streaming potentials for different values of ΔP in Figure 7. The agreement is satisfactory showing that eq 3 fits the data. Figure 8 shows how L_{21}, L_{22}, L_{211}, and L_{212} depend on the mole fraction of water.

In order to check the reliability of the streaming potential data, values of L_{21} estimated in the above manner

TABLE I: Phenomenological Coefficients for Zeokarb 225 (H^+ Form),[a] Methanol-Water System

Mole fraction of water	$(L_{21}/T)10^5$ $cm^3\ s^{-1}\ V^{-1}\ deg^{-1}$	$(L_{22}/T)10^7$ $ohm^{-1}\ deg^{-1}$	$(L_{211}/T^2)10^{17}$ amp $cm^4\ dyn^{-2}\ deg^{-2}$	$(L_{212}/T^2)10^{11}$ amp $cm^2\ dyn^{-1}\ V^{-1}\ deg^{-2}$
0.00	2.44	2.70	2.96	2.61
0.20	2.29	3.00	2.77	2.71
0.40	2.69	3.65	2.66	3.55
0.60	2.06	5.00	−1.26	1.52
0.80	2.58	5.80	−4.65	2.37
0.95	2.49	6.55	−5.89	4.20
1.00	4.52	8.50	−4.57	4.70

were compared with the values of L_{12} from electroosmotic data, with methyl alcohol as the permeant and a Zeokarb 225 (H^+ form) membrane. L_{12} was estimated using the following equation:

$$(J_v)_{\Delta P=0} = L_{12}\left(\frac{\Delta\phi}{T}\right) + \frac{1}{2}L_{122}\left(\frac{\Delta\phi}{T}\right)^2 \tag{6}$$

where $(J_v)_{\Delta P=0}$ is the volume flow when $\Delta P = 0$. L_{12} was estimated by plotting $(J_v)_{\Delta P=0}/\Delta\phi$ against $\Delta\phi$. The intercept yields L_{12}. According to the Onsager reciprocity relation $L_{12} = L_{21}$, we find

$$L_{12}/T = (1.82 \pm 0.09) \times 10^{-5}\ cm^3\ s^{-1}\ V^{-1}\ deg^{-1}$$

whereas from eq 3

$$L_{21}/T = 1.70 \times 10^{-5}\ cm^3\ s^{-1}\ V^{-1}\ deg^{-1}$$

showing thereby that the Onsagers relation is satisfied and that the streaming potential data are reliable.

The phenomenological equation (eq 3) has a restricted applicability for the Na^+, Ba^{2+}, and Al^{3+} forms of the ion exchangers. The values of the phenomenological coeffi-

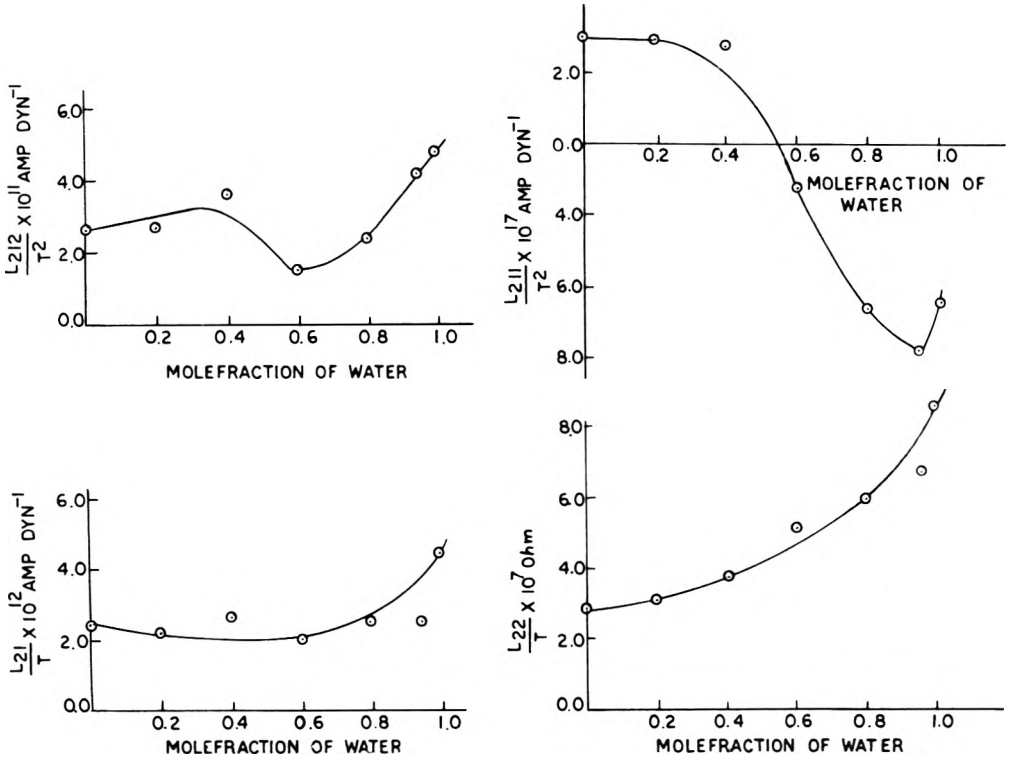

Figure 8. Dependence of phenomenological coefficients L_{21}, L_{22}, L_{211}, and L_{212} on mole fraction of water for Zeokarb 225 (H^+ form)/methanol–water system.

TABLE II: Phenomenological Coefficients for Zeokarb 225 (Na^+ Form)/Methanol-Water System

Mole fraction of water	$(L_{21}/T)10^5$ $cm^3\ s^{-1}\ V^{-1}\ deg^{-1}$	$(L_{22}/T)10^7$ $ohm^{-1}\ deg^{-1}$	$(L_{211}/T^2)10^{17}$ $amp\ cm^4\ dyn^{-2}\ deg^{-2}$	$(L_{212}/T^2)10^{11}$ $amp\ cm^2\ dyn^{-1}\ V^{-1}\ deg^{-2}$
0.00		1.10		
0.20		1.50		
0.40		2.25		
0.60	2.43	3.40	−0.89	−1.57
0.80	0.41	4.50	−1.03	−1.81
0.95	−2.41	5.25	−1.36	−1.93
1.00	15.47	7.10	−0.48	1.64

TABLE III: Phenomenological Coefficients for Zeokarb 225 (Ba^{2+} Form)/Methanol-Water System

Mole fraction of water	$(L_{21}/T)10^6$ $cm^3\ s^{-1}\ V^{-1}\ deg^{-1}$	$(L_{22}/T)10^7$ $ohm^{-1}\ deg^{-1}$	$(L_{211}/T^2)10^{16}$ $amp\ cm^4\ dyn^{-2}\ deg^{-2}$	$(L_{212}/T^2)10^{10}$ $amp\ cm^2\ dyn^{-1}\ V^{-1}\ deg^{-2}$
0.00		2.00		
0.20		2.40		
0.40		3.00		
0.60		4.05		
0.80	9.12	5.20	−1.39	−1.45
0.95	0.94	6.10	−1.88	−1.95
1.00	0.93	7.85	−3.05	−1.53

cients for different cases are recorded in Tables I–III for the H^+, Na^+, and Ba^{2+} forms, respectively. It should be noted that the results could not be analyzed in all cases.

Acknowledgment. Thanks are due to University Grants Commission, New Delhi (India) for supporting the investigation. The authors are grateful to Professor J. Th. G. Overbeek and Professor P. Mears for constructive comments.

References and Notes

(1) N. Lakshminarayanaiah and V. Subrahmanyan, *J. Polym. Sci., Part A2*, 4491 (1964).
(2) A. S. Tombalakian, *J. Phys. Chem.*, **72**, 1752 (1968).
(3) R. P. Rastogi, K. Singh, J. Singh, and R. Kumar, *Ind. J. Chem.*, **14A**, 729–731 (1976).
(4) R. P. Rastogi and K. M. Jha, *Trans. Faraday Soc.*, **62**, 585 (1966).
(5) D. K. Hale and D. C. McCauley, *Trans. Faraday Soc.*, **57**, 135 (1961).
(6) T. R. E. Kerssman, P. A. Stanbridge, and F. L. Tye, *Trans. Faraday Soc.*, **59**, 2129 (1963).
(7) A. S. Tombalakian, H. J. Barton, and W. F. Graydon, *J. Phys. Chem.*, **66**, 1006 (1962).
(8) M. Block and K. S. Spiegler, *J. Electrochem. Soc.*, **110**, 577 (1963).
(9) C. W. Carr, R. McClintock, and K. Sollner, *J. Electrochem. Soc.*, **109**, 251 (1962).
(10) A. F. Hadermann, P. F. Waters, and J. W. Weo, *J. Phys. Chem.*, **78**, 65 (1974).
(11) V. Saxen, *Wied. Ann.*, **47**, 46 (1892).
(12) G. Schmid and H. Schwarz, *Z. Electrochem.*, **56**, 35 (1952).
(13) G. Schmid, *Z. Electrochem.*, **56**, 181 (1952).
(14) Y. Toyoshima and H. Nozaki, *J. Phys. Chem.*, **73**, 2134 (1969).
(15) R. L. Blokhra and T. C. Singhal, *J. Phys. Chem.*, **78**, 2304 (1974).
(16) J. M. Diamond, *J. Physiol.*, **161**, 503–527 (1962).
(17) D. H. Smyth and E. M. Wright, *J. Physiol.*, **172**, 61–62 (1964).
(18) R. P. Rastogi, M. L. Srivastava, and S. N. Singh, *J. Phys. Chem.*, **74**, 2960 (1970).
(19) R. P. Rastogi, K. Singh, and J. Singh, *J. Phys. Chem.*, **79**, 2574 (1975).
(20) R. P. Rastogi, K. Singh, and S. N. Singh, *J. Phys. Chem.*, **73**, 1593 (1969).
(21) R. P. Rastogi, K. Singh, and S. N. Singh, *Ind. J. Chem.*, **6**, 46 (1968).
(22) R. P. Rastogi and K. M. Jha, *J. Phys. Chem.*, **70**, 1017 (1966).
(23) F. Helfferich, "Ion-Exchange", McGraw-Hill, New York, N.Y., 1962. p 101.
(24) R. E. Kesting, "Synthetic Polymeric Membranes", McGraw-Hill, New York, N.Y., 1971, pp 185–186.
(25) Reference 23, p 329.
(26) R. P. Rastogi, K. Singh, and M. L. Srivastava, *J. Phys. Chem.*, **73**, 46 (1969).

Kinetic Studies of the Complexation of Monovalent Sodium, Potassium, Rubidium, Thallium, and Silver Cations by Aqueous 15-Crown-5

Licesio J. Rodriguez,[1a] Gerard W. Liesegang,[1b] Robert D. White,[1c] Michael M. Farrow,[1b] Neil Purdie,[1d] and Edward M. Eyring*[1b]

Department of Chemistry, University of Utah, Salt Lake City, Utah 84112 *(Received June 14, 1977)*

Publication costs assisted by the Office of Naval Research and the Air Force Office of Scientific Research

A kinetic study of the rapid conformational equilibrium of aqueous 15-crown-5 (1,4,7,10,13-pentaoxacyclopentadecane) and of its complexation of monovalent sodium, potassium, rubidium, thallium, and silver cations at 25 °C in aqueous solution has been carried out by ultrasonic absorption in the 15–205-MHz frequency range. A concentration independent absorption with a maximum at 22.9 ± 0.4 MHz detected in aqueous solutions of 15-crown-5 with no cations added has been attributed to a conformational rearrangement of the crown ether. The kinetics of the complexation of the polyether with sodium, potassium, rubidium, silver, and thallium(I) ions were then investigated at various polyether and metal concentrations with concentration dependent relaxations occurring between ~15 and ~55 MHz. These data, together with the conformational rearrangement data, were analyzed in terms of a two step mechanism, $CR_1 \rightleftarrows CR_2$ (k_{12}, k_{21}) and $CR_2 + M^+ \rightleftarrows MCR_2^+$ (k_{23}, k_{32}), in which CR_2 denotes the conformation of the ether which participates in the complexation reaction, and MCR_2^+ is the complex ion. From kinetic considerations, it is possible to calculate both k_{23} and k_{32} and to demonstrate that K_{21} is much less than unity.

Introduction

Macrocyclic polyethers are ever more widely used in chemistry as complexing agents of certain cations, and much work has been done on the fundamental properties of these compounds and their metal complexes.[2] The kinetics of the complexation process have also received some attention,[3] mostly by NMR techniques.[3b-e]

Infrared,[4] x-ray crystallographic,[5] and ab initio model studies[6] indicate that the macrocyclic polyethers adopt different conformations in the complexed and uncom-

TABLE I: Experimental Absorption as (α/f^2) in Np cm^{-1} s^2 for Aqueous 15-Crown-5 at 25 °C

[15-crown-5] = 1.00 M		[15-crown-5] = 0.801 M		[15-crown-5] = 0.714 M	
$10^{17}(\alpha/f^2)_{exptl}$, Np cm^{-1} s^2	f, MHz	$10^{17}(\alpha/f^2)_{exptl}$, Np cm^{-1} s^2	f, MHz	$10^{17}(\alpha/f^2)_{exptl}$, Np cm^{-1} s^2	f, MHz
40.94	15.18	36.17	15.11	33.95	15.20
35.16	25.26	32.62	25.29	30.87	25.30
32.94	35.42	30.47	35.41	29.48	35.37
31.88	45.56	29.36	45.60	28.30	45.58
30.71	55.70	28.28	55.72	27.78	55.70
30.66	65.82	27.86	65.83	27.39	65.82
29.94	75.94	27.68	75.94	27.27	75.93
29.67	86.08	27.52	86.06	26.90	86.08
29.48	96.18	26.90	96.20	26.90	96.19
29.12	106.3	26.86	106.3	26.40	106.3
28.87	116.4	26.97	116.4	26.12	116.4
28.57	126.5	27.12	126.6	25.82	126.6
28.72	136.7	26.83	136.7	26.08	136.7
28.52	146.8	26.34	146.7	26.21	146.8
28.24	156.9	25.68	156.9	26.04	156.9
28.13	167.1	25.41	167.1	26.90	167.1
28.17	177.2	25.65	177.2	24.79	177.2
28.21	187.3	25.84	187.3	25.00	187.3
27.92	197.4	26.17	197.5	25.47	197.4
28.03	207.6			23.43	207.6
26.51	217.7				
26.16	227.8				
27.04	238.0				

plexed states. This was pointed out in Chock's pioneering temperature jump kinetic study of metal complexation by dibenzo-30-crown-10 in methanol.[3a] Previous studies in this laboratory[7,8] of 18-crown-6 in water, by an ultrasonic absorption technique, confirmed the existence of a concentration independent relaxation ($f_R \approx 101$ MHz) in aqueous solutions of that particular pure crown ether that was attributed to a conformational equilibrium.

15-Crown-5 has a similar geometry to 18-crown-6, although ring size and hole diameter of the former are smaller. The smaller ring size will cause 15-crown-5 to be more rigid and, as has been shown,[9] complexation is less favored. These facts suggest that 15-crown-5 may undergo a slower conformational change than 18-crown-6, so much so that it might interfere with and slow down cation complexation. This possibility is considered below along with a comparison between the kinetics of cation complexation by 15-crown-5 and 18-crown-6. Finally, in aqueous 18-crown-6 complexation, the enhanced stability of K^+ and Tl^+ complexes is attributable to their slower decomplexation rates. Since aqueous 15-crown-5 has no apparent cation selectivity sequence,[9] it is of interest to see whether the rates of decomplexation are also devoid of selectivity patterns.

Experimental Section

Measurements of the ultrasonic absorption were carried out at a temperature of 25.0 ± 0.1 °C over the frequency range 15–205 MHz using a laser acousto-optic technique.[10] The argon ion laser was operated at the 514.5-nm green line, and the acoustic transducer was a gold-plated, 5-MHz fundamental frequency, x-cut quartz crystal operated at odd harmonics over the frequency range. The acoustic beam was modulated under computer control to facilitate synchronous detection of the resulting optical signal, and adjustments in the ultrasonic transducer position, mirror position, and orientation of the sample cell plane to the Bragg angle were all computer controlled.

Solutions were prepared using deionized, redistilled water. The 15-crown-5 (Parish Chemical Co., Provo, Utah) was redistilled under vacuum (bp range collected 125–140 °C at 0.5 mmHg [100–135 °C at 0.2 mmHg[11]]). Stock solutions were prepared by volume at 25 °C using a density of the pure product: 1.095 ± 0.001 g/mL.[12] The inorganic ions were all of analytical reagent grade. Sodium, potassium, and rubidium ions were added as chloride salts; thallium(I) and silver ions were in the form of nitrates.

TABLE II: Relaxation Parameters from Computer Analysis for Aqueous 15-Crown-5 at 25 °C[a]

[15-Crown-5], M	$f_{r,I}$,[c] MHz	$10^{17}A$ Np cm^{-1} s^2	$10^{17}B$ Np cm^{-1} s^2	10^{18}(rms)[b] Np cm^{-1} s^2
1.00	23.1	16.3	28.3	1.0
0.801	22.5	14.8	26.3	0.7
0.714	23.1	11.9	25.8	1.0

[a] All symbols as defined in text. [b] Root-mean-square deviation. [c] $f_{r,I}$(average) = 22.9 ± 0.4 MHz.

Results

Ultrasonic absorption data, expressed as total absorption $(\alpha/f^2)_T$ Np s^2 cm^{-1}, for the pure 15-crown-5 aqueous solutions at different concentrations are presented in Table I. Analyses of the data were made in terms of a relaxational and a nonrelaxational contribution to the total absorption in accordance with the expression

$$(\alpha/f^2)_T = A[1 + (f/f_R)^2]^{-1} + B \quad (1)$$

where A is the amplitude of the relaxational process, f and f_R are the experimental and relaxational frequencies respectively, and B is the nonrelaxational background absorption. This last parameter B is meant to consist of classical solvent absorption plus contributions from very high frequency solvent-relaxational processes. A value of B equal to 21.7×10^{-17} Np s^2 cm^{-1} is commonly reported from measurements made over the frequency range of this study. The experimental data fit eq 1 very well. The calculated relaxational parameters, summarized in Table II, give evidence for the existence of a concentration independent relaxation at a frequency of 22.9 ± 0.4 MHz. Background absorption values show a dependence on solution concentration which is typical of, and is to be expected from, solutions of increased viscosity over water. The single relaxational process is appropriately assigned to the rapid equilibrium interconversion between two structural forms of the polyether in solution.

TABLE III: Relaxation Parameters from Computer Analysis

$[NaCl]_0$, M	$[15\text{-Crown-}5]_0$, M	$f_{r,II}$, MHz	$10^{17}A$	10^{18}(rms)
0.217	0.0953	17.0	284	1.6
0.327	0.0905	19.6	244	1.5
0.417	0.0906	21.9	224	0.9
$[KCl]_0$, M	$[15\text{-Crown-}5]_0$, M	$f_{r,II}$, MHz	$10^{17}A$	10^{18}(rms)
0.100	0.100	21.9	77.4	1.4
0.200	0.100	25.7	82.1	1.1
0.306	0.100	32.1	68.2	1.0
0.404	0.100	38.4	55.6	0.9
$[RbCl]_0$, M	$[15\text{-Crown-}5]_0$, M	$f_{r,II}$, MHz	$10^{17}A$	10^{18}(rms)
0.0959	0.117	31.1	39.6	0.7
0.180	0.117	35.2	51.6	0.7
0.278	0.117	37.6	50.5	2.4
0.466	0.117	44.3	43.5	0.8
$[AgNO_3]_0$, M	$[15\text{-Crown-}5]_0$, M	$f_{r,II}$, MHz	$10^{17}A$	10^{18}(rms)
0.115	0.117	24.4	184	1.2
0.215	0.117	31.8	154	1.6
0.359	0.117	43.7	85.5	1.1
0.443	0.105	55.7	51.5	0.5
$[TlNO_3]_0$, M	$[15\text{-Crown-}5]_0$, M	$f_{r,II}$, MHz	$10^{17}A$	10^{18}(rms)
0.137	0.120	20.2	222	0.9
0.170	0.120	23.5	184	1.9
0.263	0.0900	31.1	85.9	1.4
0.320	0.102	35.4	81.3	0.9

Data from ultrasonic absorption measurements on aqueous mixtures of Na^+, K^+, Rb^+, Ag^+, and Tl^+ salts with 15-crown-5 solutions as a function of cation concentration have been incorporated into an Appendix available as supplementary material. (See paragraph at end of text regarding supplementary material.) Analyses according to eq 1 showed an excellent correspondence between the data for each solution and the theoretical equation for a single relaxation expressed as the root mean square (rms) deviation in Table III. Table III also lists the relaxation parameters A and f_R. In the analyses, B was left as a variable quantity. The values of B which provided the best fit were found to differ only slightly from the background value for pure water. The relaxation frequency for the 15-crown-5 conformation equilibrium falls within the range of those relaxation frequencies calculated for the equilibria between the metal ions and the polyether. Coupling between the steps is possible and is considered in the interpretation. In a parallel study of 18-crown-6 with the same metal ions,[7,8] f_R for the conformation equilibrium was observed to be ~101 MHz, and coupling between relaxations was not found in the interpretation.

Distinguishing the two conformers of 15-crown-5 by CR_1 and CR_2 as before and arbitrarily taking CR_2 to be the one which preferentially complexes with the metal ions, the basic reaction scheme used for data interpretation is the two-step process

$$CR_1 \underset{k_{21}}{\overset{k_{12}}{\rightleftharpoons}} CR_2 \tag{2}$$

$$M^+ + CR_2 \underset{k_{32}}{\overset{k_{23}}{\rightleftharpoons}} MCR_2^+ \tag{3}$$

The concentration independent relaxation time for the conformation change in pure crown solutions is τ_1, which relates to the specific rate constants through the equation

$$\tau_1^{-1} = k_{12} + k_{21} \tag{4}$$

Reactions 2 and 3 are obviously kinetically interdependent through the commonality of CR_2, but the question remains as to how intimately they are coupled. Very close coupling of two discrete steps can, within the error limits of the absorption measurements, produce what appears to be a single relaxation. We have explored the two extreme interpretations, viz. the rigorous case of full coupling, followed by the totally uncoupled case, and have compared the results below.

Making no assumptions regarding the relaxation times, rate constants, absorption amplitudes, etc., the result of the secular determinant for the above reaction scheme is

$$\tau^{-2} - S\tau^{-1} + P = 0 \tag{5}$$

where S and P are the sum and product of the roots.

$$S = k_{12} + k_{21} + k_{32} + k_{23}\left\{\frac{1}{1+K_{21}}([\overline{CR}_1] + [\overline{CR}_2]) + [\overline{M}^+]\right\} \tag{6}$$

$$P = k_{12}k_{23}([\overline{CR}_1] + [\overline{CR}_2] + [\overline{M}^+]) + k_{32}(k_{12} + k_{21}) \tag{7}$$

and K_{21} in this context is k_{21}/k_{12}. The extent of coupling is determined by the magnitudes of k_{21} and $k_{23}[\overline{M}^+]$. Substitution for $(k_{12} + k_{21})$ with τ_1^{-1} and for k_{12} with $\tau_1^{-1}/(1 + K_{21})$ in eq 6 and 7 gives the eq 8 in k_{23} and k_{32} in which

$$\tau^{-1} = k_{32} + k_{23}\left\{\frac{([\overline{CR}_1] + [\overline{CR}_2])}{1+K_{21}} + \left(\frac{\tau^{-1} - [\tau_1^{-1}/(1+K_{21})]}{\tau^{-1} - \tau_1^{-1}}\right)[\overline{M}^+]\right\} \tag{8}$$

$\tau^{-1} = 2\pi f_r$ is the reciprocal relaxation time calculated from the experiment. The bars indicate that concentrations of reactant species are those at equilibrium. Equation 8 can be further rearranged to contain only the rate constants as unknowns:

$$\frac{\tau^{-1} - \tau_1^{-1}}{[\overline{M}^+]} = k_{32}\left\{\frac{(\tau^{-1} - \tau_1^{-1})(1 + K_T([\overline{CR}_1] + [\overline{CR}_2])) - \tau_1^{-1}[\overline{M}^+]K_T}{\tau^{-1}[M^+]}\right\} + k_{23} \tag{9}$$

K_T is the experimentally determined overall complexation constant

$$K_T = \frac{[\overline{MCR}_2^+]}{[\overline{M}^+][\overline{CR}_1 + \overline{CR}_2]} \tag{10}$$

previously measured for each cation by Izatt et al.[9] Results from the graphical solutions of eq 9, Figure 1, are given in Table IV. The equilibrium constant K_{23} for the second step, eq 3, is given by k_{23}/k_{32}, and K_{21} can then be evaluated after substitution into eq 10 from the equation

$$K_{21} = [(K_{23}/K_T) - 1] \tag{11}$$

Calculated values of K_{23} agree with experimental values of K_T to within the error limits of the latter; therefore, K_{21} cannot be calculated with acceptable precision. Considering the error margins in the K_T values, it is only possible to say that $K_{21} \leq 0.1$.

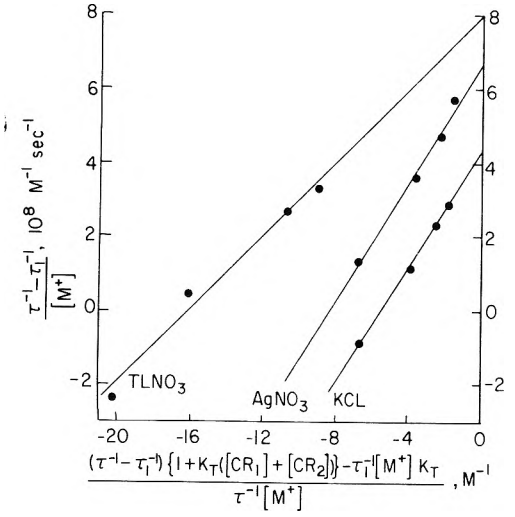

Figure 1. Plot of the silver, thallium, and potassium ultrasonic absorption data of Table III in terms of eq 9. Data for sodium and rubidium have not been included for clarity.

TABLE IV: Rate Constants and Equilibrium Constant for Complexation by 15-Crown-5 in Aqueous Solution at 25 °C When Coupling is Assumed

Cation	k_{23}, M^{-1} s^{-1}	k_{32}, s^{-1}	log K_{23} (calcd)	log K_T[a]
Na^+	2.6×10^8	5.1×10^7	0.71	0.70 ± 0.04
K^+	4.3×10^8	7.8×10^7	0.74	0.74 ± 0.04
Rb^+	4.4×10^8	1.4×10^8	0.50	0.6 ± 0.1
Tl^+	8.0×10^8	5.0×10^7	1.20	1.23 ± 0.04
Ag^+	6.7×10^8	8.2×10^7	0.91	0.94 ± 0.04

[a] Reference 9.

TABLE V: Rate Constants and Equilibrium Constant for Complexation by 15-Crown-5 in Aqueous Solution at 25 °C, No Coupling Assumed

Cation	k_{23}', M^{-1} s^{-1}	k_{32}, s^{-1}	log K_{23} (calcd)
Na^+	2.4×10^8	4.8×10^7	0.67
K^+	4.3×10^8	7.8×10^7	0.74
Rb^+	4.6×10^8	1.2×10^8	0.58
Tl^+	7.1×10^8	4.2×10^7	1.23
Ag^+	6.4×10^8	7.4×10^7	0.94

In the uncoupled case, τ_1 is considered to make no contribution to the observed relaxation times τ. The equation[13] derived for the 18-crown-6 complexation reactions was used in the interpretation,[7,8] i.e.

$$\tau^{-1} = k_{23}'\{[\overline{CR}_1] + [\overline{CR}_2] + [\overline{M}^+] + K_T^{-1}\} \quad (12)$$

Graphical presentations of the data according to eq 12 are shown in Figure 2, and the resultant rate and equilibrium constants are given in Table V.

Discussion

The backward rate constants k_{32} for each cation are essentially independent of the method of analysis (coupled or uncoupled), with the greatest discrepancy between the values occurring for Ag^+ and Tl^+ ions. The discrepancy amounts to ca. 20% and would usually be considered an acceptable limit for constancy in a rate constant measured using fast reaction techniques. Likewise, k_{23} and k_{23}' are within the acceptable limits of constancy, with the possible exception of Tl^+. Although numerically equivalent, k_{23} and k_{23}' are not kinetically equivalent in terms of the assumed mechanism. In fact, $k_{23}' = k_{23}/(1 + K_{21})$. Only if K_{21} is very small is it possible that $k_{23}' = k_{23}$. Both interpretations of the data, as coupled and as uncoupled reactions, yield the same result that $K_{21} << 1$. We might, therefore, conclude that coupling between the steps is unimportant

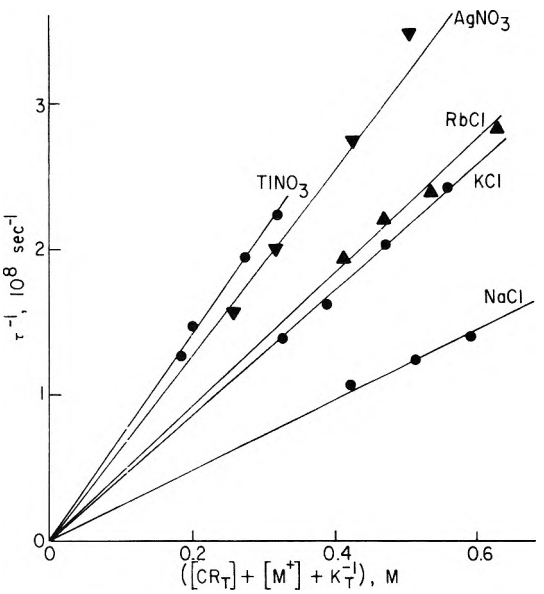

Figure 2. Plot of all the ultrasonic absorption data of Table III in terms of eq 12.

in that the coefficient of the $[\bar{M}^+]$ term in eq 8 is essentially unity. Coupling was not considered in the analogous 18-crown-6 metal complexation equilibria. In that instance, however, the decision to neglect coupling could be made from the experimental observation that the amplitude of the conformational equilibrium relaxation decreased as the concentrations of free or uncomplexed 18-crown-6 was diminished by complexation. Whether an analogous diminution of amplitude transpired on the complexation of 15-crown-5 could not be established since the relaxation times for both steps are similar in magnitude. The apparent lack of coupling between relaxations involving 15-crown-5 might indicate that again the amplitude of the conformational equilibrium relaxation has been reduced to negligible proportions compared to the amplitude for the complexation step. This is a significant conclusion because it should be pointed out that, assuming a maximum value of 0.1 for K_{21}, k_{21} is of the same magnitude as $k_{23}[\bar{M}^+]$, which would indicate coupling.

It is generally believed that the mechanism for complexation of crown ethers by metal ions is not a diffusion-controlled process. Nor does the mechanism seem to fit a dissociative scheme where the loss of the first coordinated solvent molecule is rate determining. The tendency is to believe in a stepwise loss of an indeterminate number of solvent molecules from the first solvation sphere of the cation, accompanied perhaps by a second conformational change in the ether on complexation. The present kinetic results for 15-crown-5 complexation appear to fall within this general scheme.

Comparing the kinetic data for 18-crown-6 and 15-crown-5, the values for k_{23} are constant for each of the alkali ions, which suggests that loss of cation solvation is the predominant detail in the mechanism, more so than change in ligand size or rigidity. Size and rigidity are important whenever the cation is nonsymmetrical with respect to bonding, as it is for Tl^+ and Ag^+, reducing the value of k_{23} in going from 18-crown-6 to 15-crown-5. The slower rate of complexation is indicative of a more stringent steric requirement for the smaller cyclic structure as it strains to fit the geometry of the central cation.

The most striking contrast in kinetic parameters between the ligands is found in the values of k_{32}, the decomplexation rate constants. Whereas k_{32} values vary by a factor of 16 for 18-crown-6, the spread in k_{32} values for

15-crown-5 is only a factor of 3. It is believed that variations in k_{32} account for the variation in the overall complexation constants K_T. The relative constancy in k_{32} for 15-crown-5 is consistent with the observed nonselectivity of the ligand in complexing with the univalent ions.

Without exception, k_{32} has increased in going from 18-crown-6 to 15-crown-5; that is, decomplexation is facilitated by the smaller ring size and increased rigidity. This, too, is consistent with the observation that K_T is greater for the 18-crown-6 complexes. k_{32} increases monotonically with cation radius for the alkali metal ions with an increase over the values for 18-crown-6 by a factor of 10–20 for the largest ions. For Ag^+ and Tl^+, the simple relation between rate and ion size is lost, indicative again of the increasingly important steric or geometric factors in relation to a simple size factor.

Acknowledgment. This work was sponsored by a contract from the Office of Naval Research and by Grant No. AFOSR 73-2444C from the Directorate of Chemical Sciences, Air Force Office of Scientific Research.

Supplementary Material Available: An appendix containing experimental ultrasonic absorption data (expressed in Np cm^{-1} s^2) for aqueous KCl, $TlNO_3$, NaCl, RbCl, and $AgNO_3$ with 15-crown-5 at 25 °C (5 pages). Ordering information is given on any current masthead page.

References and Notes

(1) (a) On leave from the University of Salamanca, Spain; (b) University of Utah; (c) University of Idaho; (d) Oklahoma State University.
(2) (a) C. J. Pedersen, *J. Am. Chem. Soc.*, **89**, 7017 (1967); (b) J. J. Christensen, D. J. Eatough, and R. M. Izatt, *Chem. Rev.*, **74**, 351 (1974); (c) J. H. Fendler and E. J. Fendler, "Catalysis in Micellar and Macromolecular Systems", Academic Press, New York, N.Y., 1975, p 389 *ff*; (d) K. H. Wong, K. Yagi, and J. Smid, *J. Membr. Biol.*, **18**, 379 (1974); (e) J. M. Lehn, *Struct. Bonding (Berlin)*, **16**, 1 (1973); (f) D. J. Cram and J. M. Cram, *Science*, **183** 803 (1974); (g) S. G. A. McLaughlin, G. Szabo, S. Ciani, and G. Eisenman, *J. Membr. Biol.*, **9**, 3 (1972).
(3) (a) P. B. Chock, *Proc. Natl. Acad. Sci. U.S.A.*, **69**, 1939 (1972); (b) M. Shporer and Z. Luz, *J. Am. Chem. Soc.*, **97**, 665 (1975); (c) E. Shchori, J. Jagur-Grodzinski, Z. Luz, and M. Shporer, *ibid.*, **93**, 7133 (1971); (d) E. Shchori, J. Jagur-Grodzinski, and M. Shporer, *ibid.*, **95**, 3842 (1973); (e) T. P. I. and E. Grunwald, *ibid.*, **96**, 2879 (1974).
(4) J. Dale and P. O. Kristiansen, *Acta Chem. Scand.*, **26**, 148 (1972).
(5) M. A. Bush and M. R. Truter, *Chem. Commun.*, 1439 (1970).
(6) A. Pullman, C. Giessner-Prettre, and Y. V. Kruglak, *Chem. Phys. Lett.*, **35**, 156 (1975).
(7) G. W. Liesegang, M. M. Farrow, N. Purdie, and E. M. Eyring, *J. Am. Chem. Soc.*, **98**, 6905 (1976).
(8) G. W. Liesegang, M. M. Farrow, F. Arce Vazquez, N. Purdie, and E. M. Eyring, *J. Am. Chem. Soc.*, **99**, 3240 (1977).
(9) (a) R. M. Izatt, D. J. Eatough, and J. J. Christensen, *Struct. Bonding (Berlin)*, **16**, 172 (1973); (b) R. M. Izatt, R. E. Terry, B. L. Haymore, L. D. Hansen, N. K. Dailey, A. G. Avondet, and J. J. Christensen, *J. Am. Chem. Soc.*, **98**, 7620 (1976).
(10) M. M. Farrow, S. L. Olsen, N. Purdie, and E. M. Eyring, *Rev. Sci. Instrum.*, **47**, 657 (1976).
(11) F. L. Cook, T. C. Caruso, M. P. Byrne, C. W. Bowers, D. H. Speck, and C. L. Liotta, *Tetrahedron Lett.*, **46**, 4029 (1974).
(12) Density measured in this laboratory.
(13) One implicit assumption for this case is that τ_1^{-1}, the reciprocal relaxation time for aqueous solutions of pure polyether, is indeed one of the roots of eq 5. This is not mathematically true, and therefore, although eq 12 agrees on this basis with eq 7, eq 12 does not agree with eq 6, unless K_{21} is very small. This condition, already demonstrated in the coupled case, is necessary to prevent extensive coupling between the two reactions.

Ultrasonic Absorption Studies of Aqueous Solutions of *tert*-Butyl Alcohol

Kiyoshi Tamura, Michio Maekawa, and Tatsuya Yasunaga*

Department of Chemistry, Faculty of Science, Hiroshima University, Hiroshima 730, Japan *(Received December 22, 1975; Revised Manuscript Received June 6, 1977)*

Ultrasonic absorption measurement of aqueous solutions of *tert*-butyl alcohol reveals two relaxation phenomena in the observed frequency range (4.5–220 MHz). The relaxation frequencies exhibit minima near concentrations where the corresponding relaxation amplitudes show maxima. The relaxation absorptions are interpreted by adopting a clathrate-hydrate model for the solution; the faster relaxation process is ascribed to the formation reactions of a merged clathrate hydrate, and the slower one to association reactions of alcohol molecules. After a simulation analysis, the following reaction mechanism is proposed: $AB_l + A \rightleftharpoons C \rightleftharpoons$ (fast) $^1/_2C_2$ and $3A \rightleftharpoons A_2 + A \rightleftharpoons$ (fast) A_3 where A and B are the alcohol and water molecules, respectively; AB_l is the single clathrate, and C and C_2 are the merged ones. The hydration number, l, is determined to be 25, and kinetic parameters are obtained. The results explain fairly well the observed relaxation absorptions.

Introduction

The ultrasonic absorption properties of aqueous solutions of alcohols have been the object of recent interest in relation to the effects of these compounds on water structure. The acoustic properties of these solutions are characterized by the fact that the sound absorption and the velocity of sound exhibit their maxima at some definite concentrations.[1-4] Moreover, the recent studies[5-7] have revealed that aqueous solutions of some aliphatic alcohols show two relaxation phenomena in MHz frequency range and also that the relaxation frequencies have minima near the peak sound absorption concentration (PSAC). Nevertheless, the absorption mechanism has been interpreted only in a qualitative way. Barfield and Schneider,[8] Andreae et al.,[9] and Romanov and Solovyev[10] proposed some interpretations for the ultrasonic absorption of aqueous nonelectrolyte solutions. However, these mechanisms were criticized by other workers.[11]

Study of the accumulated data reveals a direct correlation between the sound absorption phenomena and the hydrophobic character of the solute substance.[12] Bruun et al.[5] pointed out the following features: (a) an absorption maximum is generally observed in aqueous solutions of substances containing nonpolar groups, but it is absent in aqueous solutions of urea and formamide; (b) the absorption maximum is more pronounced, the larger the

TABLE I: Ultrasonic Relaxation Parameters and Related Properties for Aqueous Solution of *tert*-Butyl Alcohol at 25 °C

C_A, M	X_A	ρ, g cm^{-3}	c, m s^{-1}	f_{r1}, MHz	f_{r2}, MHz	A_1[a]	A_2[a]	B[a]	α_η/f^2[a]
0.00	0.0000	0.9970	1497.7					21.2	7.01
1.50	0.0301	0.9808	1594.3					32.7	10.4
2.03	0.0424	0.9758	1611.1	90		100		49.5	12.1
2.28	0.0486	0.9738	1609.6	75		288		57.6	13.1
2.43	0.0524	0.9720	1608.0	69		507		34.5	14.2
2.49	0.0540	0.9714	1606.7	62		564		89.8	13.8
2.61	0.0573	0.9675	1595.0	62		639		121	15.1
2.76	0.0614	0.9654	1586.4	68	11	676	452	124	16.3
3.35	0.0786	0.9561	1550.3	60	9.2	898	806	184	19.7
4.00	0.0999	0.9465	1519.0	60	8.7	937	1150	221	24.5
5.01	0.141	0.9243	1453.6	74	9.3	640	1210	205	35.4
6.01	0.192	0.9005	1393.2	69	9.0	451	850	214	47.7
7.02	0.261	0.8791	1343.6	80	9.1	299	546	184	59.1
8.02	0.358	0.8527	1286.7	114	12	147	158	174	72.5
10.5	1.000	0.7800	1129.0					322	117

[a] 10^{-17} s^2 cm^{-1}.

nonpolar part of the substance; (c) the maximum is located in the water-rich concentration range and located at lower concentrations, the larger the nonpolar group. These characteristics seem helpful in determining the absorption mechanism of aqueous solutions of alcohol.

In the present work, the ultrasonic absorption of aqueous solutions of *tert*-butyl alcohol was studied, since this alcohol has bulky methyl groups and the solution exhibits especially large relaxation absorptions. The purpose of this work is to elucidate the absorption mechanism through a kinetic treatment of the relaxation processes.

Experimental Section

tert-Butyl alcohol of a guaranteed reagent grade was purified once by distillation. The purity was verified to be not less than 99.9% by gas chromatography. Water was purified by distillation after deionization. Sample solutions were prepared by weight.

The ultrasonic absorption was measured in the frequency range 4.5–220 MHz using the pulse technique,[13] and the velocity of sound at 1.92 MHz using the sing-around method. The density and viscosity of the solution were determined by using a standard pycnometer and viscometer, respectively. All the measurements were carried out at 25.0 ± 0.1 °C.

Results

The sound absorption spectra composed of two relaxation processes are expressed by

$$\frac{\alpha}{f^2} = \frac{A_1}{1 + (f/f_{r1})^2} + \frac{A_2}{1 + (f/f_{r2})^2} + B \qquad (1)$$

where α is the absorption coefficient, and f the frequency of the sound; f_{ri} and A_i (i = 1, 2) are the relaxation frequencies and amplitudes, respectively; B is the high frequency value of α/f^2.

Figure 1 shows representative sound absorption spectra for aqueous solutions of *tert*-butyl alcohol. The spectra of the solutions at alcohol concentrations not higher than 2.61 M show characteristics of a single relaxation process (A_2 = 0), while those at concentrations not lower than 2.76 M are expressed by the equation for two relaxation processes. The double relaxation spectra were analyzed by using a non-linear least-squares routine. Table I shows the absorption parameters, together with the velocity of sound, c, and the density, ρ. Here, C_A is the molar concentration, and X_A the mole fraction, of alcohol.

As shown in Table I, the relaxation amplitudes A_1 and A_2 exhibit maxima at concentrations of about 4 M. The concentration dependence of the relaxation frequencies is shown in Figure 2. The f_{ri} values exhibit broad minima

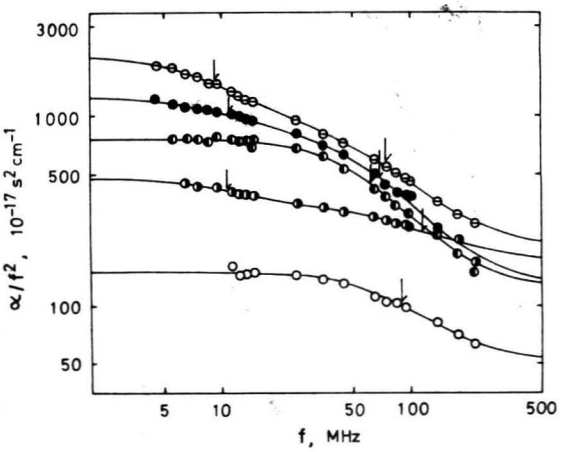

Figure 1. Ultrasonic absorption spectra for aqueous solutions of *tert*-butyl alcohol at 25 °C. The solid curves are the calculated ones. The arrows indicate relaxation frequencies: (○) 2.03 M; (◐) 2.61 M; (●) 2.76 M; (⊖) 5.01 M; (◑) 8.02 M.

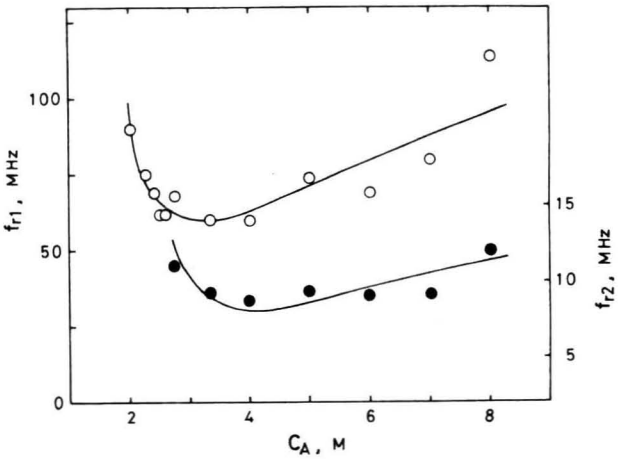

Figure 2. Graphs of f_{ri} vs. C_A plot for aqueous solutions of *tert*-butyl alcohol. The solid curves express the calculated ones: (○) f_{r1}; (●) f_{r2}.

at the concentrations which are somewhat lower than those where the corresponding A_i values show maxima. Figure 3 shows the maximum excess absorptions per wavelength, μ_{mi} ($= A_i f_{ri} c/2$), against C_A. The μ_{mi} values exhibit similar trends to those of the corresponding A_i values. Table I includes also the classical absorption, α_η/f^2, calculated by the Stokes relation

$$\alpha_\eta/f^2 = 8\pi^2 \eta/3\rho c^3 \qquad (2)$$

where η is the viscosity of the solution. Over the con-

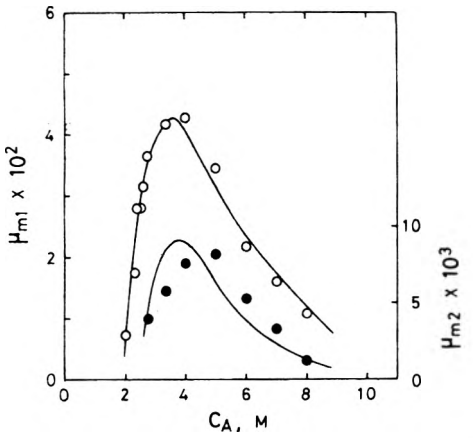

Figure 3. Graphs of μ_{mi} vs. C_A plot for aqueous solution of *tert*-butyl alcohol. The solid curves express the calculated ones: (O) μ_{m1}; (●) μ_{m2}.

centration range where relaxation absorptions are observed, the parameter B is much larger than the classical absorption and exhibits trends almost similar to that of A_1. The velocity of sound shows a maximum near the concentration where the A_1 and B values start to increase.

Interpretation of Results

In order to explain the relaxation absorptions, we must precisely know the solution structure or the nature of the species in solution. While NMR and dielectric relaxation studies[14-17] have given us some information on the molecular processes in this system, these results concern processes much faster than those observed here. Therefore, we are forced to assume appropriate solution structure or species, perform necessary calculations, and compare the calculated results with the observed ones.

Since no relaxation effects are observed in pure *tert*-butyl alcohol in the frequency range studied, the relaxation absorptions of the solution should be ascribed to processes involving the interactions between alcohol and water molecules. As shown in Table I, the sound absorption is, at low alcohol concentrations, not much different from that for pure water, but it increases steeply as more alcohol is added to the solution. This phenomenon is similar to those found for solutions of some alcohols, where the plateau length decreases with an increase in size of the nonpolar part of the alcohol.[12] For interpreting this phenomenon together with the facts pointed out by Bruun et al.,[5] the clathrate-hydrate model[6,7] seems to be adequate; i.e., each alcohol molecule is enclathrated in a water cage at low alcohol concentrations, but at high concentrations the amount of water is insufficient to accomodate all the alcohol molecules in a single water cage and two or more alcohol molecules enter a merged clathrate. The relaxation processes are plausibly associated with the merging processes. Furthermore, we must also expect the presence of bare alcohol molecules which would be predominant in the high concentration region. The ultrasonic absorption studies[18-20] on solutions containing some alcohols in organic solvents have revealed relaxation effects in the MHz frequency range, and the effects were ascribed to alcohol association reactions. This fact suggests the possibility that the relaxation processes in the present system also involve association reactions of *tert*-butyl alcohol, especially in the high concentration region.

Based on the above-mentioned facts, a quantitative interpretation of the observed relaxation absorptions was tried. After a number of reaction mechanisms had been examined, the following was found to be consistent with the characteristics of the observed relaxation absorptions:

$$AB_l + A \underset{k_{-11}}{\overset{k_{11}}{\rightleftharpoons}} C \overset{K_{12}}{\underset{(m-1)C}{\rightleftharpoons}} C_m \tag{3}$$

$$2A \underset{k_{-21}}{\overset{k_{21}}{\rightleftharpoons}} A_2 \overset{K_{22}}{\underset{(n-2)A}{\rightleftharpoons}} A_n \tag{4}$$

where A and B are the alcohol and water molecules, respectively; AB_l is the single clathrate, and C and C_m are the merged ones; K_{12} and K_{22} are the equilibrium constants for the corresponding reactions. Here, we assume that all water molecules are involved in the construction of the clathrate cages in the concentration range studied and the presence of the free water molecules can be ignored. The second step reactions of eq 3 and 4 are considered to be much faster than the others and to be in equilibrium throughout the course of the relaxation processes. By assuming that the concentrations of the species C and A_2 are much lower than the others, the above scheme gives the following rate equations:

$$m\frac{d[C_m]}{dt} = k_{11}[AB_l][A] - k_{-11}\left(\frac{[C_m]}{K_{12}}\right)^{1/m} \tag{5}$$

$$\frac{d[A_n]}{dt} = k_{21}[A]^2 - k_{-21}\left(\frac{[A_n]}{K_{22}[A]^{n-2}}\right) \tag{6}$$

where the brackets indicate the molar concentration.

Expanding eq 5 and 6 in the vicinity of the equilibrium concentrations and following the usual procedure, we obtain a secular equation $|a_{ij} - \lambda\delta_{ij}| = 0$, which gives the two solutions

$$\lambda_{1,2} = 2\pi f_{r1,2} = \frac{a_{11} + a_{22}}{2} \pm \left[\left(\frac{a_{11} - a_{22}}{2}\right)^2 + a_{12}a_{21}\right]^{1/2} \tag{7}$$

where λ_is ($i = 1, 2$) are the reciprocal relaxation times and where the a_{ij} terms are given by

$$\begin{aligned} a_{11} &= k_{11}\{[AB_l] + [A] + [AB_l][A]/(m^2[C_m])\} \\ a_{12} &= k_{11}(n/m)[AB_l] \\ a_{21} &= k_{21}mn[A] \\ a_{22} &= k_{21}(n^2[A] + [A]^2/[A_n]) \end{aligned} \tag{8}$$

The maximum excess absorptions per wavelength for the two relaxation processes are expressed by

$$\mu_{m1} = (\pi\Gamma_1/2RT\beta_s)(\Delta V_1 + \phi_1\Delta V_2)^2 \tag{9}$$

$$\mu_{m2} = (\pi\Gamma_2/2RT\beta_s)(\phi_2\Delta V_1 + \Delta V_2)^2 \tag{10}$$

where R is the gas constant, T the absolute temperature, and β_s the adiabatic compressibility of the solution; ΔV_1 is the adiabatic volume change for the formation of C_m by eq 3, and ΔV_2 that for the formation of A_n by eq 4. The Γ_i and ϕ_i terms represent the following quantities:

$$\Gamma_1 = \frac{k_{11}[AB_l][A]/m^2}{\lambda_1(1 - \phi_1\phi_2)} \qquad \Gamma_2 = \frac{k_{21}[A]^2}{\lambda_2(1 - \phi_1\phi_2)} \tag{11}$$

$$\phi_1 = (\lambda_1 - a_{11})/a_{12} \qquad \phi_2 = (\lambda_2 - a_{22})/a_{21} \tag{12}$$

If we know the values of l, m, and n, together with those of the composite equilibrium constants defined by

$$\beta_1 = (k_{11}/k_{-11})^m K_{12} \qquad \beta_2 = (k_{21}/k_{-21})K_{22} \tag{13}$$

the equilibrium concentrations of the reaction species can

TABLE II: Thermodynamic and Kinetic Parameters for Aqueous Solution of *tert*-Butyl Alcohol at 25 °C

Composition of the species AB_l, C_m, and A_n	$l = 25$, $m = 2$	$n = 3$
Equilibrium constant	$\beta_1 = 0.50$	$\beta_2 = 0.057$
Forward rate constant	$k_{11} = 1.5 \times 10^8$ M^{-1} s^{-1}	$k_{21} = 2.3 \times 10^6$ M^{-1} s^{-1}
Adiabatic volume change	$\Delta V_1 = -19$ cm^3/mol	$\Delta V_2 = 0.7$ cm^3/mol

be determined. Then, the rate constants k_{11} and k_{21} are evaluated from the observed relaxation frequencies by the relations

$$k_{21} = \frac{1}{b_{22}}\left\{\frac{\lambda_1 + \lambda_2}{2} - \left[\left(\frac{\lambda_1 + \lambda_2}{2}\right)^2 - g\lambda_1\lambda_2\right]^{1/2}\right\} \quad (14)$$

$$k_{11} = \frac{\lambda_1(\lambda_1 - k_{21}b_{22})}{b_{11}(\lambda_1 - k_{21}b_{22}/g)} \quad (15)$$

where $g = b_{11}b_{22}/(b_{11}b_{22} - b_{12}b_{21})$ and $b_{ij} = a_{ij}/k_{i1}$.

The value of l was determined from the μ_{m1} curve in Figure 3. By extrapolating the low-concentration branch of this curve to $\mu_{m1} = 0$, we obtain $C_A = 1.85$ M. At this concentration, almost all alcohol molecules are expected to be accommodated in single-clathrate cages and to be of the form AB_l. Then, the composition at this concentration gives $l = 25$. The values of the parameters m, n, β, and β_2 were determined so that the k_{11} and k_{21} values are calculated to be invariable over the whole concentration range studied. The calculating procedure was as follows. With a given set of values for the parameters, the k_{21} values were calculated by eq 14. Then, the mean value of k_{21} was employed to evaluate k_{11} by eq 15. Thus, a number of similar calculations were repeated by varying the individual values of the parameters independently. The determined values for the parameters are those which minimize the sum of the squares of the relative deviations of k_{11} and k_{21} from each mean value. The simulation was carried out using a computer program. The parameters and the rate constants obtained are shown in Table II. Here, both the root-mean-square deviations of k_{11} and k_{21} are 8.5%. Then, the relaxation frequencies were recalculated using eq 7. Figure 2 shows that the calculated f_{ri} values represent fairly well the observed ones over the whole concentration range studied.

The maximum excess absorptions per wavelength μ_{mi} were calculated by eq 9 and 10, and were fitted to the observed ones by regarding the ΔV_i values as adjustable parameters. The ΔV_i values obtained are also shown in Table II. Figure 3 shows that the calculated μ_{m1} value agrees well with the observed one. Here, it is noted that the calculated μ_{m1} value represents well a feature of the observed one; it increases steeply with increasing C_A immediately before attaining a maximum. Figure 3 also shows that the calculated μ_{m2} value conforms to the observed one in a qualitative nature, but the agreement between the two values is not satisfactory. Improvement on this point must await further study.

Discussion

Glew and his co-workers[21] argued that *tert*-butyl alcohol is surrounded by a clathrate cage in aqueous solution, and Blandamer et al.[7] discussed the ultrasonic absorption properties for aqueous solutions of the alcohol in terms of merging processes of clathrate hydrates. The NMR shifts observed in the solution also support this idea.[22] The present treatment of the faster relaxation process is associated with the results of these studies and is consistent with the concept of "iceberg" formation around the nonpolar groups.[23] The obtained hydration number of the alcohol, i.e., $l = 25$, agrees with the value from NMR measurements.[15] The merged clathrate C_2 is composed of four alcohol and fifty water molecules, and the latter is expected to be sufficient to enclose the former from the expression of Pottel and Kaatze.[17] These results are consistent with the solution model assumed. The hydration model does not envisage a permanently frozen sphere of solvent molecules around the guest molecules, but a continuously changing hydration sphere in which the water molecules possess a high degree of hydrogen bonding.[22] Then, an interpretation of the k_{11} value in Table II requires further considerations of the solution structure; probably, an additional assumption that the clathrate hydrates constitute large aggregates would explain the slow rate.

Equilibrium studies have revealed that stable trimer molecules of *tert*-butyl alcohol exist in organic solvents[24-26] as well as in pure liquid;[27] the associations are due to hydrogen bonding. The species A_3 in the present study may have some correspondence to these trimers. The ultrasonic absorption in solutions containing some alcohol in organic solvents was also interpreted as due to alcohol association reactions.[18-20] However, the kinetic results reported could not be compared with the present one owing to different reaction mechanisms. Recently, Yasunaga et al.[28] studied association reactions of benzoic acid and its derivatives in *N*,*N*-dimethylformamide and reported rate constants for the formation reactions of the cyclic dimers of $2\text{–}3 \times 10^7$ M^{-1} s^{-1} (at 20 °C). The k_{21} value in Table II lies near these values and is considered to be of reasonable order of magnitude.

As has already been mentioned, the absorption parameter B depends on the alcohol concentration and markedly exceeds the classical absorption (Table I). This fact suggests that at least one relaxation effect exists in high frequency range above the observed one. In fact, Stone and Pontinen[29] reported a concentration dependent dispersion in the velocity of sound in GHz frequency range. Since the B value exhibits analogous concentration dependence to that of A_1, the relaxation process is probably associated with some equilibrium involving the species proposed here. However, the data do not allow further detailed analysis, and the study was confined to investigating the two observed relaxation processes.

While the proposed mechanism is, of course, not unique, it is the simplest mechanism consistent as a whole with observed relaxation absorptions. Recently, the authors have observed that Rayleigh scattering for this system exhibits a maximum near PSAC. This phenomenon may be interpreted by the solution model proposed. A study is now in progress.

References and Notes

(1) C. J. Burton, *J. Acoust. Soc. Am.*, **20**, 186 (1948).
(2) D. Sette, *Nuovo Cimento*, **1**, 807 (1955).
(3) L. R. O. Storey, *Proc. Phys. Soc. B*, **65**, 943 (1952).
(4) S. Parthasarathy and M. Pancholy, *Z. Angew. Phys.*, **10**, 453 (1958).
(5) S. G. Bruun, P. G. Sørensen, and A. Hvidt, *Acta Chem. Scand., Ser. A*, **28**, 1047 (1974).
(6) M. J. Blandamer, N. J. Hidden, M. C. R. Symons, and N. C. Treloar, *Trans. Faraday Soc.*, **64**, 3242 (1968).
(7) M. J. Blandamer, D. E. Clarke, N. J. Hidden, and M. C. R. Symons, *Trans. Faraday Soc.*, **64**, 2691 (1968).

(8) R. N. Barfield and W. G. Schneider, *J. Chem. Phys.*, **31**, 488 (1959).
(9) J. H. Andreae, P. D. Edmonds, and J. F. McKellar, *Acustica*, **15**, 74 (1965).
(10) V. P. Romanov and V. A. Solovyev, *Sov. Phys.-Acoust.*, **11**, 68, 219 (1965).
(11) V. A. Solovyev, C. J. Montrose, M. H. Watkins, and T. A. Litovitz, *J. Chem. Phys.*, **48**, 2155 (1968).
(12) M. J. Blandamer, "Water-A Comprehensive Treatise", Vol. 2, F. Franks, Ed., Plenum Press, New York, N.Y., 1973, Chapter 9.
(13) N. Tatsumoto, *J. Chem. Phys.*, **47**, 4561 (1967).
(14) H. G. Hertz, *Ber. Bunsenges. Phys. Chem.*, **68**, 907 (1964); H. G. Hertz and M. D. Zeidler, *ibid.*, **68**, 821 (1964).
(15) E. V. Goldammer and H. G. Hertz, *J. Phys. Chem.*, **74**, 3734 (1970).
(16) M. V. Sarojini, *Trans. Faraday Soc.*, **57**, 1534 (1961).
(17) R. Pottel and U. Kaatze, *Ber. Bunsenges. Phys. Chem.*, **73**, 437 (1969).
(18) R. S. Musa and M. Eisner, *J. Chem. Phys.*, **30**, 227 (1959).
(19) J. Lang and R. Zana, *Trans. Faraday Soc.*, **66**, 597 (1970).
(20) F. Garland and J. Rassing, *J. Phys. Chem.*, **75**, 3182 (1971).
(21) D. N. Glew, H. D. Mak, and N. S. Rath, "Hydrogen-Bonded Solvent Systems", A. K. Covington and P. Jones, Ed., Taylor and Francis, London, 1968, p 195.
(22) R. G. Anderson and M. C. R. Symons, *Trans. Faraday Soc.*, **65**, 2550 (1969); B. Kingston and M. C. R. Symons, *J. Chem. Soc., Faraday Trans. 2*, **69**, 978 (1973).
(23) H. S. Frank and M. W. Evans, *J. Chem. Phys.*, **13**, 507 (1945).
(24) M. Saunders and J. B. Hyne, *J. Chem. Phys.*, **29**, 1319 (1958).
(25) W. Storek and H. Kriegsmann, *Ber. Bunsenges. Phys. Chem.*, **72**, 706 (1968).
(26) E. E. Tucker and E. D. Becker, *J. Phys. Chem.*, **77**, 1783 (1973).
(27) J. Feeney and S. M. Walker, *J. Chem. Soc. A*, 1148 (1966).
(28) T. Yasunaga, S. Nishikawa, and N. Tatsumoto, *Bull. Chem. Soc. Jpn.*, **44**, 2308 (1971).
(29) J. Stone and R. E. Pontinen, *J. Chem. Phys.*, **47**, 2407 (1967).

Photochemistry of Phenyl Alkyl Ketones. The Lifetime of the Intermediate Biradicals

Richard D. Small, Jr., and Juan C. Scaiano*

Radiation Laboratory,[1] University of Notre Dame, Notre Dame, Indiana 46556 *(Received April 28, 1977)*

Publication costs assisted by the Division of Physical Research of the U.S. Energy Research and Development Administration

The lifetimes of a number of biradicals produced in the photochemical Norrish type II reaction of phenyl alkyl ketones have been measured. The decay of the biradicals was followed by monitoring the competition with electron transfer to paraquat dications using nanosecond laser techniques. The lifetimes are rather insensitive to changes in temperature, substitution, and solvent, and are typically in the neighborhood of 100 ns. It is concluded that intersystem crossing is the main factor determining the biradical lifetimes. The rate constant for electron transfer to paraquat dications is 3.7×10^9 M^{-1} s^{-1} in methanol at room temperature for 1,4-ketyl–alkyl biradicals, and considerably higher for diketyl biradicals, apparently reflecting a change in path degeneracy. Oxygen behaves as a biradical scavenger with a rate constant of 6.2×10^9 M^{-1} s^{-1} in methanol. The lifetimes of the excited ketone triplets have also been determined at room temperature under the experimental conditions employed; this is an important parameter in determining the viability of the measurements of biradical lifetimes by this technique.

Introduction

With increasing frequency biradicals are being proposed as intermediates in thermal and photochemical reactions. In most cases, establishing conclusively the intermediacy of biradicals is a difficult task, and their intrinsic properties, such as lifetime, possibility of intermolecular reactions, and multiplicity usually remain a subject of considerable speculation.

The photolysis of phenyl alkyl ketones bearing γ-hydrogen atoms is known to result in the formation of 1,4-biradicals via an intramolecular hydrogen abstraction which in simple cases proceeds exclusively from the triplet manifold [i.e., the Norrish type II reaction, (1)].[2]

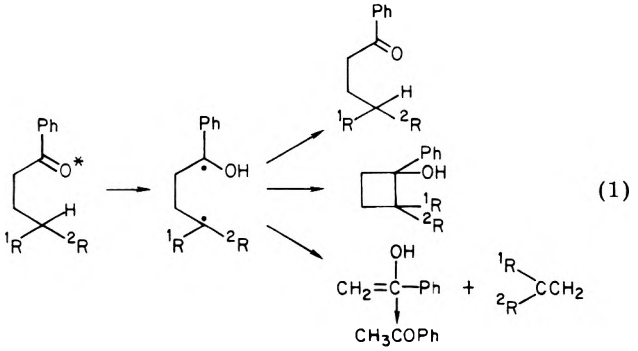

(1)

Reaction 1, where the asterisk denotes the triplet state, is probably one of the best studied examples of a process involving the intermediacy of biradicals with submicrosecond lifetimes. Quantum yield measurements and trapping experiments have led to a considerable understanding of some biradical properties.[3-6] In a number of cases, trapping experiments carried out under steady state irradiation have led to the evaluation of the product of the rate of trapping times the lifetime of the biradical ($k_T\tau_B$).[3-5] However, the value of τ_B can be evaluated only if a reasonable estimation of k_T can be made. The simplest assumption (which though reasonable has not been proved to be correct) is that the biradical reacts with the same rate constant as a free radical of similar substitution at the reactive center; this approach has been used by Wagner,[4] O'Neal,[5] and ourselves.[3] Unfortunately, the free radical reactivities of the biradical traps used in solution (e.g., thiols[4] and selenoketones[3]) are rather uncertain.

In a recent publication we reported for the first time the lifetime of the biradical from γ-methylvalerophenone (^1R = ^2R = Me) in methanol using a time-resolved laser photolysis technique.[7] This measurement involved the study of the time profiles for the formation of paraquat radical ions ($PQ^{+\cdot}$) in the reaction of the biradical with 1,1′-dimethyl-4,4′-bipyridilium dications (paraquat, PQ^{2+}), reaction 2.

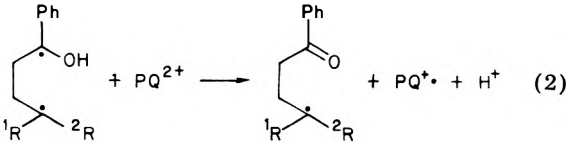

(2)

The stable paraquat radical ion ($PQ^{+\cdot}$) has a broad absorption band in the red region of the visible spectrum

SCHEME I

$$K \xrightarrow{h\nu} {}^1K$$
$${}^1K \rightarrow {}^3K$$
$${}^3K \xrightarrow{\tau_T^{-1}} B$$
$$B \xrightarrow{\tau_B^{-1}} \text{decay processes}$$
$$B + PQ^{2+} \xrightarrow{k_T} PQ^{+\cdot} + R\cdot + H^+$$

(λ_{max} 603 nm).[8] The time profile for the formation of $PQ^{+\cdot}$ incorporates information on both k_T and τ_B, since reaction 2 competes with the processes which determine τ_B.[7,9]

In this study we use the technique mentioned above to examine the lifetimes of a series of biradicals derived from phenyl alkyl ketones. We have also examined the effect of temperature, solvent, and xenon on the values of τ_B and k_T. Our studies of oxygen scavenging of biradicals[9] have been extended to include valerophenone and hexanophenone. In general the lifetimes of the biradicals have been found to be rather insensitive to substitution or changes in the media and strongly support the idea that can inversion is the main factor determining the values of τ_B, as proposed by Bartlett and Porter[10] and Closs.[11] A number of triplet lifetimes in hydroxylic solvents are also reported.

Results

Scheme I shows the relevant processes pertaining to the photochemistry of phenyl alkyl ketones in the presence of paraquat dications, where K represents the ketone and the superscripts 1 and 3 represent excited singlet and triplet states.[7,9,12] The unimolecular decay of the biradical (B) has been represented by a single reaction. No assumption is made at this point as to which are the rate-determining factors (and therefore τ_B determining). Some of the radical ions $PQ^{+\cdot}$ decay by reaction with R·,[7] but this is a comparatively slow process (even if it is nearly diffusion controlled) and need not be considered in the time scale of our experiments.

Equation 3 can be derived from Scheme I and, as shown

$$\ln \frac{[PQ^{+\cdot}]_\infty}{[PQ^{+\cdot}]_\infty - [PQ^{+\cdot}]_t} = (\tau_B^{-1} + k_T[PQ^{2+}])t \qquad (3)$$

before,[7] it represents adequately the kinetic behavior of the system. The same equation can be expressed in terms of the absorbance of the paraquat radical ions (measured at 632.8 nm), eq 4.

$$\ln \frac{A_\infty}{A_\infty - A_t} = (\tau_B^{-1} + k_T[PQ^{2+}])t \qquad (4)$$

The absorbances were determined from the oscilloscope traces in the appropriate manner. The data from the photographs was digitized and stored on paper tape; thereafter, the coefficients of eq 4 were obtained by least-squares treatment of the data from single traces or by computer averaging of the signals from several traces (see Experimental Section). The latter procedure was found to be extremely useful in the case of weak signals, e.g., for low $[PQ^{2+}]$ in *tert*-butyl alcohol–glycol mixtures (vide infra).

In order for eq 4 to be valid a number of conditions have to be fulfilled by the system.[7,9] Essentially, the formation of the biradicals has to be a fast process compared with their decay. This means that the laser pulse (8–10 ns), the singlet lifetime,[13] and the triplet lifetime[14] have to be short compared with the buildup of the concentration of radical ions. While the first two conditions are easily fulfilled, the third one (i.e., triplet lifetime) requires a careful choice of substrate and experimental conditions. γ-Methylvalerophenone has ca. 2-ns triplet lifetime[14,15] and easily fulfills this condition over a range of temperatures. Valerophenone and hexanophenone have triplet lifetimes in the neighborhood of 17 ns in methanol (vide infra) and can be studied at room temperature if one allows for some interference at high PQ^{2+} concentrations. Butyrophenone has a considerably longer lived triplet[14] and quite clearly does not fulfill the condition of short triplet lifetime.

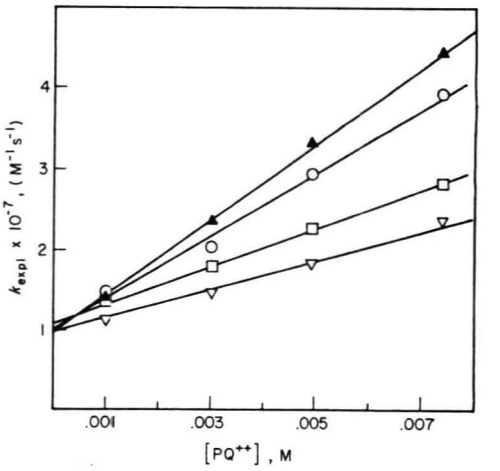

Figure 1. Dependence of k_{expt} with the concentration of paraquat dications at different temperatures for γ-methylvalerophenone in methanol: (▲) 50 °C; (○) 21 °C; (□) 5 °C; (▽) −15 °C.

Our experimental system has been improved considerably since our previous reports[7,9] (see Experimental Section) and has allowed us to extend the effective concentration range of PQ^{2+}, with a considerable improvement in the values of k_T. The rise time of the detection system is <5 ns.

The experimentally determined values correspond to k_{expt}, that is

$$k_{expt} = \tau_B^{-1} + k_T[PQ^{2+}] \qquad (5)$$

The values of k_{expt} are then plotted vs. $[PQ^{2+}]$, leading to k_T and τ_B. Figure 1 shows the results for γ-methylvalerophenone at several temperatures. The values of τ_B^{-1} (i.e., the intercept) are constant within our experimental error and do not show any definite trend with temperature. Therefore, the rate of decay of the biradicals is temperature independent [$E_a = (0 \pm 0.3)$ kcal/mol].

The values of k_T show considerable temperature dependence in the range examined. The rate for the trapping reaction can be adequately fitted by

$$k_T = 10^{11.4} \exp(-2500/RT)\ M^{-1}\ s^{-1}$$

For comparison, a plot of $-R[\ln (T/\eta)]$ vs. T^{-1} for methanol gives a formal activation energy for diffusion of 3.0 kcal/mol.

The temperature dependence of the triplet lifetimes makes it impossible to extend these studies to hexanophenone or valerophenone, since our experience indicates that the behavior of the triplet state significantly affects the kinetic plots when $k_{expt}^{-1} \sim 2.5\tau_T$, where τ_T is the lifetime of the triplet state.

The effect mentioned above is exemplified in Figure 2 for hexanophenone in methanol. The error introduced by the slight curvature has more effect on k_T than on τ_B, since at low concentrations of PQ^{2+} the triplet lifetimes do not have a significant effect on the measurements.

TABLE I: Solvent and Substituent Effects

Ketone (solvent), τ_B, k_T	[PQ][a]	N[b]	$10^{-7}k_{expt}$[c]
γ-Methylvalerophenone[d]	0.0062	7	2.86
(wet acetonitrile)[e]	0.0041	2	2.63
τ_B = (70 ± 10) ns	0.0031	3	2.15
k_T = (2.4 ± 0.5) × 10^9 M^{-1} s^{-1}	0.0021	3	1.91
	0.0010	7	1.70
γ-Methylvalerophenone	0.0051	5	0.99
(*tert*-butyl alcohol-glycol)[f]	0.0034	6	1.02
τ_B = (103 ± 15) ns	0.0020	3	0.98
$k_T \leq 2 \times 10^8$ M^{-1} s^{-1}	0.0010	4	0.97
Valerophenone	0.0074	4	3.19
(methanol)	0.0049	4	2.71
τ_B = (102 ± 15) ns	0.0030	5	2.10
k_T = (3.6 ± 0.8) × 10^9 M^{-1} s^{-1}	0.0010	5	1.34
Valerophenone	0.0062	4	2.84
(wet acetonitrile)	0.0047	3	2.56
τ_B = (71 ± 10) ns	0.0031	3	2.13
k_T = (2.4 ± 0.5) × 10^9 M^{-1} s^{-1}	0.0021	2	2.00
	0.0010	3	1.63
	0.0005	2	1.56
Hexanophenone	0.0080	5	2.48
(methanol)	0.0059	5	2.23
τ_B = (107 ± 15) ns[g]	0.0046	4	2.11
k_T = (3.5 ± 1.0) × 10^9 M^{-1} s^{-1}	0.0043	5	2.06
	0.0023	11	1.65
	0.0014	5	1.48
	0.0011	4	1.42
	0.0009	4	1.22
	0.0004	5	1.03

[a] In mole/liter. [b] Number of oscilloscope traces used for computer averaging (see Experimental Section). [c] In units of M^{-1} s^{-1}. [d] See also ref 7 and 9 for methanol as solvent. [e] 10% water (v/v). [f] 3:2 mixture in volume (η = 13.0 cP at 24 °C). [g] The error is larger than in the other examples because of some curvature, see Figure 2.

Table I shows the results for γ-methylvalerophenone, valerophenone, and hexanophenone in various solvents at room temperature.[16] The biradical lifetimes are only slightly dependent on the solvent. In the case of *tert*-butyl alcohol–glycol mixtures, the quantum yield of trapping is very small and essentially leads to $k_{expt} \sim \tau_B^{-1}$, while A_∞ was roughly proportional to $[PQ^{2+}]$ in the concentration range examined.

We have considered the possibility that the lifetime of the biradicals could be dependent on the presence of heavy atoms. We carried out a number of experiments using xenon at a pressure of several atmospheres, sufficient to produce a concentration of ca. 0.5 M in methanol. A series of experiments were carried out in the low concentration region ([PQ] < 0.0015 M). The effect is very small and within experimental error; however, repetition of the

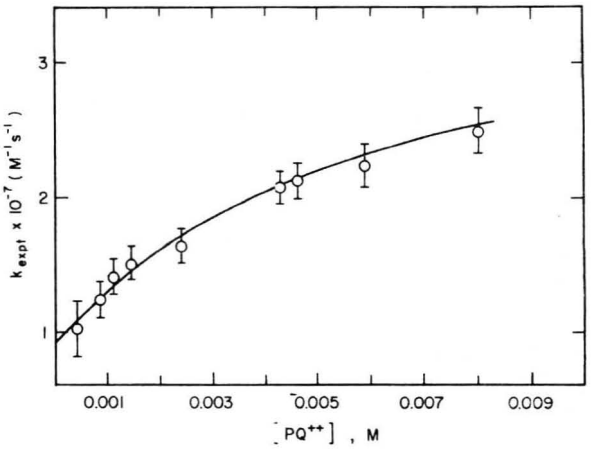

Figure 2. Plot of k_{expt} vs. $[PQ^{2+}]$ for hexanophenone in methanol at 21 °C, see text.

experiment several times systematically produced a ratio of τ_B(degassed)/τ_B(xenon) > 1.0, the best estimate being 1.05 ± 0.07. At higher concentrations of PQ^{2+} the same effect is apparent but the ratio of k_{expt} values tends to approach to one, while the error limits remain essentially constant.

We have extended our studies of oxygen scavenging or biradicals[9,17] to include hexanophenone and valerophenone in methanol. Oxygen formally decreases the biradical lifetime, which is now given by

$$(\tau_B')^{-1} = \tau_B^{-1} + k_{O_2}[O_2] \quad (6)$$

where k_{O_2} is the rate of interaction with oxygen and τ_B' is the formal lifetime in the presence of a constant concentration of oxygen. In both cases we obtain k_{O_2} = 6.2 × 10^9 M^{-1} s^{-1}, a value essentially identical with that previously reported for γ-methylvalerophenone.[9] Each value of k_{O_2} is based on five concentrations of PQ^{2+} and two oxygen concentrations, using between three and six oscilloscope traces for each pair of values of $[PQ^{2+}]$ and $[O_2]$.

We have also carried out a number of experiments with butyrophenone, for which the assumption of short triplet lifetime mentioned above does not hold. In principle, the reaction can be analyzed as two first-order consecutive processes, where the product measured ($PQ^{+\cdot}$) is produced only in the second step. Some triplet quenching by PQ^{2+}, though rather inefficient, tends to complicate the results (that is, the pseudo-first-order rate constants for *both* steps depend on $[PQ^{2+}]$). After attempting to interpret the data from the time profiles using a variety of mathematic approaches we felt that the only reliable conclusion is that

TABLE II: Summary of Kinetic Parameters at Room Temperature

Ketone	Solvent	$k_q\tau_T$[a,b]	τ_T[c]	τ_B[c]	k_T[d]
γ-Methylvalerophenone	Benzene	9.5[e]	1.9[e]	42[f]	
γ-Methylvalerophenone	Methanol	26	4.7	97[g]	3.8 × 10^9
γ-Methylvalerophenone	Wet acetonitrile[h]	18	2.5	70	2.4 × 10^9
γ-Methylvalerophenone	*tert*-Butyl alcohol-glycol[i]	6.6	28	103	≤2 × 10^8 [j]
Valerophenone	Methanol	90	16	102	3.6 × 10^9
Valerophenone	Wet acetonitrile[h]	63	8.7	71	2.4 × 10^9
Butyrophenone	Wet acetonitrile[h]	1100	150	(110)[k]	(2.4 × 10^9)[k]
Hexanophenone	Methanol	96	17	107	3.5 × 10^9
1,4-Diphenyl-1-hydroxy-4-butanone	Methanol	8.1	1.5	84[l]	9 × 10^9[l]

[a] In units of M^{-1}. [b] k_q taken as 5 × 10^9 M^{-1} s^{-1} in benzene for *cis*-1,3-pentadiene and assumed dependent solely on viscosity, leading to 5.5 × 10^9 M^{-1} s^{-1} in methanol, 7.2 × 10^9 M^{-1} s^{-1} in wet acetonitrile, and 2.3 × 10^8 M^{-1} s^{-1} in 3:2 *tert*-butyl alcohol-glycol. [c] In nanoseconds. [d] In units of M^{-1} s^{-1}. [e] Reference 14. [f] Reference 9. [g] Reference 7 and this work. [h] Acetonitrile containing 10% water (v/v). [i] *tert*-Butyl alcohol:ethylene glycol 3:2 (v:v). [j] k_{expl} almost independent of $[PQ^{2+}]$, see Table I. [k] Assuming k_T and basing τ_B on an A_∞^{-1} vs. $[PQ^{2+}]^{-1}$ plot (eq 7), neglecting triplet quenching by PQ^{2+}. The error could be as large as ±50 ns. [l] Based on initial rates, see text.

the lifetime of the biradical was within a factor of 2 of the triplet lifetime.

An alternative approach is to use the values of A_∞ to obtain a value of $k_T\tau_B$. The values of A_∞ are not affected by the lifetime of the triplet. The quantum yields of $PQ^{+}\cdot$ generation are proportional to A_∞, i.e., $[\Phi(PQ^{+}\cdot) = \alpha A_\infty]$ therefore we can write[7]

$$\frac{1}{A_\infty} = \alpha + \frac{\alpha}{k_T\tau_B[PQ^{2+}]} \tag{7}$$

above α is a proportionality constant.

From a plot of A_∞^{-1} vs. $[PQ^{2+}]^{-1}$ we obtain $k_T\tau_B = 290$ M^{-1} in wet acetonitrile. Assuming $k_T = 2.4 \times 10^9$ M^{-1} s^{-1}, i.e., the same value as for γ-methylvalerophenone and valerophenone, we obtain $\tau_B = (110 \pm 50)$ ns, where the large error reflects the uncertainty of this type of methods involving intercept-to-slope ratios, as well as the fact that the method ignores triplet quenching. These experiments were carried out in wet acetonitrile because significant photoreduction takes place in methanol and the $\dot{C}H_2OH$ and PrĊ(OH)Ph radicals generated in the process react with PQ^{2+} yielding $PQ^{+}\cdot$ via electron transfer.[8,18]

Another example examined is the photolysis of 1,4-diphenyl-1-hydroxy-4-butanone, which produces a diketyl biradical which is then trapped at both ends, reactions 8–10.

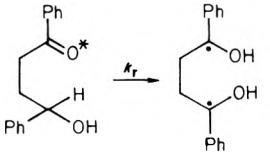

(8)

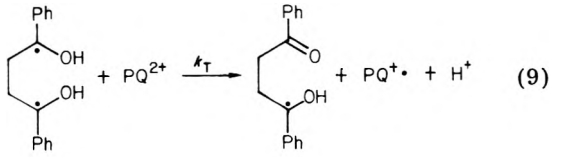

(9)

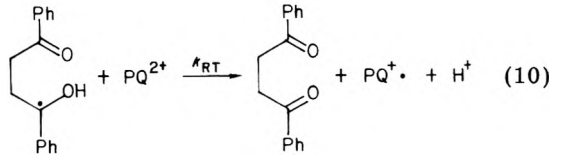

(10)

The detection of 1,4-diphenyl-1,4-butanedione in the products,[12] as well as the absence of a decay following the buildup of $PQ^{+}\cdot$ in the oscilloscope traces, supports the mechanism proposed. In this case the time profile for the formation of $PQ^{+}\cdot$ reflects reactions 9 and 10 and their competition with the unimolecular decay of the biradical. The kinetics of the process correspond to that of a series of two consecutive first-order (or pseudo-first-order) reactions giving the same product with rate constants k_1 and k_2, respectively, so that

$$k_1 = \tau_B^{-1} + k_T[PQ^{2+}]$$
$$k_2 = k_{RT}[PQ^{2+}]$$

This type of kinetic scheme has been known for a long time;[19] the analysis of the time profiles is a difficult problem since both k_1 and k_2 are dependent on $[PQ^{2+}]$. We attempted several of the mathematical approaches suggested in the literature,[19] and found that the use of initial rates for k_1 and "tails" for k_2, in both cases combined with computer averaging of the signals from several oscilloscope traces gave the best results. The rate constant k_T is the one most affected by error; k_{RT} can be determined from the "tails" where reaction 9 is essentially complete. In the case of the lifetime, since this is determined in the limit when $[PQ^{2+}] \to 0$, then, in the low concentration region $k_1 \sim \tau_B^{-1} >> k_2$ and τ_B is not largely affected by error. For studies in the 0.0004–0.0070 M region we obtain: $\tau_B = (84 \pm 15)$ ns; $k_T = (9 \pm 3) \times 10^9$ M^{-1} s^{-1}; and $k_{RT} = (4.8 \pm 1.4) \times 10^9$ M^{-1} s^{-1}.

The observation that k_T is larger than k_{RT} seems to be real and apparently reflects the different path degeneracy of reactions 8 and 9.

As pointed out throughout this section, the lifetime of the triplet state is a critical parameter in determining the viability of biradical lifetime measurements using the technique described herein. While the triplet lifetimes are well known in benzene, the values in methanol and the other solvents in Table I have not been reported.[20]

Table II shows a summary of triplet and biradical lifetimes under several experimental conditions. The triplet lifetimes have been determined by quenching with *cis*-1,3-pentadiene. The rates of quenching were assumed to be solely dependent on the viscosity of the solvent and k_q was taken as 5×10^9 M^{-1} s^{-1} in benzene.

Discussion

In recent reports we have established that the generation of $PQ^{+}\cdot$ in the systems considered herein is a biradical process and cannot be attributed to interaction with the ketone triplet state.[7,9,12] Further, we have shown that the values of k_T and τ_B obtained from the analysis of the time profiles are consistent with the $k_T\tau_B$ values which can be obtained by alternative techniques.[7]

The values of k_T are similar to the rate of electron transfer from a number of ketyl radicals.[22] The activation energy for the reaction in methanol (2.5 kcal/mol) seems to reflect mainly the temperature dependence of the viscosity of the solvent. The same is true when we compare the values in methanol and in *tert*-butyl alcohol–ethylene glycol mixtures (Table I).

We have mentioned above that a common assumption in steady state irradiation studies has been that the rate of reaction of the biradical can be taken as that of a free radical with the same substitution at the reactive center. This assumption seems to be correct *for this particular example*.[24] Whether this conclusion can be generalized or not remains an open question and the answer can only be provided by the study of a series of biradical traps, in particular examples involving slower rates of trapping.

Table II shows a summary of the biradical lifetimes obtained in this study, along with those previously reported. The main characteristic of the results seems to be their insensitivity to substitution and temperature. There is a trend of the τ_B values to increase with increasing solvent viscosity, an effect which we also observed in nonpolar solvents.[3]

We come now to the question of which factors determine these lifetimes. Two simple explanations can be proposed: (a) spin inversion, which is a requirement for the unimolecular decay of the biradical (see reaction 1), is the rate-determining step, and (b) the lifetime is determined by the rate of the chemical reactions involved in the decay processes, with spin flip being fast compared with these. The possibility of the decay being controlled by bond rotation is regarded as belonging to possibility (b). We have recently suggested that (a) is the simplest way in which the difference in biradical lifetimes between gas-phase and solution experiments can be accomodated.[5,7]

The idea that spin inversion (or triplet–singlet intersystem crossing) is the rate-determining process has been previously suggested by Bartlett and Porter in a study of the photochemistry of cyclic-azo compounds;[10] other authors have argued against it.[26] Closs[11] has examined

CINDP effects in the photochemistry of cyclic ketones, to which the radical-pair theory of polarization was applied. These results also support the idea that intersystem crossing is the rate-determining step, while the singlet biradicals generated in the process have subnanosecond lifetimes.

The results reported in this paper strongly support spin flip as the main factor determining the biradical lifetimes. For example, if we want to assume that chemical reaction is the rate-determining process, then the temperature independence of the lifetimes would mean that the rate of decay has to be attributed to roughly the preexponential factor for the fragmentation, i.e., $A \sim 10^7$ s^{-1}. This seems to low for a unimolecular reaction involving the loss of three internal rotations, the expected value being in the vicinity of 10^{10} s^{-1},[27] taking into account the spin multiplicity; further, we would expect some dependence of τ_B with the stability of the olefin produced. On the other hand, if we assume that the rate of intersystem crossing determines τ_B, then temperature independence follows as a natural consequence.

The dependence of the lifetimes with the viscosity of the solvent seems consistent with a similar effect observed in nonpolar solvents.[3] The interpretation of these results seems difficult, particularly in view of the fact that the theories which apply to intersystem crossing in biradicals involve approximations which are only valid for weakly correlated biradicals (i.e., longer biradicals).[11,28] Until more general theories become applicable we can only speculate that the changes in τ_B reflect an effect on the tumbling of the biradical.[29]

On the basis of our conclusion that τ_B is determined by spin inversion, then its temperature independence can be taken to mean that the triplet level in the biradical cannot lay more than 0.5 kcal/mol below the singlet level.

Following the observations mentioned above we thought τ_B could be sensitive to heavy atom effects, particularly if spin–orbit coupling played an important role in the decay process. Our experiments with γ-methylvalerophenone in the presence of ~0.5 M xenon suggest a ratio of lifetimes of 1.05 ± 0.07 in the absence and presence of xenon. If the effect is real (and it is difficult to decide whether this is the case) it would correspond to a rate constant for assisted intersystem crossing in the neighborhood of 10^6 M^{-1} s^{-1}. In any case, it is clear that the effect, if any, is small and presumably reflects the importance of modes of interaction other than spin–orbit coupling.

The curvature observed in the plot in Figure 2 deserves some comment. When the triplet lifetime becomes comparable with k_{expt}^{-1} the plots show negative curvature. In the limiting case, i.e., for very large concentrations of PQ^{2+} the plot should become horizontal and reflect the triplet lifetime

$$\lim_{[PQ^{2+}] \to \infty} (k_{expt}) = \tau_T^{-1}$$

As in the case of butyrophenone (see above) eq 7 should hold. This was confirmed to be the case for hexanophenone in methanol. The equation is only valid for laser pulses of constant intensity.[7]

Lewis[30] has examined the photochemistry of 1,4-diphenyl-1-hydroxy-4-butanone and its monodeuterated derivative (in the γ position). From a study of the isotopic "memory" of the biradical back reaction to the ketone, he concludes that the ratio of rate constants for bond rotation and reabstraction is 0.17. Combining this value with the lifetime of 84 ns reported above we estimate that the barrier to bond (β–γ) rotation is ca. 7.2 kcal/mol,[31] which should be compared with a value of 4–5 kcal/mol for the less hindered biradical from γ-methylvalerophenone.[7,33]

Finally, the interaction of oxygen with type II biradicals seems to be a general reaction. The enhancement of quantum yields of fragmentation observed in benzene for γ-methylvalerophenone[9,17] is probably also a rather general phenomenon, but tends to be masked by oxygen quenching of the triplet state in other cases. We are currently trying to develop general methods for the unequivocal separation of biradical and excited state reactions.

Conclusion

While biradicals are proposed as reaction intermediates quite frequently, absolute measurements of lifetimes or reactivities are uncommon.[7,9,25,35]

A systematic study of the effect of substitution, solvent, and temperature on the lifetime of the biradicals generated in the Norrish type II reaction from the triplet manifold shows, as the main characteristic, its insensitivity to all these parameters. Note, for example, that for all the ketones and conditions in Figure 1 and Table II the dispersion of τ_B values in polar solvents is not large. This observation supports triplet–singlet intersystem crossing as the main, if not the only, factor determining the biradical lifetimes, with the singlet biradical virtually collapsing to molecular products before spin–flip or intermolecular reactions can occur.[11] If the triplet state of the biradical lies below the singlet,[36] the energy gap cannot exceed 0.5 kcal/mol.

Diketyl biradicals react in electron transfer reactions somewhat faster than alkyl–ketyl biradicals, apparently reflecting a change in path degeneracy.

While the behavior of the excited triplet does not seem to affect or determine the behavior of the resulting biradical, it does have a decisive effect on the viability of biradical studies using the paraquat trapping technique.

Experiment Section

Materials. Butyrophenone, valerophenone, and hexanophenone were Aldrich products. γ-Methylvalerophenone was a generous gift from Dr. K. U. Ingold; 1,4-diphenyl-1-hydroxy-4-butanone was prepared by the method of Lutz and Gillespie.[37] Methanol and ethylene glycol were Fisher products, acetonitrile was MCB (spectroquality), *tert*-butyl alcohol was obtained from Baker and recrystallized several times.

Paraquat dichloride was a K & K product and high purity xenon was obtained from Baker.

cis-1,3-Pentadiene (K & K) was used for the quenching studies.

Laser Photolysis. A Molecton UV-400 nitrogen laser was used for excitation and a Spectra Physics Model 135 He/Ne laser as monitor. A scheme of the apparatus has been published.[7] A few improvements in the detection system deserve mention: A modified selected RCA 1P28 photomultiplier was used with a circuit developed by D. W. Schutt, G. Beck, *et al.* The phenolic base of the photomultiplier was opened to permit the addition of ferrite beads concentric with the active dynode leads and to allow direct connection and shield bypassing of the signal coaxial cable to dynode number five. Additional dampling was provided by 47-ohm resistors in each of the dynode leads which then were connected to the bypassed voltage divider. This results in a very fast response and a significant improvement in the signal-to-noise ratios. The beam from the monitor laser was incident on a light guide (0.25 in., 50 cm long of Suprasil quartz from Jena) which in turn transmitted the light to the photomultiplier cathode. This acts as an diffusor for the light, while at the

same time eliminates scattered light (because of the angular dependence of the transmittance by fiber optics). This detection system, combined with a Tektronik 7623 storage oscilloscope gave a rise time of ≤5 ns.

The optical path of the reaction cells was 0.3 cm, which combined with the narrow beam from the He/Ne laser gives an effective reaction volume of ca. 3×10^{-3} mL; this allows the concentration of the light from the nitrogen laser using a combination of spherical and cylindrical lens which leads to the generation of a comparatively high initial concentration of biradicals.

Quenching Studies. The data on triplet lifetimes in Table II were obtained by standard quenching techniques using *cis*-1,3-pentadiene as quencher taking $k_q = 5 \times 10^9$ M^{-1} s^{-1} in benzene[14] and assuming viscosity dependence for k_q in all other solvents. Analysis for acetophenone was carried out on a 5-ft. column of DC-11 silicone oil on Chromosorb W using a Beckman GC-5 chromatograph equiped with f.i.d. detection.

Preparation and Irradiation of the Samples. The technique employed for the laser experiments was the same as in previous studies.[7,9] The samples containing xenon were examined prior to addition of the gas, then under xenon, and finally degassed again and reexamined. The results in degassed solutions were the same regardless of whether the measurements were carried out before or after the xenon experiments suggesting that the changes in τ_B, if any (see Results section), do not reflect an effect resulting from changes in the composition of the samples.

In the quenching studies the samples (1 cm^3) were contained in matched tubes made of precision bore tubing (i.d. 0.2500 ± 0.0002 in., from Lab Crest Scientific, made of Corning 7740 glass). They were degassed by three freeze–pump–thaw cycles. They were irradiated in a merry-go-round using a Rayonet reactor fitted with 16 RPR-3500 lamps.

Treatment of the Data. The oscilloscope traces were photographed and the information was then digitized and stored on paper tape. The data from one or several traces were used to obtain k_{expt}. In the latter case the program would define by extrapolation back to the baseline a "zero time" for each trace, then calculate the optical densities and the left side term in eq 4, and average the data from several pictures, typically between three and eight.

References and Notes

(1) The research described herein was supported by the Division of Physical Research of the U.S. Energy Research and Development Administration. This is Document No. NDRL-1756 from the Notre Dame Radiation Laboratory.
(2) E.g., P. J. Wagner, *Acc. Chem. Res.*, **4**, 168 (1971).
(3) J. C. Scaiano, *J. Am. Chem. Soc.*, **99**, 1494 (1977).
(4) P. J. Wagner and R. G. Zepp, *J. Am. Chem. Soc.*, **94**, 287 (1972); P. J. Wagner, P. A. Keslo, and R. G. Zepp, *ibid.*, **94**, 7480 (1972).
(5) H. E. O'Neal, R. G. Miller, and E. Gunderson, *J. Am. Chem. Soc.*, **96**, 3351 (1974).
(6) M. Hamity and J. C. Scaiano, *J. Photochem.*, **4**, 229 (1975).
(7) R. D. Small and J. C. Scaiano, *J. Phys. Chem.*, **81**, 828 (1977).
(8) P. Hyde and A. Ledwith, *J. Chem. Soc., Perkin Trans. 2*, 1768 (1974).
(9) R. D. Small and J. C. Scaiano, *Chem. Phys. Lett.*, **48**, 354 (1977).
(10) P. D. Bartlett and N. A. Porter, *J. Am. Chem. Soc.*, **90**, 5317 (1968).
(11) G. L. Closs, *Adv. Magn. Reson.*, **7**, 157 (1974); G. L. Closs and C. E. Doubleday, *J. Am. Chem. Soc.*, **94**, 9248 (1972); **95**, 2735 (1973); **94**, 9248 (1972).
(12) R. D. Small and J. C. Scaiano, *J. Photochem.*, **6**, 453 (1977).
(13) J. Faure, J. P. Fouassier, and D.-J. Lougnot, *J. Photochem.*, **5**, 13 (1976); D.-J. Lougnot, J. P. Fouassier, and J. Faure, *J. Chim. Phys.*, **72**, 125 (1975).
(14) J. Grotewold, D. Soria, C. M. Previtali, and J. C. Scaiano, *J. Photochem.*, **1**, 471 (1972–1973).
(15) This value corresponds to benzene. See below for studies in methanol and water–acetonitrile.
(16) For γ-methylvalerophenone in methanol at room temperature refer to Figure 1 or ref 7 and 9.
(17) J. Grotewold, C. M. Previtali, D. Soria, and J. C. Scaiano, *J. Chem. Soc., Chem. Commun.*, 207 (1973).
(18) L. K. Patterson, R. D. Small, and J. C. Scaiano, *Radiat. Res.*, in press.
(19) A. A. Frost and R. G. Pearson, "Kinetics and Mechanism", 2nd ed, Wiley, New York, N.Y., 1961, Chapter 8; D. French, *J. Am. Chem. Soc.*, **72**, 4806 (1950); C. G. Swain, *ibid.*, **66**, 1696 (1944).
(20) Wagner[21] has examined the lifetime of triplet valerophenone in a number of solvents.
(21) P. J. Wagner, *J. Am. Chem. Soc.*, **89**, 5898 (1967).
(22) For $\dot{C}H_2OH$ the rate constant for electron transfer to PQ^{2+} is 3×10^8 M^{-1} s^{-1} (ref 18). More substituted ketyl radicals react considerably faster.[23]
(23) L. K. Patterson, R. D. Small, and J. C. Scaiano, to be published.
(24) Another example where this assumption holds has been recently reported by Berson et al.[25] in the case of trimethylenemethane biradicals.
(25) M. S. Platz and J. A. Berson, *J. Am. Chem. Soc.*, **98**, 6743 (1976).
(26) L. M. Stephenson and J. I. Brauman, *J. Am. Chem. Soc.*, **93**, 1988 (1971).
(27) H. E. O'Neal and S. W. Benson, *J. Phys. Chem.*, **71**, 2903 (1967); S. W. Benson, "Thermochemical Kinetics", Wiley, New York, N.Y., 1968.
(28) Atkins et al. have developed a theory for short chains; however, we could not find any quantitative examples of the application of this model to biradical lifetimes. P. W. Atkins and G. T. Evans, *Chem. Phys. Lett.*, **24**, 45 (1974).
(29) Attempts to carry out biradical lifetime measurements in neat-glycol led to complex kinetics, apparently because the radical produced in reaction 2 abstracts from glycol producing $CH_2(OH)\dot{C}HOH$ which also generates $PQ^{+}\cdot$. The radical ion $PQ^{+}\cdot$ also shows some unusual properties in this solvent, e.g., it is very stable to oxygen. There is however indication that τ_B is somewhat longer in glycol than the ~100 ns values which are given in Table II for other solvents.
(30) F. D. Lewis, *J. Am. Chem. Soc.*, **92**, 5602 (1970).
(31) Using a preexponential factor of ca. $10^{11.5}$ s^{-1} for bond rotation.[32] If intramolecular hydrogen bonding in the biradical is very important the *A* factor could be somewhat higher, leading also to an increase in the barrier to rotation. In any case this should not exceed 8.5 kcal/mol.
(32) D. M. Golden, S. Furuyama, and S. W. Benson, *Int. J. Chem. Kinet.*, **1**, 57 (1969).
(33) In a recent report[7] we estimated the barrier for bond rotation in the biradical from γ-methylvalerophenone as 4–5 kcal/mol, based on a comparison with Wagner's results[4] for 4-methyl-1-phenyl-1-hexanone. It has been recently suggested[34] that the rotational barriers in biradicals are rather sensitive to substitution. In this particular example the changes do not occur at the radical center and are unlikely to introduce differences of more than a fraction of a kilocalorie per mole. We are grateful to the referees of a previous publication[7] for calling to our attention this point.
(34) P. B. Dervan and T. Uyehara, *J. Am. Chem. Soc.*, **98**, 1962 (1976).
(35) S. L. Buchwalter and G. L. Closs, *J. Am. Chem. Soc.*, **97**, 3857 (1975).
(36) W. G. Dauben, L. Salem, and N. J. Turro, *Acc. Chem. Res.*, **8**, 41 (1975).
(37) R. E. Lutz and J. S. Gillespie, Jr., *J. Am. Chem. Soc.*, **72**, 2002 (1950).

COMMUNICATIONS TO THE EDITOR

Further Evidence on the Formation of Trapped Electrons in γ-Irradiated Crystals of Hydrocarbon–Urea Clathrates as Studied by Electron Spin Resonance

Publication costs assisted by Hiroshima University

Sir: The formation of trapped electrons (e_t^-) in urea clathrates (inclusion compounds) was first reported by Nowak and Stachowicz.[1] They found that 77-K radiolysis of urea clathrates containing *n*-octane (*n*-C_8) or 1-octene gave an ESR spectrum composed of wide-spread multilines and an intense single line and that the singlet decays under illumination with visible light or thermal bleaching at 180 K. Because of its instability and ESR characteristic, the singlet was attributed to e_t^-. Recently, the present author observed independently of their work a similar single ESR line in γ-irradiated urea clathrates containing various hydrocarbon derivatives. The finding of their work prompted me to report the interesting nature of e_t^- formed in urea clathrates, for e_t^- formation in crystals is rare except in alkali halide crystals ("F" centers).[2]

n-Octane (*n*-C_8), which was obtained from Tokyo Kasei Kogyo with 99% purity, was further purified by stirring with H_2SO_4 containing 5% HNO_3, washing with water and aqueous solutions of K_2CO_3, followed by drying over $CaCl_2$ and passage through a 30-cm column containing a fine grade of silica gel. The effluent was fractionally distilled using a packed distillation column with 20 theoretical plates and the middle fraction was used for the preparation of samples. Other organic compounds (reagent grade) were used as received.

Reagent grade urea (Wako Pure Chemical Ind. Ltd.) was further purified by crystallization from methanol solutions and dried over $CaCl_2$ under vacuum. Perdeuterated urea was prepared by the deuterium exchange of urea in solutions of D_2O (Merck Sharp and Dohm, Canada with 99.7% D). Deuterium oxide (30 mL) was introduced into an ampoule containing urea (3 g) in the vacuum line. After the urea dissolved, the resultant D_2O–H_2O mixture was vacuum-distilled. This treatment was repeated three times. Accordingly, the content of D is expected to be >98%.

A single crystal with a long hexagonal needle was obtained by slow cooling of a methanol solution containing *n*-C_8 and urea.[3] After being dried over calcium chloride in a desiccator, the single crystal was sealed in an ESR quartz tube on the vacuum line. Usually, polycrystalline urea clathrates were prepared by keeping mixtures of organic compounds (0.2 mL), methanol (about 0.01 mol per mol of urea),[4] and urea (0.25 g) in quartz ESR tubes (4-mm i.d., Suprasil) for several days. The temperatures of the complex formation were −55 °C for *n*-butane, −30 °C for *n*-pentane, 0∼5 °C for *n*-hexane and *n*-heptane, 10∼20 °C for *n*-octane, 1-octene, 1-octanol, *n*-octylamine, and di-*n*-butyl ether, 30 °C for *n*-hexadecane, and 80 °C for *n*-dotriacontane.

γ Irradiation was made with a ^{60}Co source (a dose rate of 1 Mrad h^{-1}) at 77 K in the dark for 3 h. In the single crystal work, the other end of the ESR tube was annealed at 300 °C to bleach out color centers formed in the quartz tube. The single crystal then was transferred to the annealed end and positioned in such a way that the crystal needle was vertical to the axis of the ESR tube. ESR measurements were done at 77 K in the dark using a conventional X-band spectrometer at a microwave power of 0.1 mW with 100-kHz modulation.

A stream of nitrogen gas which had been precooled and then brought to a controlled temperature with an electrical heater was used to warm samples. Photobleaching was carried out with a 100-W tungsten lamp, from which radiation was passed through glass filters.

Figure 1A shows the first derivative spectra of the single crystal. Both the intensity and the line shape of all the lines did not change during annealing at temperatures around 170 K.[5] An intense singlet which can be seen in the middle of the spectrum disappeared when the crystal was warmed at 195 K (Figure 1B). At the same time, signals due to alkyl radicals[6] were intensified; the spectra in Figures 1A and 1B were recorded with the same instrument gain.[7] Signals from urea radicals distort somewhat the alkyl radical lines in Figure 1B. The line width (ΔH) of the singlet as measured between points of maximum slope varied slightly with the orientation of the crystal needle about the magnetic field; $\Delta H_{\parallel} = 14.5 \pm 0.3$ and $\Delta H_{\perp} = 13.0 \pm 0.3$ G. The *g* factor varied from 2.0029 ± 0.0001 ($g_{\parallel}$) to 2.0026 ± 0.0001 ($g_{\perp}$). In the parallel run the singlet resolved into a doublet with the spacing of 5.1 ± 0.3 G when the second derivative spectrum was taken (Figure 1C). This splitting is attributable to the alkyl-radical lines superimposed on the singlet concerned, because the spacing of the doublet is exactly same as that between the two lines in the center of the solid line spectrum in Figure 1B as shown by arrows.

Figure 2A shows the effect of succesive photobleaching of finely powdered crystals of *n*-C_8–urea clathrates. Each photobleaching was done at 77 K for 10 min. Only 10% of the singlet species disappeared during the first photobleaching (λ_1 >780 nm), while under the same experimental conditions e_t^- produced in glassy 3-methylheptane was almost completely bleached. This low photobleaching efficiency would be due to the reflection of incident light by sample crystallites. It is to be noted that about 33% of the alkyl radicals disappeared after succesive photobleachings. The amounts which disappeared correspond to 65% of the singlet species bleached.[8]

Figure 2B shows the additive effect of 1-chlorooctane on *n*-C_8–urea clathrates. It can be seen that alkyl radicals originated from the chloride are produced instead of the singlet species. It is well known that electrons produced by ionizing radiation of glassy alkanes are preferably captured by added alkyl halides by the reaction, $RX + e^- \rightarrow R + X^-$.[9] Therefore, the singlet species can be ascribed to anionic species, i.e., urea radical anions or e_t^-. The spectrum of γ-irradiated polycrystalline urea consists of wide-spread asymmetrical lines (Figure 2C). The result shows that urea by itself does not give a singlet as observed in Figure 1. This fact strongly suggests that the singlet species is due to e_t^-. γ Irradiation of polycrystalline *n*-C_8–urea clathrates, which were prepared by keeping a mixture of *n*-C_8 and powdered urea (without methanol) in an ESR tube at 10 °C for several days, also gave an ESR spectrum similar to Figure 2A. The result indicates that the formation of e_t^- is not related to the presence of

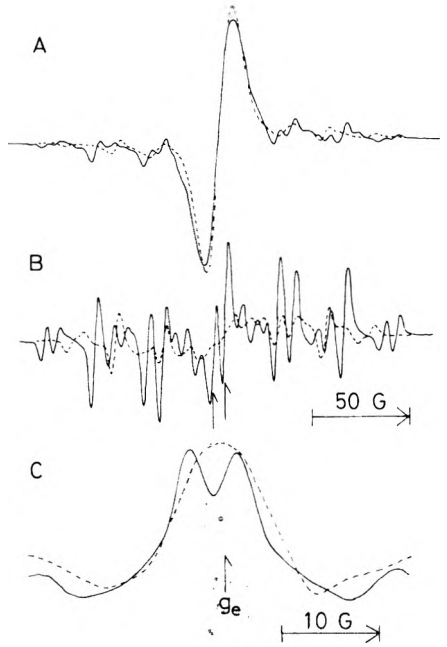

Figure 1. ESR spectra of a γ-irradiated single crystal of n-C_8–urea clathrate (solid (dotted) line spectra were recorded when the magnetic field is parallel (vertical) to the crystal needle): (A) measured at 77 K; (B) after bleaching at 195 K. (C) Second derivative presentation of the central singlets in spectra A. Magnetic field for free electron resonance is indicated by g_e (2.0023), whose position was calibrated by signals from water solutions of Fremy's salt: a = 13.05 ± 0.03 (M. T. Jones, *J. Chem. Phys.*, **38**, 2829 (1963)) and g = 2.005 560 ± 0.000 004 (M. T. Jones, S. A. Trugman, V. Rapini, and R. Hameed, *J. Phys. Chem.*, **81**, 664 (1977)).

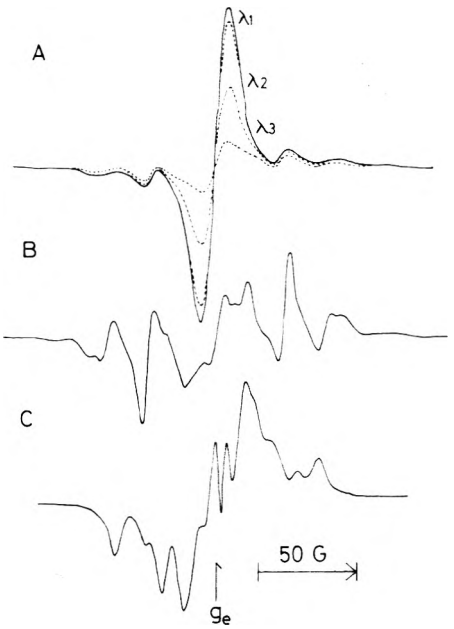

Figure 2. (A) ESR spectra showing the effect of succesive photobleaching (Toshiba IR-D1B (λ_1 >780 nm), V-R65 (λ_2 >625 nm), and V-O55 (λ_3 >525 nm) glass filters) of γ-irradiated finely powdered crystals of n-C_8–urea clathrates. (B) An ESR spectrum of γ-irradiated polycrystalline urea clathrates which were prepared by adding a mixture of 1-chlorooctane (30 vol %) and n-C_8 (70 vol %) to powdered urea. (C) An ESR spectrum of γ-irradiated polycrystalline urea.

methanol added as a solvent for clathrate formation. An ESR signal due to e_t^- could not be detected in γ-irradiated polycrystalline pure n-C_8 under the present experimental condition (minimum microwave power of 0.1 μW, 80-Hz modulation, and superheterodyne detection).[10]

The line width of e_t^- signals in polycrystalline n-C_8–urea clathrates was found to change from 13.8 ± 0.3 to 9.8 ± 0.3 G when urea-d_4 was used as the host molecule. This indicates interaction of e_t^- with urea protons and probably nitrogen nuclei also. A series of n-alkanes (n-C_5, n-C_6, n-C_7, n-C_{16}, and n-C_{32}) as guest molecules gave a line width ranging from 13.8 to 14.0 G. The values obtained in other hydrocarbon derivatives were 13.0 (n-butane), 14.2 (1-octene), 14.5 (1-octanol), 15.3 (n-octylamine), and 16.5 G (di-n-butyl ether).[11] It appears that the line width of e_t^- is induced to increase a little by substitution by nitrogen or oxygen.

The power saturation behavior of e_t^- was found to be more like that of alkyl radicals rather than that of e_t^- in glassy alkanes. The peak-to-peak amplitude of the e_t^- singlet in polycrystalline n-C_8–urea clathrates (a dose of 1 Mrad) reached a maximum at the microwave power of 3 mW. The corresponding microwave powers for e_t^- and alkyl-radical lines in glassy 3-methylheptane (a dose of 0.26 Mrad) were 0.03 and 10 mW, respectively. Since the anisotropic g factor of the paramagnetic species is closely related to power saturation phenomena,[12] the above result is rather consistent with the observation that the g factor of e_t^- in the single crystal of n-C_8–urea clathrates is anisotropic. The line-width change of the e_t^- singlet in the single crystal work may be attributed to unresolved anisotropic hyperfine couplings of protons and nitrogen nuclei. The yield of e_t^- vs. dose was studied in polycrystalline n-C_8–urea clathrates. It was observed that the yield increases linearly at first, then reaches a maximum around 20 Mrad. Doses given for the maximum yield of e_t^- in 3-methylpentane and 2-methyltetrahydrofuran glasses have been reported to be 1.6 and 4 Mrad, respectively.[13]

The anisotropic ESR parameters of e_t^- obtained in the present work suggest that the ground state wave function of e_t^- in urea clathrates cannot be described by a spherically symmetrical s-type wave function only and that nuclei surrounding e_t^- are situated in an orderly manner according to the symmetry of the crystal. Possible e_t^- sites may be suggested to be a space between a guest molecule and a tubular wall composed by urea and/or a tubular void between guest molecules. Further experiments are needed for determination of the e_t^- sites.

In a previous report[14] we postulated that in the radiation-induced polymerization of 1,3-butadiene in urea clathrates the observed monomer radical $CH_3CH{=}CH{-}CH_2\cdot$ is produced by proton transfer from urea to the intermediately produced butadiene radical anion. The observation of the e_t^- formation in n-butane–urea clathrates will support this scheme. Urea clathrates containing a mixture of n-butane (90 vol %) and 1,3-butadiene (10 vol %) did not yield e_t^- but the monomer radical from the butadiene.[15]

Trapped electron formation in thiourea clathrates was also examined. Thiourea clathrates with 2,3-dimethylbutane, 2,2,4-trimethylpentane, cyclohexane, and cyclooctane did not give a strong central singlet as observed in n-alkane–urea clathrates, but in the low field side they showed a broad line superimposed on free-radical lines. Cyclohexane–thiourea clathrates containing small amounts of benzene or cyclooctatetraene produced the corresponding radical anions from the additives together with free radicals from cyclohexane; cyclooctatetraene–thiourea clathrates chiefly yielded the radical anions of the guest molecules.[15] Experiments to investigate ionic processes in urea and thiourea clathrates are in progress.

Acknowledgment. I thank the Research Institute for Nuclear Medicine and Biology of Hiroshima University for

use of its facility for γ irradiation.

References and Notes

(1) Z. Nowak and W. Stachowicz, *Nukleonika*, **14**, 1113 (1969).
(2) L. Kevan, *Adv. Radiat. Chem.*, **4**, 181 (1974).
(3) W. Schlenk, *Annales*, **565**, 204 (1949).
(4) The addition of methanol is not always necessary for complex formation with *n*-alkanes.
(5) In the case of polycrystalline *n*-C_6–urea clathrates, the intensity of the central singlet was decreased by 40% on warming to 130 K. The residual disappeared around 165 K.
(6) A. Lund, *J. Phys. Chem.*, **76**, 1411 (1972).
(7) It is noted that areas under the integrated curves of Figure 1B are larger by about 30–40% than areas under those of the underlying alkyl-radical spectra in Figure 1A and that the ratios of yields between the singlet species (e_t^-) and the alkyl radicals in Figure 1A was 1:1.52. The integrated curves were obtained using an electronic integrator.
(8) These values were obtained from the corresponding integrated curves of Figure 2A.
(9) D. W. Skelly, R. G. Hayes, and W. H. Hamill, *J. Chem. Phys.*, **43**, 2795 (1965).
(10) The formation of e_t^- in polycrystalline *n*-alkanes, however, has been reported (M. Iwasaki, K. Toriyama, and T. Ohmori, *J. Phys. Chem.*, **72**, 4347 (1968).
(11) *n*-Butyronitrile and 1,3-diaminopropane gave weak e_t^- signals in comparison with underlying free-radical signals. *n*-Butyric acid and propionic acid *n*-butyl ester (*n*-butyl propionate) did not yield e_t^-. The formation of e_t^- could not be ascertained from the spectra of 2-butanone and 1,6-hexanediol. 1-Octanethiol gave a broad singlet on the low field side.
(12) A. Carrington and A. D. MacLachlan, "Introduction to Magnetic Resonance", Harper and Row, New York, N.Y., 1967.
(13) D. Lin and L. Kevan, *J. Chem. Phys.*, **55**, 2629 (1971).
(14) T. Ohmori, T. Ichikawa, and M. Iwasaki, *Bull. Chem. Soc. Jpn.*, **46**, 1383 (1973).
(15) T. Ichikawa, unpublished results.

Department of Applied Chemistry **Takahisa Ichikawa**
Hiroshima University
Senda-Machi, Hiroshima 730, Japan

Received May 11, 1977

Raman Investigations of 4A Molecular Sieves

Publication costs assisted by Merck Sharp and Dohme Research Laboratories

Sir: I. *N_2 Adsorption.* Molecular sieves and especially sieves of the A type provide a unique method for the separation of N_2 from other gases.[1] N_2 adsorption capacities of powdered 4A sieves have been reported for a variety of conditions.[1-3] Typically, such studies have relied on thermodynamic measures, e.g., measurement of the volume of gas desorbed, to estimate adsorptivity.[1b] We now report the use of Raman spectroscopy to estimate relative amounts of adsorbed N_2 on 4A sieves. As an example we show N_2 adsorptivity data for sieves[4] under ambient conditions (25 °C, 1 atm) which have (a) had no pretreatment, (b) been calcined to 400 °C in a muffle furnace; and (c) been washed in 0.2 N NaOH and then calcined to 400 °C in a muffle furnace.

Figure 1a displays part of the Raman spectrum of air.[5] The observed vibrational bands at 1555 and 2329 cm^{-1} are those characteristic of $^{16}O_2$ and $^{14}N_2$, respectively.[6a] Figure 1b displays the same portions of the Raman spectrum of 4A molecular sieves in air. Besides the normal scattering bands of air, two additional maxima at 2324 cm^{-1} (band separation = 4.3 ± 0.3 cm^{-1}) and 1548.5 cm^{-1} can be observed. Band positions were obtained from repeated scans[5] on several samples of sieves. These extra bands are due to adsorbed $^{14}N_2$ and $^{16}O_2$ since they show (a) shifts upon adsorption characteristic of nonpolar molecules,[7,8] (b) band widths less than 2 cm^{-1},[9] and (c) an experimental depolarization ratio of ca. 0.8, characteristic of randomized reflections from the powdered solid[5b] rather than the true depolarization of the gas, ρ_{N_2} = 0.02.

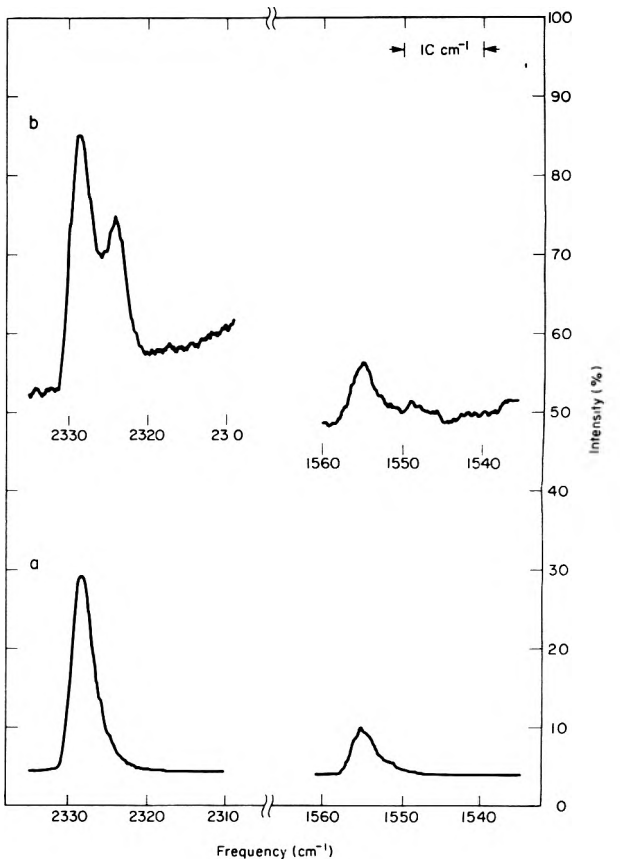

Figure 1. Raman spectra of (a) air and (b) 4A molecular sieves in the frequency regions of $^{14}N_2$ and $^{16}O_2$ scattering: Cary 82, slit = 2 cm^{-1}, excitation frequency = 514.5 nm, power = 500 mW.

TABLE I: Measured and Literature N_2/O_2 Ratios

	Raman measurements[a]	Literature
Air	4.0 ± 0.3	3.7[b]
Adsorbed to 4A sieves	8.4 ± 1.0	7.4 ± 1.0[c]

[a] Height 2324 cm^{-1} band/height of 1547 cm^{-1} band; ± average deviation of four samples. [b] Reference 15. [c] Extrapolated from Figures 1a and 1b of ref 1a.

TABLE II: Relative Scattering Intensities[a] of N_2 Adsorbed to NaA (4A) Molecular Sieves

Sieve identification no.	Relative adsorption: No pretreatment	400 °C calcination	0.2 N NaOH wash, 400 °C calcination
034	1.61	0.80	0.49
104	0.63	1.10	0.46
110	0.48	1.11	0.54
144	0.73	1.03	0.47

[a] Relative adsorptions are taken from the ratio of the height of the 2324-cm^{-1} band (adsorbed $^{14}N_2$) to that of the 2329-cm^{-1} band (atmospheric $^{14}N_2$).

Table I contains N_2/O_2 Raman scattering intensity ratios of free air and air adsorbed to 4A molecular sieves. That such relative ratios are proportional to gas concentrations can be seen by comparing these measured ratios to their respective literature values, also in Table I. Clearly, the Raman method distinguishes the concentration of the free gases (±10%) from that of the gases adsorbed to the 4A sieve (±15%).

As an example of the use of Raman spectroscopy to evaluate N_2 adsorptivity, we show relative N_2 scattering intensities (Table II), as defined by the ratio of the band

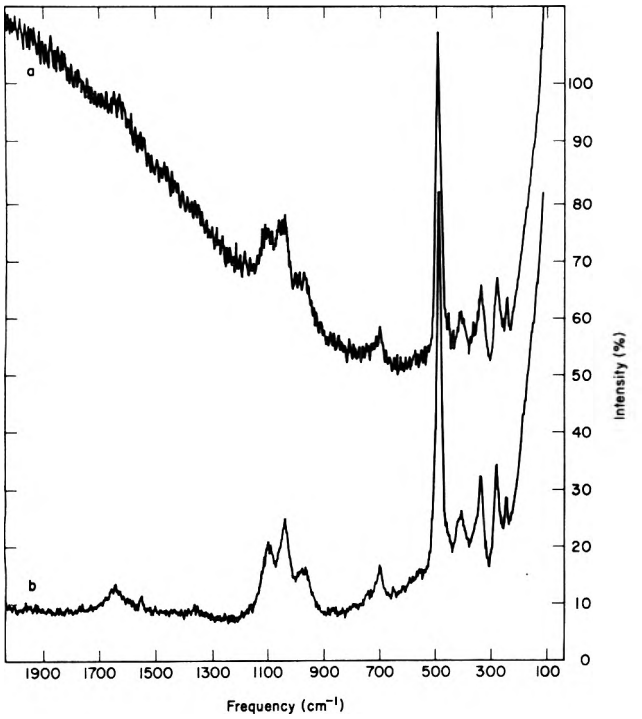

Figure 2. Raman spectra with associated fluorescence of 4A sieves (a) calcined at 400 °C and (b) washed with NaOH prior to calcining at 400 °C: Cary 82, slit = 5 cm^{-1}, excitation frequency = 514.5 nm, power = 200 mW.

height at 2324 cm^{-1} to that at 2329 cm^{-1}, for four different samples of sieves. The effect upon relative adsorptivity of calcining and caustic extracting[10] the sieves is also included. The untreated sieves show a 3.5-fold range in their N_2 capacities, whereas the treated sieves are more uniform in their adsorption capacities. The spread in N_2 adsorption capacities of the untreated sieves probably reflects a poisoning effect by adsorbed species (both organic and inorganic) on the sieve surface. Dry sieves[4] which are calcined at 400 °C show increased N_2 adsorption due to the removal of the organic surface impurities.[11] Sieves which are washed in 0.2 N NaOH and then calcined exhibit a somewhat diminished capacity for N_2 sorption as a result of "steaming" effects which occur when wet sieves are dehydrated at elevated temperatures.[8,12b]

Thus, Raman scattering can provide a unique in situ measurement of N_2 adsorbed on sieves which might be useful in kinetic and other studies.

II. *Reduction of Fluorescence.* The typical Raman spectrum of 4A molecular sieves,[7] as well as other adsorbents,[11] is often obfuscated by low-level fluorescent impurities. When these fluorescent impurities are caused by adsorbed species, e.g., hydrocarbons, rather than by structural impurities such as color centers, the fluorescence can be minimized by (1) removal of the impurity through pretreatment or burning with the laser, and (2) changing the excitation wavelength. The usual pretreatment method for A-type sieves involves heating at 350–500 °C for ca. 24 h, usually under vacuum, to desorb the impurities.[1-3,7] For other closely related material, e.g., silica, porous vycor, heating at 500–600 °C under O_2 for ca. 12 h is recommended for removing impurities.[11] While these methods are satisfactory for fluorescence reduction, they are time consuming, and, moreover, if the latter method were used for the A sieve, complete dehydration of the sieve would occur.[12a]

An interesting consequence of washing sieves with NaOH[10] is the diminution of the associated fluorescence in a relatively short period of time, 2 h, at temperatures well below those which cause complete sieve dehydration. Figure 2 shows Raman spectra[13] of the same sieve lot calcined at 400 °C for 1 h before (a) and after (b) washing with 0.2 N NaOH. The spectrum of the untreated sieve is identical with that in Figure 2a. Clearly the spectrum of the sieve washed with NaOH has considerably less background fluorescence and, therefore, more pronounced features. For example, the 1550-cm^{-1} $^{16}O_2$ band is prominent (S/N ~ 3) in the caustic washed sieves whereas it is obscured by fluorescence (S/N ~ 0.2) in the unwashed sieve.

Sieves that are heated to much higher temperatures, e.g., 600 °C for 5 h, also show fluorescence reduction but the improvement is only two-thirds of that achieved by washing. Moreover, such high temperatures alter cation positions in 4A sieves[12a] thus affecting subsequent adsorption. The reduction of fluorescence through washing with NaOH appears quite general[14] and, therefore, may be a useful technique for improving Raman spectra of 4A sieves and other alumina/silica adsorbents.

Acknowledgment. We thank Dr. Seemon Pines for his aid in the preparation of this manuscript.

References and Notes

(1) (a) A. M. Arkharov, B. P. Bering, I. A. Kalinnikova, and V. V. Serpinskii, *Izv. Akad. Nauk. SSSR, Ser. Khim.*, **6**, 1434 (1972); (b) A. M. Arkarov, I. A. Kalinnikova, and V. V. Serpinskii, *ibid.*, **3**, 538 (1972).
(2) E. I. Borzenko, *Zh. Prikl. Khim. (Leningrad)*, **42**(4), 891 (1969).
(3) M. Nakagaki and T. Fujie, *Yakugaku Zasshi*, **90**(3), 384 (1970).
(4) Linde 4A Molecular Sieves, powdered, 600 Mesh, ca. 2–4% hydration.
(5) Cary 82 spectrophotometer, Spectra-Physics argon laser Model 165, power = 500 mW, λ_{exc} 514.5 nm, slit = 2.0 cm^{-1}, pen period = 10 s, scan speed = 0.1 cm^{-1}/s, sensitivity = 1000 counts/s full scale.
(6) S. K. Freeman, "Applications of Laser Raman Spectroscopy", Wiley-Interscience, New York, N.Y., 1974: (a) p 314; (b) p 30.
(7) C. L. Angell, *J. Phys. Chem.*, **77**, 222 (1973).
(8) N. T. Tam, R. P. Cooney, and G. Curtheys, *J. Chem. Soc., Faraday Trans. 1*, **72**, 2577 (1976).
(9) H. Förster and M. Schuldt, *J. Chem. Phys.*, **66**, 5237 (1977).
(10) 1 gram of sieves is boiled for 15 min in a 0.2 N NaOH solution, washed free of excess base, filtered, pulverized, and calcined at 400 °C for 1 h.
(11) (a) E. Buechler and J. Turkevich, *J. Phys. Chem.*, **76**, 2325 (1972); (b) T. A. Egerton, A. H. Hardin, Y. Kozirovski, and N. Sheppard, *Chem. Commun.*, 887 (1971); (c) R. O. Kagel, *J. Phys. Chem.*, **74**, 4518 (1970).
(12) D. W. Breck, "Zeolite Molecular Sieves", Wiley, New York, N.Y.: (a) see p 133 and 442 *ff*; (b) p 490.
(13) Power = 200 mW, λ_{exc} = 514.5 nm, slit = 5.0 cm^{-1}, pen period = 5 s, scan speed = 1.0 cm^{-1}/s, sensitivity = 5000 counts/s full scale.
(14) Silica gel (J. T. Baker Co.) washed with 0.2 N NaOH[7] shows a 50% higher S/N (lower fluorescence) throughout its Raman spectrum (20–2500 cm^{-1}) than does either untreated silica gel or silica gel calcined at 600 °C in air for 2 h.
(15) R. C. Weast, Ed., "Handbook of Chemistry and Physics", 56th ed, Chemical Rubber Co., Akron, Ohio, 1976.

Merck Sharp and Dohme Research Laboratories
Division of Merck and Company, Inc.
Rahway, New Jersey 07065

David D. Saperstein*
Alan J. Rein*

Received June 20, 1977

High Protonic Conduction of Polybenzimidazole Films[1]

Publication costs assisted by the National Science Foundation

Sir: Pressed disks of polybenzimidazole[2] (PBI) are known to be insulators for electronic conduction.[3] We have confirmed this finding for polybenzimidazole film, but find that protonic conduction is high, the conductivity being in the semiconductor range.

TABLE I: Protonic Conductivity Results for PBI Film

Premeasurement humidity, %	Resistance, Ω		Conductivity	
	Bulk	Surface	Bulk,[a] Ω^{-1} cm^{-1}	Surface,[b] Ω^{-1}
0	7	16	2×10^{-4}	4×10^{-3}
7	3	11	5×10^{-4}	6×10^{-3}
15	2	4	8×10^{-4}	2×10^{-2}
31	3		5×10^{-4}	
100	2	13	8×10^{-4}	5×10^{-3}

[a] $\sigma(\Omega^{-1}\ \text{cm}^{-1}) = (1/R)(L/A) = 1.58 \times 10^{-3}(1/R)$. [b] $\sigma = (1/R)\{(r_1 - r_2)/2\pi[(r_1 + r_2)/2]\}$ where r_1 = i.d. of guard ring, 0.375 in. and r_2 = radius of small disk, 0.25 in.

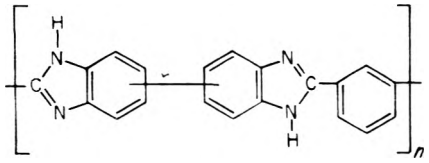

structural unit of PBI

Bulk and surface resistances were measured simultaneously with guard ring electrodes made of brass, using a modified Wheatstone bridge.[4] The electrodes were two disks, one 0.5-in in diameter, the other 0.25-in. with a guard ring of 0.5-in. o.d. and 0.375-in. i.d. They were set in a lucite holder and applied to the film with slight pressure. These electrodes measure electronic conduction. If they are covered with platinum black and exposed to hydrogen gas so that the hydrogen is absorbed onto the electrode surface they become "protodes" [$Pt/H_2 \rightleftarrows H^+$ (in polymer film) + e^- (in wire)][5] and measure protonic conduction. We have found that the hydrogen remains absorbed on the Pt black even when the electrodes are exposed to air for several weeks. This convenient property let us measure protonic conductivity without exposing the polymer film to gaseous hydrogen.

The PBI film was provided by Dr. H. J. Davis of Celanese Corp. and was fiber quality, approximately 0.01 mm thick. The film was boiled in distilled water for several hours to remove traces of lithium chloride, resulting in a salt-free film containing approximately 4 mol of tightly held water per structural unit.[6] Conduction measurements were made at room temperature in the presence of air. Because of the abundant evidence that absorbed water affects *electronic* conduction in polymers, the PBI films were pretreated by exposing them to a controlled humidity for 24 h and then quickly transferred to the measuring apparatus. Bulk and surface conductivity for electronic conduction were so low that they could not be measured with our equipment, but we could place an upper limit of $10^{-13}\ \Omega^{-1}\ \text{cm}^{-1}$ on them. On switching to the protodes the results shown in Table I were obtained. The change from the conductivity of an insulator to that of a semiconductor proves a change in conduction mechanism, probably from electronic conduction to protonic conduction. The results show no significant trend in conductivity as a function of premeasurement humidity.

The hypothesis that conduction involves a protonic mechanism has been put forward to explain the d.c. conductivity and low frequency dielectric loss of pressed disks of polyhexamethylene sebacamide, a linear polyamide.[7] Additional work[8,9] has led to the generalization that polyamide solids as a class exhibit proton conduction which is associated with the disordered parts of the solid. However, the conductivities of these materials were smaller by at least six orders of magnitude than our values for PBI film.

In explaining the high conductivity of PBI film, it may be significant that the polymer chains are linear, that the aromatic rings have a marked tendency to be coplanar, and that the film contains tightly held water molecules which may assist bifunctional proton transfer. Our decision to search for polymers with a high protonic conductivity was prompted by the known high speed of intramolecular proton transfer of diamines in aqueous solution.[10-13]

References and Notes

(1) This work was supported by the National Science Foundation.
(2) C. S. Marvel and H. A. Vogel, U.S. Patent No. 3 174 947; *Chem. Abstr.*, **63**, P7137h.
(3) H. A. Pohl and R. P. Chartoff, *J. Polym. Sci. Part A*, **2**, 2787-2806 (1964).
(4) A. P. Zielinger, M. Tapiera, and C. Noguet, *J. Phys. E*, **6**, 579 (1973).
(5) L. Glasser, *Chem. Rev.*, **75**, 21-65 (1975).
(6) Private communication from Dr. D. R. Wilson of Celanese Corp. and confirmed by us.
(7) W. O. Baker and W. A. Yager, *J. Am. Chem. Soc.*, **64**, 2171 (1942).
(8) R. H. Boyd, *J. Chem. Phys.*, **30**, 1276 (1959).
(9) D. W. McCall and E. W. Anderson, *J. Chem. Phys.*, **32**, 237 (1960).
(10) D. W. Fong and E. Grunwald, *J. Am. Chem. Soc.*, **94**, 7371 (1972).
(11) E. Grunwald, K. C. Chang, P. L. Skipper, and V. K. Anderson, *J. Phys. Chem.*, **80**, 1425 (1976).
(12) K. C. Chang and E. Grunwald, *J. Am. Chem. Soc.*, **98**, 3737 (1976).
(13) K. C. Chang, E. Grunwald and L. R. Robinson, *J. Am. Chem. Soc.*, **99**, 3794 (1977).

Chemistry Department
Brandeis University
Waltham, Massachusetts 02154

Donna Hoel*
Ernest Grunwald

Received June 24, 1977

ADDITIONS AND CORRECTIONS

1976, Volume 80

Maurice L. Huggins: Thermodynamic Properties of Liquids, Including Solutions. 12. Dependence of Solution Properties on Properties of the Component Molecules. Page 1318. Equation 3 should read

$$\epsilon_\Delta = \sigma_1^0(2\epsilon_{12} - \epsilon_{11} - \epsilon_{22})/2$$

Nothing else in the paper is affected by this correction.
—Maurice L. Huggins

Journal of Chemical and Engineering Data

OCTOBER 1977, Vol. 22, No. 4

TABLE OF CONTENTS

NEW COMPOUND SECTION

Supplementary material for this paper is available separately by direct order (consult the masthead page for ordering information); it will also appear following the paper in the microfilm edition of this journal.

* In papers with more than one author, the asterisk indicates the name of the author to whom inquiries about the paper should be addressed.

PULSED NANOSECOND FLUOROMETER SYSTEMS

For use in:

- Fluorescence and phosphorescence decay.
- Fast reactions and complex mechanisms.
- Time-resolved emission spectroscopy.
- Decay measurements in the vacuum UV.
- Fluorescent probe studies.
- Time-resolved fluorescence polarization anisotropy.

Total system with simplicity and versatility of operation.

Competent consulting and backup staff with expert knowledge in instrumentation and applications.

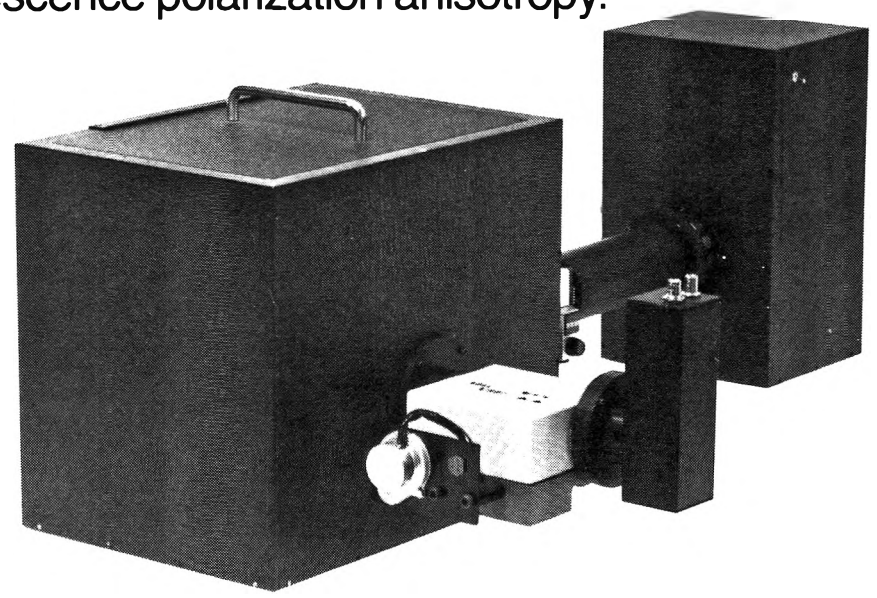

- High excitation source intensity and stability.
- High signal to noise ratio ● Low RF interference.
- Low scattered light levels ● Complete with computer interlace and software ● System installed, training in use of instrument.

SCIENTIFIC EXCELLENCE WITH EFFICIENT BUSINESS PRACTICES

PRA

Photochemical Research Associates Inc.
University of Western Ontario
Department of Chemistry
London, Ont., Canada N6A 3K7
(519) 679-6181 Telex 064-7597